# The Evolution of Escaping Ionizing Radiation from Galaxies and Active Galactic Nuclei Through Cosmic Time

by

Brent Matthew Smith

A Dissertation Presented in Partial Fulfillment
of the Requirements for the Degree
Doctor of Philosophy

Approved November 2019 by the
Graduate Supervisory Committee:

Rogier A. Windhorst, Chair
Judd Bowman
Sanchayeeta Borthakur
Nathaniel Butler
Phillip Mauskopf

ARIZONA STATE UNIVERSITY

December 2019

ABSTRACT

Reionization is the phase transition of intergalactic atoms from being neutral to becoming fully ionized. This process began $\sim 400$ Myr after the Big Bang, when the first stars and black holes began emitting ionizing radiation from stellar photospheres and accretion disks. Reionization completed when all of the neutral matter between galaxies became ionized $\sim 1$ Gyr after the Big Bang, and the Universe became transparent as it is today.

Characteristics of the galaxies that drove reionization are mostly unknown. The physical mechanisms that create ionizing radiation inside these galaxies, and the paths for this light to escape are even more unclear. To date, only a small fraction of the numerous searches for this escaping light have been able to detect a faint signal from distant galaxies, and no consensus on how Reionization was completed has been established.

In this dissertation, I discuss the evolution of the atomic matter between galaxies from its initially ionized state, to its current re-ionized state, potential sources of re-ionizing energy, and the theoretical and observational status of the characteristics of these sources. I also present new constraints on what fraction of the ionizing radiation escapes from galaxies using Hubble Space Telescope UV imaging, theoretical models of the stellar and accretion disk radiation, and models of the absorption of ionizing radiation by the intergalactic medium.

# DEDICATION

"*I believe our future depends powerfully on how well we understand this cosmos, in which we float, like a moat of dust, in the morning sky.*" – Carl Sagan

To my parents,

To my siblings, Amanda, Tyler, and Brendan,

To Melissa

TABLE OF CONTENTS

CHAPTER Page

APPENDIX Page

LIST OF TABLES

LIST OF FIGURES

Figure Page

# Chapter 1

# INTRODUCTION

## 1.1 The First Epoch of Ionization

The atomic matter of the Universe that comprises all galaxies, the stars and planets within them, and all matter between galaxies was initially in an ionized, or plasma state. This was a period that began in the first few seconds after the Big Bang, the time when the first atomic nuclei in the Universe formed. This period is known as Big Bang Nucleosynthesis (BBN), and marks the epoch when the Universe was filled with an expanding field of leptons, photons, protons, and neutrons. The universe was also hot and dense, and in thermal equilibrium at early time, which allowed for very high collision rates between these particles.

Reactions from the weak-interactions of neutrons, protons, electrons, positrons, electron neutrinos and anti-electron neutrinos evolved the ratio of neutrons to protons (n/p) over a time-scale of $\sim$200 s, which freezes at n/p $\sim 1/6$ (Mukhanov 2004). As the Universe expands and cools, neutrons become free to decay into protons, electrons, and an anti-electron neutrino, lowering n/p $\sim 1/7$. At this point, *nuclear* reactions mark the beginning of BBN, and the protons and neutrons rapidly combine to form deuteron, triton, helion, and $\alpha$-particles. The first deuteron particles form only when the Universe cools to a temperature below their binding energy of $\sim 2.2$ MeV, otherwise all particles are destroyed by photo-dissociation of the intense energy field of photons pervading the Universe. A much smaller amount of $^7$Li, $^7$Be, and $^6$Li nuclei are produced within a time-span of $\sim$1000 s, bringing BBN to a close.

The relative abundances of nuclei to hydrogen set by BBN are $\sim 0.245$ for alpha-particles, $\sim 10^{-5}$ for both deuteron and helion, $\sim 10^{-10}$ for $^{7}$Li and $^{7}$Be nuclei, and trace amounts of triton and $^{6}$Li. The temperature of the Universe after BBN is such that these particles exist in a plasma state with surrounding leptons, and pervading photons are thermalizing the plasma through collisions with these particles. The entirety of the plasma throughout the Universe is expanding and cooling, while early over-density fluctuation in the energy density of the Universe collapse from gravity. The collapse is followed by subsequent expansion again from internal pressure of the plasma over-densities, and these density fluctuations oscillate in this state until the end of this era at $\sim 380{,}000\,\mathrm{yr}$ after the Big Bang.

## 1.2 Recombination and the Cosmic Dark Ages

Once the Universe expanded and cooled to a temperature below the ionization energy of hydrogen (i.e., $k_B T < 13.6\,\mathrm{eV}$), free electrons and protons combined to form neutral hydrogen atoms (Peebles 1968; Zel'dovich, Kurt, and Syunyaev 1969). Neutral helium was able to form earlier on when the Universe was hotter, due to helium's higher ionization energy of $54.4\,\mathrm{eV}$. Electrons fall into lower energy atomic orbitals successively, emitting UV photons equal to the energy gap between these orbitals in the process. The Universe was still very opaque to the unbounded electrons that have yet to combine with free protons and atomic nuclei, and pervading photons continue to scatter continuously off of these electrons until the average temperature of the Universe fell to $T \sim 3000\,\mathrm{K}$. This phase transition of the matter in the Universe from ionized to neutral is known as the Recombination Era.

Once photons were no longer trapped by free-electrons, they became free to radiate

out into the Universe. These photons are observable today as the Cosmic Microwave Background (CMB), and are a relic of the light produced by the thermalization of energy from the Big Bang. The CMB began initially as optical red light following a blackbody spectrum, and was redshifted by the expanding universe by a factor of $z \sim 1089$ (e.g., Bennett et al. 2003) into the microwave region as observed today. Here, the redshift parameter $z$ is defined as

$$z = \frac{\lambda_{\rm obs} - \lambda_{\rm emit}}{\lambda_{\rm emit}} \tag{1.1}$$

where $\lambda_{\rm emit}$ is the wavelength of the light at the time of emission, and $\lambda_{\rm obs}$ is the wavelength of the light at the time of observation. A vast amount of information is imprinted on the spectrum and spatial anisotropies of the CMB, including the optical depth to the free-electrons, both before recombination and during the reionization of the Universe. Reionization introduces secondary anisotropies on the polarization map of the CMB, and is discussed more in §1.4.

The Universe at this point is in a state characterized by permeating hot, neutral, gaseous atoms, and remains mostly neutral for $\sim 1\,$Gyr. This gas cools as the Universe continues its expansion from $T \sim 3000\,$K to $\sim 60\,$K. The era when the Universe is filled with this cold, neutral gas is known as the Cosmic Dark Ages (Miralda-Escudé 2003). Relict CMB photons, redshifted to the infrared, are free to propagate unimpeded for long distances during this period, with no new light emitting sources producing photons. Neutral hydrogen atoms occasionally decay into a lower energy state through a spin-flip transition of its electron, releasing a photon with wavelength $\lambda \simeq 21\,$cm (Shapiro et al. 2006).

Since the Universe was expanding, not all electrons were able to combine with nuclei in time, and the recombination era grew less efficient at neutralizing atoms. This left a small amount of ions and free-electrons in the pervading medium. Simple

molecules were able to form through radiative, chemical processes in the cold, neutral matter. These reactions also cause the emission of photons in the infrared to radio, and some optical red light can even be present (Shchekinov and Entel 1984; Loeb and Barkana 2001; Mizusawa, Omukai, and Nishi 2005; Coppola et al. 2012). The most important molecule to form is molecular hydrogen, $H_2$, since the gravitational collapse of giant clouds of $H_2$ led to the birth of the first stars in the Universe. The Cosmic Dark Ages were brought to a close when these first massive structures formed, emitting optical and UV light into the Universe once again for the first time in $\sim 1\,\mathrm{Gyr}$.

## 1.3 Hierarchical Structure Formation and the First Sources of Light

Density fluctuations in the cold, neutral gas formed early on, when the Universe was in its oscillating plasma state before recombination. When the universe expanded and cooled enough, these fluctuations in density were frozen in place, and the oscillations from thermal expansion and gravitational collapse ceased. The size of these fluctuations are observed in the CMB map (e.g., Planck Collaboration 2018), and are on scales of galaxy clusters. Dark matter halos, as observed surrounding nearly all galaxies via gravitational effects on stellar structures, become important early on in the formation of galactic-sized structures. Numerical simulations show that the scale distribution of dark matter halos increase in frequency for smaller structures (e.g., Diemand, Moore, and Stadel 2005), and small halos eventually merge hierarchically to form larger structures. The gas in the universe does not initially trace the dark matter, though eventually falls into the potential well of these halos.

Internal gas pressure, as well as residual velocities from the recombination era initially supports the gas from collapse (Barkana and Loeb 2001; Tseliakhovich,

Barkana, and Hirata 2011). Simulations show that these effects limit the first structures of gas embedded in dark matter halos to be on the order of $\gtrsim 10^{5-6}\,M_\odot$. As the gas accretes onto these halos, it becomes heated by adiabatic compression and shocks up to the temperature of thermal and kinetic equilibrium. Here, the cold, denser cores in the halos, and outer layers accelerate and fall onto the outer layers of the cores, creating a shock through the collision at the interface of these layers (Vázquez-Semadeni et al. 2006). The shock increases the temperature at the shock front, which expands from internal pressure then cools isobarically (Shapiro and Kang 1987; Clarke and Bromm 2003). Once the shock forms, turbulence and thermal instabilities cause the matter to quickly fragment into smaller clumps (Padoan et al. 2001; Vázquez-Semadeni et al. 2006, e.g.,). These clumps fragment into masses at least as large as the local Jeans mass (Jeans 1902) of the region, with some turbulence transferred into the formed clump itself (e.g., McKee and Ostriker 2007; Hennebelle and Falgarone 2012).

The main factors that define the masses and sizes of these clumps are the collapse from self-gravity and internal support opposing collapse from internal pressure from heat, turbulence, and magnetic fields (e.g., Basu et al. 2009; Chen and Ostriker 2014). These magnetic fields typically form from either residual ions left from over from recombination, or from collisionally ionization from shocks (e.g., Glover et al. 2014). In the presence of low magnetic field strengths, or no fields, filamentary structures are seen to form from fragmentation of collapsed sheets of gas (e.g., Carroll-Nellenback, Frank, and Heitsch 2014), whereas the presence of magnetic fields shows a more spherical morphology (e.g., Banerjee et al. 2009; Gómez and Vázquez-Semadeni 2014). As the atomic gas cools and collapses, a gradual phase transition occurs, and the gas becomes molecular (Heitsch and Hartmann 2008; Heiner, Vázquez-Semadeni, and Ballesteros-Paredes 2015). The subsequent cooling of these clouds via molecular

ro-vibrational decay collapses these clouds further, producing molecular clouds with typical mass on the order of $\sim 10^6\,\mathrm{M}_\odot$ (Couchman and Rees 1986; Tegmark et al. 1997; Johnson and Bromm 2006). These structures are seen in the knots of filaments in the large-scale structure of the Universe (Yoshida, Hosokawa, and Omukai 2012), otherwise known as the Cosmic Web (Bond, Kofman, and Pogosyan 1996). These knots are the nurseries of the first protogalaxies in the Universe.

The gas in protogalaxies undergoes further cooling via $H_2$ radiative emission, and the internal thermal pressure decreases, allowing for gas to flow towards the center and compress the core. The cooling also decreases the local Jeans mass, allowing more fragmentation of smaller clumps (e.g., Bromm, Coppi, and Larson 2002). These smaller clumps then begin to collapse more rapidly, once they exceed the local Jeans mass of $\sim 10^3\,\mathrm{M}_\odot$ (Abel, Bryan, and Norman 2002). Eventually, $H_2$ cooling mechanisms (e.g., Omukai and Nishi 1998; Ripamonti and Abel 2004) become ineffective, and the collapse of the molecular cloud can heat its core adiabatically through collisions of molecules to a point of dissociation of the $H_2$ molecule. These temperatures restrict further collapse, leading to a dense core of mass $\sim 0.01\,\mathrm{M}_\odot$ with size $\sim 0.1\,\mathrm{AU}$ (Yoshida 2008).

These cores are surrounded by large envelopes of dense gas, which eventually collapse onto it. Through the accretion onto this core, the first star in the Universe is born (Abel, Bryan, and Norman 2002; Bromm, Coppi, and Larson 2002). Binary stellar systems also arise in this same scenario (Turk, Abel, and O'Shea 2009), though more fragmentation is believed to not occur in current models. The masses of these first stars can grow to masses typically between 20–500 $\mathrm{M}_\odot$ (O'Shea and Norman 2007), and as the first stars begin to contract further onto their main sequence, the bright ultraviolet (UV) emitted by stars limits their size by ionizing the surrounding

medium, preventing further collapse (McKee and Tan 2008; Hosokawa et al. 2011). This gives the first stars, otherwise known as Population III stars, a typical mass of $\sim 20\,\mathrm{M}_\odot$.

Population III stars in the mass range of $130 \lesssim \mathrm{M} \lesssim 250\,\mathrm{M}_\odot$ are known to end their lives via pair-instability supernovae (SNe; Fraley 1968), which leads to the complete destruction of the star, leaving no remnant behind. Stars with mass $15 \lesssim \mathrm{M} \lesssim 45\,\mathrm{M}_\odot$ die via core-collapse SNe (Zhang, Woosley, and Heger 2008) and $45 \lesssim \mathrm{M} \lesssim 100$ and $\mathrm{M} \gtrsim 260\,\mathrm{M}_\odot$ can collapse directly into black holes (BHs; Whalen and Fryer 2012). Some models also propose that the collapse of primordial gas can directly form BHs as well (e.g., Haehnelt and Rees 1993). These early black holes can accrete gas from their surrounding medium, and the accreting material will be heated from frictional collisions in the disk. The accreting disk begins shining light in the optical–X-ray spectrum from blackbody radiation of the disk itself, and from Compton up-scattering of lower-energy photons from high-energy electrons on the corona of the disk (e.g., Kuhlen and Madau 2005; Tanaka, Perna, and Haiman 2012). Both of these sources of light are predicted to emit abundant amounts of ionizing photons, which will contribute to next phase transition of the atomic matter of the Universe, the *re*ionization back into plasma.

## 1.4 The Reionization of the Intergalactic Medium

At the end of the cosmic dark ages, radiation emitted by the first luminous objects in the universe began to reionize the matter between galaxies, known as the intergalactic medium (IGM). Observations of the CMB constrain the median time of the beginning of this era to $\simeq 200$–$500\,\mathrm{Myr}$ after the Big Bang (Hinshaw et al. 2013; Planck

Collaboration 2018). These constraints are obtained by determining the scattering optical depth of CMB photons by free electrons in the Universe. These scattering events linearly polarize CMB photons on spatially large scales (Rees 1968), which can be observed in all-sky polarization maps of the CMB (e.g., Planck Collaboration 2016) and can be used to determine the redshift when free electrons pervaded the IGM, which was in the range $z\,simeq\,10$–$20$.

The far-ultraviolet (FUV) and X-ray ionizing radiation emitted by the first massive stars in the first star-forming galaxies (SFGs), or accretion disks around supermassive black holes in early Active Galactic Nuclei (AGN), are the main candidates to have initiated the epoch of cosmic reionization (e.g., P. Madau et al. 2004). Of particular interest is the UV ionizing continuum produced by these sources with wavelength $\lambda \leq 912$Å, also known as Lyman Continuum (LyC). This radiation has the energy required to free a bound electron in a hydrogen atom, equal to 13.6 eV. Photons with wavelengths shorter that 912Å (known as the Lyman limit) impart additional energy onto electron's kinetic energy. Hydrogen is highly opaque to neutral hydrogen, with a photoionization cross section described by

$$\sigma_H(\lambda) \simeq \sigma_{H,0} \left( \frac{\lambda}{912\text{Å}} \right)^3 \tag{1.2}$$

where $\sigma_{H,0} = 6.3 \times 10^{-18}\,\mathrm{cm}^2$ and $\lambda \leq 912\,$Å (Paresce, McKee, and Bowyer 1980). In contrast, galactic dust is much less opaque, though with a non-negligible cross section $\sigma_{\mathrm{dust}} \simeq 1\text{–}5 \times 10^{-22}\,\mathrm{cm}^2$ (Gnedin, Kravtsov, and Chen 2008). Helium requires photons with wavelength $\lambda < 505\,$Å to remove only one of its electron, and approximately one $H_2$ molecule exists for every $\sim 10^6$ neutral hydrogen atom (Vonlanthen et al. 2009). Thus, hydrogen has little competition with other absorbers of the LyC radiation field, and LyC is readily absorbed by neutral hydrogen gas.

Additional sources of LyC radiation and high energy, ionizing particles within

galaxies may have contributed to the reionization of the IGM as well. These sources include early high mass X-ray binaries (Mirabel et al. 2011; Bluem et al. 2019), galactic outflows/inflows and jets from AGN (e.g., Reynolds, Heinz, and Begelman 2002; Roychowdhury et al. 2004; Wilcots, Hess, and Grcevich 2008) and SNe superwinds (e.g., Strickland and Stevens 2000; Strickland and Heckman 2009; Bravo-Guerrero and Stevens 2017), shock-heating via accretion onto dark matter halos (Sternberg, McKee, and Wolfire 2002; Putman, Peek, and Joung 2012), massive pre-galactic Pop III stars (Kulkarni et al. 2014), X-rays produced by SNe (Oh 1999; McQuinn 2012), and young globular clusters (Ricotti 2002). This LyC radiation would have formed bubbles of ionized hydrogen around these UV bright galaxies, which then expanded and merged until the IGM became completely ionized (e.g., Gnedin 2000; Miralda-Escudé, Haehnelt, and Rees 2000; Loeb and Barkana 2001; Fan et al. 2002).

Observations of AGN spectra constrain the end of this phase transition of the neutral IGM to $\sim 1\,\mathrm{Gyr}$ after the Big Bang ($z \simeq 6$; Mesinger and Haiman 2004; Fan, Carilli, and Keating 2006; Fan et al. 2006; Schroeder, Mesinger, and Haiman 2012; McGreer, Mesinger, and D'Odorico 2014; Becker et al. 2015). The signature of the completion of reionization in these spectra is known as the Gunn-Peterson effect (Gunn and Peterson 1965), which indicates the presence of neutral hydrogen absorption along the line-of-sight of the observation. Here, the UV emission from AGN at $\lambda < 1216\,\text{Å}$ can bring a neutral hydrogen atom from it's ground state to it's first excited state, where the electron in the atom is promoted to it's second atomic orbit. This transition requires a photon of wavelength $\lambda = 1216\text{Å}$, also known as Lyman-$\alpha$. As the AGN light with wavelength $\lambda_{\mathrm{emit}} < 1216\,\text{Å}$ is redshifted from the expansion of the universe, it becomes absorbable by neutral hydrogen through the Lyman-$\alpha$ transition at varying distances from the AGN. This effect is known as the Lyman-alpha forest (Lynds 1971),

where intervening neutral hydrogen clumps at various distances absorb Lyman-$\alpha$ photons at their respective redshift. A trough in the AGN spectra appears when the IGM is still mostly neutral, and can be used to observationally constrain the redshift when reionization was completed. Observations of Lyman-alpha emitting galaxies also show (volume averaged) neutral fractions in excess of $>0.3$ at $z\sim7$ (e.g., Dijkstra, Mesinger, and Wyithe 2011; Jensen et al. 2012; Mesinger et al. 2014; Choudhury et al. 2015).

The main sources of reionization are still somewhat unclear, though current observational constraints on which sources may have ionized the IGM in the local and distant Universe are ongoing. These observation will be discussed in the next section, and the work presented here will also put constraints on the importance of stellar and AGN sources of ionizing radiation.

# Chapter 2

# OBSERVATIONAL CONSTRAINTS ON THE SOURCES OF REIONIZATION

## 2.1 Introduction

The most likely sources of ionizing photons responsible for the reionization of IGM are believed to be massive stars in early galaxies and super-massive black holes (SMBH) in the centers of those galaxies. Actively accreting SMBHs, or AGN, convert a portion of their gravitational potential energy into thermal energy of the accreting disk of infalling matter, which causes the accretion disk to emit black-body radiation that peaks in the UV (Shields 1978; Malkan and Sargent 1982). The interaction between this radiation and the matter of the accretion disk, the dust torus surrounding the SMBH, the gas and dust clouds surrounding the AGN, and viewing angle determine the observed spectrum.

Several physical mechanisms are understood to create the various features observed in AGN spectra (Koratkar and Blaes 1999). The non-ionizing and ionizing UV is thought to be created primarily by thermal emission from the accretion disk, although observations of AGN spectra exhibit a more complex, double power-law continuum with a break near $\lambda_{\rm rest} \sim 1000$Å (Zheng et al. 1997; Telfer et al. 2002; Scott et al. 2004; Shull, Stevans, and Danforth 2012; Lusso et al. 2015). This feature is believed to be the low energy wing of Comptonized photons produced by cooling electrons in the warm, optically thick, magnetized plasma of accretion disk coronae. The physical origin of this warm, optically thick component is not well determined (Walton et al. 2013; Różańska et al. 2015; P. O. Petrucci et al. 2018), though it is proposed to be

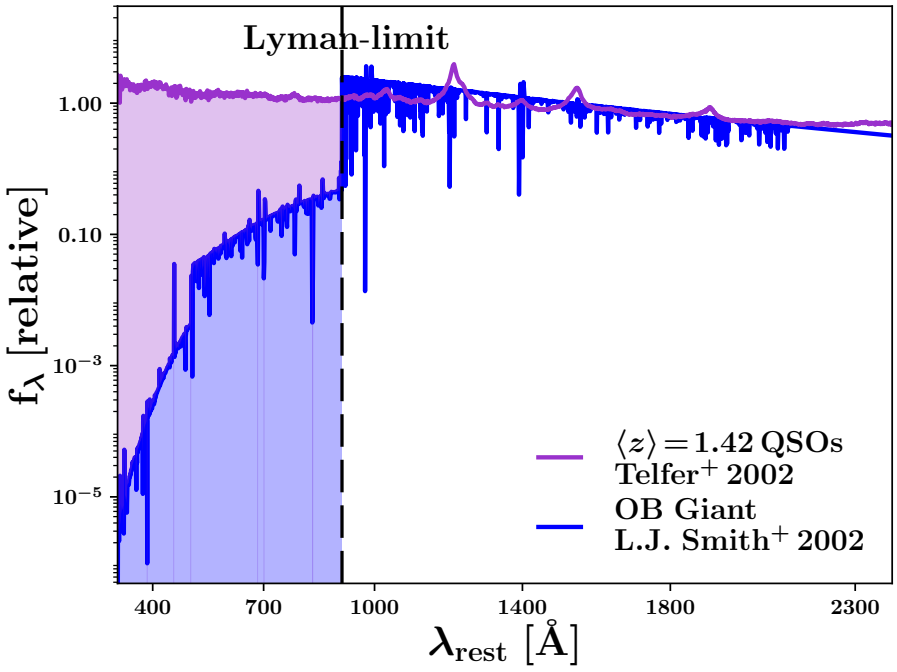


Figure 1. Comparison of SEDs for AGN and OB Giant Stars

The stacked spectra of 182 Quasi-Stellar Object (QSOs) at $z > 0.3$ ($\langle z \rangle = 1.42$) observed with the Hubble Space Telescope (*HST* Telfer et al. 2002) in purple, along with the OB Supergiant model of Smith, Norris, and Crowther (2002) with $T_{\rm eff} = 2.5 \times 10^4$ K and $Z = 0.05\, Z_\odot$ in blue. The Lyman-limit, where the hydrogen ionization spectrum begins, is indicated by a vertical dashed black line. The hydrogen-ionizing regions of these spectra are shaded by their respective colors. Both curves are normalized by the integral of their $1400 < \lambda_{\rm rest} < 1600$ Åflux. The production of ionizing radiation integrated from $300 \leq \lambda_{\rm rest} \leq 912$ Åfrom AGN is seen to surpass OB giant stars on this relative scale by a factor of $\simeq 100$ times.

responsible for the observed soft X-ray excess seen in some AGN spectra (Kaufman, Blaes, and Hirose 2017; P. O. Petrucci et al. 2018).

Ionizing photons from stars are produced by their photospheres, and massive O and B type stars are likely the most important contributors to the stellar ionizing radiation emitted by galaxies (Barkana and Loeb 2001; Stark 2016). A comparison of the UV spectra of AGN and O/B Giant stars can be seen in Fig. 1. Because O and B type stars typically form from multiple open star clusters known as OB associations,

in galactic nuclei, and/or starburst regions, the surrounding gas is transformed into giant H 2 regions several pc in diameter (e.g., Tremblin et al. 2014). The stellar LyC flux that exceeds the recombination rate of hydrogen can escape into the IGM as long as it is not absorbed by intervening H 1 gas in the interstellar medium (ISM) or circum-galactic medium.

Determining which of these two sources of LyC plays the dominant role in the ionizing the IGM during the epoch of reionization is one of the main focuses of research in this area. A key quantity that can help address this questions is determining the efficiency of galaxies to emit their produced LyC into the IGM, otherwise known as the LyC escape fraction. Determining this value for a large number of galaxies can give clues to which source is statistically the most effective ionizer.

## 2.2 The Lyman Continuum Escape Fraction

Because neutral hydrogen and dust are opaque to FUV radiation, LyC photons can only escape from galaxies in regions where the surrounding neutral hydrogen column density, $N_H$, and dust extinction are low. The fraction of ionizing radiation produced by stars and AGN that escapes into the IGM is known as the LyC escape fraction ($f_{esc}$). Here, $f_{esc}$ is simply the ratio of the intrinsically produced LyC flux to the LyC flux that makes it out of the galaxy before encountering the IGM, or

$$f_{esc} = \frac{F_{\nu,obs}(\lambda_{rest} \leq 912\text{Å})}{F_{\nu,int}(\lambda_{emit} \leq 912\text{Å})} \tag{2.1}$$

where $F_{\nu,obs}(\lambda_{rest} \leq 912\text{Å})$ is the observed flux density of LyC emitted by the galaxy, corrected for redshifting to the rest-frame emission of the galaxy, and $F_{\nu,int}(\lambda_{emit} \leq 912\text{Å})$ is the flux density of LyC produced inside of the galaxy by stars, accretion disks around BHs, or other exotic mechanisms (see §1.4 for examples).

In order for a fraction of the produced LyC photons to escape into the IGM, the interstellar medium (ISM) in the galaxy and its surrounding circumgalactic medium must be cleared. This can be accomplished by supernova winds (Fujita et al. 2003), which can also suppress the formation of low mass stars and increase the formation of LyC producing high mass stars, and can be further enhanced by AGN outflows (Silk and Norman 2009). High star-formation rates can also increase the porosity of the ISM (Clarke and Oey 2002). The semi-analytical models of Dove, Shull, and Ferrara 2000 showed that LyC emitted by OB associations can become trapped in super-bubbles until they expand outside of the disk. Once the surrounding medium is either cleared or fully ionized, it becomes transparent to LyC radiation, which can then escape through these regions of the galaxy, or be Thomson scattered by free electrons and/or dust. The escaping LyC can then be observed along some lines-of-sight, which can be distributed randomly in a galaxy, and is in some cases offset from the galactic center (e.g., I. Iwata et al. 2009; Vanzella, Giavalisco, et al. 2010; Vanzella et al. 2012).

The escape fraction, $f_{\rm esc}$, as defined above is also sometimes referred to as the absolute Lyman continuum escape fractions ($f_{\rm esc}^{\rm abs}$). This distinction specifies that this escape fraction value is not relative to any other quantity, but incorporates only the LyC flux of the galaxy itself. In contrast, the *relative* LyC escape fraction is defined as ratio of the escaping LyC to the observed LyC, relative to the escaping non-ionizing UV-continuum (UVC; $\sim$1400 Å $\lesssim \lambda_{\rm rest} \lesssim$ 1800 Å), or

$$f_{\rm esc,rel} = \frac{(f_{1500}/f_{\rm LyC})_{\rm int}}{(f_{1500}/f_{\rm LyC})_{\rm obs}} e^{\tau_{\rm IGM}(z)} \tag{2.2}$$

where $f_{1500}$ is the rest-frame 1500Å flux, $f_{\rm LyC}$ is the LyC flux, and $\tau_{\rm IGM}(z)$ is the optical depth of the IGM at redshift $z$ (Steidel, Pettini, and Adelberger 2001; Inoue et al. 2005; Siana et al. 2007; Siana et al. 2010). This parameter is related to $f_{\rm esc}$ by $f_{\rm esc} = f_{\rm esc,rel} 10^{-0.4 A_{1500}}$, where $A_{1500}$ is the galactic extinction at 1500 Å in magnitude

units. Literature sources do not consistently reference only one escape fraction or provide both quantities, though one can be converted to the other, as long as the source provides the amount of dust extinction in the visual or $V$–band ($A_V$) in units of magnitudes and the wavelength-dependent dust-attenuation curve of the galaxy. The $f_{\rm esc}^{\rm abs}$ is useful for understanding the amount of intrinsically produced LyC that escapes the galaxy, and $f_{\rm esc}^{\rm rel}$ can be used to convert to $f_{\rm esc}^{\rm abs}$ using fiducial values of the ratio of the intrinsic 1500 Å and LyC flux without the need of modeling the intrinsic spectral energy distribution (SED) of the galaxy (e.g., Siana et al. 2007; Siana et al. 2010).

### 2.3 Review of Searches for Escaping LyC in the Literature

The literature often states that stellar LyC escaping from high-redshift, star-forming, possibly low-mass galaxies are likely the dominant sources of LyC that reionized the IGM at $z \lesssim 6$–7 (e.g., Bouwens et al. 2012; Wise et al. 2014; B. E. Robertson et al. 2015; Duncan and Conselice 2015), and require $f_{\rm esc} \sim$10–20% to complete this phase transition (e.g., Steven L. Finkelstein et al. 2012; B. E. Robertson et al. 2015; Bouwens et al. 2016). An AGN can produce more LyC than a SFG, though they are not believed to be the dominant sources of LyC since much more rare than galaxies at these redshifts (Willott et al. 2010; Glikman et al. 2011; Masters et al. 2012). This conclusion is drawn from the decline in and their space density and luminosity function at $z \gtrsim 2$ (e.g., Silverman et al. 2008; Ebrero et al. 2009; Aird et al. 2015; Kulkarni, Worseck, and Hennawi 2019). Therefore, SFGs are regarded as the most likely candidates that started the reionization of the IGM at $z \gtrsim 6$.

Since the opaque IGM at $z \gtrsim 6$ prevents a direct study of LyC emission from SFGs at this epoch, we must study lower redshift analogs in order to understand

the sources of reionization of the IGM. Observations of the local Universe reveal that H 2 regions in nearby galaxies release 40–75% of the LyC photons produced by massive stars into the IGM (Ferguson et al. 1996; Leitherer et al. 1996; Oey and Kennicutt 1997; Zurita et al. 2002). In the local group, Bland-Hawthorn and Maloney (1999) and Putman et al. (2003) find LyC escape fractions of only 1–2%. Despite many attempts, rest-frame FUV observations of higher redshift star-forming galaxies (SFGs) at $0.5 \lesssim z \lesssim 3$ have so far not yielded significant detections of escaping LyC flux (e.g., Ferguson 2001; Giallongo et al. 2002; Fernández-Soto, Lanzetta, and Chen 2003; Malkan, Webb, and Konopacky 2003; Inoue et al. 2005; Siana et al. 2007; Siana et al. 2010; Cowie, Barger, and Trouille 2009; Bridge et al. 2010; Grazian et al. 2016; Rutkowski et al. 2016; Sandberg et al. 2015; Guaita et al. 2016; Japelj et al. 2017). Ground-based spectra (Steidel, Pettini, and Adelberger 2001; Shapley et al. 2006; Cooke et al. 2014; de Barros et al. 2016; Steidel et al. 2018) and optical narrow-band and broadband imaging of SFGs at $3 \lesssim z \lesssim 4$ (I. Iwata et al. 2009; Vanzella, Giavalisco, et al. 2010; Boutsia et al. 2011; Nestor et al. 2011; Vanzella et al. 2012; Nestor et al. 2013; Mostardi et al. 2013; Grazian et al. 2017; Smith et al. 2018; Ikuru Iwata et al. 2019) have revealed evidence for escaping LyC photons along several sight-lines, with $f_{\rm esc} \simeq 1$–40% despite higher IGM opacities at these higher redshifts (Haardt and Madau 1996, 2012). Furthermore, Vanzella et al. (2012) estimate $f_{\rm esc}$ for one LBG (GDS J033216.64−274253.3 at $z$=3.795) to be >25%, although ground-based measurements of escaping LyC may be contaminated with non-ionizing flux from blended lower redshift foreground interlopers due to the lower resolution of ground-based seeing (Vanzella, Siana, et al. 2010; Nestor et al. 2013; Mostardi et al. 2015; Siana et al. 2015).

The dearth of high $f_{\rm esc}$ values for more massive SFGs found throughout the

literature, as well as the decline in the AGN luminosity function at $3 \lesssim z \lesssim 6$, have led to conclusions that low mass, star-forming dwarf galaxies may be more likely candidates for the agents of reionization (Steven L. Finkelstein et al. 2012; Stark 2016; Weisz and Boylan-Kolchin 2017). Simulations show that $f_{\rm esc}$ should increase with decreasing halo mass (Yajima, Choi, and Nagamine 2011; Kimm and Cen 2014; Wise et al. 2014), and recent works have found that low-mass, low-metallicity, compact star-forming galaxies with extreme [O 3] emission and [O 3]/[O 2] line ratios exhibit detectable LyC emission at low-redshift ($0 \leq z \lesssim 1$; Y. I. Izotov et al. 2016; Y I Izotov et al. 2017; Y I Izotov et al. 2018) and at $z \simeq 3.1$ (Fletcher et al. 2019). Observations of some local starburst galaxies have shown significant, yet varying $f_{\rm esc}$ values (Leitherer et al. 1995; Hurwitz, Jelinsky, and Dixon 1997; Tumlinson et al. 1999; Deharveng et al. 2001; Heckman et al. 2001; Borthakur et al. 2014; Y. I. Izotov et al. 2016), although Hanish et al. (2010) find that local starburst galaxies do not exhibit higher escape fractions compared to ordinary local SFGs.

Tanvir et al. (2018) constrain the average $f_{\rm esc}$ of low-mass SFGs at $2 < z < 5$ to $\langle f_{\rm esc} \rangle < 1.5\%$ using 138 gamma-ray burst afterglows, and present evidence that their $f_{\rm esc}$ does not change at $z > 5$. They first determine the neutral hydrogen column-density ($N_H$) of these galaxies and infer an $f_{\rm esc}$ from their total sample and find no evolution of $N_H$ with redshift. Typical GRB hosts show higher $N_H$ column densities at $z > 2$, similar to those of damped Ly $-\ \alpha$ systems (Jakobsson et al. 2006). Two of the GRBs in Tanvir et al. 2018 do show sufficiently low $N_H$ to allow more LyC radiation to escape, suggesting that stellar feedback can clear the ISM to allow higher $f_{\rm esc}$ in *rarer* cases. The $f_{\rm esc}$ is likely anisotropic in a galaxy (Wise and Cen 2009; Kim et al. 2013; Paardekooper, Khochfar, and Dalla Vecchia 2015), therefore some lines-of-sight may have much higher $f_{\rm esc}$ near regions associated with SNe winds (Fujita et al. 2003;

Trebitsch et al. 2017; Herenz et al. 2017). Spectroscopy of gamma-ray burst afterglows from $2 < z < 8$ have also been used to constrain $f_{\rm esc}$ to <6% at these redshifts (Chen, Prochaska, and Gnedin 2007; Fynbo et al. 2009; Wyithe et al. 2010). Since GRB host galaxies are often dwarfs with high specific star-formation rates (Svensson et al. 2010; Hunt et al. 2014; McGuire et al. 2016), and the bulk of low-redshift dwarfs exhibit very low $f_{\rm esc}$ (e.g., at $z \simeq 0.5$, $f_{\rm esc} < 3\%$; Rutkowski et al. 2016), hypotheses that propose dwarf galaxies to be the main reionizers at $z > 6$ may be in conflict with observation and additional sources of ionizing flux would be needed.

Grazian et al. (2018) discuss how several well-studied, nearby dwarf galaxies with measured $f_{\rm esc}$ and $f_{\rm esc}^{\rm rel}$ values have been detected in X-rays, potentially indicating an AGN component. Kaaret et al. (2017) detect point-source X-ray flux with *Chandra* from the $z = 0.048$ SFG Tololo 1247–232 ($f_{\rm esc}^{\rm rel} = 21.6\%$, $1.5\% \pm 0.5$, measured by Leitherer et al. 2016 and Puschnig et al. 2017, respectively), and shows variability on the order of years, suggesting the presence of a low-luminosity AGN ($L_X \simeq 10^{41}\,{\rm erg\,s^{-1}}$). Prestwich et al. 2015 detect a bright point-source ($L_X \simeq 10^{41}\,{\rm erg\,s^{-1}}$) within Haro 11 ($f_{\rm esc}^{\rm rel} \sim 3\%$; Leitet et al. 2011) with a very hard spectrum (X-ray photon index $\Gamma = 1.2 \pm 0.2$). Borthakur et al. (2014) find LyC flux emitted by a $z = 0.235$ SFG (J0921+4509, $f_{\rm esc} \simeq 20\%$), which has been detected in hard X-rays with *XMM-Newton* ($L_X \simeq 10^{42}\,{\rm erg\,s^{-1}}$; Jia et al. 2011), suggesting a possible AGN component as well.

The process of combining images or spectra that observe the LyC from different galaxies can increase the total signal-to-noise ratio (SNR) of those observations, a process known as stacking. This can enhance the faint LyC signal that may be present in the data by summing these signals together, *and* reduce systematic uncertainties in the observation from detector noise and/or background shot-noise. Stacks of ground-based spectra have shown that AGN produce more LyC than star-forming Lyman

Break Galaxies (LBG; Vanden Berk et al. 2001; Shapley et al. 2003), though LBGs selected via drop-out techniques may have fainter LyC emission due to their selection criteria compared to other UV bright SFGs (Vanzella et al. 2015). Rest-frame UV spectra of AGN taken with *HST* and the Far-Ultraviolet Spectroscopic Explorer (*FUSE*; Moos et al. 2000) have shown significant detections of escaping LyC flux at $0.5 \lesssim z \lesssim 2.5$ (e.g., Telfer et al. 2002; Scott et al. 2004; Shull, Stevans, and Danforth 2012; Lusso et al. 2015), but only upper limits of $f_{\rm esc} \lesssim 1$–$2\%$ from galaxies at the same redshifts (e.g., Bridge et al. 2010; Siana et al. 2010; Sandberg et al. 2015; Rutkowski et al. 2016).

More recent studies on the sources of reionization have emphasized the role of AGN (Giallongo et al. 2015; Madau and Haardt 2015; Vikram Khaire et al. 2016; Mitra, Choudhury, and Ferrara 2017). Their findings suggest that AGN display significant emission of ionizing flux, and stellar sources within SFG alone may not emit LyC at a sufficient rate required to complete reionization. If SNe winds in SFGs with no AGN component could clear enough channels in the ISM to allow more LyC to be emitted into the IGM, then SFGs should have higher $f_{\rm esc}$ values than observed throughout the literature. Although AGN are believed to not be the main sources that reionized the IGM at $z \gtrsim 3$, they are believed to be the only sources responsible for He 2 reionization at $z \simeq 3$ (Haardt and Madau 2012; Worseck et al. 2014).

The following chapters will present a statistical method for constraining $f_{\rm esc}$ for both SFG and AGN, which will allow for direct comparison of the contribution of ionizing photons to reionization, assuming the galaxies in this study are representative of galaxies that existed during the epoch of reionization.

# Chapter 3

# DETERMINING THE ESCAPE FRACTION FROM FAINT LYC SOURCES

## 3.1 Image Stacking Methodology

Since LyC escape fractions have been measured to be very low, and the detected LyC emission to be very faint or not detected at all at $z \lesssim 3$ (e.g., Steidel, Pettini, and Adelberger 2001; Shapley et al. 2006; I. Iwata et al. 2009; Siana et al. 2010; Mostardi et al. 2013), a technique of stacking the *observed* LyC emission in images or spectra from multiple galaxies can be used to increase the total SNR and sensitivity to the faint, potentially low surface-brightness LyC flux from individuals. Stacking LyC emission from galaxies at similar redshifts can also be used to quantify the *average* LyC emission from galaxies at their average redshift. This method also reduces small scale residual systematic errors in the stacked LyC images or spectra left from bias, dark current, sky-subtraction, flat-fielding, and/or any gradients from variations in exposure time or photon noise between exposures. These noise sources can remain in the background of image mosaics or extracted 1-dimensional spectra, as effects from random systematics are averaged out in a stack.

Stacks of images, for example, are created by summing the weighted pixel values of LyC image cutouts, excised from larger mosaic images. The weighted sum of each pixel is then normalized by the sum of their weights, i.e.,

$$\langle f_j \rangle = \sum_i W_{i,j} f_{i,j} / \sum_i W_{i,j} \tag{3.1}$$

where $f_{i,j}$ represents the flux in counts per second measured in pixel $j$ for sub-image $i$

and $W_{i,j}$ is the weight of pixel $j$ for sub-image $i$. $\langle f_j \rangle$ represents the weighted average value in pixel $j$.

Mosaic images are typically comprised of multiple smaller images of overlapping regions of sky, with typical exposure times of several minutes, and are often dithered around a central pointing. A similar stacking method to the above equation is used to create an image mosaic of a large region of sky, typically a degree or so in spatial extent. The weight map of the image can be constructed from calibration frames and known detector systematics, which quantify the *inverse variance*, or $W_j = \frac{1}{\sigma_j^2}$ of each pixel $j$. The dispersion $\sigma_j$ is described by

$$\sigma_j = \frac{\sqrt{f_j(D_j + B_j)/g + \sigma_{\rm read}^2}}{f_j\, t} \tag{3.2}$$

where $f$ is the inverse of the flat field calibration image, which is used to normalize the varying inter-pixel sensitivities of raw exposures, and $D$ represents the counts per pixel caused by thermal, or dark, current noise, which is typically very low for cooled detectors ($\sim$8 electrons/hr/pixel e.g., Dressel 2019). $B$ is the counts from background light. $g$ represents the gain value of the detector used for converting electrons collected in each pixel to digital values of an image, performed by the analog to digital converter (ADC) during exposure readout. $\sigma_{\rm read}$ is the inherent read noise in the image created by the ADC, which is characterized by a Gaussian distribution and is on the order of $\sim$1–5 electrons per digital unit, and t is the exposure time in seconds (the appendix of Casertano et al. 2000 gives the full derivation and explanation of this formula with regard to *HST* images in more detail).

Stacked weight maps for each LyC stack can be created by summing the inverse of the pixel values of the corresponding region in the weight maps where the galaxy

sub-images were extracted, then inverting the sum. This is expressed as

$$W_j = 1/\sum_i \frac{1}{W_{i,j}} \tag{3.3}$$

where $W_j$ is the weight for pixel $j$ in sub-image $i$. These weight maps give the relative weight of each pixel in the LyC stacks, and are useful for quantifying uncertainties when measuring the faint LyC signal in the observations.

## 3.2 Generating Flux Distributions of the LyC Photometry

Because the LyC flux escaping from galaxies in stacks of images or spectra is typically very faint, popular methods of performing photometry, such as those employed by the widely used program SExtractor (Bertin and Arnouts 1996), may not provide accurate estimates of the *mean* flux and its associated uncertainties. Therefore, a more statistical approach based on the systematic noise of the detector and local shot-noise in the sub-images should be used for more sensitive and realistic estimates. These uncertainties can be approximated by Gaussian Random Variables (GRV), which numerically model a Gaussian distribution by generating pseudo-random numbers $n$ with mean $\mu$ and dispersion $\sigma$, defined by

$$p(n) = \frac{1}{\sqrt{2\pi\sigma^2}} e^{-\frac{(n-\mu)^2}{2\sigma^2}} \tag{3.4}$$

As mentioned in §3.1, the noise from a detector is largely Gaussian, since the largest contributor is read noise. Although shot-noise is Poissonian in nature, the Central Limit Theorem states that for a large number of events, i.e., counts in an image, a Poisson distribution is well approximated by a Gaussian. Such a method as outlined below can be used to generate distributions of LyC flux in a stack, based on these systematics.

The generation of the stacked flux distribution begins with creating a flux datacube for each galaxy based on the LyC subimage excised from a mosaic image and its

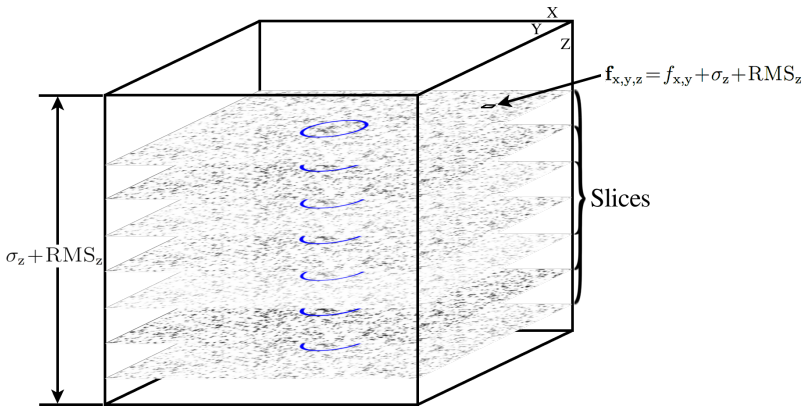


Figure 2. Flux Datacube Diagram Used for Photometry

A 3-dimensional graphical representation of the photometric method used to estimate the flux inside a measurement aperture of a stacked image. The x and y-axes correspond to an image-slice from the datacube, and the z-axis corresponds to a possible range of values in the pixels of a 2-dimensional slice. The various values along the z-axis can be positive or negative and have values with frequency corresponding to a Gaussian probability distribution. These z-axis ranges account for variance in the pixel values corresponding to detector noise and local shot noise in the subimage. The average value along the z-axis corresponds to the actual subimage excised from the mosaic image. These datacubes can then be stacked as described in §3.1, and photometry can be analyzed within a central aperture for each slice in the stacked datacube to produce the flux distribution of the stack.

corresponding weight map. Two dimensions of the datacube correspond to the pixel values in the LyC subimage, and the third dimension was based on the dispersion of the sky-background in the LyC subimage and the pixel's RMS value, calculated from the weight image. Thus, the voxels along each slice in the datacube had a mean value equal to the original pixel value of the LyC subimage and a variance equal to the sum of the total sky variance in the LyC subimage and the inverse of the corresponding pixel value in the weight map; i.e., the flux value of the voxel at coordinate x, y, z in the data cube is generated by

$$\mathbf{f}_{\mathrm{x,y,z}} = f_{\mathrm{x,y}} + \sigma_{\mathrm{z}} + \mathrm{RMS}_{\mathrm{z}} \tag{3.5}$$

where $f_{\mathrm{x,y}}$ is the pixel value of the LyC subimage at location x, y in the pixel grid, $\sigma_{\mathrm{z}}$ is

the randomly selected sky-background value from a GRV defined by $\mathcal{N}(0, \sigma^2_{\rm sky})$, where $\sigma_{\rm sky}$ is the sky-background dispersion, and $\rm RMS_z$ is the randomly selected detector noise value from the GRV $\mathcal{N}(0, \sigma^2_{\rm RMS})$, where $\sigma_{\rm RMS} = \sqrt{\frac{1}{W_{x,y}}}$ and $W_{x,y}$ is the pixel value in the weight map. This method is also known as a Gaussian additive noise model, and a diagram of this procedure is shown in Fig. 2

Since the LyC flux in the stack is expected to be faint, matched aperture photometry is the most advantageous method to use when measuring the flux in each slice of the datacube. This method uses a detection image to determine where flux should be measured in the corresponding measurement image. In this case, an image with much higher signal can be used for detection, such as a stacked image of the same galaxies at brighter wavelengths, and the measurement can be made in the same region in the LyC stack, corresponding to the bright emission found in the detection image. Here, SExtractor can be used for determining the measurement aperture and for counting the flux inside this aperture.

To generate a representative distribution of the LyC flux, each 2-dimensional slice in the datacube along the z-dimension can be iterated through, and the flux can be measured within the detection image aperture. Any number of samples in the distribution can be generated, though $\sim 10^4$ possible flux values give accurate results and are less computationally expensive. The mean of the flux distribution and the $16^{\rm th}$ and $84^{\rm th}$ percentile can therefore represent the estimated flux value in the stack and its -1$\sigma$ and +1$\sigma$ uncertainty bounds, respectively. The ratio of the mean and the uncertainty can be used to calculate the SNR. When dealing with low SNR, the 84th percentile from the distribution can be used to place a 1$\sigma$ upper limit to the LyC flux.

## 3.3 The Stacked LyC Escape Fraction

Estimating the escape fraction of LyC photons from galaxies is non-trivial, as it requires modeling of their apparent *intrinsic* LyC flux, $F^{\rm int}_{\nu,\,\rm LyC}$, and the wavelength-dependent transmission of LyC photons through the IGM, $\mathcal{T}^{\rm LyC}_{\rm IGM}(z,\nu)$, for a galaxy at redshift $z$. Quantitatively, the average *observed* LyC flux ($F^{\rm obs}_{\nu,\,\rm LyC}$) from a stack of galaxies, measured by a photon counting device such as a CCD, is given by:

$$\langle F^{\rm obs}_{\nu,\,\rm LyC}\rangle = \sum_{\rm i=1}^{N_{\rm gal}} \frac{\int W_i T^{\rm LyC}_{\rm obs}(\nu)\mathcal{T}_{\rm IGM}(z_{\rm i},\nu) f_{\rm esc,i} F^{\rm int}_{\nu,\rm i}(\nu)\frac{d\nu}{\nu}}{\int T^{\rm LyC}_{\rm obs}(\nu)\frac{d\nu}{\nu}} \Bigg/ \sum_{\rm i=1}^{N_{\rm gal}} W_i \tag{3.6}$$

where $N_{\rm gal}$ denotes the number of galaxies in the stack, $F^{\rm int}_{\nu,\rm i}$ denotes the *intrinsic* (i.e. produced) stellar and/or AGN SED from galaxy 'i', $f_{\rm esc,i}$ denotes the fraction of the observed LyC flux that escaped from the galaxy into the IGM, $\mathcal{T}_{\rm IGM}(z_{\rm i},\nu)$ denotes the wavelength-dependent IGM transmission curve for galaxy 'i' at redshift $z$, $W_i$ is the weight applied to galaxy $i$ during image stacking, and the $T^{\rm LyC}_{\rm obs}(\nu)$ term denotes the combined transmission of the throughput from the Optical Telescope Assembly (OTA), the filter throughput, and the Quantum Efficiency (QE) of the detector used for the LyC observation.

$f_{\rm esc}$ is generally expected to vary between individual objects. However, since the observed LyC emission from all galaxies is stacked to boost the SNR, we can simplify the analysis by assuming a constant $f_{\rm esc}$ value for all galaxies within a given redshift bin. This *sample-averaged* escape fraction is therefore denoted by $\langle f_{\rm esc}\rangle$. We can then take $\langle f_{\rm esc}\rangle$ outside of the sum in Eq 3.6, and write:

$$\langle f_{\rm esc}\rangle = \frac{\langle F^{\rm obs}_{\nu,\,\rm LyC}\rangle}{\sum\limits_{\rm i=1}^{\rm N_{gal}} \frac{\int W_i T^{\rm LyC}_{\rm obs}(\nu)\mathcal{T}_{\rm IGM}(z_{\rm i},\nu) F^{\rm int}_{\nu,\rm i}(\nu)\frac{d\nu}{\nu}}{\int T^{\rm LyC}_{\rm obs}(\nu)\frac{d\nu}{\nu}} \Bigg/ \sum\limits_{\rm i=1}^{N_{\rm gal}} W_i}, \tag{3.7}$$

which can also be expressed as:

$$\langle f_{\rm esc} \rangle = \frac{\langle F^{\rm obs}_{\nu,\,\rm LyC} \rangle}{\sum\limits_{\rm i=1}^{\rm N_{gal}} W_i F^{\rm int}_{\nu,\,\rm LyC,i} \Big/ \sum\limits_{\rm i=1}^{N_{\rm gal}} W_i} = \frac{\langle F^{\rm obs}_{\nu,\,\rm LyC} \rangle}{\langle F^{\rm int}_{\nu,\,\rm LyC} \rangle}. \tag{3.8}$$

A more thorough analysis should also take into account that the impact of the IGM varies substantially around this mean for individual objects and sight-lines (see, e.g., Inoue and Iwata 2008; Nestor et al. 2011). $F^{\rm int}_{\nu,i}(\nu)$ can be determined for each galaxy from a minimized $\chi^2$ fit to observed multi-wavelength images or spectral data. The most popular synthetic stellar population model SEDs come from Bruzual and Charlot 2003 (BC03). These allow four degrees of freedom during the $\chi^2$ minimization, i.e., the age of the stars, the stellar mass, the amount of dust extinction in the $A_V$ in units of magnitudes, and the exponentially decreasing star-formation rate (SFR) timescale ($\tau$).

A variety of dust-attenuation curves should be explored when attempting to ascertain the best-fit. Popular models include the Milky Way (Savage and Mathis 1979, MW), the Large Magellanic Cloud (Bless and Savage 1972, LMC), (Prevot et al. 1984, SMC), the average dust-attenuation from SFGs (Calzetti et al. 2000), or the average dust-law of Kriek and Conroy (2013). For comparison, the ratio of the extinction at 1500Å to the $V$-band extinction is $A_{1500}/A_V = 2.55$, 2.66, 4.37, 2.79, and 2.91, for the MW, LMC, SMC, Calzetti et al. 2000, and Kriek and Conroy 2013 extinction curves, respectively.

It is advantageous to fit multi-wavelength photometry to a grid of SEDs using a wide range of each parameter, in order to obtain a best-fitting SED that is more representative of the true SED. Thus, the best fit SEDs corresponds to the observed $F_\nu$ of the galaxy *with* dust-attenuation applied to the *intrinsic* SED, thereby determining the best fit $A_V$ value. A standard initial mass function (IMF), such as the Salpeter

(1955) IMF, can be adopted, and a variety of stellar metallicities, e.g., solar ($Z$=0.02), subsolar ($Z$=0.004, 0.008), and supersolar ($Z$=0.05), should be explored.

Occasionally, a galaxy will be harboring an AGN, made most apparent from broad emission lines seen in its UV–optical spectrum (Osmer and Hewett 1991), luminosity and spectral shape in X-rays (Mushotzky, Done, and Pounds 1993), and/or from its radio luminosity (Willott et al. 2002). In this case, an SED with two components should be fit, i.e. one with a stellar and AGN component. AGN SEDs are very complex, and therefore simplified models are available (e.g., Done et al. 2012; Kubota and Done 2018). A typical approach to fitting the SED of a galaxy with an AGN can also incorporate AGN spectral templates, e.g., fiducial Seyfert galaxy spectra, Type-1 and Type-2 AGN spectra, spectra of broad absorption lines quasars, and obscuring dust tori applied to those templates (Silva, Maiolino, and Granato 2004; Polletta et al. 2007).

In order to determine the fraction of escaping LyC $f_{\rm esc}$, which compares the apparent flux of LyC photons produced by stars in the galaxy to the observed LyC emission (i.e., $F^{\rm obs}_{\nu,\,\rm LyC}/F^{\rm int}_{\nu,\,\rm LyC}$), the effects from dust must be removed from the SED to obtain its *intrinsic* LyC flux, $F^{\rm int}_{\nu,\,\rm LyC,i}(\nu)$. Since the SED fit to photometry will include attenuation by dust, the intrinsic stellar population photospheric flux can be uncovered by inverting the reddening effect by dust using the $A_V$ value of the best-fit SED. Thus, the escape fraction quantifies the amount of LyC that is not absorbed by dust, the multiphase ISM, or other sources of LyC absorption in the galaxy.

The sample average escape fraction of LyC flux *relative* to the non-ionizing UVC flux ($F_{\nu,\rm UVC}$), denoted as $f^{\rm rel}_{\rm esc}$, is defined the as:

$$\langle f^{\rm rel}_{\rm esc}\rangle = \sum_{\rm i=1}^{\rm N_{gal}} \frac{W_i F^{\rm int}_{\nu,\rm UVC,i}/F^{\rm int}_{\nu,\,\rm LyC,i}}{F^{\rm obs}_{\nu,\rm UVC,i}/F^{\rm obs}_{\nu,\,\rm LyC,i}} \Bigg/ \sum_{\rm i=1}^{N_{\rm gal}} W_i \simeq \frac{\langle F^{\rm obs}_{\nu,\,\rm LyC}\rangle}{\langle F^{\rm obs}_{\nu,\rm UVC}\rangle} \sum_{\rm i=1}^{\rm N_{gal}} \frac{W_i F^{\rm int}_{\nu,\rm UVC,i}}{F^{\rm int}_{\nu,\,\rm LyC,i}} \Bigg/ \sum_{\rm i=1}^{N_{\rm gal}} W_i \quad (3.9)$$

Using Eq. 3.8, we can further simplify this expression as:

$$\langle f_{\rm esc}^{\rm rel}\rangle \simeq \langle f_{\rm esc}\rangle \frac{\sum\limits_{\rm i=1}^{\rm N_{gal}} W_i F_{\nu,{\rm UVC,i}}^{\rm int} \Big/ \sum\limits_{\rm i=1}^{N_{\rm gal}} W_i}{\sum\limits_{\rm i=1}^{\rm N_{gal}} W_i F_{\nu,{\rm UVC,i}}^{\rm obs} \Big/ \sum\limits_{\rm i=1}^{N_{\rm gal}} W_i} = \langle f_{\rm esc}\rangle \Big\langle \frac{F_{\nu,{\rm UVC}}^{\rm int}}{F_{\nu,{\rm UVC}}^{\rm obs}} \Big\rangle, \tag{3.10}$$

where $F_{\nu,{\rm UVC,i}}^{\rm obs}$ is the observed UVC flux from galaxy 'i' as measured in the ACS/WFC UVC filters and:

$$F_{\nu,{\rm UVC,i}}^{\rm int} = \frac{\int T_{\rm obs}^{\rm UVC}(\nu) F_{\nu,{\rm i}}^{\rm int}(\nu) \frac{d\nu}{\nu}}{\int T_{\rm obs}^{\rm UVC}(\nu) \frac{d\nu}{\nu}} \tag{3.11}$$

for UVC observations with a total system throughput of $T_{\rm obs}^{\rm UVC}(\nu)$. Thus, the relative and absolute escape fractions differ by a factor of $\Big\langle \frac{F_{\nu,{\rm UVC}}^{\rm int}}{F_{\nu,{\rm UVC}}^{\rm obs}} \Big\rangle = \langle f_{\rm esc}^{\rm UVC}\rangle^{-1}$ for the total sample, which deviates from unity depending on the $A_V$ and $\chi^2$ values of the SED fits. The escape fraction of non-ionizing UVC photons, $f_{\rm esc,i}^{\rm UVC}$, is related to the observed reddening in galaxy 'i' as $f_{\rm esc}^{\rm UVC} = 10^{-0.4\,A_{\rm UVC}}$. Note that this term can be omitted from Eq. 3.9 when using the *intrinsic* (unreddened) model SEDs instead of the observed ones. The ratio of intrinsic fluxes of the LyC and UVC emission from all galaxies can be determined by:

$$\Big\langle \frac{F_{\rm UVC}}{F_{\rm LyC}} \Big\rangle_{\rm int} = \frac{\sum\limits_{\rm i=1}^{\rm N_{gal}} F_{\nu,{\rm UVC,i}}^{\rm int}}{\sum\limits_{\rm i=1}^{\rm N_{gal}} F_{\nu,\,{\rm LyC,i}}^{\rm int}} \tag{3.12}$$

without applying the $\mathcal{T}_{\rm IGM}(z_{\rm i},\nu)$ term to $F_{\nu,\,{\rm LyC,i}}^{\rm int}$. The *observed* LyC and UVC flux ratios can be obtained by performing photometry on stacked images of the LyC and UVC emission as described in §3.2. Typical ratios of the *intrinsic* UVC flux to the *intrinsic* stellar LyC flux of galaxies increases by a factor $\sim$3 (e.g., Siana et al. 2010).

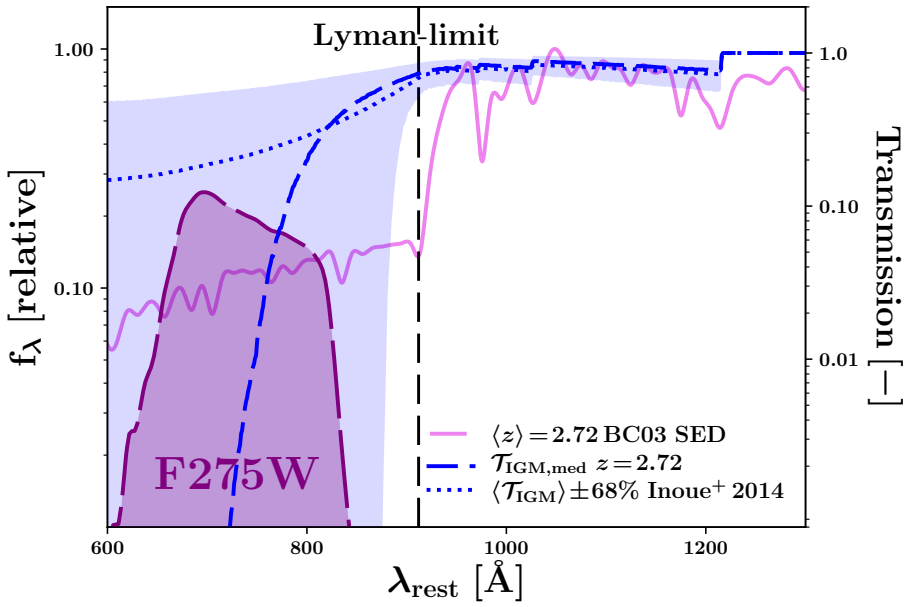


Figure 3. Example Models used for Calculating the Intrinsic LyC flux

An example stacked BC03 SED at $\langle z\rangle = 2.72$ fit from the sample of galaxies *without* AGN in §5.3 is shown in pink, along with the WFC3/UVIS F275W filter transmission curve in violet, shifted to the rest-frame wavelength of the SED where LyC at $z = 2.72$ can be observed. The average and median IGM transmission curves at $z = 2.72$ from Inoue et al. (2014) are shown as blue dotted and dashed curves, respectively. The inner 68% of $10^4$ sight-lines are shown as a shaded light-blue region, displaying the variation of transmission curves through the IGM of randomly selected sight-lines. The inner product of these curves will result in the probability distribution of the intrinsic LyC of the galaxies fit to the SED shown.

### 3.4 Estimating the LyC Escape Fraction: Monte Carlo Analysis

Since we cannot measure the amount of intrinsic LyC radiation produced by stars and AGN within galaxies directly, we must use the best available synthetic stellar population SED, dust attenuation, AGN SED, and IGM absorption models to estimate the fraction of LyC that escapes from galaxies at high redshift in a statistical way. An example of the models needed to estimate the *average* intrinsic LyC of galaxies is shown in Fig. 3. The galaxies to be used for estimating $f_{\rm esc}$ at some average redshift

must have correctly determined redshifts, so that the LyC escape fraction does not include any spurious, non-ionizing flux in its estimation. This also simplifies SED fitting, since the wavelengths of the SEDs used during fitting can all be redshifted to the known redshift of the galaxy.

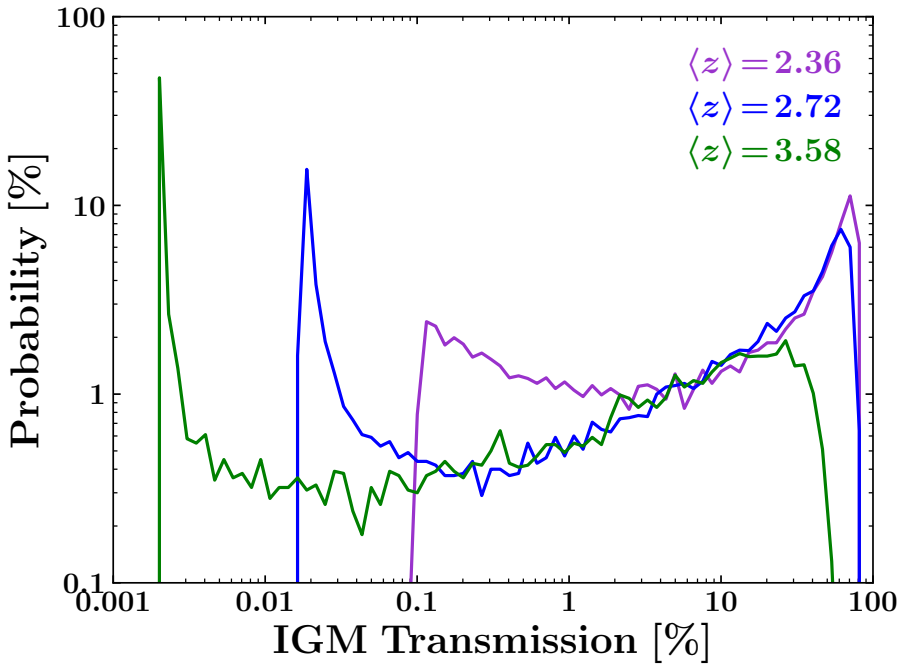


Figure 4. Filter-weighted Probability Curves of Transmission of LyC Through the IGM

The filter-weighted IGM transmission values vs. the relative probability of encountering the transmission values. The IGM transmission curves from Inoue et al. (2014) for $10^4$ lines of sight at $z = 2.36$, 2.72, and 3.58 were weighted by the wavelength-dependent transmission of the WFC3/UVIS F225W, F275W, and F336W filter curves and are shown in violet, blue and green, respectively. The redshifts used in these curves corresponds to the average redshifts of the sample from §5.3. The highest redshift transmission curve shows the highest probability of no transmission of LyC through the IGM. The lowest redshift curve shows that transmission through the IGM with little to no attenuation is more likely than at higher redshift, and the minimum transmission value is higher than at high redshift. The transmission of LyC through the IGM at higher redshift will become even less likely, until no LyC is expected to be observed at $z \sim 6$.

The SED must also be attenuated by the absorption of UV photons from hydrogen through the IGM to model the intrinsic LyC emission for calculation of $f_{\rm esc}$. Several models simulate this absorption of UV light propagating through the IGM at various redshifts (e.g., Madau 1995; Meiksin 2006; Tepper-Garcıa and Fritze 2008). In the work presented here, we use the models of Inoue et al. (2014) which simulates the transmission through the IGM of UV-light with wavelength $600\,\text{Å} < \lambda_{\rm rest} < 1300\,\text{Å}$. This model allows for the selection of wavelength dependent transmission through the IGM for a variety of sight-lines, and at various redshifts. The transmission through these sight-line will depend on the distribution of intervening absorption clouds out to the distance of the galaxy, and the wavelengths of light shorter than Lyman-$\alpha$ will be prone to absorption after being redshifted. The probability distributions of the filter-weighted transmission values at redshifts $z = 2.36$, 2.72, and 3.58 are shown in Fig. 4. The Inoue et al. (2014) model uses observed distribution statistics of the Lyman-$\alpha$ forest, Lyman-limit systems (LLSs), and damped Lyman-*alpha* absorbers (DLAs). LLSs and DLAs are both concentration of intervening hydrogen gas (with smaller amounts of other elements, e.g., Levshakov, S. A. et al. 2002), but LLSs show spectral breaks in the spectra of distant quasar corresponding to the Lyman-limit ($\lambda_{\rm rest} < 912\,\text{Å}$) at the redshift of the LLS (e.g., Prochaska 1999), and DLAs show an absorption line in quasar spectra corresponding to Lyman-$\alpha$ absorption at the redshift of the DLA (e.g., Rao and Turnshek 2000). DLAs are also $\sim 10^3$ times denser than LLSs (Péroux et al. 2003).

The distribution of these intergalactic absorbers allows for $f_{\rm esc}$ to be computed in a MC fashion. In this methodology, random sight-lines corresponding to unique transmission curves (based on unique numbers of intervening absorption clouds) are chosen, and the $f_{\rm esc}$ is computed using Eq. 3.7. Uncertainties in the estimate of the

SED fits, i.e. the $\chi^2$ value, should also be incorporated into the estimation of $f_{\rm esc}$ when calculating the intrinsic LyC flux. This is akin refitting the SEDs via statistical subsampling (Politis, Romano, and Wolf 1999) within the observed continuum errors. The *model* LyC flux distribution is the *observed* continuum data points the SEDs were fit to within their error bars, and refitting the SED by least squares, i.e.,

$$F'_\nu(\nu) = \alpha F_\nu(\nu), \text{ with } \alpha = \mathbf{F^r_\nu} \cdot \mathbf{F^m_\nu} / ||\mathbf{F^m_\nu}||^2 \tag{3.13}$$

and where $\mathbf{F^r_{\nu,i}}$ and $\mathbf{F^m_{\nu,i}}$ are the randomized *observed* flux measurements and continuum band *model* fluxes, respectively. This error estimate is equivalent to applying a convolution to the intrinsic SED LyC flux with a Gaussian kernel with dispersion equal to the quadratic sum of the variances of the photometry used to fit the SED. The main uncertainty in the SED fitting is *not* the $\chi^2$ values of fitted data, but the uncertainty in the applied internal extinction values $A_V$ to each SED, which is unknown, though can be estimated using a method of MC fitting SEDs with a range of $A_V$ values.

Since the IGM transmission through various sight-lines is highly non-linear and cannot be approximated by a Gaussian distribution, the standard deviation from the mean of the the distribution may not be the best estimator of the uncertainty range of $f_{\rm esc}$. For a Gaussian distribution, values between one standard deviation on either side of the mean correspond to $\sim$68.27% of the area under the curve. Thus, a better estimation of the uncertainty range of $f_{\rm esc}$ will correspond to $\sim$68% of the data in the distribution at equal probability about the mode.

The extent of the uncertainties in the $A_V$ correction go back to the original formulation of the attenuation curves. For example, Calzetti et al. (2000) empirically derived the dust attenuation curves of nearby starburst galaxies and found a total to selective extinction value of $R_V = 4.05 \pm 0.8$. SEDs fit to multi-wavelength photometry

are reddened with various dust screen $A_V$ values by $F_\nu^{\rm obs}(\lambda) = F_\nu^{\rm int}(\lambda) 10^{-0.4 A_\lambda}$, where: $A_\lambda = k(\lambda) A_V / R_V$. The attenuation for wavelengths shorter than 630 Å and longer than 2200 Å can be extrapolated from the interpolated slope of the endpoints of the attenuation curves, since this data is not used for any analyses. The applied reddening does not include the uncertainty in the $R_V$ value. Estimating the reddening error in the flux of our sample galaxies would require a more extensive SED fitting analysis, which takes into account the equally probable $A_V$ values that fall within the measurement errors of the observed continuum data points.

Uncertainties in the stacked $f_{\rm esc}$ values will be dominated by the variation of the IGM transmission of LyC at the various redshifts and sight-lines, and the dispersion of the LyC flux if this has a low SNR. Thus, incorporating a full dust correction error will only increase the uncertainty in $f_{\rm esc}$, which may not be an accurate source of uncertainty due to the many unknowns involving dust correction.

In the next chapter, the methodology outlined above will be applied to a sample of galaxies located in the first *HST* UV mosaic images constructed for extragalactic study. These mosaics are ideal for studying ionizing sources and their $f_{\rm esc}$, and may be the best UV mosaics that exist today for studying faint LyC emission from galaxies. The findings presented in the next section were published in Smith et al. (2018).

Chapter 4

# THE LYC ESCAPE FRACTION FROM GALAXIES AND AGN IN THE EARLY RELEASE SCIENCE FIELD

## 4.1 Introduction

The Early Release Science (ERS) field is a region of sky centered on the right ascension (R.A.) 53.1° and declination (Dec.) -27.7°, and has an area of $\sim 58\,\mathrm{arcmin}^2$. This field was imaged with the Hubble Space Telescope (*HST*) using its, at the time, newly install Wide Field Camera 3 image detectors, the UV/visible (UVIS) and infrared (IR) channels (Windhorst et al. 2011). These cameras replaced the Wide Field Planetary Camera 2 detector in May 2009 during Shuttle Servicing Mission SM4. The UVIS channel has a *native* pixel resolution of $\sim 0\farcs039$/pixel and the IR channel has a native resolution of $\sim 0\farcs13$/pixel. The ERS UVIS and IR imaging program was conducted to provide a small, but representative sampling of the capabilities of WFC3 to examine the formation and evolution of galaxies in the epoch of $z \sim 1$–3 while galaxy assembly was at it's peak (Madau and Dickinson 2014).

The ERS UV data was taken in September 2009, less than four months after SM4 installed WFC3 onto *HST*. This an important feature of this data, since cameras exposed to the constant bombardment of high-energy particles in space degrade with time. One of the most severely affected properties during this degradation of the camera is the charge transfer efficiency (CTE). The CTE of a camera describes how efficiently electrons ($e^-$) are shifted between pixels during readout. A standard readout of an exposure occurs serially along the rows of the 2-dimensional grid of pixels. A

Figure 5. Color image of the Early Release Science Field
A color composite of *HST* images taken by the WFC3 and ACS cameras in the Early Release Science Field. 10 mosaic images, corresponding to different wavelength passband filters were used in its creation. The WFC3/IR F125W + F160W is represented by red, ACS/WFC F606W + F775W + F850LP + WFC3/IR F098M is green, and ACS/WFC F435W + WFC3/UVIS F225W + F275W + F336W is blue. These 10 bands, represented in this color image are all used extensively throughout the work presented here.

Credit: R. Windhorst, S. Cohen, M. Mechtley, and M. Rutkowski (Arizona State University, Tempe), R. O'Connell (University of Virginia), P. McCarthy (Carnegie Observatories), N. Hathi (University of California, Riverside), H. Yan (Ohio State University), and R. Ryan and A. Koekemoer (STScI)

single row gets shifted down row by row to a final row of unexposed pixels called the serial register. Each pixel in the serial register is then readout one by one and the electrons are counted by the ADC. A typical CTE of a well functioning camera is ∼99.99%.

High energy cosmic ray collisions with the detector, and encounters with relativistic protons and electrons during *HST*'s frequent passages through the South Atlantic Anomaly damage the silicon of the CCD, and can cause areas where electrons become trapped in the detector's crystal lattice during readout. The WFC3/UVIS detectors suffer from a CTE loss of ∼0.1 mag per year. After several years in orbit, faint objects

($\lesssim$300 $e^-$) can lose up to 50% of their flux during readout (Noeske et al. 2012; Bourque and Kozhurina-Platais 2013).

CTE degradation can also cause charge trails to be visible in the images, caused by the delayed release of trapped electrons embedded in the pixels during readout. Partial recovery and correction of CTE trails in post-processing of the images is only possible for brighter sources (Anderson and Bedin 2010; Massey et al. 2014). Flux from very faint objects cannot be corrected in this manner, as their low electron counts are lost in the background noise of the detector.

Because the WFC3 UV data were taken less than four months after Shuttle Servicing Mission SM4 that installed WFC3 onto *HST*, the WFC3/UVIS ERS data does not suffer from significant CTE losses or artifacts. The pristine ERS images are therefore an excellent dataset for searching for the faint signals of LyC emitted by high redshift galaxies. The ERS data is described in more detail in the next section, and the sample of galaxies within the ERS images, their properties, and their $f_{\rm esc}$ values are presented in subsequent sections.

## 4.2 Data Description

The ERS field was observed by *HST* using its WFC3/UVIS channel in the F225W, F275W, and F336W filters. These filter curves are shown in Fig. 6, along with example stacked spectra of typically observed galaxy types, i.e., quasars, Lyman-break galaxies (LBGs), Lyman-$\alpha$ emitting galaxies, and Lyman-$\alpha$ absorbing galaxies. This figure demonstrates how the filters used during observation of the ERS field can capture the LyC with negligible amounts of non-ionizing light entering the filter from galaxies at

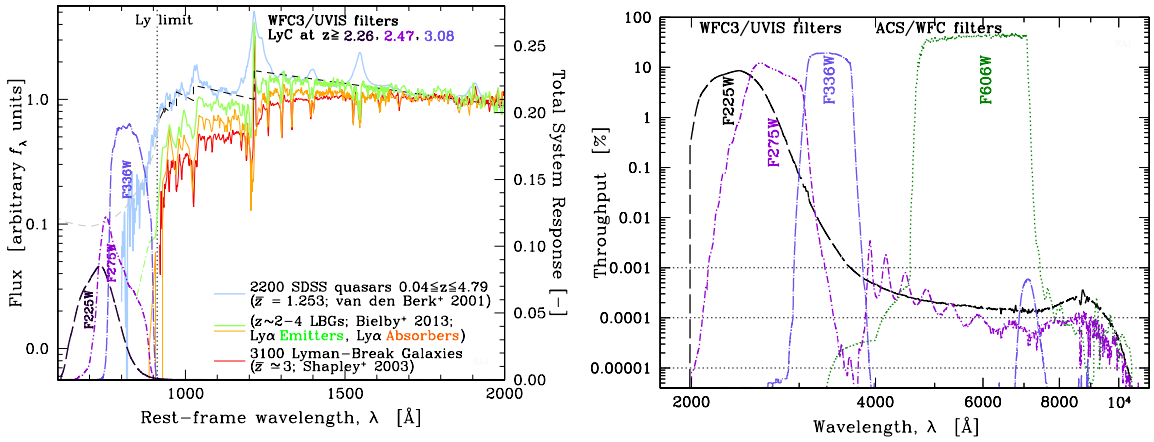


Figure 6. WFC3/UVIS LyC Filters and Example Galaxy and AGN Spectra

[*a*] Example composite rest-frame FUV spectra of QSOs at $\langle z \rangle \sim 1.3$ observed with the Sloan Digital Sky Survey (SDSS) (Vanden Berk et al. 2001 [*blue*]) and of LBGs at $z \simeq 2$–4 (Bielby et al. 2013 [*green* and *orange*]; Shapley et al. 2003 [*red*]). The WFC3/UVIS F225W, F275W, and F336W filter transmission curves are ideally positioned to capture LyC at $z \geq 2.26$, $z \geq 2.47$, and $z \geq 3.08$, respectively. The combined SEDs of SDSS QSOs suggest a strong LyC signal, whereas the SEDs of LBGs suggest fainter LyC flux. [*b*] Total system throughput curves (observed wavelengths) of the same WFC3/UVIS and ACS/WFC filters (Dressel et al. 2015; Avila et al. 2015) are shown on a logarithmic scale to emphasize their out of band transmission ("red-leak"). These WFC3 UVIS filters were designed to simultaneously maximize throughput and minimize such red-leaks. In Appendix B.1.1 the percentage of non-ionizing UVC flux with $\lambda > 912$Å leaking in the filter is assessed. The ACS/WFC F606W filter capturing the UVC of these spectra is shown for reference.

redshifts $z \geq 2.26$. The ERS UV data reaches a ∼2 orbit depth ($m_{\rm AB} < 26.4$ at $5\sigma$ for F275W).

Complementary optical *HST* data using the Advanced Camera for Surveys Wide Field Camera (ACS/WFC) was taken in July 2002-May 2003 as part of the Great Observatories Origins Deep Survey (GOODS; Dickinson, Giavalisco, and GOODS Team 2003). The corresponding rest-frame non-ionizing UVC imaging of galaxies in the ERS field were taken with ACS/WFC in the F606W, F606W, and F775W, respectively. These filters sample rest-frame $\lambda_{\rm eff}$∼1400-1800Å for each of corresponding

WFC3/UVIS filter. We also utilized photometry from WFC3/IR F098M, F125W, and F160W imaging in the ERS field (Windhorst et al. 2011) and WFC3/IR F105W, F125W, and F160W from the Cosmic Assembly Near-infrared Deep Extragalactic Legacy Survey (CANDELS Grogin et al. 2011; A. M. Koekemoer et al. 2011), as well as photometric catalogs in GOODS-South (Guo et al. 2013) for object selection and SED fitting.

Table 1 summarizes the data in the ERS and GOODS South fields available for studying LyC emission, and the redshift range over which each of these filters can sample LyC emission with negligible contamination from non-ionizing flux. Each lower redshift bound was carefully chosen such that *no* light with $\lambda > 912$Å is sampled below the filter's red edge (defined at 0.5% of the filter's peak transmission, as tabulated in Dressel et al. (2015) and references therein). The upper redshift bound of each bin in Table 1 occurs at the redshift where the next redder filter can trace LyC emission more sensitively. Fig. 6 suggests that the observed escaping LyC emission strongly declines towards shorter wavelengths. For this reason, the broadband filters use are most sensitive to LyC emission at the low redshift end of each of the three redshift ranges of Table 1.

#### 4.2.1 Image Calibration, Drizzling and Astrometric Accuracy

The *HST* cameras are well known to undersample the resolution of the 2.4 meter diameter mirror. *HST* has a diffraction limit of $\sim 0\farcs03$ in the UV and the UVIS CDD detectors have resolutions of $\sim 0\farcs04$/pixel. A sufficient sampling rate, also known as the Nyquist sampling rate, requires that at least two pixels contain one resolution element, i.e., at least two pixels should have the same resolution as the mirror's

diffraction limit. Sampling the resolution of *HST*'s optics below its diffraction limit can lead to aliasing, and smaller features *HST* can resolve are lost by the detector. Fortunately, the Drizzle algorithm (Williams et al. 1996; Fruchter and Hook 2002), adopted as the primary image processing tool for *HST*, can reconstruct the information lost to undersampling.

The algorithm essentially maps subsampled images onto further subsampled output pixels, e.g., native 0.″04 WFC3/UVIS pixels onto output a 0.″03/pixel grid, taking into account shifts and rotations of the telescope pointing between exposures and distortions in the image created by the optics of *HST*. The native pixels are first shrunk down to "drops", and are rained down, or *drizzled* onto the output pixel grid. The electron counts in the native pixels are then averaged over the output pixels. When native pixels overlap with multiple output pixels, their counts are added into the output pixel proportionately by the physical area of the overlapping size. Because of this proportionate weighting of the native pixels, Drizzle can reconstruct images while preserving the flux measured in individual exposures. The distortions caused by the optics can generally be corrected by applying a geometric transformation on the raw images, which warps the shape of the image so that the distortions are removed. The geometrically corrected images can be used as inputs in the drizzle algorithm to produce the final mosaic, which combines and calibrates all raw input images.

The point spread function (PSF) of a telescope defines the shape of a point-like source of light, such as a distant star, on an image. A single, perfect mirror has a PSF described by an Airy disk, which is the 2-dimensional Fourier transform of a circular aperture, e.g., a mirror or lens. Because telescopes involve intricate optical setups to correct for various distortion effects of mirrors, such as field curvature or spherical aberration (Redding et al. 1995), the PSF deviates from the ideal Airy disk.

Thus, only simulations using ray-tracing through the optical setup or measurements on the images themselves can describe the true PSF of the optical telescope array (OTA). The smearing out of information caused by the subsampling of a native pixel can be partially recovered by the Drizzle algorithm if the input images are dithered by amounts smaller than a pixel. Here, dithering describes the change in location of the pointing direction by *HST*. Sub-pixel dithering can allow the camera to sample the PSF at several points in its spatial profile, which can later be reconstructed onto a finer grid by Drizzle.

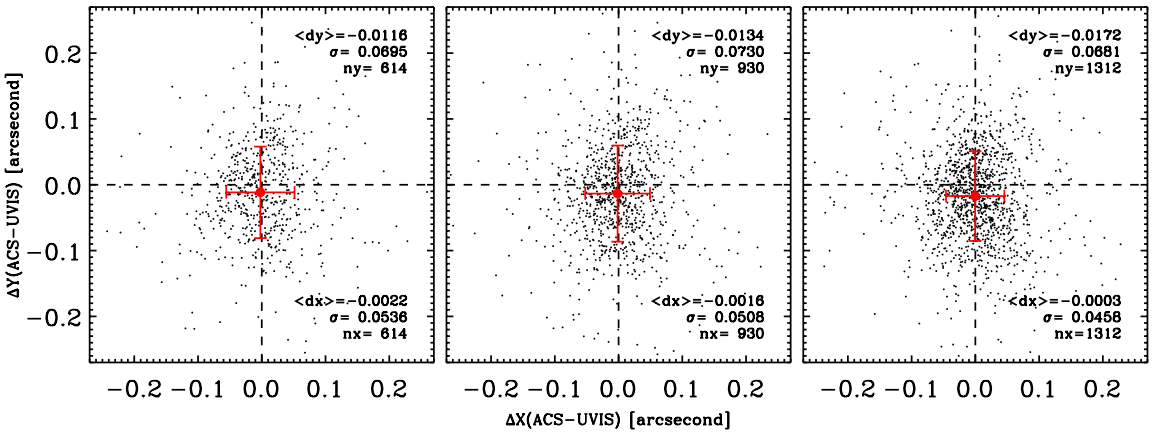


Figure 7. Astrometric Offsets of Improved ERS Mosaics

Residual astrometric errors in the improved WFC3/UVIS ERS mosaics in F225W [*left*], F275W [*middle*], and F336W [*right*], respectively, as measured relative to the ACS/WFC F435W ERS mosaic. The new WFC3/UVIS geometric distortion corrections provided a significantly improved registration of all 8 WFC3/UVIS tiles to the ACS/WFC F435W mosaics compared to the 2009 ERS mosaics of Windhorst et al. (2011). The measured residual systematic offsets are $\langle \Delta X \rangle \lesssim 0\farcs0022$ and $\langle \Delta Y \rangle \lesssim 0\farcs0172$ compared to ACS (indicated by the dashed lines), and random deviations less than $0\farcs054$ in X and $0\farcs073$ in Y.

The ERS UV image mosaics were constructed using the Astrodrizzle program, a Drizzle program that applies a number of calibration and mosaicing steps into one process. These steps include, e.g., improved geometric and astrometric calibration of

the raw images (Fruchter and et al. 2010). These improvements are in essence, better algorithmic treatment of the geometric and astrometric distortion using higher-order polynomial coefficients (Shupe et al. 2005). The ERS mosaics used here were drizzled to a plate scale of 0.″03/pixel.

The initial astrometric calibration of the WFC3/UVIS ERS mosaics, described in Windhorst et al. (2011), left systematic offsets between individual WFC3 CCDs of up to $\sim 5$ drizzled pixels ($\sim 0.''5$) compared to the GOODS v2.0[1] F435W mosaics, especially at the edges of each UVIS mosaic tile (see Appendix A of Windhorst et al. 2011). These offsets occurred in part due to the way the ERS UVIS exposures were taken, but were primarily due to the rather uncertain geometric instrument distortion correction (IDC) tables available at the time (Kozhurina-Platais et al. 2009). The lack of UV bright astrometric reference sources in the shallow ($\sim 900$–$1400$ s) individual exposures further prevented accurate registration and drizzling of the F225W, F275W, and F336W images. This issue was resolved with the improved IDC tables of Kozhurina-Platais et al. (2013) and Kozhurina-Platais (2014). Using these new IDC tables, we re-drizzled the UVIS ERS images into mosaics at a plate scale of $0.''03\,\mathrm{pix}^{-1}$.

Fig. 7 shows the residual astrometric errors of the new ERS mosaics (which we refer to as ERS "v2.0") for the F225W, F275W, and F336W filters, measured relative to the ACS/WFC F435W mosaics. Residual systematic offsets from the ACS/WFC F435W GOODS v2.0 mosaics for the 8 WFC3/UVIS ERS tiles are now measured to be $\langle \Delta X \rangle \lesssim 0.''0022$ (0.024 pix) and $\langle \Delta Y \rangle \lesssim 0.''0172$ (0.19 pix), with $1\sigma$ random deviations less than $0.''054$ (0.60 pix) in X and $0.''073$ (0.81 pix) in Y. Any remaining systematic astrometric offsets are at the sub-pixel level, and are sufficiently small that they

[1]http://archive.stsci.edu/pub/hlsp/goods/v2/h_goods_v2.0_rdm.html

no longer affect our SB sensitivity to LyC flux, nor do they add contamination from neighboring sources that can potentially blend in with the LyC signal due to astrometric uncertainties.

The photometric and astrometric calibration and drizzling of the publicly available ACS/WFC mosaics used alongside the UV data in the LyC analyses presented here are described in Giavalisco et al. (2004). These mosaics were also constructed using the Drizzle algorithm, with optimized input parameters for the ACS/WFC detector. This optical ACS/WFC data was taken in July 2002-May 2003 as part of GOODS (Dickinson, Giavalisco, and GOODS Team 2003). We also utilized photometry from WFC3/IR F098M, F125W, and F160W imaging in the ERS field (Windhorst et al. 2011) and CANDELS WFC3/IR F105W, F125W, and F160W (Grogin et al. 2011; A. M. Koekemoer et al. 2011) photometric catalogs in GOODS-South (Guo et al. 2013) for object selection and SED fitting, which is described in §5.3.

Table 1. Summary of HST WFC3/UVIS Images and Image Stacks in the ERS Field

| Filter | $\lambda$ / $\Delta\lambda$[a] | $z_{\rm LyC}$[b] | Obs. Date | $t_{\rm exp}$[c] | PSF[d] | $SB$(obs)[e] |
|---|---|---|---|---|---|---|
| F225W | 2359 / 467 | 2.26–2.47 | 2009 Sep 7–11 | 5,688 | 0.″087 | 29.80 |
| F275W | 2704 / 398 | 2.47–3.08 | 2009 Sep 7–11 | 5,688 | 0.″087 | 29.82 |
| F336W | 3355 / 511 | 3.08–4.35 | 2009 Sep 7–12 | 2,778 | 0.″088 | 29.76 |

[a]Central wavelength / bandwidth of filter in Å; [b]Redshift range over which rest-frame LyC emission can in principle be sampled. The high end of each bin occurs at the redshift where the next redder filter can better sample LyC emission at the same or higher redshift.; [c]Average integration time of the mosaics in seconds; [d] Typical stellar PSF FWHM.; [e] Measured $1\sigma$ surface brightness sensitivity limit of our mosaics for a source of uniform SB in a 2.″00 diameter aperture in AB mag arcsec$^{-2}$ (see Windhorst et al. 2011 and Table 1)

.

### 4.2.2 WFC3/UVIS Residual Sky-Background

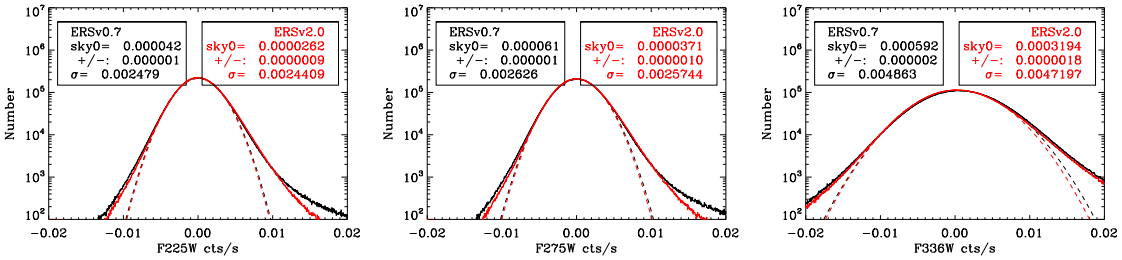


Figure 8. UV Sky-background Levels in the ERS Field

Residual sky-background levels in the drizzled WFC3/UVIS ERS mosaics in the F225W [*left*], F275W [*middle*], and F336W [*right*] filters, determined as described in §4.2.2. The best fit to the 2009 ERS mosaics of Windhorst et al. (2011) ("v0.7") is shown in black, while the improved mosaics discussed here ("v2.0") are shown in red. Dashed lines show Gaussian fits to the two histograms. Each panel lists the best fit *residual sky-background level (in counts/sec)*, equivalent to 30.29, 29.99, and 28.15 mag arcsec$^{-2}$, respectively, and the uncertainties thereon across the entire WFC3 ERS mosaic.

The original WFC3/UVIS thermal vacuum flats created while WFC3 was still on Earth left residual gradients and patterns in the sky-background when used for processes raw exposures. These deviations from the mean sky-background were at the 5–10% level (Sabbi 2009). For the reprocessing of the ERS data, we use the flat-fields from Mack, Sabbi, and Dahlen (2013), which include on-orbit "delta-flat" corrections to the ground-based thermal vacuum flat-fields, significantly reducing the large scale flat-field patterns seen in earlier ERS mosaics.

Windhorst et al. (2011) measured zodiacal sky-background surface-brightness (SB) levels in the ERS of 25.46, 25.64, and 24.82 mag arcsec$^{-2}$ in the WFC3/UVIS F225W, F275W, and F336W mosaics respectively. When drizzling the data, this sky-background is subtracted (e.g., Anton M. Koekemoer et al. 2013). For the 5688, 5688, and 2788 s effective exposure times in these filters, this corresponds to a subtraction of

$\sim 2.43\times10^{-4}$, $2.24\times10^{-4}$, and $7.82\times10^{-4}\,e^-/0\farcs03$ pixel, respectively. To determine the best fit *residual* sky background level across the WFC3/UVIS ERS mosaics, we use the Freedman-Diaconis rule (Freedman and Diaconis 1981), who define the sampled bin width for optimal histogram fitting as $2\times\mathrm{IQR}\times\mathrm{N}^{-1/3}$, where IQR is the inner quartile range of the pixel distribution (i.e., the range within 75% and 25%, or $\pm\,1.349\,\sigma/2$ for a Gaussian distribution), and $N$ is the total number of pixels used in the image to construct that histogram. We fit the logarithm of the sky pixel histogram between $-3\sigma$ and $+1\sigma$ to a Gaussian function by least squares to obtain the peak value of the fitted functions.

Fig. 8 shows the sky pixel histograms and best fit *residual* sky-background levels in the WFC3/UVIS F225W, F275W, and F336W ERS mosaics of Windhorst et al. (2011) in black, while the red curves and measurements indicate the best fit to the data in the improved mosaics used here. The slight narrowing of the negative tail of the Gaussian noise distributions in the new mosaics reflects the better flat-fielding. Our best fit *residual* sky background values and their uncertainties are $(2.62\pm0.09)\times10^{-5}$, $(3.71\pm0.10)\times10^{-5}$, and $(31.94\pm0.18)\times10^{-5}$ counts/s in the F225W, F275W, and F336W filters, respectively. These levels correspond to residual sky SB levels of 30.29, 29.99, and 28.15 mag arcsec$^{-2}$ left in the UVIS images *after* drizzling, which subtracted the sky-background in individual exposures to first order. Compared to the observed ERS sky-backgrounds measured in Windhorst et al. (2011), these residual sky SB level values are 4.84, 4.35, and 3.33 mag fainter than the UV sky (1.2%, 1.8%, 4.7% of the UV sky), respectively. These residual sky-background levels can be accurately determined locally and subsequently subtracted, which we employed in our subimage stacking technique to further increase our sensitivity to extended, low SB LyC signal.

## 4.3 Sample Selection Criteria and Characteristics

### 4.3.1 Spectroscopic Sample Selection

In order to obtain accurate estimates of LyC escape fractions as low as $f_{\rm esc}\lesssim 1.0\%$, we must require the low-redshift interloper fraction to be very small. Thus, any potentially contaminating, low redshift, interloping galaxies that might create a false-positive LyC signal must be identified and removed from our sample. We therefore required each galaxy we included in our analysis to have a highly reliable spectroscopic redshift.

Several wide field ground-based spectroscopic surveys have been performed in the GOODS fields, including the ERS region, at low and high redshift with the Very Large Telescope (VLT) (e.g., S. Cristiani et al. 2000; Le Fèvre et al. 2004; Szokoly et al. 2004; Wolf et al. 2004; Vanzella et al. 2008; Popesso et al. 2009; Wuyts et al. 2009; Balestra et al. 2010; Silverman et al. 2010; Fiore et al. 2011; Kurk et al. 2012; Le Fèvre et al. 2015; Tasca et al. 2017) as well as *HST* (Momcheva et al. 2016). We retrieved the reduced 1-dimensional FITS spectral data from the ESO archives[2] along with their corresponding 3D-HST grism spectra[3] for galaxies at $z \geq 2.26$ in order to verify the designated redshifts of these galaxies. We plotted each spectrum at both the original spectral resolution and smoothed with a $\sigma = 3$ Å Gaussian convolution kernel to reduce the noise in the spectrum for inspection. Typical spectral emission or absorption features for SFGs and AGN were indicated, and portions of the spectra

[2]http://archive.eso.org/, http://www.eso.org/sci/activities/garching/projects/goods/MasterSpectroscopy.html, and http://cesam.lam.fr/vuds/DR1/

[3]http://3dhst.research.yale.edu/Home.html

around these features were magnified for closer examination. An example classification diagram of all available ground-based and *HST* grism spectra and imaging used for sample selection is shown in Fig. 9.

The emission or absorption features we focused on include the Lyman Break at 912Å, Ly $-\alpha$ 1216Å, Si 2 1260Å, O 1 1304Å, C 2 1335Å, Si 4 1398Å, C 4 1549Å, and C 3] 1909Å, and when present, C 2] 2326Å, Fe 2 2344Å, and sometimes N 5 1240Å, Fe 2 2600Å, Mg 2 2798Å, O 2 3727Å, [Ne 3] 3869Å, He 2 4686Å, H 0$\beta$ 4861Å, and [O 3] 4959+5007Å. In addition, we included high contrast cutout images of the galaxies in the filter sampling the rest-frame LyC emission, and all available longer wavelength filters for inspection and removal of contaminating objects.

We recruited 5 experts in spectroscopy to help us visually inspected all spectra and we unanimously selected the highest quality spectra available from the spectroscopic surveys and compose our spectroscopic sample of galaxies and AGN. We found that including objects with spectra that had less reliable redshifts improved our SNR, but likely added contaminating flux rather than true escaping LyC flux. Hence, we *only* included galaxies with the highest quality spectra that coincided with their predicted emission/absorption lines exactly.

Note that 12 of the 46 objects in our spectroscopic sample are galaxies hosting a *weak* AGN, as evidenced by the (broad) emission lines in their spectra, for example Ly $-\alpha$, N 5, Si 4, C 4, He 2, C 3], and Mg 2. We also cross-correlated the positions of our galaxy sample with Chandra 4 Ms and Very Large Array 1.4 GHz source catalogs to identify possible obscured/type II AGN using their radio/X-ray luminosities and photon indices (e.g., Xue et al. 2011; Fiore et al. 2012; Miller et al. 2013; Rangel et al. 2013; Xue et al. 2016). We identified five of the 12 galaxies hosting AGN from their X-ray emission. For our LyC analyses in the ERS field, we study the

subsamples of 34 galaxies *without* AGN signatures, and 12 galaxies *with* weak AGN, both separately and combined. This allows us to make direct comparisons of these two classes of ionizers, and how they may have contributed to reionizing the IGM at $z \gtrsim 6$, if our sample of galaxies are analogous to those that existed during the epoch of reionization.

### 4.3.2 Completeness and Representativeness of the Spectroscopic Samples

Initially, our sample of galaxies was limited to those with *known* spectroscopic redshifts. Our selection of galaxies with high quality spectra in GOODS-S, which solely determined which objects were included in our analysis, reduced our sample to galaxies that can be observed with ground-based spectroscopy at a high SNR. This, of course, can bias our results and their subsequent interpretations, e.g., if $f_{\rm esc}$ is a strong function of luminosity ($M_{\rm AB}$), dust extinction ($A_V$), metallicity, and/or age. We therefore must consider how representative the characteristics of our selected galaxy samples are in order to understand differences in the results of our analyses of the populations.

In Fig. 10 we plot the distribution of observed apparent magnitudes ($m_{\rm AB}$), and the corresponding absolute magnitudes ($M_{\rm AB}$) of the rest-frame non-ionizing UVC flux ($\lambda_{\rm eff} = 1500 \pm 100$ Å) of our samples. We consider all galaxies (Fig. 10*a*), galaxies hosting weak AGN (Fig. 10*b*), and galaxies without AGN (Fig. 10*c*). These values were derived from the apparent flux of the galaxies at the same rest-frame wavelengths, using their best fit SED models, so no k-corrections are necessary to directly compare the $M_{\rm AB}$ values of the galaxies at various redshifts.

If the spectroscopic samples were complete, their apparent magnitude distributions

would resemble the galaxy count distributions of the full $V$ and $i$-band mosaics (Giavalisco et al. 2004; Windhorst et al. 2011) to a given AB magnitude limit, since these filters sample the UVC emission indicated in Fig. 10, and because the spectroscopic samples were $r$ band or $i$ band selected. Their $M_{\rm AB}$ distribution would also reflect the galaxy UV luminosity function slope at their effective $M_{\rm AB}$ to the effective completeness limits at these redshifts, which typically sample rest-frame wavelengths $\lambda_{\rm eff} \simeq 1500-1700$Å (e.g., Reddy and Steidel 2009; S. L. Finkelstein et al. 2015).

It is clear from Fig. 10 that our spectroscopically selected samples are incomplete for $m_{\rm AB} \gtrsim 24.0$ mag, both for galaxies with and without weak AGN. For $m_{\rm AB} \lesssim 24.0$ mag, the distributions are consistent with the expected slope of the galaxy counts from Windhorst et al. (2011), so the selected samples may be representative for LyC studies, but only for these brighter fluxes. We also note that our selection of galaxies with high SNR spectra will have favored the broad emission lines of (weak) AGN, and Lyman-$\alpha$ emission or strong absorption line galaxies, while LBGs and other galaxies without prominent spectroscopic features are less likely to have yielded the highly reliable redshifts required to be included in our highest fidelity sample, even for $m_{\rm AB} \lesssim 24.0$ mag.

The UVC luminosities of the galaxies in our sample span $-22.2 \lesssim M_{\rm AB} \lesssim -19.0$ mag, with an average of $M_{\rm AB} \simeq -21.1^{+0.9}_{-0.5}$ mag ($1\sigma$), indicative of predominantly luminous galaxies about as bright as $M^*$ at $2.5 \lesssim z \lesssim 4$ (e.g., Hathi et al. 2010), or of galaxies hosting *weak* AGN. Since this is the only sample for which reliable redshifts currently exist, this is strictly the only luminosity range over which the measurements and analyses of any escaping LyC emission that follows will be valid. These galaxies may

also be more luminous than galaxies that contributed to reionization at $z>7$ (e.g., Bouwens et al. 2012).

Our sample also does not fully sample the parameter space of the age, stellar mass, star-formation rate (SFR), and $A_V$ values for galaxies at these redshifts, indicated by their SED fits. These biases are also more prominent in the individual redshift subsamples. Fig. 11 shows the distribution of these parameters for the spectroscopic sample of galaxies without AGN. These galaxies more or less evenly sample the mass and SFR distribution, which are are generally quite massive and indicative of active star-formation, with masses ranging from $\sim 10^{9.5}$–$10^{10.9}$ ($\langle \mathrm{mass} \rangle = 10^{10.2\pm0.3}$) $\mathrm{M}_\odot$ and SFRs from $\sim 10^{0.8}$–$10^{3.1}$ ($\langle \mathrm{SFR} \rangle = 10^{1.5\pm0.4}$) $\mathrm{M}_\odot$/yr, respectively. Their ages and $A_V$ distributions range from $\sim 10^{7.7}$–$10^{9.4}$ yr ($\langle \mathrm{t_{age}} \rangle \simeq 10^{8.2^{+0.9}_{-0.4}}$ yr) and $A_V = 0.0$–$0.8$ mag ($\langle A_V \rangle_{\mathrm{med}} \simeq 0.3\pm0.3$ mag), respectively. We note that the variation in these parameters from sample to sample is most likely due to the selection of the spectroscopic sample, rather than any real correlation in redshift, as the higher redshift galaxies were generally selected in the redder ACS filters.

The incomplete sampling of these various parameters should be taken into account when interpreting the $f_{\mathrm{esc}}$ values for these individual subsamples. In order to obtain a more representative sample of galaxies in each redshift bin, we must include more galaxies that sample the full range of these parameters at their respective redshifts, with average parameters that reflect the true averages for all galaxies at these redshifts, and probe fainter luminosities. This should be a focus of future deeper spectroscopic surveys, either from the ground or with the James Webb Space Telescope (*JWST*).

## 4.4 Results

### 4.4.1 Sub-Image Stacking of LyC Signal

Since LyC escape fractions have been measured to be very low, and the detected LyC emission is likely to be very faint or not detected at all, we applied our stacking algorithm described in §3.1 to the *observed* LyC emission from our galaxy sample to increase their total SNR and sensitivity to the faint, low SB LyC flux from the individual galaxies.

For each galaxy, we extracted 151×151 pixel ($4\farcs53 \times 4\farcs53$) subimages from the WFC3/UVIS mosaics in the respective filter that samples the LyC emission of each galaxy. The size of these cutouts provided sufficient sampling of the photon statistics in the sub-images for fitting the pixel count-rate distribution, while minimizing the potential area of neighboring sources of non-ionizing flux. Each sub-image was centered on the R.A. and Dec. of the centroid of the individual galaxy indicated in the 3D-HST photometric catalog (Skelton et al. 2014).

We then created SExtractor (Bertin and Arnouts 1996) segmentation maps from $\chi^2$ images (Szalay, Connolly, and Szokoly 1999) generated from all available *HST* data for each LyC sub-image in order to identify *all* neighboring objects detected at a $\geq 1\sigma$ threshold above the local sky. These $\chi^2$ images are effectively composites of multiband images where the pixel values correspond to probabilities of that pixel being background, i.e., not statistically associated with a source of real flux from an object. The combination of all available multiband into one image also has the advantage of increasing the signal of faint sources of flux that would otherwise not be

visible in any single image. Each pixel $g_i$ in the $\chi^2$ image corresponds to

$$g_i = \frac{f_i - \mu_i}{\sigma_i} \tag{4.1}$$

where $f_i$ is the original pixel value in the subimage, $\mu_i$ is the mean of the pixel values, and $\sigma_i$ is the standard deviation of the pixel values. This equates to converting a subimage going into the $\chi^2$ image to a normalized Gaussian, i.e., a Gaussian with $\mu = 0$ and $\sigma = 1$. The $\chi^2$ image is constructed by summing these normalized subimages, i.e. the probability distribution of the $\chi^2$ image $x$ is described by

$$x = \sum_{\mathrm{i=1}}^{\mathrm{N_{gal}}} g_i^2 \tag{4.2}$$

and the PDF of pixels $y$ in the $\chi^2$ image is defined as

$$dP(y) = \frac{x^{\frac{N}{2}-1} e^{-\frac{x}{2}}}{2^{\frac{N}{2}}\Gamma(\frac{N}{2})} dx \tag{4.3}$$

where $\Gamma(\frac{N}{2})$ denotes the gamma function. Integrating the pixels of a $\chi^2$ image within an aperture thus describes the probability of those pixels not being drawn from the sky-background.

SExtractor has the capability of automatically detecting sources above the sky-background and fitting isophotal apertures around those sources, then summing the flux withing those apertures. We set the threshold of object detection in SExtractor to $3\sigma$, corresponding to the flux within the aperture having a 99.7% probability of not belonging to sky. We used SExtractor to also produce segmentation maps of these sources in the $\chi^2$ image, which were used for object identification, and subsequent masking of sources in the subimage not associated with the galaxies in our sample.

We exclude *all* pixels of surrounding detections outside of a central circular aperture with a $0\farcs5$ radius ($\mathrm{r} \simeq 17\,\mathrm{pix}$) found in the LyC segmentation maps. We

preserve all flux from any objects inside this central aperture when we stack the sub-images, while also excluding those detected on the border of the central aperture. This masking was applied to ensure that all potential sources of non-ionizing flux from lower redshift neighbors along the line-of-sight are removed before stacking. On average, $\sim 3 \pm 2$ objects were removed from each sub-image. We note that this procedure would not be possible when stacking LyC emission of galaxies using ground-based observations alone, as effects from seeing can blend neighboring non-ionizing contaminants with the true LyC signal (e.g., Nestor et al. 2013; Siana et al. 2015; Mostardi et al. 2015). Each individual masked sub-image was visually inspected to verify that no surrounding objects indeed remained in the sub-images, including those seen only at longer wavelengths in the 10 band ERS mosaics. Thus, it is possible that the rigorous removal of surrounding flux can sometimes result in the removal of more extended (i.e., at $r \geq 0\farcs5$) LyC flux from the stacked images if this were detectable at $\geq 1\sigma$ above the local sky-background.

We also subtracted a constant from each of the sub-images before object removal in order to bring the mode of the sky-background of the images as close to zero as possible. We calculated the mode of the background level from the count-rate histogram of the surrounding pixels outside the central circular aperture, binning their values according to the Freedman-Diaconis rule (see §4.2.2). We then fit each sky histogram to a Gaussian function by least squares, taking the mode of the fitted Gaussian as the background constant. This local sky-background removal was applied in order to sum the actual LyC flux *above* the background from each subimage, rather than LyC+background, as variations in background levels between sub-images can suppress the flux contribution from the faintest LyC emission in the stack. The subtraction also removed any residual small scale gradients between the sub-images

left from bias/sky-subtraction, flat-fielding, and/or exposure time/noise variations in the mosaics.

We then stacked the processed sub-images of all the galaxies in each WFC3/UVIS image with spectroscopic redshifts, where LyC can be observed in their respective filter, using the average of the pixel count rates of the sub-images, weighted by their corresponding AstroDrizzle weight maps. We did this using the methodology described in §3.1. We created stacks for the *total* sample of galaxies and separate stacks for the galaxy and AGN samples, since each sample likely produces the majority of their LyC photons by different mechanisms, which must be taken into account when determining $f_{\rm esc}$ for these galaxies. We also created corresponding UVC stacks for each LyC stack from subimages extracted from the ACS/WFC mosaics of the ERS/GOODS-S fields that sample the UVC emission of our galaxies. For the redshift intervals that sampled LyC emission in the F225W, F275W, and F336W, filters that sample the UVC emission correspond to F606W, F606W, and F775W, respectively. This allows us to perform matched aperture photometry on the LyC stacks, as described in §3.2.

The galaxies stacked in the WFC3/UVIS F225W filter contain co-added sub-images frames of 19 galaxies over the redshift range $2.276 \leq z \leq 2.450$ ($\langle z \rangle = 2.352$), the F275W stack contains 14 galaxies at $2.470 \leq z \leq 3.076$ ($\langle z \rangle = 2.685$), and the F336W stack contains 13 co-added galaxies at $3.132 \leq z \leq 4.149$ ($\langle z \rangle = 3.537$). These stacks, as well as the corresponding UVC stacks, are shown in Fig. 12. Stacks for the subsamples of galaxies with weak AGN and galaxies without AGN are shown in Fig. 13 and 14, with elliptical apertures indicating regions where photometry was performed.

The deepest galaxy counts in $J$ and $H$-band of Windhorst et al. (2011) give us an estimate the total number of contaminating objects that could be present in our r$\simeq$0.″5 radius LyC apertures (Fig. 12–14). To the ERS limit of $J$, $H \lesssim$27.55–27.25 mag,

respectively, there are $\lesssim 5.2\times10^5$ galaxies deg$^{-2}$ (Windhorst et al. 2011), yielding a $\lesssim$3% probability of finding one unrelated foreground object in, or overlapping with, the LyC aperture. For our sample of 46 galaxies, this would amount to $\lesssim$2 interlopers. Due to the possible interloper's proximity to the LyC candidate, it is not always possible to obtain reliable spectroscopic or photometric redshifts for these neighbors. Nonetheless, in these few cases, light from the nearby neighbors was masked out with SExtractor segmentation maps. This was then repeated for *all* other objects in the 151×151 pixel image sections outside the central r$\simeq$0.″5 aperture, to exclude contaminating objects in the photometry in the central aperture, and to assure that accurate measurements of the surrounding sky could always be obtained.

### 4.4.2 Rest-frame Lyman Continuum Photometry

The results from our photometry measured in the apertures shown in Fig. 12–14 are summarized in Table 2. As outlined in §3.2, we perform all of our photometry on the LyC stacks with SExtractor using detection images in dual-image mode. As our reference images, we use the corresponding non-ionizing UVC stacks to measure any possible escaping LyC flux detectable within the aperture of brighter UVC counterpart.

We used the individual weight maps and the sky-background variance for each sub-image in a given stack to create 10,000 random variations of each pixel for each stack based on the combinations of these uncertainties, in order to assess photometric errors and upper limits as described in §3.2. An example flux distribution generated using this methodology is shown in Fig. 15. We quote the mean and 1$\sigma$ value of the flux distributions in Table 2, or the 1$\sigma$ value as the upper-limit for non-detections.

Table 2. LyC Stack Photometry in ERS

| Filter (1) | $z$-range (2) | $\langle z \rangle$ (3) | $N_{\rm obj}$ (4) | $m_{\rm LyC}$ (5) | ABerr$_{\rm LyC}$ (6) | SNR$_{\rm LyC}$ (7) | $A_{\rm UVC}$ (8) | $m_{\rm UVC}$ (9) | SNR$_{\rm UVC}$ (10) |
|---|---|---|---|---|---|---|---|---|---|
| All Galaxies: | | | | | | | | | |
| F225W | 2.276–2.450 | 2.352 | 19 | >28.26 | ... | (1.00)$^{\dagger}$ | 1.034 | 24.41 | 426.7 |
| F275W | 2.470–3.076 | 2.685 | 14 | 28.11 | 0.45 | 2.41 | 0.681 | 24.76 | 323.8 |
| F336W | 3.132–4.149 | 3.537 | 13 | >28.62 | ... | (1.00)$^{\dagger}$ | 0.553 | 24.63 | 247.5 |
| Galaxies without AGN: | | | | | | | | | |
| F225W | 2.276–2.449 | 2.350 | 17 | >27.91 | ... | (1.00)$^{\dagger}$ | 1.015 | 24.36 | 423.8 |
| F275W | 2.566–3.076 | 2.752 | 7 | >28.12 | ... | (1.00)$^{\dagger}$ | 0.932 | 24.46 | 268.3 |
| F336W | 3.132–4.149 | 3.603 | 10 | >30.73 | ... | (1.00)$^{\dagger}$ | 0.555 | 24.75 | 192.7 |
| Galaxies with AGN: | | | | | | | | | |
| F225W | 2.298–2.450 | 2.374 | 2 | >27.91 | ... | (1.00)$^{\dagger}$ | 0.637 | 25.21 | 85.0 |
| F275W | 2.470–2.726 | 2.618 | 7 | 28.26 | 0.41 | 2.66 | 0.253 | 25.12 | 232.7 |
| F336W | 3.217–3.474 | 3.316 | 3 | 27.42 | 0.44 | 2.47 | 0.486 | 24.38 | 158.7 |

Table columns: (1): WFC3 filter used; (2): Redshift range of galaxies included in LyC/UVC stacks; (3): Average redshift of stack; (4): Number of galaxies with high quality spectroscopic redshifts used in the stacks; (5): Observed total AB magnitude of LyC emission from stack (SExtractor `MAG_AUTO` aperture matched to UVC, indicated by the blue ellipses in Figs. 12–14; (6): $1\sigma$ error of average LyC AB-mag (7): Measured SNR of the LyC stack flux within matched UVC aperture ($^{\dagger}$ indicates a $1\sigma$ upper limit); (8): Area (in arcsec$^2$) of the UVC aperture; (9): Observed total AB magnitude of the UVC stack; (10): Measured SNR of the UVC stack.

We convert the flux measured by SExtractor to AB magnitudes, using the infinite aperture zeropoints listed on the STScI instrument websites[4].

From these distributions, we measure an average LyC flux from galaxies and AGN at $m_{\rm AB} \simeq 28.11$ mag, with a SNR value at $\sim 2.41$ for the F275W stack. We measure $1\sigma$ upper bounds of $m_{\rm AB} > 29.02$ and 28.62 mag for the F225W and F336W stacks, respectively. For only the galaxies without AGN (Fig. 13), we place $1\sigma$ upper bounds for the flux measured in the F225W, F275W and F336W stacks at $m_{\rm AB} > 27.91$, 28.12 and 30.73 mag, respectively. The flux from galaxies with AGN was measured at $m_{\rm AB} \simeq 28.26$ and 27.42 mag, with SNR $\sim 2.66$ and 2.47 for the F275W and F336W

[4]http://www.stsci.edu/hst/wfc3/phot_zp_lbn

stacks, respectively, and we placed a $1\sigma$ upper bound to the F225W stack flux at $m_{\rm AB} > 27.91$ mag (see Table 2). Our photometry indicates that the AGN stacks are brighter than galaxies without AGN and have higher SNR, despite having fewer contributing sub-images in the stacks.

We note that, although some LyC flux might exist at the $\sim 1\sigma$ level outside the measurement apertures, we do not incorporate this flux into our measurement, as this would require us to increase our aperture size and add extra noise in the aperture, which would increase the uncertainty of our measurements, as well as the interloper contribution.

### 4.4.3 Composite stacks of LyC Emission from Galaxies at $2.3 \leq z \leq 4.1$

In order to determine at what SNR our observations can measure the LyC flux from our total sample of galaxies that span the $2.3 \leq z \leq 4.1$ redshift range, and probe the faintest LyC emission from our galaxies, we construct a stack of the observed LyC flux in $f_\nu$ of *all* the galaxies in our sample as follows. We first extract the sub-images from the F225W, F275W, and F336W and apply our sky-subtraction and neighbor masking procedures, as outlined in §4.4.1. We then scale all sub-images in the stack to a common zeropoint and stack the sub-images by a weighted average, as described in §3.1. We created stacks for the full sample of all galaxies and separate stacks for the galaxies with and without AGN, as shown in Fig. 16. We note that these composite stacks represent the average *observed* LyC flux from our sample integrated from $z = 2.3$–$4.1$ through the various sight-lines, and so the flux in these stacks will be dominated by the galaxies with the brightest apparent LyC flux.

Due to the very low sky-background in the F225W and F275W filters (Windhorst et

al. 2011), the relative scaling of the count rates in the sub-images slightly amplified the contribution of detector noise from these filters in the stack. However, since the F336W filter is limited by photon noise from the much brighter zodiacal background at these wavelengths, these composites therefore also have more significant sky-background. We find that the stack of the total sample reaches a SNR of $\sim$2.3$\sigma$, while the LyC stacks of galaxies with and without AGN achieve SNR ratios of 3.9$\sigma$ and 0.7$\sigma$ in their UVC matched apertures, respectively. We also find that the average apparent AGN LyC flux outshines that from galaxies without AGN by a factor of $F_\nu^{\rm AGN}/F_\nu^{\rm Gal}\simeq$7.7 ($\Delta m_{\rm AB}\simeq$2.2 mag).

Since these composite stacks were created solely for the purposes of visualization and probing the SNR of the total observed LyC signal from our samples, we do not perform any further analysis of the LyC flux measured in these stacks. Because the absorption of ionizing photons by the IGM is non-linearly dependent on redshift, modeling of the combined intrinsic LyC flux from galaxies spanning $2.3\lesssim z\lesssim 4.1$ through various sight-lines would become increasingly divergent, such that the resulting total $f_{\rm esc}$ value of these galaxies would be highly uncertain.

This exceedingly faint LyC emission emerging from the stack of the 12 galaxies with AGN appears to have a flat spatial distribution that is *not* centrally concentrated. This may allude to the manner in which LyC escapes from galaxies. In order to ionize the IGM, LyC photons must escape through holes in the surrounding gaseous and/or dusty material between stars, the central point source, and the line-of-sight IGM, which can be distributed randomly within or around galaxies. With at most a few clear sight-lines per galaxy, these stacked images suggest that some escape paths of LyC may be on average somewhat offset from the galaxy center, i.e., escaping more from the outskirts than the centers of these galaxies. Given the random orientation

of galaxies in each stack, this would explain the faint, non-centrally concentrated, and extended morphology of the detected LyC emission. This may indicate that LyC photons produced by accretion disks in AGN escape from galaxies with weak AGN via scattering. We discuss the radial profiles of galaxies further in §4.4.4.

In the adopted Planck Collaboration 2018 cosmology, the angular size scale decreases by ∼16% and the apparent fluxes dim by ∼75% from $z \simeq 2.3$ to $z \simeq 4.1$. We deliberately did *not* scale any of the pixel values or resample the pixel scale to account for these these changes during the stacking process over all redshifts, as we only created these composite stacks to quantify the SNR of the average *observed* LyC flux for our entire sample. Using a varying pixel scale for each galaxy would have introduced correlated inter-pixel resampling noise, which would also decrease the sky SB limits and the effect of averaging over residual subtle systematics. Stacking with the same plate scale for all redshifts also preserves the observed photon statistics, which are needed for accurate sky-subtraction. Hence, resampling all the images as a function of redshift would reduce the SNR of the resulting stacked LyC signal. We note that the physical scale of the galaxies that we stack changes by ±4% within each redshift bin and by ±16% for the entire sample. This does not noticeably affect the LyC and UVC light profiles in each of our three redshift bins, which are discussed in §4.4.4, but does "blur" the light distribution seen in the composite stacks in Fig. 16 by approximately these amounts in the radial direction from the center. Fig. 16 can thus only be used to visualize the combined *observed* LyC signal over the entire redshift range $z \simeq$2.3–4.1, but cannot be used for further quantitative analysis.

### 4.4.4 The Observed Radial Surface Brightness Profiles in UVC and LyC

The radial profiles of our LyC and UVC stacks from Fig. 14 for F275W and F336W are shown in Fig. 17. We constructed all observed radial SB profiles by summing successive annuli of 3 pixel radii beginning with the central pixel, where each pixel is treated as a GRV with the mean set to the pixel value in the stack and variance set to the sum of the variance from the square of the pixel value in the corresponding weight map, and the variance from the sky-background. This allowed us to estimate uncertainties on a per pixel basis for generating flux distributions of the sum of several pixels. The averages and $\pm 1\sigma$ errors or $1\sigma$ upper bounds to these distributions are indicated as vertical bars and downwards triangles, respectively.

The stacked UVC profiles are shown as solid curves, and those for LyC are dashed. The *observed* PSFs in the WFC3/UVIS F275W and ACS/WFC F606W mosaics are indicated by dotted curves, normalized to the central surface brightness of the corresponding LyC SB profile. The PSF in F336W is very similar to the F275W PSF, so we do not plot it. These are available in Table 1 and Fig. 7*b* of Windhorst et al. (2011). Note that these PSFs measured in the 0.″03 mosaics are undersampled. The $1\,\sigma$ SB sensitivity limit for the LyC profile in the F275W stack is indicated by a horizontal dashed line at $M_{\rm AB} \simeq 30.5\,{\rm mag\,arcsec^{-2}}$. These SB sensitivity limits are consistent with the $1\sigma$ sky-subtraction errors discussed in §4.2.

Both UVC SB profiles are clearly extended with respect to their corresponding filter PSFs, as expected for stacked galaxy radial light profiles at $z \simeq 3$–6 (e.g., Hathi et al. 2008). The much deeper HUDF UVC stacks of Hathi et al. (2008) suggested a possible "break" (or slight change in slope) near $r \gtrsim 0.''3$–$0.''4$, from exponential in the inner parts to a somewhat less steep profile in the outskirts. Our stacked UVC light

profiles do not clearly show a change in slope at $r \gtrsim 0\farcs3$–$0\farcs4$, since our (77–180 orbit) UVC stacks are not nearly as deep as their ∼1680–4300 orbit stacks, and because of our much more stringent method of masking neighbors.

Both LyC SB profiles are also clearly extended with respect to their *observed* PSFs, and remain extended to $r \simeq 0\farcs5$, beyond which errors in the sky-subtraction start to become substantial. The very faint, flat, non-centrally concentrated appearance of the combined LyC signal makes the extraction of its SB profile uncertain at larger radii. The relatively flat LyC SB profiles may indicate a more complicated LyC escape scenario, in which the light distribution of the LyC flux of a stack of galaxies is largely dependent on the porosity of the ISM in those galaxies, and/or the scattering processes that the LyC photons undergo before escape. We find that the UVC SB profiles are well fit to Sérsic profiles of index of $n \simeq 2.4 \pm 0.7$, where a Sérsic intensity profile is defined by

$$I(r) = I_e e^{-b_n\left[\left(\frac{r}{R_e}\right)^{\frac{1}{n}}-1\right)\right]} \tag{4.4}$$

where $I_e$ is the intensity at the effective radius ($R_e$), which encloses half of the total light from the profile, and $b_n \simeq 2n - \frac{1}{3}$ determines the shape of the profile (Sérsic 1963). The LyC SB profiles could not converge to a Sérsic fit but are better fit to straight lines with slope $\sim 2.5 \pm 0.6\,\mathrm{mag\,arcsec^{-2}}$ per arcsec. The difference in linear slope between UVC and LyC is $\sim 6\,\mathrm{mag\,arcsec^{-2}}$ per arcsec with a SNR of ∼2.8, so the LyC is therefore likely flatter. This may also be indicative of a decreasing LyC opacity with radius, as the LyC and UVC escape morphology differs radially.

After integrating these SB profiles as elliptical frustums between each isophote, we find reasonable agreement with our photometric analysis shown in Table 2, although the flux represented by the radial SB profiles is consistently fainter by ∼0.3±0.2 mag. This discrepancy is expected, given that our SB profiles do not extend out to the

larger aperture sizes used in the photometry of the stacks, and therefore miss some real LyC flux that might be present at larger radii and at very faint SB levels.

### 4.4.5 Modeling the UVC and LyC Radial Surface Brightness Profiles

For the highest SNR measurements in the LyC stacks (i.e., F275W and F336W), the radial SB profile of escaping LyC flux appears to be flatter than the corresponding *non-ionizing* UVC profile (the dashed and solid colored curves in Fig. 17, respectively).

A LyC SB profile that is measurably flatter than the corresponding UVC SB profile could arise naturally in a porous ISM, in which the covering factor of neutral gas decreases with increasing galacto-centric distance. To illustrate this quantitatively, we consider the transfer of UVC and LyC photons through simplified models of galaxies with a multiphase ISM.

To calculate this, we assumed that the UVC sources are spatially extended and characterized by a volume emissivity $\epsilon_{\rm UVC}(r)$. We assumed an exponential distribution with galactic radius:

$$\epsilon_{\rm UVC}(r) = \epsilon_{\rm UVC,0} e^{\frac{-r}{r_0}} \tag{4.5}$$

The normalization constant $\epsilon_{\rm UVC,0}$ and scale length of $r_0$ are obtained by matching the observed SB profiles in Fig. 17. We further assumed that LyC emission traces the UVC emission. We attributed differences in observed SB profiles to the fact that neutral clumps of gas are opaque to LyC radiation, but not to UVC.

We also assumed a spherical distribution of neutral gas clumps, which is described completely by its covering factor,

$$f_{cov}(r) \equiv n_{\rm c}(r) A_{\rm c}(r) \tag{4.6}$$

Here, $n_{\rm c}$ and $A_{\rm c}(r)$ denote the number of clumps and area of a clump at $r$, respectively. The covering factor $f_{\rm cov}$ then denotes the probability that a sight-line intersects a clump per unit length. For example, for clumps of fixed size that are outflowing at *an assumed constant* velocity $v$, we have a number density dependence as $f_{cov} \propto n_{\rm c} \propto r^{-2}$ (a more detailed description of this covering factor can be found in Dijkstra and Kramer 2012).

The precise radial dependence of $f_{cov}$ is not known. However, when $f_{cov}$ decreases with $r$ we generally expect increased LyC escape fractions at larger galacto-centric distances. We consider two parameter models for $f_{cov} = Ar^{-x}$, and fit for $A$ and $x$. Both $A$ and $v$ can also depend on radius. Hence, $f_{cov}$ generally is some unknown power law of $r$ (i.e., $\mathrm{r}^{-x}$), where $x$ typically ranges between 0 and 3. This calculation shows that when sight-lines with low impact parameter see the largest $f_{cov}$, we see a reduced $f_{\rm esc}$ in these directions.

For the UVC and LyC SB models in Fig. 17, we generate the UVC surface brightness as:

$$SB_{\rm UVC}(b) = \int_{-\infty}^{\infty} ds\, \epsilon_{\rm UVC}(b,s). \tag{4.7}$$

where $b$ denotes the impact parameter, $s$ denotes the line-of-sight coordinate, and $\epsilon_{\rm UVC}(b,s)$ denotes the emission rate of UVC photons per unit volume at $(b,s)$. The distance from the galaxy $r$ is defined as $r = \sqrt{b^2+s^2}$ (Note that $2rdr = 2sds$ and $ds = \frac{r}{s}dr = \frac{r}{\sqrt{r^2-b^2}}dr$, since $r^2 = s^2 + b^2$). We then obtain the LyC surface brightness from:

$$SB_{\rm LyC}(b) = \int_{-\infty}^{\infty} ds\, \epsilon_{\rm UVC}(b,s) \frac{f_{\rm LyC}}{f_{\rm UVC}} f_{\rm esc}(b,s). \tag{4.8}$$

where $f_{\rm esc}(b,s)$ denotes the fraction of LyC photons that can escape from $(b,s)$, and the factor $\frac{f_{LyC}}{f_{UVC}}$ simply rescales the flux at UVC frequencies to that at LyC.

In our model of a clumpy ISM $f_c(r)$ denotes *the number of self-shielding clumps per unit length at r* (see Dijkstra and Kramer 2012). We therefore find that $f_c(r)dr$ denotes the number of self-shielding clumps along a differential length $dr$. We assume that each clump is optically thick to ionizing photons. In this case, the escape fraction from $(b, s)$ is simply the probability of finding *at least* one clump on a sight-line to $(b, s)$, $P_{clump}(b, s)$, which is given by:

$$P_{clump}(b, s) = 1 - P_{noclump}(b, s) = 1 - \exp[-N_{clump}(b, s)], \tag{4.9}$$

where in the last step we assumed that the number of clumps along a given line-of-sight follows a Poisson distribution with mean $N_{clump}(b, s)$. This mean is given by:

$$N_{clump}(b, s) = \int_{-\infty}^{s} ds' \; f_c(b, s'). \tag{4.10}$$

An interesting possibility is that the neutral gas clouds can theoretically *scatter* LyC photons: LyC photons penetrate the neutral clumps over an average distance that corresponds to $\tau \simeq 1$. Direct recombination to the ground state produces LyC photons that can escape from the neutral cloud, as the optical depth to the edge of cloud is $\tau \simeq 1$. This "scattering" (absorption and re-emission of LyC photons occurs on the recombination time scale inside the cloud) of LyC photons could further flatten the predicted surface brightness profile. The possible effects of LyC scattering can be expanded to include scattering off free electrons and dust grains (which also differs between LyC and UVC).

While the dot-dashed curve in Fig. 17 is only a single example (matching our F275W LyC observations at $\langle z \rangle \simeq 2.62$) of these model LyC SB profiles, model predictions with similar parameter values fit the SB profiles in the other redshift bin. With these models, we can integrate out to larger impact parameters and get a constraint on the total escape fraction that accounts for the difference in SB profiles. This procedure

gives a slightly larger value for $f_{\rm esc}$ than those given in Table 3 (This is, of course, almost identical to the constraints one would obtain simply by extrapolating the surface brightness profiles to larger impact parameters, and integrating over them.)

### 4.4.6 The LyC Escape Fraction from Galaxies in the ERS Field

Table 3. LyC Escape Fraction Constraints from Galaxies Without AGN in the ERS Sample

| $\langle z \rangle$ | $N_{obj}$ | $\langle f_{\rm UVC}/f_{\rm LyC}\rangle_{\rm obs}$ | $\langle f_{\rm UVC}/f_{\rm LyC}\rangle_{\rm int}$ | $\langle t_{\rm age}\rangle$ [yr] | $A_{V\,med}$ [mag] | $\langle \mathcal{T}_{\rm IGM}\rangle$ | $\langle f_{\rm esc}^{\rm abs}\rangle$ [%] |
|---|---|---|---|---|---|---|---|
| (1) | (2) | (3) | (4) | (5) | (6) | (7) | (8) |
| Galaxies without AGN: | | | | | | | |
| 2.350 | 17 | $27^{+61}_{-5}$ | $20.2 \pm 0.1$ | $10^{8.2^{+0.9}_{-0.3}}$ | $0.40^{+0.20}_{-0.40}$ | $0.326^{+0.062}_{-0.085}$ | $22^{+44}_{-22}$ |
| 2.752 | 7 | $< 98.0$ | $12.8 \pm 0.1$ | $10^{7.9^{+0.6}_{-0.1}}$ | $0.40^{+0.21}_{-0.02}$ | $0.218^{+0.102}_{-0.085}$ | $< 53$ |
| 3.603 | 10 | $< 50.1$ | $15.6 \pm 0.2$ | $10^{8.5^{+0.6}_{-0.8}}$ | $0.0^{+0.4}_{-0.0}$ | $0.066^{+0.045}_{-0.033}$ | $< 55$ |

Table columns: (1): Average redshift of each stack; (2): Number of objects in each redshift bin, as in Table 2; (3): Average *observed* flux ratio $f_{\nu,\rm UVC}/f_{\nu,\rm LyC}$ and its $\pm1\sigma$ error range, as measured from the LyC and UVC stacks in their respective apertures (see §4.4.2 and Table 2); (4): Average *intrinsic* flux ratio $f_{\nu,\rm UVC}/f_{\nu,\rm LyC}$ and its $\pm1\sigma$ error range, as derived from the BC03 best fit SED models galaxies without AGN in each of our redshift bins (see §3.3 and Eq. 3.12); (5): Average age of the stellar populations from the best fit BC03 models and their $\pm1\sigma$ standard deviations in years; (6): Median dust extinction $A_V$ and its $\pm1\sigma$ error range of the best fit BC03 SED model (the median $A_V$ is more representative, as the distributions of each subsample is asymmetric; see §B.3.1); (7): Average filter-weighted IGM transmission of all sight-lines and redshifts in the stacks and their $\pm1\sigma$ standard deviations, calculated from the Inoue et al. (2014) models; (8) ML and $\pm1\sigma$ or upper limit values of the Monte Carlo analysis of $f_{\rm esc}^{\rm abs}$ in percent, i.e., the escape fraction of LyC including effects from all components of the ISM and reddening by dust as described in §3.3 (Eq. 3.8)

We applied the method outlined in §3.3–3.4 to infer our $f_{\rm esc}$ values for the LyC stacks described in §4.4.1. Using the models of Inoue et al. (2014), we apply the IGM transmission to our *model* LyC flux by attenuating the SED with the wavelength dependent IGM transmission coefficient curve at the redshift of the galaxy for $10^4$

simulated lines-of-sight. We then convolve the IGM attenuated model flux with the model error that we calculated to obtain our final model LyC flux distribution (i.e., $F^{\rm int}_{\nu,\,{\rm LyC,i}}$). We then stacked all of the IGM attenuated *model* LyC fluxes distributions of all the galaxies in their respective redshift bins to obtain our stacked *model* LyC flux distribution as denoted in Eq. 3.7. The stacked *model* LyC flux distribution was then used to calculate $f_{\rm esc}$ as shown in Eq. 3.8.

Since we performed a non-correlated sum of the model LyC flux GRVs to estimate this intrinsic stacked LyC flux, we run this $f_{\rm esc}$ calculation for a total of $10^3$ trials, which we combined into one in order to generate a statistically significant sample of possible $f_{\rm esc}$ values. The PMF of the $f_{\rm esc}$ distribution was then constructed by optimally binning the simulated $f_{\rm esc}$ samples according to the Freedman-Diaconis rule, and normalizing by $N_{samples}$ to give their relative probabilities. The full $f_{\rm esc}$ PMFs are shown in Fig. 18 for galaxies without AGN. The statistics of the PMF, i.e., the ML values, averages, and $\pm1\sigma$ error ranges were computed and are shown in Fig. 18 and Cols. (8) and (9) of Table 3.

These *model* LyC fluxes also represent the lines-of-sight where escaping LyC flux was transmitted through the IGM before being absorbed by Lyman Limit Systems and Damped Lyman-$\alpha$ systems within $\Delta z \simeq 0.5$. The opaque lines-of-sight, where the IGM transmission peaks near $\mathcal{T}^{\rm LyC}_{\rm IGM} \simeq 0.01$, represent $\sim$30–40% of our potential model LyC flux values. These lines-of-sight result in higher $f_{\rm esc}$, as the model LyC would have been attenuated by more absorbers. However, $\sim$40–50% of our lines-of-sight have average IGM transmission values $\mathcal{T}^{\rm LyC}_{\rm IGM} \gtrsim 0.4$ (where the transmission distribution is at a local minimum), and corresponds to the peak of the $f_{\rm esc}$ PMFs, where the model LyC flux encountered fewer absorbers. These lines-of-sight have a local maximum

transmission near $\mathcal{T}_{\rm IGM}^{\rm LyC} \simeq 0.7$, and about $\sim$0.3% of these sight-lines can be as high as $\mathcal{T}_{\rm IGM}^{\rm LyC} \simeq 0.85$.

### 4.4.7 Implications of the $f_{\rm esc}$ MC Results

We list the results of our $f_{\rm esc}$ MC simulations in Table 3. The average absolute escape fraction, $\langle f_{\rm esc}^{\rm abs} \rangle$, from galaxies at various redshifts can be used to determine what fraction of LyC produced by the stellar photospheres in those galaxies escapes, i.e., is not absorbed by interstellar neutral H 1, dust, etc., at their average redshift. However, variations in IGM transmission can cause these values to become highly uncertain when stacking LyC emission from galaxies over too broad of a redshift range. Thus, in order to ascertain any meaningful evolution in $f_{\rm esc}$, we must stack galaxies at similar redshifts and compare their $f_{\rm esc}$ values from sample to sample. Then, any trends in the independent subsamples can be used to constrain correlations of $f_{\rm esc}$ with galaxy properties or evolution with redshift. Modeling these properties can also be used to determine their impact on $f_{\rm esc}$, and to see if trends in these properties with redshift can affect the apparent evolution of $f_{\rm esc}$ with cosmic time.

The constraints we place on $f_{\rm esc}$ are valid for the luminosity range $M_{\rm AB}^{\rm UVC} \simeq -21.1^{+0.9}_{-0.5}$ mag present in the sample which was selected to have reliable spectroscopic redshifts (see Fig. 10). The galaxies selected in our $\langle z \rangle \simeq 2.35$ and $\langle z \rangle \simeq 2.75$ stacks have, on average, younger stellar populations and more dust than the $\langle z \rangle \simeq 3.60$ stack. The $f_{\rm esc}$ value for galaxies *selected* at $\langle z \rangle \simeq 3.60$ are indicative of somewhat older stellar populations (of $\sim$1 Gyr), but are not significantly affected by the lower amount of dust observed in these galaxies. The $\langle z \rangle \simeq 2.35$ and $\langle z \rangle \simeq 2.75$ stacks sample galaxies that are undergoing a period of more active star-formation

compared to the two higher redshift samples, which may have led to the accumulation of more H 1 gas and dust in these galaxies, but also a brighter *intrinsic* LyC flux. Thus, these $f_{\rm esc}^{\rm abs}$ values also imply that the ISM can absorb a larger fraction of LyC flux from older stellar populations than from younger ones when comparing $f_{\rm esc}^{\rm abs}$ from older and younger stellar populations.

Although young stellar populations can produce more intrinsic LyC than older ones, which then has a higher probability of escaping the ISM, higher extinction from dust in the UVC may correlate to a reduced efficiency of LyC escape. Although dust is the dominant factor for attenuation for $\lambda$>912Å, ionizing radiation is more strongly absorbed by neutral hydrogen due to the higher cross sectional area (Richings, Schaye, and Oppenheimer 2014). LyC escape requires very low neutral Hydrogen column densities ($N_H$<$10^{17}$). Since the amount of extinction from dust is strongly correlated to the column density of Hydrogen (e.g., Bohlin, Savage, and Drake 1978; Fitzpatrick 1999; Rachford et al. 2002), higher extinction may then be indicative of low $f_{\rm esc}$. This apparent correlation of high dust extinction and low $f_{\rm esc}$ is consistent with the results of several observational and analytical studies that investigate the impact of various galactic parameters on $f_{\rm esc}$ (e.g., John S. Mathis 1971; Leitherer et al. 1995; Inoue 2001; Bergvall et al. 2013).

## 4.5 Discussion of Results

### 4.5.1 Summary of Available Data on the LyC Escape Fraction vs. Redshift

The constraints we placed on $f_{\rm esc}$ are valid for the luminosity range $M_{\rm AB}^{\rm UVC} \simeq -21.1^{+0.9}_{-0.5}$ mag present in the sample which was selected to have reli-

able spectroscopic redshifts (see Fig. 10), with the two lowest redshift subsamples being dominated by relatively younger stellar populations with active star-formation and significant dust extinction, the $\langle z \rangle = 3.60$ subsample comprises mostly lower extinction galaxies with somewhat older stellar populations. For faint galaxies to have finished reionization by $z \simeq 6$–7, their $f_{\rm esc}$ values need to be $\gtrsim$10–20% (Ouchi et al. 2009; Wilkins et al. 2011; Kuhlen and Faucher-Giguère 2012) beyond $z \simeq 6$ *and* their luminosities need to reach as faint as $M_{\rm UVC} \simeq$ –15 to –13 mag (e.g., Brant E. Robertson et al. 2013). Hence, if faint (dwarf) galaxies contributed significantly to reionization at $z \lesssim 6$–7, one should consider how much their $f_{\rm esc}$ fraction might have increased *both* towards higher redshifts due to the expected lower metallicities and lower dust extinction, *and* at fainter luminosities due to the larger impact that SN driven outflows have on lower mass dwarf galaxies (e.g., Ricotti and Shull 2000; Razoumov and Sommer–Larsen 2007; Wise and Cen 2009; Fernandez and Shull 2011). Given that our spectroscopic selection samples luminous galaxies in all three redshift bins, our LyC detections can only constrain the first possibility.

Fig. 19 shows the present ERS ML and $1\sigma$ upper bound $f_{\rm esc}$ values generated from the MC simulation listed in Table 3 for galaxies without AGN (purple filled circles and triangles, respectively). We show the interquartile range of the $\langle z \rangle$=2.35 $f_{\rm esc}$ data to emphasize it's highly asymmetric PMF, which has more data below the ML point. We also plot similarly derived, $f_{\rm esc}$ data available in published work summarized in §2.3 as light blue points, with upper limits indicated as blue triangles. The light blue $f_{\rm esc}$ points indicate galaxies with restframe 1500Å luminosities close to those sampled in Fig. 5a–5c (i.e., $\langle M_{AB} \rangle \simeq -21.1^{+0.9}_{-0.5}$ mag). The dependence of the $f_{\rm esc}$ values of galaxies on luminosity is not well determined, but no clear dependence on luminosity

is obvious in Fig. 19. We will therefore discuss the redshift dependence of $f_{\rm esc}$ here for the luminosities sampled in Fig. 10.

We first converted the published $f_{\rm esc}^{\rm rel}$ values to $f_{\rm esc}$ when necessary using the quoted extinction values from the literature source. We note that these $f_{\rm esc}$ values were derived from different observational analyses, including both space and ground based spectra and imaging, with different object selection, reduction techniques, error assessment, and application of IGM attenuation models. We plot only the quoted $f_{\rm esc}$ values from the literature source most analogous to this study, i.e. those derived from their full, stacked sample, with galaxies of similar luminosities to ours. Some of the published errors may not account for the same uncertainties that we address in §3.4. When necessary, we converted the quoted published uncertainties to $1\sigma$ error bars, so they are comparable to our results in Table 3.

Although the $f_{\rm esc}$ values plotted in Fig. 19 were derived with different methods, the present ERS data appears to suggest a correlation of $f_{\rm esc}$ with redshift. However, any such relation may not be a simple power law in $(1+z)$. Several authors (e.g., Inoue, Iwata, and Deharveng 2006; Razoumov and Sommer–Larsen 2010; Finlator et al. 2012; Kuhlen and Faucher-Giguère 2012; Becker and Bolton 2013; Dijkstra et al. 2014) have suggested that redshift averaged $f_{\rm esc}$ values for galaxies may increase significantly with redshift, possibly as steeply as $\propto(1+z)^3-(1+z)^5$. This only holds only for $z\lesssim 7$, beyond which the implied escape fraction would approach 100% for the upper bound, but decrease monotonically at higher redshift (e.g., Razoumov and Sommer–Larsen 2010). If the $(1+z)^\kappa$ exponent values were as steep as $\kappa\simeq 2.0$, this prediction would provide $f_{\rm esc}$ values at $z\gtrsim 6$ in excess of $\sim$30%, as required for hydrogen reionization to have completed by $z\sim 6$ (Brant E. Robertson et al. 2013). However, none of the

simple $(1+z)^{\kappa}$ power laws for $f_{\rm esc}$ seem to be consistent with the data points in Fig. 19 to within their stated $1\sigma$ errors.

### 4.5.2 A Redshift Dependence Faster than $(1+z)^{\kappa}$?

Since the plotted 21 independent data points in Fig. 19 deviate from published power laws, *no* single $(1+z)^{\kappa}$ curve seems to fit all the $f_{\rm esc}$ data for galaxies without AGN. We therefore suggest the possibility that *a more sudden decrease* of $f_{\rm esc}^{\rm abs}$ with redshift may instead have to be considered. The combined data in Fig. 19 suggests, however, that $f_{\rm esc}$ may have declined by a factor of nearly $\sim$10 from $\gtrsim$20% at $z \gtrsim 2$ to $\sim$1% at $z \lesssim 2$. These low $f_{\rm esc}$ values at $z \lesssim 2$ are predicted by some cosmological radiative transfer models as well, which also require a "steep rise" in $f_{\rm esc}$ at $z \gtrsim 2$ for massive galaxies to reionize the Universe (e.g., V. Khaire et al. 2015), and have also been suggested in studies of the Ly $-$ $\alpha$ escape fraction over redshift (e.g., Blanc et al. 2011).

Fig. 19 indicates that the sudden decrease in $f_{\rm esc}$ may have occurred within the epoch of $z\sim$2, or within about $\pm$1 Gyr of the observed peak in the cosmic star-formation history (SFH; Piero Madau et al. 1996; Faucher-Giguère et al. 2008; Cucciati et al. 2012; Burgarella et al. 2013). This period may indicate the epoch where the universe transitions from infall/merger driven star-forming galaxies at $2 \lesssim z \lesssim 6$ to a more passively evolving universe by giant galaxies at $z \lesssim$ 1–2 (Driver et al. 1998). This transition may have resulted in dust and gas rapidly accumulating in the disks and central bulges of forming galaxies, with a SN rate that has progressively less impact on clearing gas and dust from the galaxies that are steadily growing in mass with cosmic time. It is possible that this process may have caused $f_{\rm esc}$ to rapidly drop

over a relatively narrow interval of cosmic time in luminous galaxies, as massive LyC producing stars formed during the period of high SFR become either SNe II or AGB stars, which then enrich the ISM with dust within $\sim$1 Gyr (J. S. Mathis 1990; Bekki 2015). The infall of hydrogen in these galaxies could have then caused $f_{\rm esc}$ to decrease substantially (Rauch et al. 2011; van de Voort et al. 2012).

The subsequent increase of dust can then prevent the collapse of cold gas by photoelectric heating from stars or AGN in the galaxy (Krumholz and Dekel 2012; Forbes et al. 2016). This would then lead to a decrease in the galaxy's SFR, as feedback from heating inhibits the formation of new massive stars (e.g., Inoue 2001; Inoue, Hirashita, and Kamaya 2001). The decline in SFR would also lead to a decreasing SN rate (Botticella et al. 2012), further preventing the escape of LyC, as there would have been fewer clear channels produced by SN for the LyC to escape. LyC produced by AGN can be absorbed by gas and dust in the disk of the galaxy itself, depending on viewing angle. When galaxies produce stronger AGN outflows, more of their LyC radiation may escape approximately *perpendicular to* the galactic disk (e.g. Windhorst, Keel, and Pascarelle 1998; Reunanen, Kotilainen, and Prieto 2003), which contributes to maintaining the ionized state of the IGM, as AGN begin to dominate the ionizing background at $z \lesssim 3$.

### 4.5.3 The Role of Galaxies with Weak AGN in Reionization

Fig 14 shows the stacked LyC and UVC images of the known galaxies with AGN in our sample. The $\langle z \rangle$=2.374 stack only includes two AGN with a LyC flux of $m_{\rm AB} > 27.91$ mag (UVC aperture). The $\langle z \rangle \simeq 2.61$ and 3.32 samples contain 7 and 3 stacked AGN with measured LyC fluxes of $m_{\rm AB} \simeq 28.3$ and 27.42 mag with SNR$\sim$2.7

and 2.5, respectively. These fluxes are typically more luminous in LyC and have higher SNR than their non-AGN counterparts, despite having fewer stacked galaxies. This is most likely due to LyC originating from the central accretion disk, made visible by stronger AGN outflows when viewed under the right angle. AGN outflows can also increase the porosity of the ISM in its host galaxy (e.g., Silk 2005), thereby increasing $f_{\rm esc}$ of the LyC produced by stars, which further contributes to the total measured LyC flux from that galaxy.

The stacks in Fig 12 suggest some variety of LyC morphologies, though the UVC images exhibit more compact light profiles compared to the non-AGN stacks in all three cases (see the discussion in §4.4.5–4.4.4). The $\langle z \rangle \simeq 2.62$ stack is the most extended of the AGN both in LyC and UVC, which is most likely due to the increased sensitivity to fainter flux at low redshift, with a central bright point source from radiation escaping along the observed line-of-sight. The radial dependence of the LyC SB profile for this stack may be due to the viewing angle of the AGN relative to the direction of the escaping LyC radiation, or possibly due to the fact that the LyC undergoes a more complex escape process, where photons can be reflected off of relativistic electrons in the AGN corona and accretion disk, or by hot dust in the torus via Thomson and/or inverse Compton scattering (e.g., Haardt and Maraschi 1993). The $\langle z \rangle \simeq 3.32$ AGN LyC stack appears to be more point-like, indicating that these observed LyC photons may be escaping predominantly along the line-of-sight, which is supported by the presence of broad emission lines in their spectra, although the more extended LyC emission may not be visible due to the average SB of these AGN at higher redshift being dimmed by an additional $\sim$61% from $\langle z \rangle \simeq 2.62$ to $\langle z \rangle \simeq 3.32$.

Fig. 10 shows that the *average* UVC luminosities of "Galaxies with weak AGN" in our sample is about the same, or somewhat fainter than that of galaxies without

AGN. Their average luminosity in Fig. 10 $M_{\rm AB} \simeq$ –20.4±0.9 mag at $z \simeq 2.3$–4.1 does not indicate clearly QSO dominated luminosities or SEDs. Table 2 shows that the LyC flux measured from the stacks of (weak) AGN at all redshifts is typically *brighter* than galaxies without AGN. Thus, precise modeling of the intrinsic LyC emission must include the contribution of flux emitted by, or reprocessed from, the AGN accretion disk. The SED of the AGN accretion disk is more complicated than a simple blackbody curve, as the SED must account for the broad and narrow emission line regions, as well as energy lost to relativistic jets and photons scattered/absorbed by the corona and central torus and non-AGN dust, which is also viewing angle dependent. We did not fit both stellar+AGN SED models to the 4–6 band continuum data in this initial study, and therefore we do not calculate escape fractions for these galaxies. From the compact appearance in some of our stacked images — and from the fact that they are on average brighter than galaxies without AGN — the LyC flux in galaxies with weak AGN may be dominated by light originating from their accretion disks.

Further data and modeling is needed to better constrain $f_{\rm esc}^{\rm abs}(z)$ for both galaxies and weak AGN to confirm these observed trends. The ERS LyC data for AGN may be consistent with a more modest drop in $f_{\rm esc}^{\rm abs}(z)$ than for galaxies that may have occurred close to the peak in the epoch of AGN activity around $z \simeq 2.5$ (e.g., Fontanot et al. 2007; Croom et al. 2009; Ikeda et al. 2011; Ikeda et al. 2012). Since AGN activity can affect the SFRs, it is possible that when AGN outflows started to ramp up after the peak in the cosmic star-formation history at $z \simeq 2$ (Springel, Di Matteo, and Hernquist 2005; Hopkins et al. 2006), their outflows cleared enough paths in the host galaxy ISM to increase $f_{\rm esc}$ of a possibly AGN induced top-heavy stellar population IMF.

Because galaxies far outnumber AGN, and despite being fainter in LyC on average,

their $f_{\rm esc}$ values suggest that galaxies may have produced sufficient LyC radiation to maintain reionization at $z \gtrsim 3$, while AGN likely dominated in the production of ionizing LyC flux at $z \lesssim 2$–3. Even though our spectroscopically selected sample of galaxies outnumber the *weak* AGN by a factor of ∼3 (see col. 4 of Table 2), the total ionizing flux from AGN is brighter than that from galaxies *without* AGN by ∼7.7×12/34∼2.7.

The ERS samples are still very small, and clearly need further confirmation through much larger samples, both through additional deep UV/optical imaging of wider HST fields and through spectroscopy on fields with high quality existing HST data. Further theoretical work is needed to outline exactly how quickly $f_{\rm esc}$ may have increased towards higher redshifts *and* at fainter luminosities, as well as at lower metallicities and lower extinction at higher redshifts, while producing enough escaping LyC photons from faint galaxies to finish and maintain reionization at $z \lesssim 6$–7.

There is already a significant issue in accounting for reionization with the faint galaxy population observed via cluster lensing at $z \simeq 9$. At redshifts larger than 8, the Hubble Frontier Fields reveal a strong drop in rest-frame UV luminosity density (e.g., Ishigaki et al. 2015). Hence, it is also possible that one may need to consider an additional source of reionizing photons beyond $z \simeq 6$–7. This source might include feedback on both the IGM ionization and clumpiness via hard ionizing photons from high mass X-ray binaries (e.g., Mirabel et al. 2011). Other astrophysical sources such as Population 3 stars or mini AGN seem strongly constrained via chemical evolution (Kulkarni et al. 2014) and the X-ray background (Dijkstra, Haiman, and Loeb 2004), though these observations may be limited by Malmquist bias. It is possible that $f_{\rm esc}$ may evolve with redshift and/or with galaxy properties as well (e.g., mass, $A_V$, SFR, and/or age).

## 4.6 Conclusions

This chapter presented LyC emission that may be escaping from galaxies using improved *HST* WFC3 of the ERS fields in three filters, where LyC may be observed from galaxies at $z \simeq 2.3$–$4.1$. The data used in our analysis was drizzled with the much more accurate 2013 WFC3 geometric distortion correction tables, which resulted in the correction of significant astrometric offsets that remained in earlier ERS UVIS mosaics. The WFC3 ERS UV images were taken in 2009 September, when the CTE was still at a level where faint flux could still be measured without significant losses. We verified that any loss in CTE is not the primary limitation to our measurements (see Appendix B.1).

We extracted sub-images centered on galaxies with high quality spectroscopically measured redshifts from the ERS mosaics, and averaged the LyC flux of those galaxies. We payed careful attention to the removal of potentially nearby contaminating objects and low level variations in the UV sky-background during this stacking process. We ensured that no significant amount of contaminating flux longwards of the Lyman-break ($\lambda > 912$Å) was included in our stacks. The following are our main findings:

(1) Our measurements of the average LyC flux in the stacks for galaxies at $z \simeq 2.3$–$4.1$ is summarized in Table 2. We find that the LyC flux of faint galaxies at $\langle z \rangle \simeq 2.35$, 2.69, and 3.54 is generally constrained at the $<$1–3$\sigma$ level, in typical image stacks of 13–19 objects in the WFC3/UVIS F225W, F275W, and F336W filters, respectively. These upper limits corresponds to total LyC fluxes of $m_{\rm AB} \gtrsim 28.1$–$29.0$ mag. The LyC flux of weak AGN is detected to be brighter on average at $z \simeq 2.3$–$3.5$, but over $\sim$2–10$\times$ fewer objects per stack.

(2) The combined LyC emission averaged over the three filters suggests an overall

LyC flux distribution that is non-centrally concentrated, which may be explained by a radial dependence in the ISM porosity and/or scattering of the LyC photons. We find that the LyC flux from AGN is flatter than its UVC counterpart. This may suggest a complex escape process that may be determined by the distribution and extent of neutral (dusty) gas clouds within a porous multiphase ISM.

(3) From our best fit BC03 SED models fit to *HST* continuum observations longwards of Ly $-\,\alpha$, the observed LyC flux corresponds to an *average* absolute LyC escape fraction constrained to $f_{\rm esc}\sim 22^{+44}_{-27}\%$ at $\langle z\rangle\simeq 2.4$ and $\lesssim 55\%$ at $\langle z\rangle\simeq 2.8$–$3.6$. While the error bars on the implied $f_{\rm esc}$ values in each of the three redshift bins remain large, within the error bars, the data suggest an increasing trend of $f_{\rm esc}$ with redshift at $z\gtrsim 2$.

(4) The available published $f_{\rm esc}$ data for galaxies may suggest *a more sudden increase* in $f_{\rm esc}^{\rm abs}$ with redshift that occurred around $z\sim 2$. For galaxies, the steepest drop in $f_{\rm esc}$ occurs at $z\lesssim 2$, near the peak of the cosmic star-formation history within an interval of $\pm 1$ Gyr from this peak in cosmic time.

(5) If galaxies *without* AGN at $z\sim 2$–$4$ are analogous to those at $z\gtrsim 6$, the upper limits to their $f_{\rm esc}$ values suggest that they may have had a sufficient LyC escape fraction to reionize the IGM by $z\gtrsim 6$. The SEDs of galaxies with weak AGN is likely dominated by *stellar light* in the non-ionizing continuum. Galaxies with weak AGN outshine galaxies *without* AGN in our sample by a factor of $\sim 7.7$, or $m_{\rm AB}\sim 2.3$ mag. Hence, while galaxies without AGN likely began and maintained cosmic reionization at $z\gtrsim 3$, galaxies with (weak) AGN likely dominated the contribution to the cosmic ionizing background and maintain reionization at $z\lesssim 2$–$3$, although the role of massive galaxies without AGN may not have been negligible at $z\lesssim 2$.

The transition from galaxy dominated reionization to weak AGN reionization

appears to have occurred at $z \sim 2$–3, i.e., right around the peak in the cosmic SFR ( Piero Madau et al. 1996), which may indicate the epoch where the universe transitions from infall/merger driven SFGs at $2 \lesssim z \lesssim 6$ to a more passively evolving universe by giant galaxies at $z \lesssim 1$–2. This may result in gas and dust rapidly accumulating in the disks and nuclei of forming galaxies, combined with a SN rate that has progressively less impact on clearing gas/dust in galaxies that are steadily growing in mass with cosmic time. The accumulating H 1 gas and decreasing SFR may have caused $f_{\rm esc}$ to *rapidly drop* over a relatively narrow interval of cosmic time ($\sim$1 Gyr), as the LyC flux heats the dust and inhibits the formation of new massive stars. When AGN outflows began to increase after the peak in the cosmic star-formation history at $z\sim$2, their outflows may have cleared enough paths in the ISM of host galaxies to enhance the fraction of escaping LyC radiation produced by massive stars and from the accretion disk, resulting in AGN beginning to dominate the ionizing background at $z \lesssim 2$.

(6) Further data on LyC $f_{\rm esc}$ are essential for both galaxies and weak AGN to confirm both their trends in $f_{\rm esc}^{\rm abs}(z)$. The ERS samples are still very small, and clearly need further confirmation through much larger samples, both through deep imaging of wider HST fields in the UV and through deeper spectroscopy on fields with high quality existing *HST* data, e.g., with the *JWST* FGS/NIRISS grisms and with NIRSpec (Gardner et al. 2006). Further theoretical work is needed to outline exactly how quickly $f_{\rm esc}$ may have increased towards higher redshifts *and* at fainter luminosities, as well as at lower metallicities and lower dust extinction at higher redshifts, while producing enough escaping LyC photons from faint galaxies to complete and maintain reionization.

The following chapter presents a continuation of the work presented here, but with an expanded sample of more than twice the galaxies. In this case, the sample was

expanded after incorporating the recently acquired *HST* UV imaging in the GOODS North and South fields.

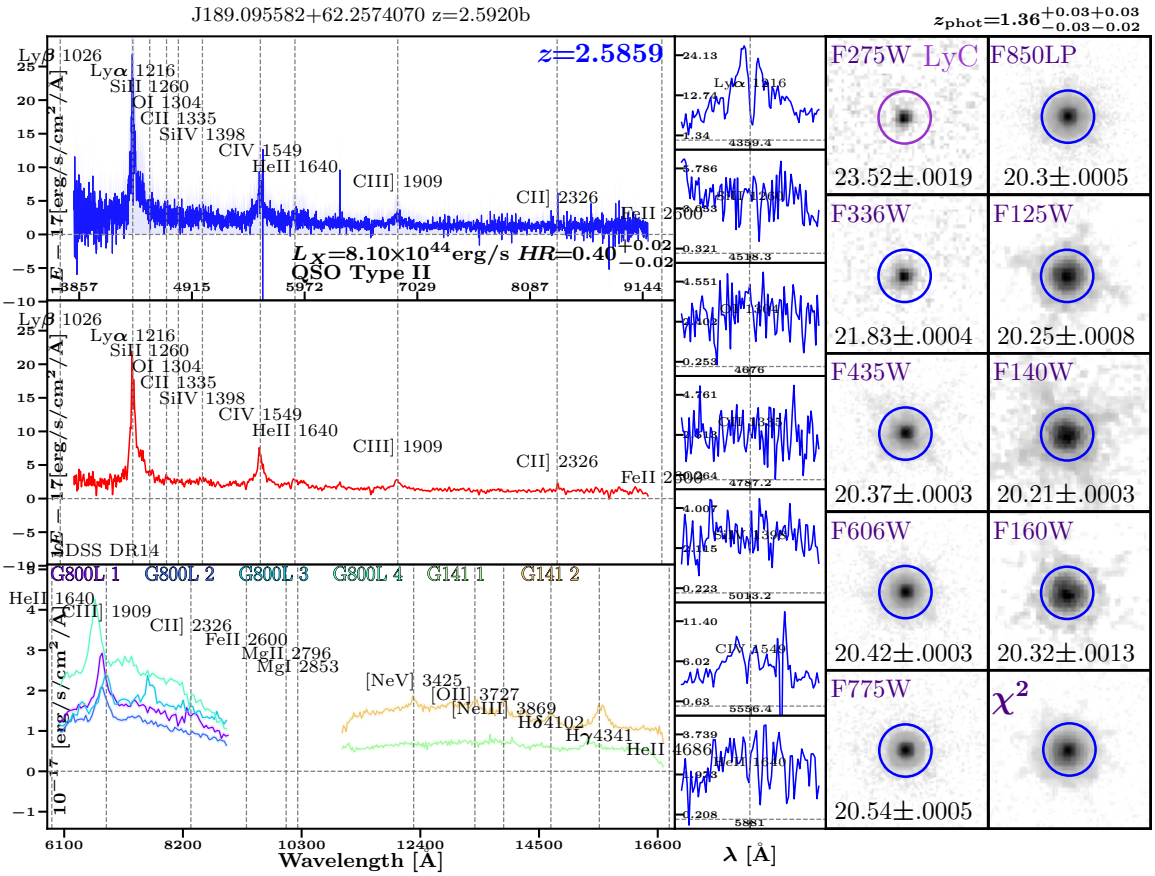


Figure 9. Example Spectral Classification Diagram used for Sample Selection

An example spectrum of a highly reliable redshift of an AGN, as determined by the observed broad Ly − $\alpha$ and C 4 lines, X-ray luminosity, and X-ray photon index $\Gamma$. The expected AGN emission lines are seen to coincide exactly where they are expected at the indicated redshift of $z = 2.5859$ in the ground-based blue and 3D-HST grism spectra shown in the bottom-left panel. The red curve in the middle panel is equal to the blue curve, but convolved with a 3 Å Gaussian filter. Zoomed-in segments of the spectrum around the most common emission/absorption lines are shown along the middle column. All available *HST* images from WFC3/UVIS, WFC/ACS, and WFC3/IR where the galaxy could be excised are shown in the right two columns, with a $\chi^2$ image (Szalay, Connolly, and Szokoly 1999) composed of all other *HST* images shown plotted on the bottom right. The *HST* filter that captures LyC is indicated by a violet circle. The photometric redshift found by the 3D-HST collaboration (Momcheva et al. 2016) is shown at the top right, which was not always correct due to the unavailability of some *HST* UV-imaging at the time. The position-based ID of the galaxy is shown above the ground-based spectrum, with the "b"-suffix distinguishing it as the second available ground-based spectrum for this galaxy. The source archive of the spectrum is indicated in the bottom-left of the convolved spectrum panel. This particular galaxy is discussed more in detail in §5.4.

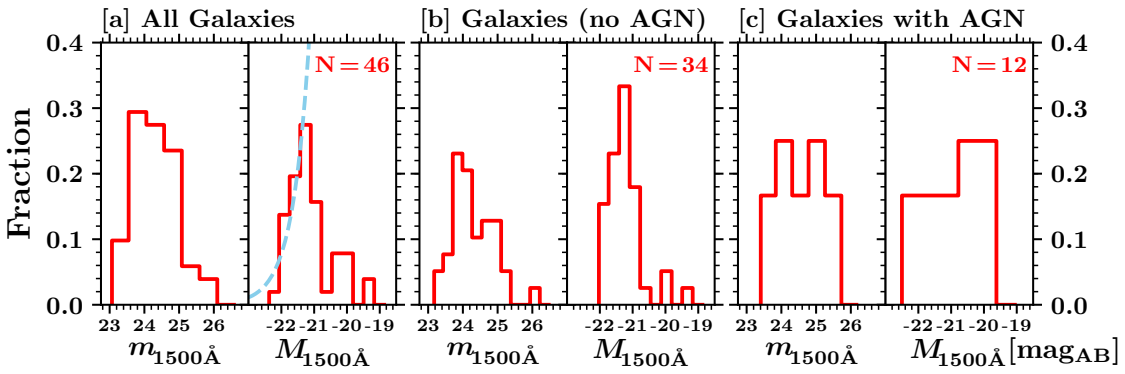


Figure 10. Apparent and Absolute Magnitude Distributions of Galaxies and AGN in the ERS Sample

[*a*] Absolute and apparent magnitude distributions at the rest-frame 1500±100Å of the spectroscopic samples for all galaxies. [*b*] Same, for just the galaxies without AGN activity. [*c*] Same, for galaxies with indications of AGN activity. These magnitudes were derived from the observed SED fits (see §3.3), and therefore do not require k-corrections. The blue dashed curve indicates the slope of the luminosity function of $\langle z \rangle$=3.46 galaxies at $M_{AB}$=–20.8, equal to 0.84 dex/mag.

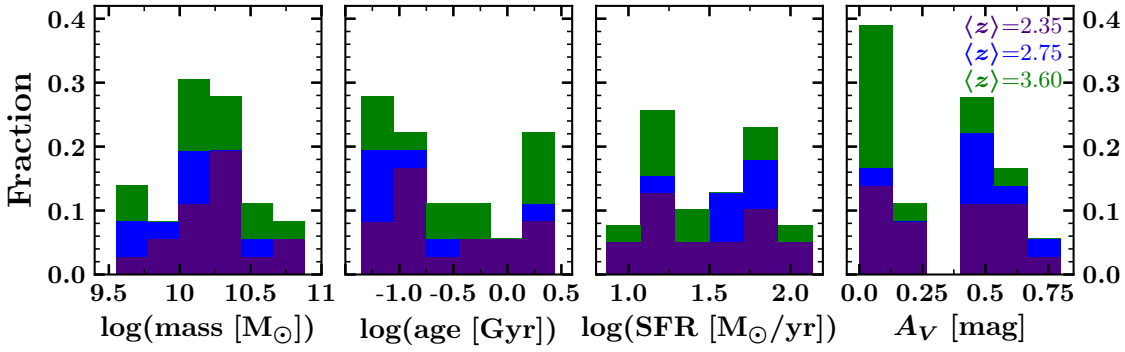


Figure 11. SED Parameter Distribution of Galaxies Without AGN in the ERS Sample

Stacked BC03 SED fit parameter distributions of the spectroscopic samples for galaxies without AGN. The purple, blue, and green bars represent the $\langle z \rangle$=2.35, $\langle z \rangle$=2.75, and $\langle z \rangle$=3.60 samples, respectively.

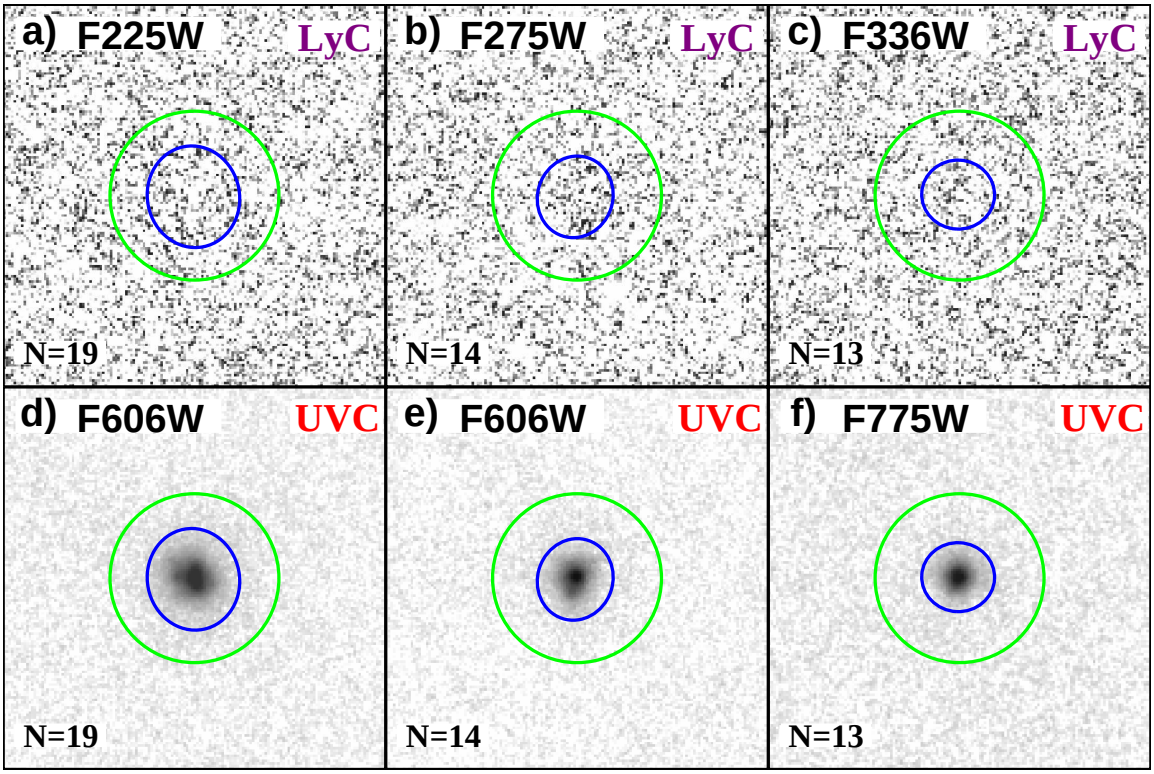


Figure 12. Stacks of All Galaxies in the ERS Sample

Sub-image stacks for the three different redshift bins in our sample of *all* galaxies, sampling LyC emission in: [*a*] F225W at $2.28 \leq z \leq 2.45$, [*b*] F275W at $2.47 \leq z \leq 3.08$, and [*c*] F336W at $3.13 \leq z \leq 4.15$; and corresponding UVC ($\sim 1400 \lesssim \lambda_0 \lesssim 1800$Å) emission in: [*d*] F606W, [*e*] F606W, and [*f*] F775W. Note that the objects contributing to panels [*d*] and [*e*] differ, since they correspond to different redshift bins. Blue ellipses indicate the SExtractor `MAG_AUTO` UVC detected matched apertures, while green apertures are $2\farcs0$ diameter circles for comparison. All sub-images are 151×151 pixels ($4\farcs53 \times 4\farcs53$) in size.

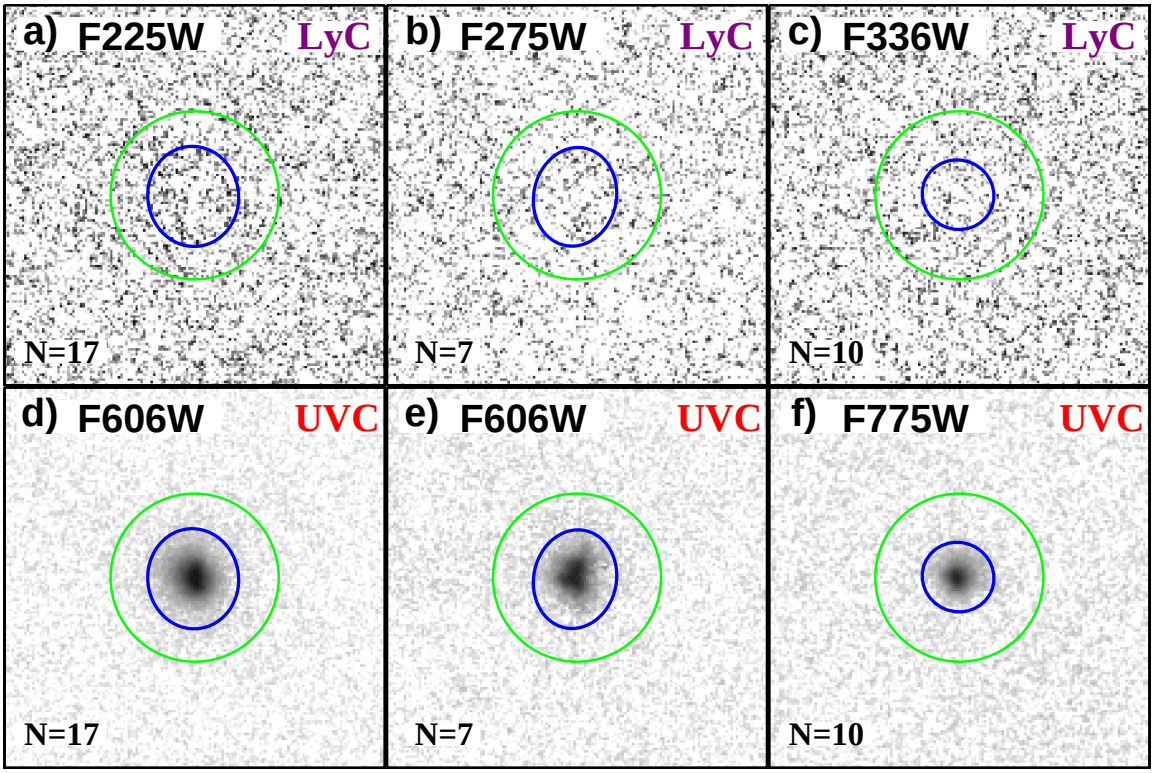


Figure 13. Stacks of Galaxies Without AGN in the ERS Sample

As Fig. 12 for galaxies *without* AGN (i.e., no obvious signs of nuclear activity from their spectra or X-ray/radio luminosities/photon indices.

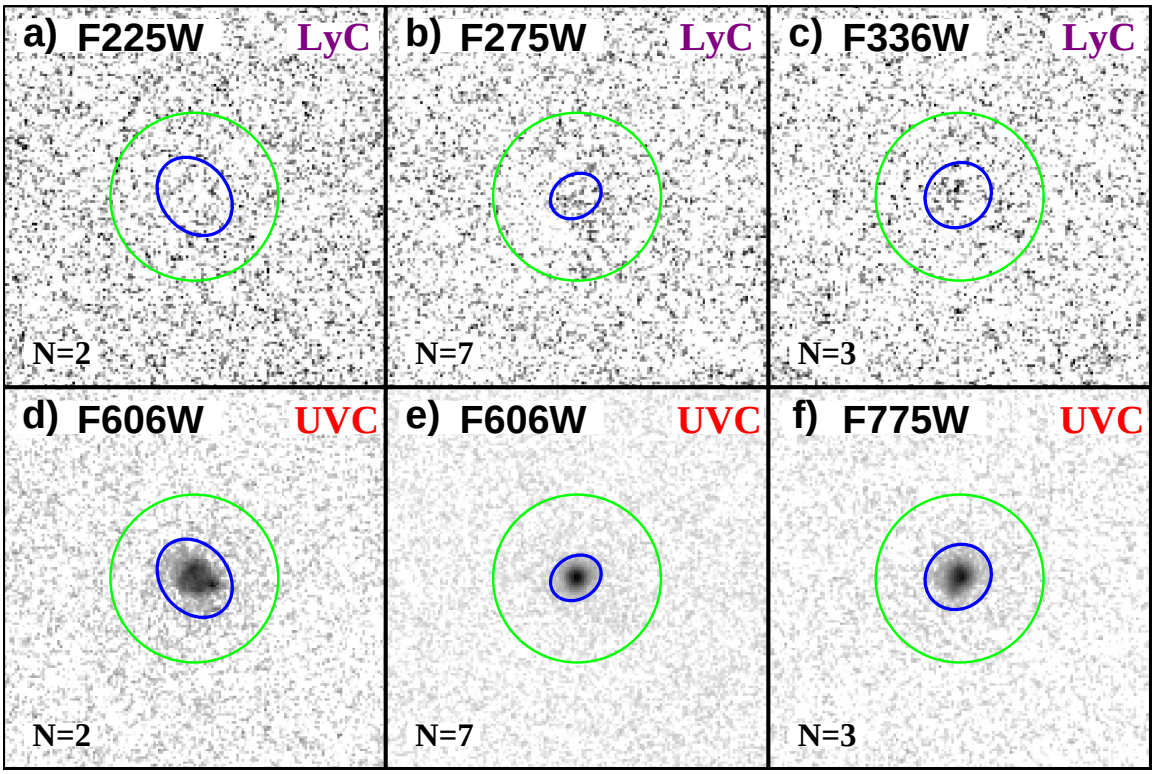


Figure 14. Stacks of Galaxies With AGN in the ERS Sample

As Fig. 12 for only the galaxies hosting weak AGN.

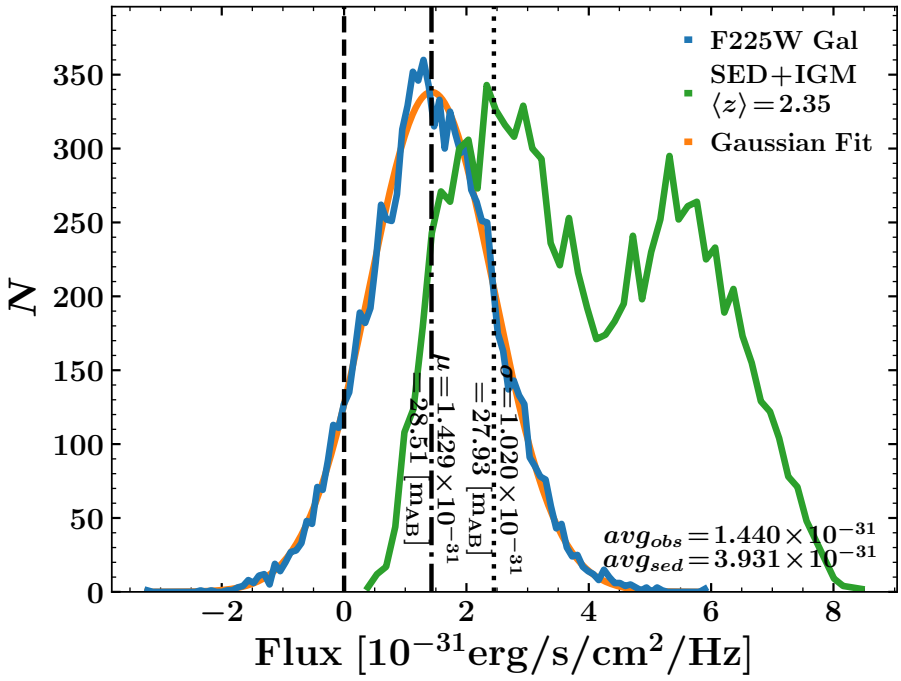


Figure 15. Example of Resulting Photometric Analysis Method

Example flux distribution for the F225W galaxies *without* AGN stack used for our photometric analysis listed in Table 2. Each pixel in the stack was given a mean based on the pixel value in the stacked F225W image, and a variance from the sum of the sky-background variance and the square of the corresponding pixel value in the stacked RMS map. The blue distribution was generated by summing the pixel flux distributions inside the blue aperture from Fig. 13 for each realization of the stack, as described in §3.2. The orange line is the Gaussian curve fit to the blue distribution. The mean and $+1\sigma$ values are shown as vertical dash-dot and dotted lines, respectively. The green distribution is the modeled intrinsic flux using the stacked best fit SED convolved with the IGM transmission models of Inoue et al. (2014) and fitting error. The average value of the blue and green distributions is indicated as $avg_{obs}$ and $avg_{sed}$, respectively.

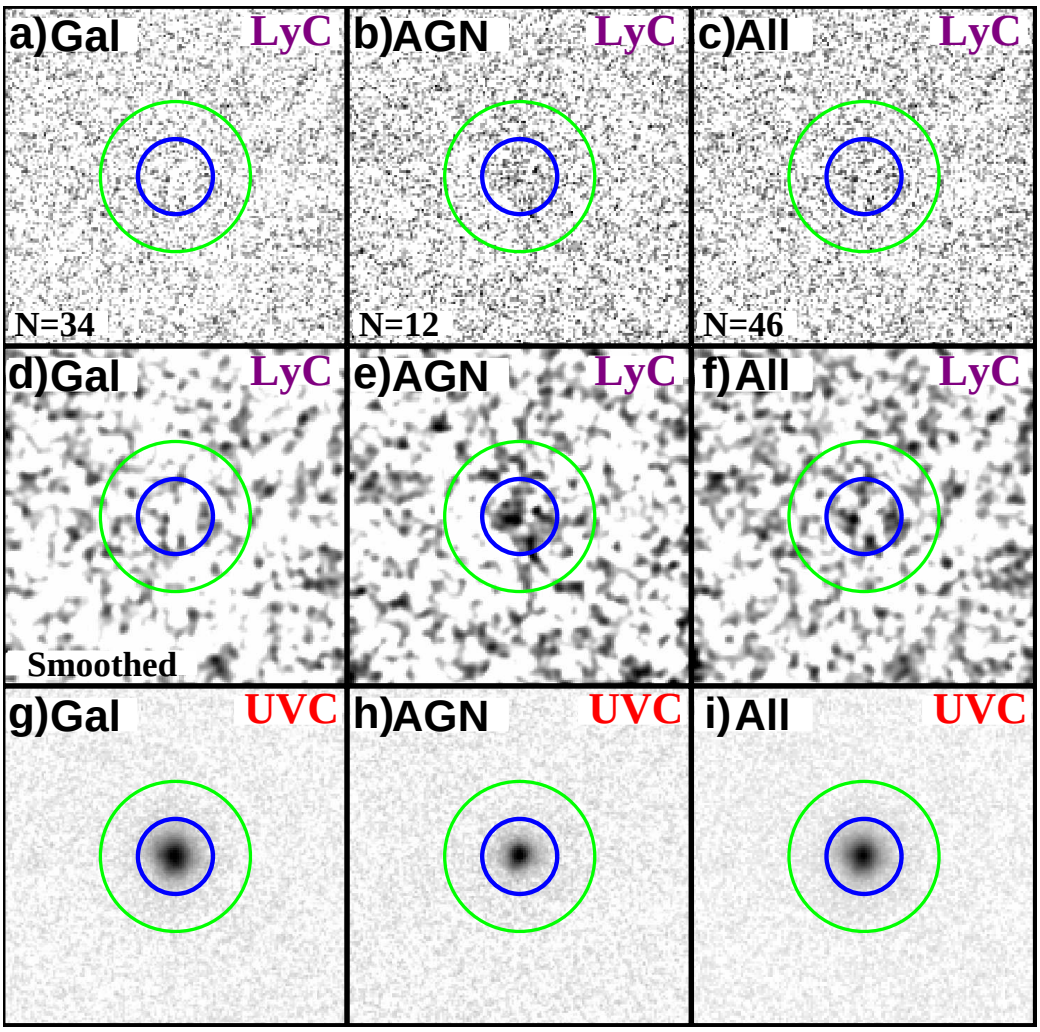


Figure 16. Composite Stacks of All Galaxies in the ERS Sample

[*Top Row*]: LyC stacks of all galaxies in our sample with high quality spectra and reliable redshifts; [*Middle Row*]: The same as the top row but convolved with a $1\sigma$ Gaussian kernel. [*Bottom Row*] The UVC counterparts of the top row; *a, d, and g* [Left column of panels:] Composite stacks of all galaxies without AGN in our spectroscopic sample observed in the F225W, F275W, and F336W filters; *b, e, and h* [2nd column:] Composite stacks of all galaxies hosting (weak) AGN; *c, f, and i* [3rd column:] Composite stacks of all 46 galaxies in our sample. These stacks represent the average *observed* LyC $F_\nu$ from all galaxies integrated from $2.3 \lesssim z \lesssim 4.1$, scaled to a common zeropoint magnitude. The blue and green circles have radii $0\farcs5$ and $1\farcs0$, respectively. The measured SNR of the combined LyC emission in these stacks is $\sim$2.3, 0.7, and $3.9\,\sigma$ for the stack of all galaxies, all galaxies without AGN, and all galaxies with AGN, respectively. The AGN stacks exhibit both a centrally concentrated and extended component in their flux distributions, from contributions of a central AGN point source and perhaps also from scattered photons (Fig 13). These images suggest that LyC escape paths may be slightly offset from a galaxy center, including point source emission from the AGN. Given the random orientation of galaxies in each stack, this would explain the faint, non-centrally concentrated, and extended morphology of the detected LyC emission.

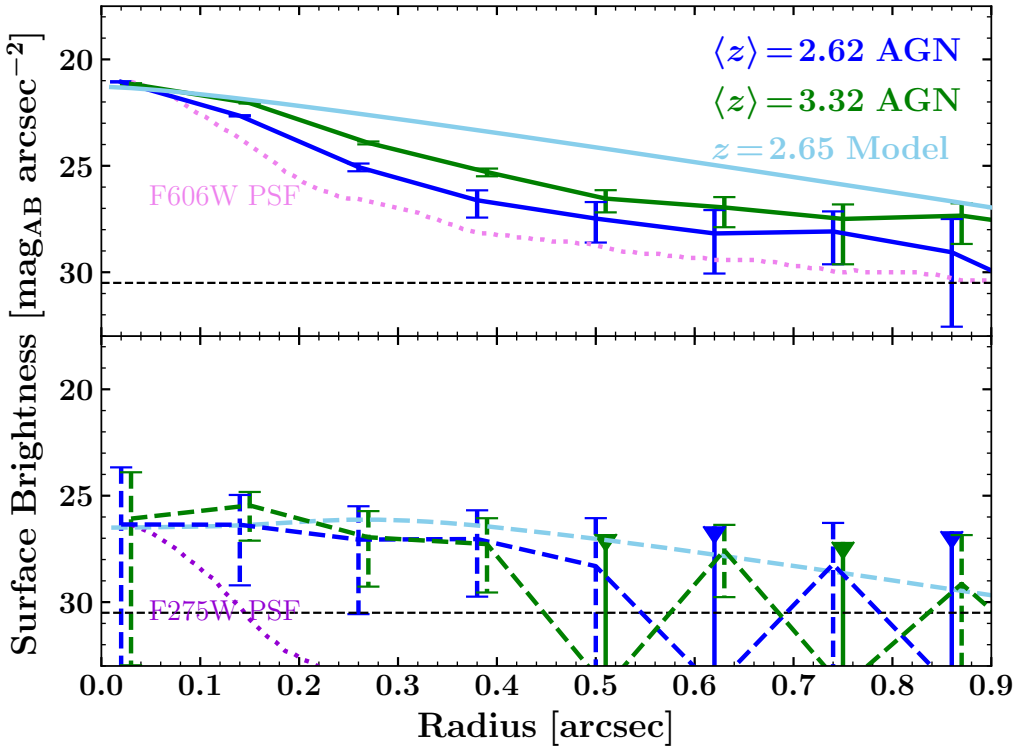


Figure 17. Modeled and Observed LyC Radial Profiles of Galaxies with AGN in the ERS Sample

Radial surface brightness profiles of the non-ionizing UVC signal (*solid curves*) and the LyC signal (*dashed curves*) measured in the stacks (Fig. 14) for the galaxies with AGN samples. The curves are color-coded according to their mean redshift (filter): $\langle z \rangle$=2.68 (F606W and F275W; blue) and $\langle z \rangle$=3.49 (F775W and F336W; green). The *observed* PSF in F275W and F606W are indicated by dotted purple and pink curves, which were normalized to the central SB of the corresponding LyC surface brightness profiles. The horizontal black dashed line indicates the $1\sigma$ sensitivity limit for the LyC profile in F275W. Both UVC surface brightness profiles are extended with respect to the corresponding PSF curves. The observed LyC stack SB profiles are also extended *and* flatter than the UVC profiles, which is also predicted from our LyC scattering model (*light blue dashed curve*), where scattering of the escaping LyC photons off electrons and/or dust with a porous ISM spreads the LyC emission beyond the distribution of the stellar UVC light (*light blue solid curve*). The *light blue solid curve* is scaled from *light blue dashed curve* by a single ratio of $\frac{f_{\rm UVC}}{f_{\rm LyC}}$, which may depend on radius. See §4.4.5 for further details of the model.

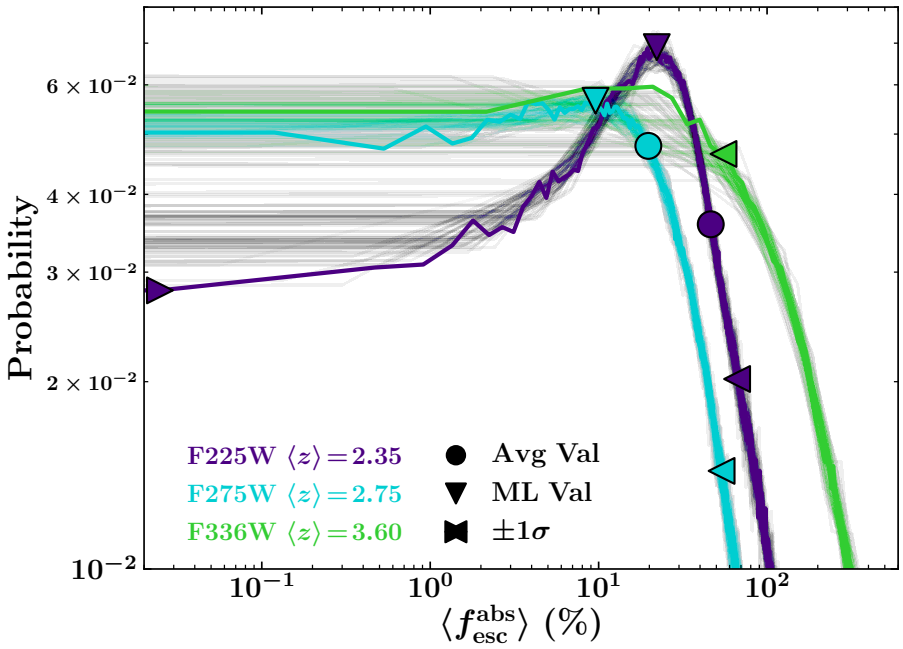


Figure 18. Probability Mass Function of the LyC Escape Fraction from Galaxies Without AGN in the ERS Sample

PMFs of $f_{\rm esc}$ values from the MC simulations described in §3.3 plotted against their relative probability. This analysis was performed $10^3$ times using the measured and modeled intrinsic stacked *apparent* LyC flux and their $\pm 1\sigma$ ranges. We apply the IGM attenuation models of Inoue et al. (2014) to our modeled LyC fluxes. These $f_{\rm esc}$ values were optimally binned according to the Freedman-Diaconis rule (see §4.4.6). Downwards triangles and circles indicate the resulting ML and average $f_{\rm esc}$ values in each probability distribution function, respectively, while the left/right facing triangles indicate the $\pm 1\sigma$ range around the mode.

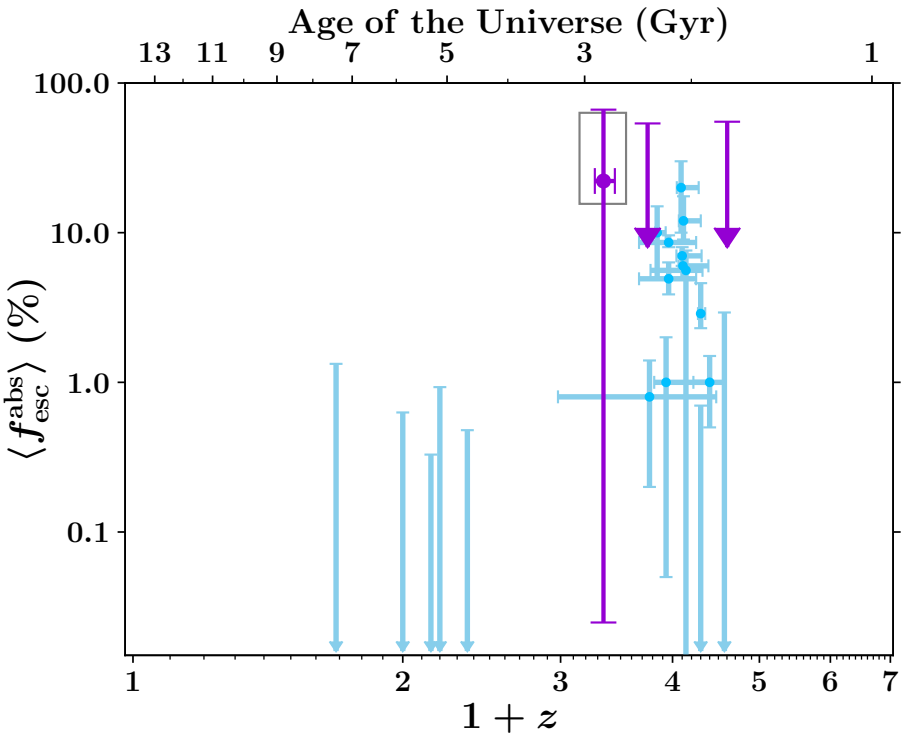


Figure 19. The Evolution of the LyC Escape Fraction for Galaxies Without AGN in the ERS Sample

The LyC escape fraction for various galaxy samples as a function of redshift. Plotted is present ERS ML average $f_{\rm esc}$ value with their $\pm1\sigma$ range and $1\sigma$ upper limits for our galaxies *without* AGN sample (purple filled circled and triangles) taken from the probability mass functions of Fig. 13, generated from our MC simulations described in §3.3. The interquartile range of the $\langle z \rangle$=2.35 data is indicated by a box to highlight the high asymmetry of it's PMF. The blue points indicate available published data as referenced in §2.3, some of which were converted from quoted $f_{\rm esc}^{\rm rel}$ values using extinction values from the literature source (see §3.3, Eq. 3.10). All vertical error bars are the $\pm1\sigma$ uncertainty on the $f_{\rm esc}$ values. Some errors were converted from the quoted 2–3$\sigma$ uncertainties. Upper limits are shown as blue downward triangles. Although the blue points represent galaxy samples with different properties from our samples, and the quoted errors were derived from uncertainties with different error assessment, the combined data suggests a correlation of $f_{\rm esc}$ with redshift, which may not be a simple power law in $(1+z)$. This compiled dataset does not rule out the possibility that massive galaxies may have had high enough LyC $f_{\rm esc}$ values to complete hydrogen reionization by $z\sim6$, if galaxies at $2\lesssim z\lesssim4$ and $z\gtrsim6$ are analogous.

Chapter 5

# THE LYC ESCAPE FRACTION FROM GALAXIES AND AGN IN THE GOODS NORTH AND SOUTH FIELDS

## 5.1 Introduction

The Great Observatories Origins Deep Survey (GOODS) is an observational campaign that performed deep, multi-wavelength observations from multiple space and ground-based telescopes to provide publicly available data to be used for exploring a range of scientific topics that study the distant Universe. These Great Observatories include *HST* in the UV, optical, and near-IR, *Chandra* and *XMM-Newton* in the X-ray, *Spitzer* in the mid-IR, *Herschel* in the far-IR and submillimeter, the Very Large Array (VLA) in the radio, and multi-band imaging and spectroscopy from the ground-based Atacama Large Millimeter/submillimeter Array (ALMA), VLT, Keck, Subaru, and Kitt Peak 4-meter telescope, and will undoubtedly be observed with the upcoming *JWST*. The primary science goals of the GOODS program were to study the mass assembly history of galaxies and the SEDs of galaxies from radio to X-rays generated by stars and AGN over a wide range of redshifts. The GOODS data was also used to study extragalactic background light in the multi-wavelength data the program compiled (Dickinson, Giavalisco, and GOODS Team 2003).

The survey was performed in two regions of sky, one in each celestial hemisphere. Data in the northern hemisphere was collected in the vicinity of the Hubble Deep Field North (HDF-N) and the southern hemisphere data was collected in the Chandra

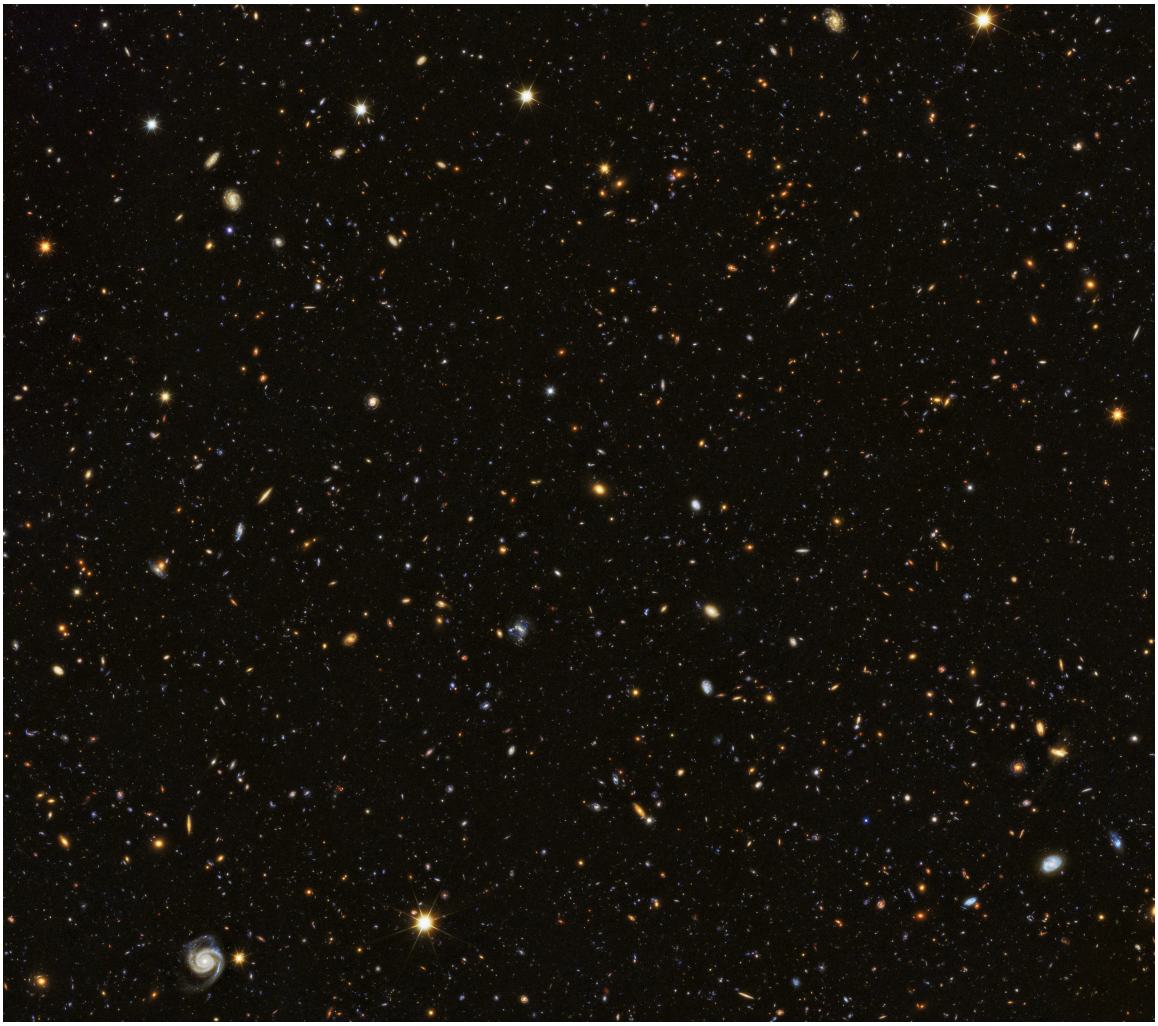

Figure 20. Color image of the GOODS North Field

This color image of GOODS North is comprised of multiple *HST* images taken by the WFC3/UVIS, ACS/WFC, and WFC3/IR cameras. The WFC3/UVIS F275W filter corresponds to violet in the image, WFC3/UVIS F336W is blue, ACS/WFC F435W + F606W data is represented by green, WFC3/IR F775W is yellow, ACS/WFC F814W + F850LP + WFC3/IR F105W is orange, WFC3/IR F125W + F140W is red, and WFC3/IR F160W is magenta. The 11 bands displayed in this color image are also used extensively throughout the work presented in this chapter.

Credit: ESA/Hubble & NASA

Figure 21. Color image of the GOODS South Field

This color image of GOODS South was constructed using the same filters and color scheme as in Fig. 20

Credit: ESA/Hubble & NASA

Deep Field South (CDF-S). GOODS-N is centered at R.A. $\simeq 189.2°$ and Dec. $\simeq 62.2°$ and GOODS-S is centered at R.A., Dec. $\simeq 53.1°$, $27.8°$, and each subtends an area of $\sim 74\,\mathrm{arcmin}^2$ and $28\,\mathrm{arcmin}^2$ on the sky, respectively. The observations carried out by the GOODS campaign provided the data for $\gtrsim 500$ journal publications and dissertations to date. The GOODS program has indeed achieved its goal of providing one of the best legacy astronomical datasets for studying the distant Universe.

In this chapter, the recent *HST* WFC3/UVIS imaging of the GOODS North and South field is used to study the LyC emission escaping from galaxies and AGN, which extends the previous work presented in Chapter 4 and published in Smith et al. (2018). The considerable investment in observational efforts focused on these fields provide a substantial increase to the available data that can be used in this work, and greatly exceeds that available in the ERS field. The next few sections in this chapter describe the GOODS UV mosaics we constructed for our LyC analyses, the sample of galaxies we selected from these fields, the results of our LyC photometric analyses and $f_{\mathrm{esc}}$ constraints, unexpected findings that arose during our analyses, and a discussion and conclusions of these results.

## 5.2 Data Description and Processing

The archival *HST* image data we used for our LyC studies presented here includes WFC3/UVIS data from the ERS (Windhorst et al. 2011), the CANDELS (Grogin et al. 2011; A. M. Koekemoer et al. 2011), the Hubble Ultraviolet Ultra Deep Field (UVUDF; Teplitz et al. 2013), and the Hubble Deep UV Legacy Survey (HDUV; Oesch et al. 2018), which we independently drizzled using the Astrodrizzle tool found

in the DrizzlePac software[5]. The ERS WFC3/UVIS data is described in detail in §4.2. We used optical ACS/WFC data in F606W, F775W, and F850LP from GOODS (Dickinson, Giavalisco, and GOODS Team 2003; Giavalisco et al. 2004), WFC3/IR F098M, F125W, and F160W imaging in the ERS field (Windhorst et al. 2011), CANDELS WFC3/IR F105W, F125W, F160W and WFC/ACS F814W, and 3DHST WFC3/IR F140W imaging (Momcheva et al. 2016) for SED fitting (see §5.3.2) and for studying the rest-frame, non-ionizing UVC ($\lambda_{\rm rest} \simeq$1400-1800Å) of galaxies.

Our new mosaics include all available CANDELS and HDUV data in F275W and F336W taken in the GOODS North field, as well as all available data in F225W, F275W, and F336W from the HDUV and UVUDF surveys that covered the GOODS South field. We refer to both mosaics as the "GOODS/HDUV" data since much of this data came from the HDUV program, and the ERS imaging presented in §4.2 is simply referred to as the "ERS" data. The ERS mosaics reach ∼2 orbit depth ($m_{\rm AB} < 26.4$ at $5\sigma$ for F275W) over a wide ∼58 arcmin$^2$ area in the F225W, F275W, and F336W filters (Windhorst et al. 2011), where an orbit corresponds to an exposure time of $\sim 2300$ s. The HDUV imaging reaches 4–8 orbit depth in F275W and F336W ($m_{\rm AB} < 27.6$ at $5\sigma$ for F275W) in a combined ∼100 arcmin$^2$ area across the GOODS North and South fields (Oesch et al. 2018). The UVUDF data covered a single pointing in GOODS South for 16, 16, and 14 orbits in F225W, F275W, and F336W, respectively ($m_{\rm AB} < 27.8$ at $5\sigma$ for F275W; Rafelski et al. 2015). The CANDELS survey also observed GOODS North in F275W and reached a ∼6 orbit depth ($m_{\rm AB} < 27.1$ at $5\sigma$; A. M. Koekemoer et al. 2011) that brought the F275W GOODS North data to a total depth of ∼10 orbits. The HDUV imaging required the use of post-flash at the time of

[5]http://www.stsci.edu/scientific-community/software/drizzlepac.html

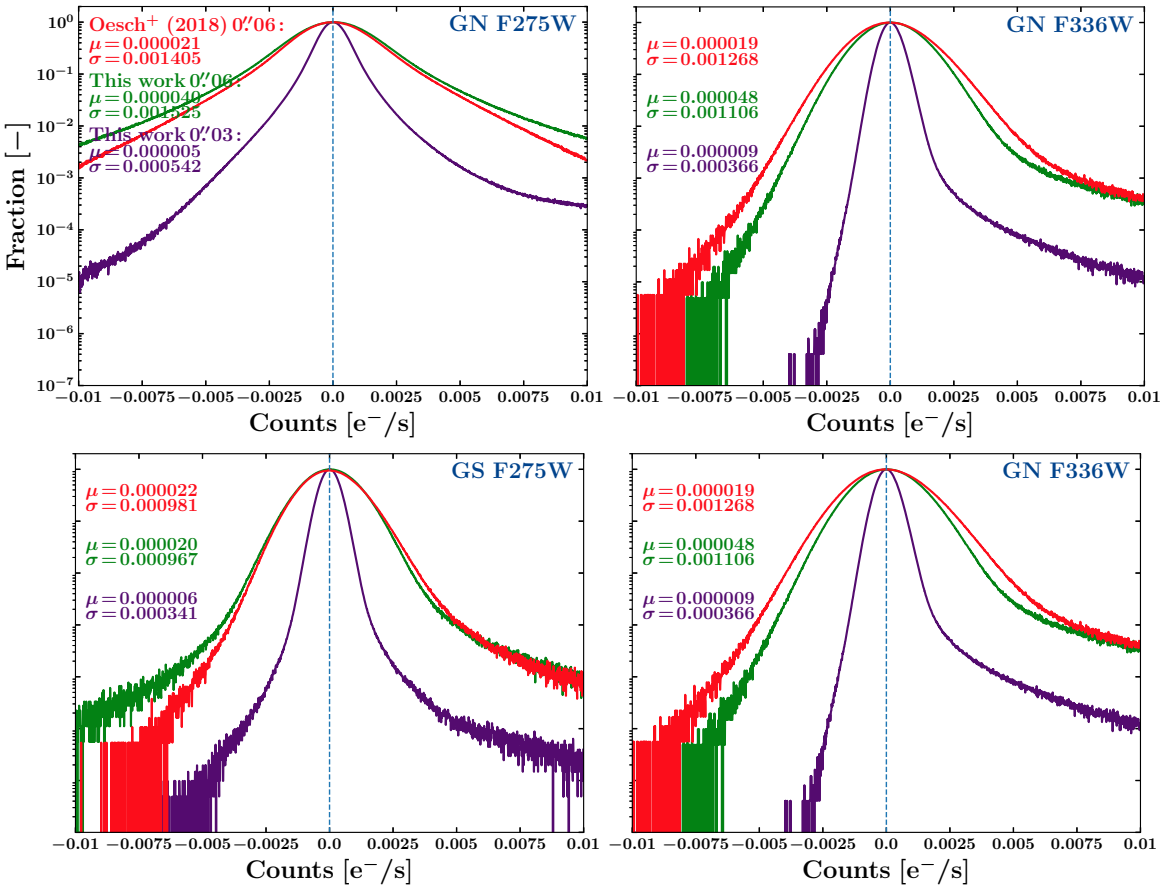


Figure 22. Pixel Histograms of the GOODS/HDUV Mosaics

Pixel histograms of the GOODS/HDUV mosaics from Oesch et al. (2018) and this work in the WFC3/UVIS F275W and F336W filters for the GOODS North (GN) and GOODS South (GS) fields. Our mosaics were sky-subtracted and drizzled to 0.″03 and 0.″06 pixels and the Oesch et al. (2018) data was drizzled to 0.″06 pixels. The mean ($\mu$) and dispersion ($\sigma$) of the histograms is indicated in each plot for all three versions of the GOODS/HDUV mosaics. The 0.″06 mosaic pixel-value distributions are generally consistent in the four cases, and our mosaics show modest improvement in $\mu$ and $\sigma$ in three. The 0.″03 mosaic pixel-value distributions have the smallest $\mu$ and $\sigma$ in all four images, due to its smaller pixels and resulting lower correlated noise.

observation to mitigate CTE degradation effects, such as the loss of faint flux in the raw image data during readout. Flashing the WFC3/UVIS CCDs with a diffuse light source *before* readout attempts to raise the overall sky-background level in order to fill charge traps in degraded pixels. This strategy can mitigate most effects from CTE

loss, but some faint flux is still lost, and the raw images suffer a penalty of increasing the overall background noise (Biretta and Baggett 2013).

Fig. 22 shows sky histograms of our versions of the GOODS/HDUV mosaics presented here, drizzled at 0.″03 and 0.″06 pixels for comparison to the public Oesch et al. (2018) mosaics drizzled at 0.″06 pixels. Our mosaics show modest improvements in the sky-subtraction level $\mu$ and the dispersion of the sky-background noise $\sigma$, with reduced values for $\mu$ and $\sigma$ in some cases. The 0.″03 pixel-value distributions show the most improvements in $\mu$ and $\sigma$, due to the smaller pixel size and associated lower pixel values and correlated noise between pixels (more details of noise scaling effects in drizzled images can be found in the Appendix of Casertano et al. 2000). The pixel distributions are generally consistent with Oesch et al. (2018), and the slight improvements in the 0.″06 images are likely due to differences in processing the raw *HST* frames and Astrodrizzle parameters used for constructing the mosaics. Our image processing steps before drizzling included subtracting a stacked dark current image from each frame to remove any thermal structure, more robust cosmic ray removal resulting in fewer bad pixels, and the removal of gradients caused by scattered background light. Each frame of the GOODS/HDUV mosaics was also CTE-corrected (Anderson and Bedin 2010) and aligned to the same pixel grid as the GOODS ACS/WFC F435W v2 image[6]. We drizzled the GOODS/HDUV data to a 0.″06 pixel scale for comparing to the public Oesch et al. (2018) mosaics, and to 0.″03 for our LyC studies (i.e., our LyC photometric analysis and $f_{\rm esc}$ constraints).

We chose to use the 0.″03 mosaics primarily because the smaller pixels increase the ability to resolve smaller features. This allowed for improved deblending of neighboring galaxies that can potentially contaminate LyC measurements with non-ionizing flux.

[6]https://archive.stsci.edu/prepds/goods/

Such compact galaxies can be detected at higher S/N ratios in optical ACS/WFC *HST* images and masked in the WFC3/UVIS mosaics. The smaller pixel scale also allowed us to determine more accurate statistics on the local sky-background noise due to the increased number of pixels in a given area of sky. This also improved subsequent photometric estimates of LyC, which we based on the total count rate in the drizzled mosaic image within a measurement aperture, the local sky-background dispersion, and the RMS-values of the pixels used for photometry within the aperture. The improvements in the photometric statistics also led to improvements in the accuracy of the constraints of subsequent MC analyses of the LyC escape fraction, which are directly proportional to this photometry.

## 5.3 Sample Selection and Characteristics

Our sample used for LyC studies at $2.26 \leq z \leq 4.3$ in the GOODS fields was selected from a compilation of spectroscopic surveys including the 3D-HST (Brammer et al. 2012; Momcheva et al. 2016), GMASS (Kurk et al. 2013), GOODS/FORS1 (S. Cristiani et al. 2000), GOODS/FORS2 (Vanzella et al. 2006; Vanzella et al. 2008), GOODS/VIMOS (Popesso et al. 2009; Balestra et al. 2010), K20 (Mignoli et al. 2005), MUSE-Wide (Herenz et al. 2017), SDSS DR14 (Abolfathi et al. 2018), TKRS (Wirth et al. 2004), TKRS2 (Wirth et al. 2015), VANDELS (Pentericci et al. 2018), VUDS (Tasca et al. 2017), VVDS (Le Fèvre et al. 2013), and the Szokoly et al. (2004), Reddy et al. (2006), Wuyts et al. (2009), Silverman et al. (2010), and Xue et al. (2016) surveys. This redshift range was selected so that the non-ionizing continuum ($\lambda_{\rm rest} > 912\,\text{Å}$) of a typical SFG SED would *not* exceed more that 0.5% of the total flux transmitted through the WFC3/UVIS filters. Including galaxies with redshifts lower than our

defined redshift-bin ranges from Table 1 would introduce more "red-leak" of non-ionizing flux into the filter, and in some cases become comparable or dominate the LyC flux by several times. Since LyC flux can be 3–4 mag fainter than the UVC (see Table 4 and Table 2), we used the same redshift bins in Table 1 to keep the percentage of red-leak to $\simeq 0.3\%$.

### 5.3.1 Sample Selection Criteria

We repeated the same selection process of ranking 265 individual objects with 330 spectra among 8 experts in spectroscopy this time, as described in §4.3.1. To summarize, the main objective was to select galaxies with spectra showing multiple, clearly visible emission/absorption lines that align with their expected positions at the stated redshift of the galaxy. These lines include the Lyman Break at 912Å, Lyman-$\alpha$ 1216Å, Si 2 1260Å, O 1 1304Å, C 2 1335Å, Si 4 1398Å, C 4 1549Å, and C 3] 1909Å, and when present, C 2] 2326Å, Fe 2 2344Å, and sometimes N 5 1240Å, Fe 2 2600Å, Mg 2 2798Å, O 2 3727Å, [Ne 3] 3869Å, He 2 4686Å, H 0$\beta$ 4861Å, or [O 3] 4959+5007Å. This was to ensure that all galaxies in our sample would not introduce any contaminating, non-ionizing flux into our LyC analyses from erroneous redshift determinations. This selection criterion does bias our sample towards predominantly luminous galaxies about as bright as $M^*$ at these redshifts (see Fig. 23), and also towards galaxies with blue SEDs (see Fig. 24–25). This should be taken into account when interpreting our subsequent LyC analyses on this sample.

Using the multi-band *HST* image data, we also ensured that each galaxy had no nearby, potentially contaminating neighbors, and that the flux of the galaxy under consideration showed a drop-out in the expected band. Of those 265 unique objects,

eight of us selected and agreed on 65 unique objects to have high quality spectra with accurate redshifts. Combining these with the 46 galaxies in the ERS field selected in Chapter 4 (also Smith et al. 2018), our total sample was increased to 111 galaxies with high quality spectra. This sample includes 17 galaxies *with* AGN and 94 galaxies *without* AGN. We identified AGN from typical (broad) emission lines in their spectra, for example Lyman-$\alpha$, N 5, Si 4, C 4, He 2, C 3], and Mg 2. We also checked the positions of our spectroscopic sample against *Chandra* 4 Ms and *Very Large Array* 1.4 GHz source catalogs to identify possible obscured/type II AGN using their radio/X-ray luminosities and photon indices (e.g., Xue et al. 2011; Fiore et al. 2012; Miller et al. 2013; Rangel et al. 2013; Xue et al. 2016).

After discovering one variable AGN amongst the 17 in our sample, the total sample was reduced to 110 galaxies after discarding this object from further study. This left 16 galaxies *with* AGN in our sample. We exclude this object from our sample because unstable flux measured across non-coeval surveys can lead to unreliable SED fits. More details for the signatures of variability are discussed in §5.3.3. Our subsequent analyses are based upon the remaining 110 galaxies in the ERS and GOODS/HDUV fields. We perform our LyC analyses on the sample of galaxies selected from each of these fields separately and combined to determine if differences in LyC results are due to differences in the mosaics themselves. We also perform analyses on the sample of galaxies *with* AGN *separately* from galaxies *without* AGN. We further sub-divide these galaxies by field, which results in 9 subsamples. These include galaxies *without* AGN in ERS, GOODS/HDUV, and both fields, which we refer to as "Total," galaxies *with* AGN in ERS, GOODS/HDUV, and Total, and *all* galaxies in our sample (referred to as "All"), again in ERS, GOODS/HDUV, and the Total sample.

In Fig. 23 we show the distributions of $m_{\rm AB}$ and $M_{\rm AB}$ sampled at $\lambda_{\rm rest} = 1500 \pm 100$Å

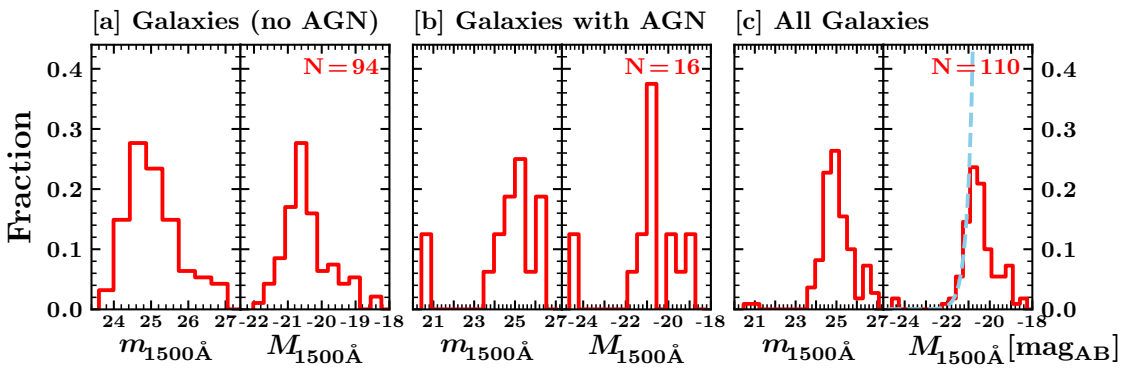


Figure 23. Apparent and Absolute Magnitude Distributions of Galaxies and AGN in the GOODS/HDUV+ERS Samples

[*a*] Absolute and apparent magnitude distributions at rest-frame 1500Å of the spectroscopic samples for galaxies *without* AGN. [*b*] Same, for galaxies *with* evidence of AGN activity in their spectra. [*c*] Same, for all galaxies in the sample. These magnitudes were derived from the observed SED fits at $\lambda_{\rm rest} = 1500 \pm 100 Å$, and therefore do not require k-corrections. The blue dashed curve indicates the slope of the luminosity function (LF) of $\langle z \rangle \simeq 2.97$ galaxies with $M^*_{\rm AB} \simeq$–20.86, and $\alpha \simeq 1.45$ dex/mag. The Total sample is approximately representative of the galaxy LF at their $\langle z \rangle$ to $M_{\rm AB} \leq$-21 mag and $m_{\rm AB} \leq 24.5$ mag.

for (a) galaxies without AGN signatures in the spectra, (b) galaxies *with* AGN, and (c) the Total sample. The rightmost panel shows that our sample generally follows the luminosity function of galaxies to $M_{\rm AB} \simeq -21$ mag ($m_{\rm AB} \simeq 24.5$ mag) at their average redshift of $\langle z \rangle \simeq 2.97$, with $M^* = -20.86$ mag and $\alpha = 1.45$ dex/mag. The Total sample is seen to be approximately representative of the galaxy LF at their average redshift to $M_{\rm AB} \leq$-21 mag and $m_{\rm AB} \leq 24.5$ mag. These histograms are also consistent with the ERS sample from Chapter 4 and Smith et al. (2018).

Two galaxies stand out in these histograms, both exceptionally bright galaxies with an AGN. One was found in the GOODS North field measured to be $m_{\rm AB} \simeq 20.4$ mag in all observed optical+IR *HST* bands, and the other was found in GOODS South measured at $m_{\rm AB} \simeq 21$ mag in the optical *HST* bands. The brighter QSO in GOODS North had a significant detection of LyC, while the other showed no detectable flux. We refer to this LyC-detected AGN at $z = 2.5920$ as QSO $J189.095582+62.257407$.

We detect the LyC emitted by this AGN in the F275W band, which allows negligible redleak into the filter (see Appendix B.1.1), at $m_{\rm AB}$=23.19±0.01 mag. Bianchi, Shiao, and Thilker (2017) also detect this source at $m_{\rm AB} = 23.77 \pm 0.08$ mag with the Galaxy Evolution Explorer (*GALEX*) Near-Ultraviolet (NUV) detector. Their *GALEX* Far-Ultraviolet (FUV) flux was determined to be $m_{\rm AB}$=26.02 mag with a signal-to-noise ratio S/N $\sim 1.8\sigma$, centered on the flux detected in the NUV, and thus not considered to be a significant FUV detection. We study this object and its LyC emission in more detail in §5.4.2.

Since this object has the brightest LyC detection by far, with S/N $\simeq$ 133, it will likely dominate any LyC analyses that include it. We therefore study this object individually, combined with all other AGN in GOODS/HDUV, and combined with All galaxies in the ERS, GOODS/HDUV, and the Total samples. We refer to the sample of AGN excluding QSO $J$189.095582+62.257407 as the AGN$^-$ sample, and likewise the sample of all objects excluding this QSO as the All$^-$ sample. Measurements performed on samples that include or exclude this object are useful for understanding cosmological averages of LyC emission for galaxies and AGN at their average redshifts, and the impact of very rare, unusually bright AGN.

### 5.3.2 SED Fitting

We fit SEDs to each of the 110 objects in our sample of galaxies and AGN with reliable spectroscopic redshifts. We incorporated all available *HST* WFC/ACS and WFC3/IR photometry longwards of Lyman-$\alpha$ at the fixed spectroscopic redshift of the galaxy. We used two versions of the FAST software (Kriek et al. 2009) written in C++ and IDL to fit both galaxies *with* and *without* AGN.

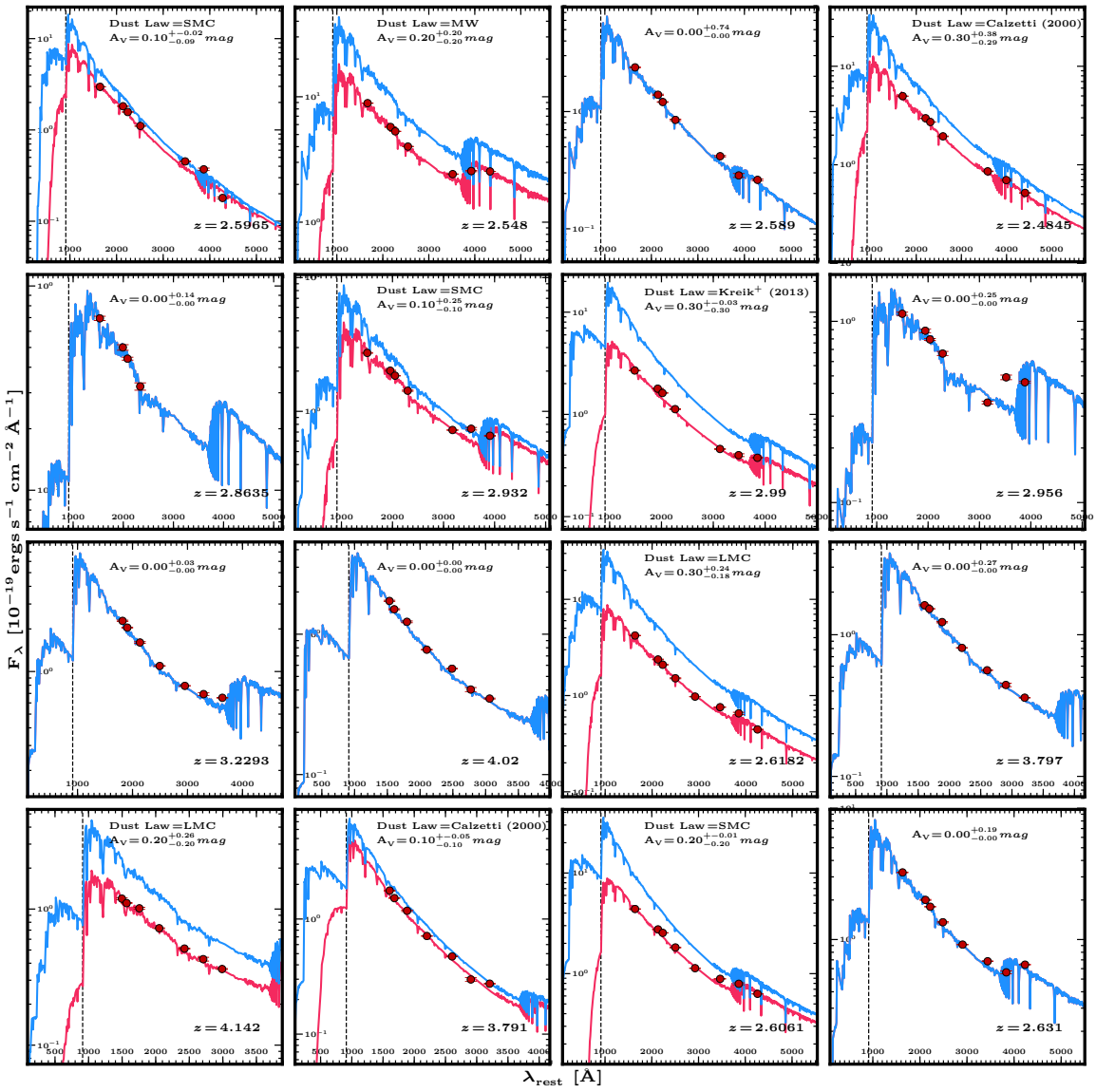


Figure 24. Example Best-fitting SEDs of the GOODS/HDUV and ERS Samples

Example set of best-fitting BC03 SEDs using FAST (red curve; Kriek et al. 2009) fit to observed *HST* ACS/WFC and WFC3/IR photometry (red filled circles), and the intrinsic BC03 SED with no extinction applied (blue). The best-fitting dust extinction law and $A_V$ is indicated for each SED. The spectroscopic redshift is shown, along with the corresponding Lyman limit plotted as a black vertical dashed line. The remaining SEDs are shown in Appendix A.1, and their age, mass, star-formation rate, and metallicity are listed in Table 7.

Due to our large sample of 94 galaxies *without* AGN, we used the C++ based

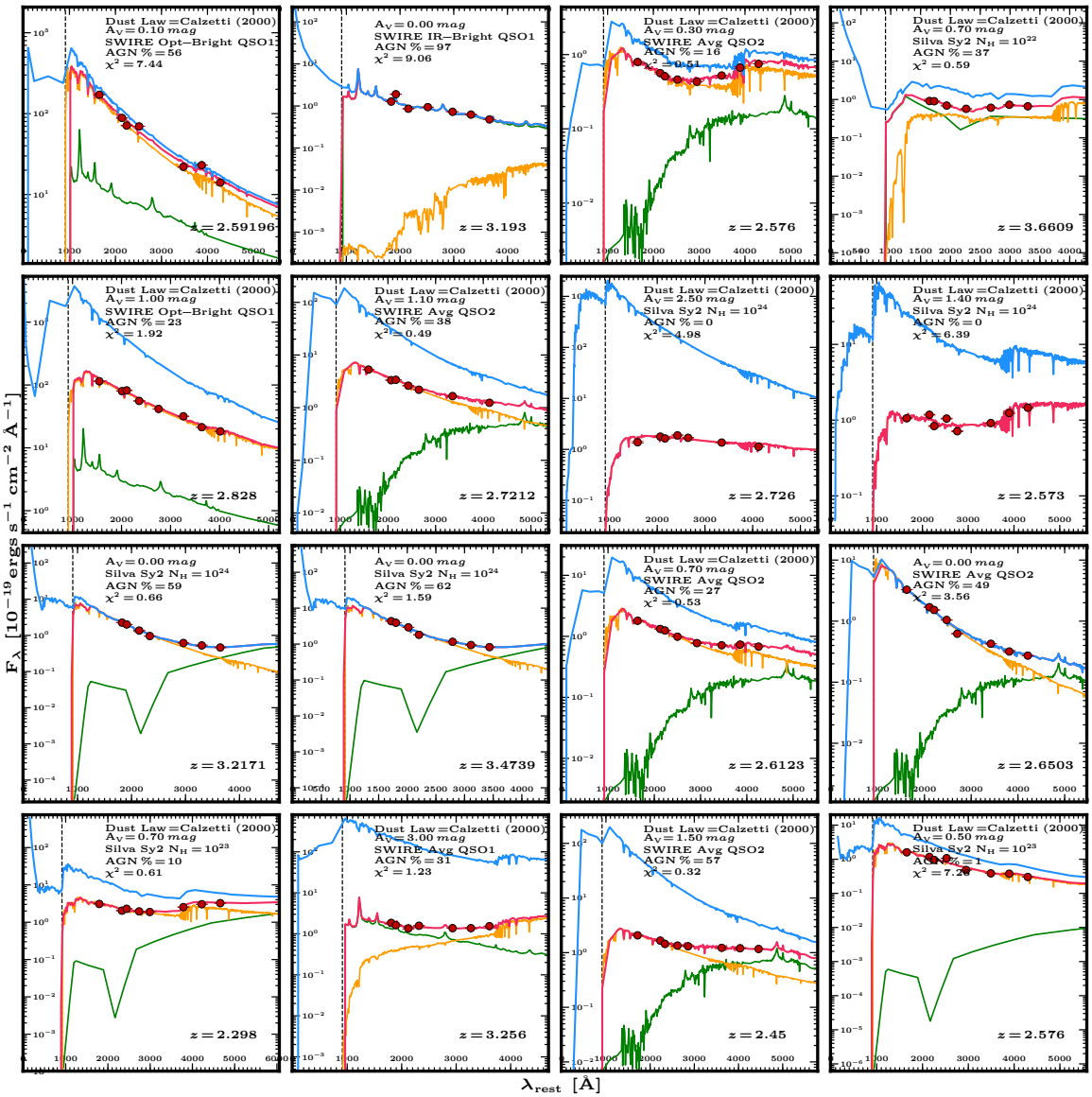


Figure 25. Best-fitting AGN SEDs of the GOODS/HDUV and ERS Samples

Best-fit two-component SEDs from FAST (red curve; Aird, Coil, and Georgakakis 2018). The best-fit SEDs (red curve) were fit to the plotted *HST* ACS/WFC and WFC3/IR photometry (red filled circles), and are the sum of a BC03 SED (orange) and the best-fit AGN template (green; Silva, Maiolino, and Granato 2004; Polletta et al. 2007). $N_H$ indicates the H 1 column density absorption applied to the AGN template. The blue line is the un-reddened SED, i.e., equivalent to the red line without the Calzetti et al. (2000) extinction law applied. The best-fit BC03 SED parameters for dust extinction law and $A_V$, AGN template, and AGN SED flux percentage at $\lambda_{rest}$=5000Å are indicated. Their age, mass, star-formation rate, and metallicity are listed in Table 7

FAST++ program[7] (Schreiber et al. 2018) for fitting their SEDs. FAST++ is advantageous for use with large galaxy samples as it has a faster runtime and supports multi-threading for fitting SEDs in parallel or for parallelizing MC simulations to estimate SED parameter uncertainties. For galaxies *with* AGN, we use the IDL version of FAST[8] (Kriek et al. 2009; Aird, Coil, and Georgakakis 2018) since this software can simultaneously fit two-component SEDs, i.e. a SED with a stellar and an AGN component. Example best-fitting SEDs are shown in figs. 24–25, where the best-fit is defined to be the SED fit with the lowest $\chi^2$ value between the available measured WFC/ACS and WFC3/IR photometry and the synthetic photometry calculated from the inner product of the corresponding filter curve and the SED.

We fit our galaxies *without* AGN to the synthetic stellar SEDs from the Bruzual and Charlot (2003) (BC03) program GALAXEV, and galaxies *with* AGN to BC03 *and* AGN templates from Silva, Maiolino, and Granato (2004) and Polletta et al. (2007). Their best-fitting BC03 parameters are listed in Table 7, and are also indicated in the example SEDs in Fig. 24. We also list the best-fitting AGN template and the percentage of flux produced by the AGN component at 5000Å in Fig. 25 and Table 7. The AGN template was allowed to vary from 0-100% of the total SED, in increments of 1%.

Histograms of the BC03 SED parameters $A_V$, mass, age, and star-formation rate (SFR) of our galaxies *with* and *without* AGN are shown in Fig. 26. These parameters are more representative of the dominant UV-bright stellar population since the SEDs were fit to the rest-frame UV and optical photometry, and not necessarily representative

[7]https://github.com/cschreib/fastpp

[8]https://github.com/jamesaird/FAST

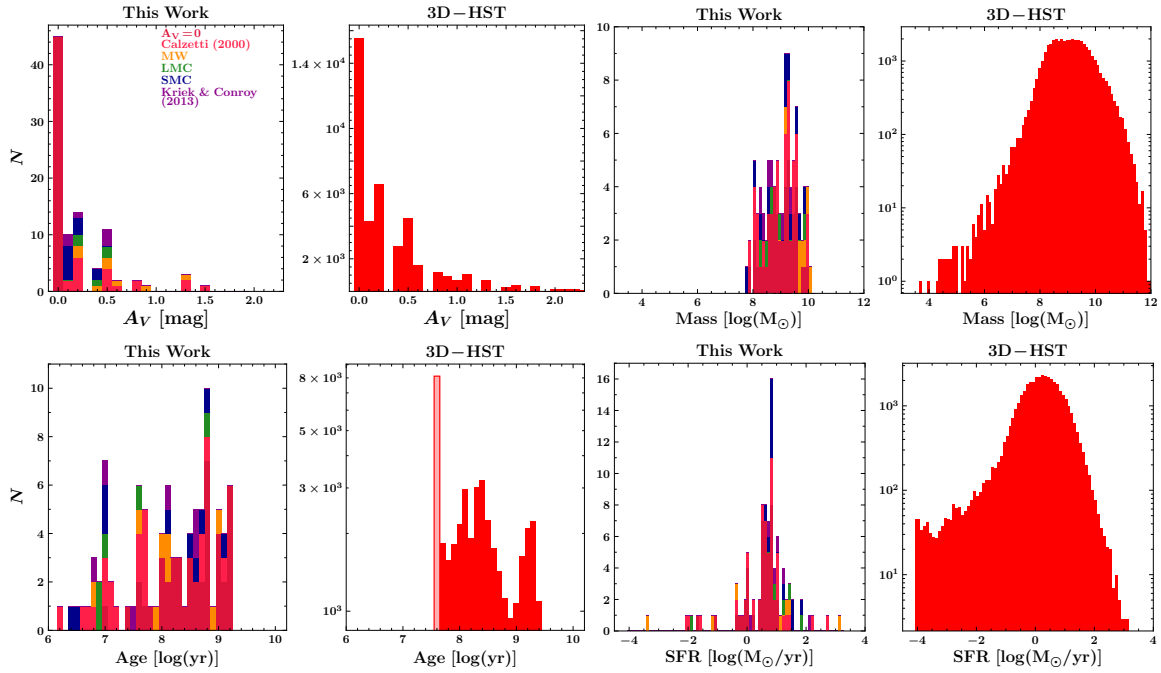


Figure 26. GOODS/HDUV+ERS SED Parameter Comparison with 3D-HST
Histograms of best-fitting BC03 SED parameters of the GOODS/HDUV+ERS galaxies *without* AGN that have reliable spectroscopic redshifts, compared to the SED parameters in the 3D-HST catalogs (Brammer et al. 2012; Momcheva et al. 2016) within the same redshift-range (right panel in each pair). The applied SED dust attenuation law is indicated in each of the left panels. The light-red bin in the 3D-HST age histogram indicates that the authors did not fit to SEDs below log(Age/yr)<7.6. The y-axis of the 3D-HST mass, age, and SFR histograms are in log-scale and all others are linear. The general shape of the histograms from our sample is similar to the much larger 3D-HST sample of ∼42,000 galaxies.

of the bulk of the stellar population. We also show the same parameters from SED fits performed by the 3D-HST Collaboration (Brammer et al. 2012; Skelton et al. 2014; Momcheva et al. 2016) for galaxies within the same redshift range $z = 2.26 - 4.3$. We use a minimum SFR of $10^{-4}\,M_\odot$/yr, and the 3D-HST survey restricted the age of their SEDs to $\geq 40$ Myr. We shade this 3D-HST age-bin light-red, since it is artificially large and encompasses many galaxies that may have younger ages than 40 Myr. In contrast to the 3D-HST study that only uses the Calzetti et al. (2000) dust-law, we fit all of our galaxies to SEDs attenuated by the Calzetti et al. (2000), Milky Way (MW),

Small Magellanic Cloud (SMC), Large Magellanic Cloud (LMC), and the average dust-law of Kriek and Conroy (2013) ($A_{1500}/A_V = 2.55$, 2.66, 4.37, 2.79, and 2.91, respectively). Since several of the AGN templates used in the SED fitting included a dusty torus component, we do not apply a secondary dust-attenuation law to the AGN template. The respective best-fitting dust-attenuation law of the BC03 SEDs are color coded in Fig. 26 in each $A_V$ bin. We also fit SEDs with solar ($Z$=0.02), subsolar ($Z$=0.004, 0.008), and supersolar ($Z$=0.05) metallicities. Despite the constraints in SED parameter space and increase in degrees of freedom in our fits, the profile of our parameter histograms are very similar to those from the 3D-HST SEDs.

We also compare the redshift $z$ vs. $A_V$ and $A_V$ vs. log(mass) of our galaxies to the 3D-HST sample in Fig. 27. This allows us to compare the distributions of these parameters to the 3D-HST sample, and how the parameters correlate with one another in the two samples. Our SED parameters are seen to reside in the densest regions of the 3D-HST parameter space. The few outliers in our sample are seen to be consistent with the less dense regions in the 3D-HST parameter space as well. From these plots, we conclude that our sample resembles the larger 3D-HST sample and is approximately representative of galaxies at these redshifts.

The rightmost panel in Fig. 27 compares the $\chi^2$ value of the SED fits using only a Calzetti et al. (2000) dust-law to the $\chi^2$ of SED fits using the MW, SMC, LMC, and Kriek and Conroy (2013) dust-laws. We plot the Calzetti et al. (2000) $\chi^2$ vs the difference in the best-fitting SED dust-law and the Calzetti et al. (2000) dust-law, normalized by the Calzetti et al. (2000) dust-law $\chi^2$. We find mostly marginal improvements in $\chi^2$ for most cases. However, we find a subset of galaxies with substantial improvements when the best-fitting SED used a SMC dust-law. We indicate these larger improvements using a dashed horizontal line. This suggests that

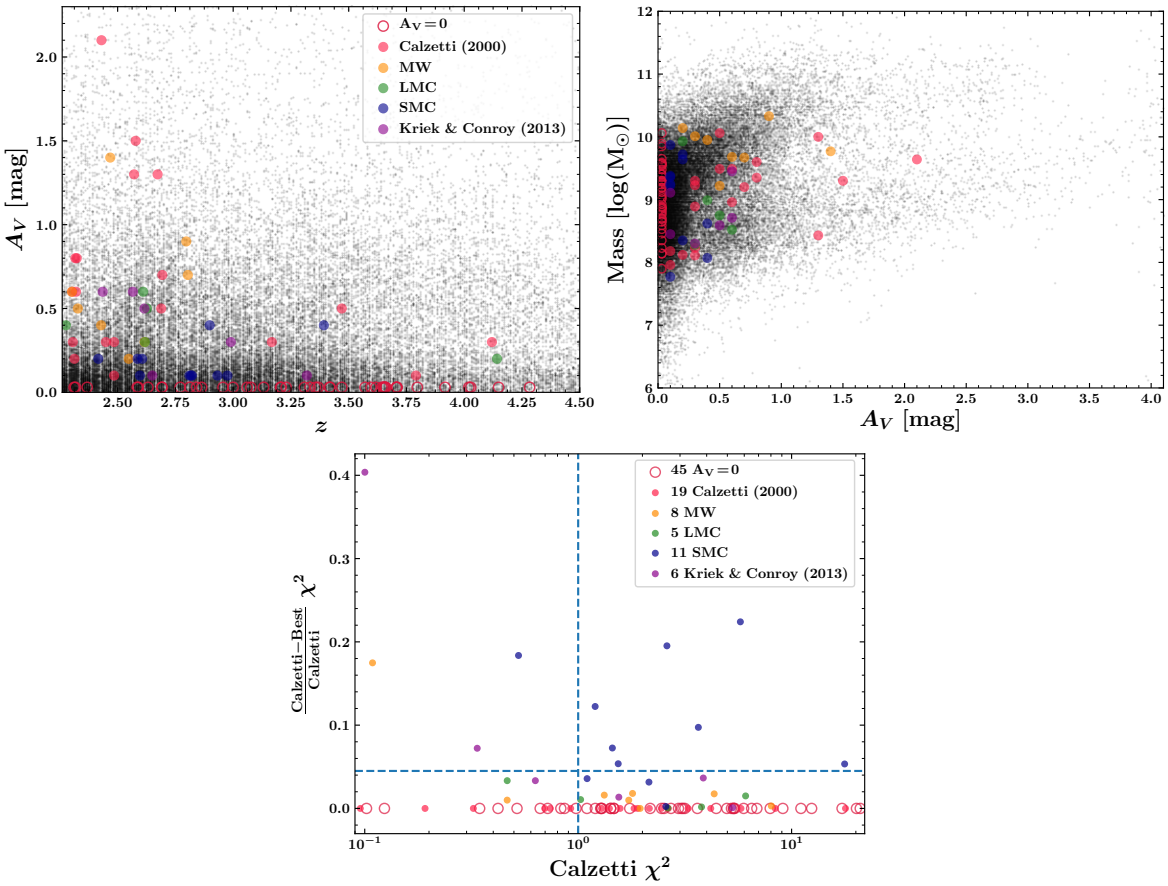


Figure 27. SED Parameter Space Comparison with 3D-HST

[Top Left]: $A_V$ vs. spectroscopic redshift of galaxies in our sample taken from their best-fitting BC03 SED, plotted according to their dust-attenuation law. The $A_V$ and redshift of galaxies in the 3D-HST catalog are plotted as black dots for comparison; [Top Right]: Same, but comparing the SED log(mass) vs. $A_V$; [Bottom Middle]: The normalized difference of the $\chi^2$ from the best-fit SED using the Calzetti et al. (2000) dust-attenuation law and the better fitting SED with a different dust-law vs. the original $\chi^2$ using a Calzetti et al. (2000) dust-attenuated SED, indicated by the color of the plotted dot. As indicated by the dashed lines, a subset of the SED fits using a SMC dust-attenuation law shows the greatest improvements in $\chi^2$ compared to fits using Calzetti et al. (2000).

simply using a Calzetti et al. (2000) dust-law may not result in the most accurate SED fits for this subsample.

### 5.3.3 AGN Variability

In order to maximize the accuracy of our SED fits and $f_{\rm esc}$ analyses that use them for modeling intrinsic LyC, we do not include any galaxies with AGN that display obvious signs of variability. For a galaxy with variable flux, the photometry measured from non-coeval data in different bands may not fit well to a SED based on a static, physically-based stellar or AGN model. The resulting fit may therefore not accurately predict flux in bands not used in the fitting, e.g. bands used for LyC photometry. Thus, variable AGN may provide a source of statistical error in $f_{\rm esc}$ analyses that include them, unless the variability is accounted for in the AGN SED model.

Our first indication of AGN variability in $J53.034441{-}27.698210$ [9] was the resulting poor SED-fit ($\chi^2$=30.9; see Fig. 28). The two-component SED fitting of FAST has an added degree of freedom compared to a single-component BC03 template, and the majority of AGN SED $\chi^2$-values were comparatively much lower, as seen in Fig. 25.

The optical WFC/ACS data, indicated by red-open circles in the left and right panels in Fig. 28, were taken by the GOODS and Type Ia SNe surveys (Riess et al. 2007) and collected from July 2002–Feb. 2003 in cycle 11 and from Apr. 2004–Feb. 2005 in cycles 12–13. The WFC3/IR and ACS/WFC F814W data, indicated in those panels by red-filled circles, were collected in Aug. 2010–Feb. 2012 by CANDELS. The wavelength captured by the CANDELS F814W photometry lies between the GOODS F775W and F850LP photometric data, and is seen to differ substantially from these earlier data points. The only other possibility to explain this offset might be a very bright emission line. However, no lines exist in this spectral region. $J53.034441-27.698210$

[9] Not to be confused with the LyC-bright QSO $J189.095582{+}62.257407$

was also found to be variable by Sarajedini et al. (2011) at a high significance. This AGN was one of 85 to be classified as varying, with their population statistics showing a 74% chance of variability in broad-line AGN and 15% in narrow-line AGN, and a 2% chance among all galaxies they surveyed. This roughly reflects our population as well, which was 1/17∼6% variable for our AGN sample and 1/111∼1% in our total sample of galaxies.

In the middle panel of Fig. 28, we show how much the non-coeval data differs from one another. Here, we interpolated the later epoch WFC3/IR CANDELS photometry (blue circles) using a spline function (blue curve), then determined the average multiplicative difference between this curve and the observed early epoch WFC/ACS data (red circles). We find that the optical ACS/WFC flux decreased by a factor of ∼2.1 over the timespan between two epochs of ∼5–6 years. The Sarajedini et al. (2011) study found variability in $J53.034441-27.698210$ over a span of ∼6 months, however, our findings may indicate variability of this object over a timespan of years as well. We scale the flux down by this factor and perform the same fitting on this object with the modified photometry to compare the two fits. We see a substantial improvement in the $\chi^2$ value by a factor of ∼60 down to $\chi^2$=0.51 as shown in the right panel of Fig. 28, which is consistent with our 16 other two-component SED fits listed in Table 7 and Fig. 25. Since this AGN clearly displays variability in its photometry, we exclude it from all subsequent analyses.

### 5.4 Quasar LyC Detections and Escape Fractions

Our sample contains a single object (QSO $J189.095582+62.257407$) with a highly significant individual detection of LyC at $m_{\rm AB}$=23.19±0.01 mag in WFC3/UVIS

F275W (S/N $\simeq$ 133) and with *GALEX* NUV at $m_{\rm AB}$=23.77$\pm$0.08 mag (S/N $\simeq$ 13). We therefore study QSO $J$189.095582+62.257407 in more detail in an attempt to infer why this AGN has such a bright LyC signal while other AGN in our sample show no significant LyC flux individually.

### 5.4.1 Quasar SED Fitting

To characterize this LyC bright QSO, we first determine a physically-based model that fits well to all the available observations, from the *Chandra* X-ray to the optical *HST* data. We selected the OPTXAGNF model (Done et al. 2012) since it incorporates the accretion disk black-body emission *and* the optically thin and optically thick Comptonization components of the inner disk and SMBH corona. The Comptonization component of the OPTXAGNF model accounts for AGN SED flux from $\lambda\simeq$1–900 Å, which is important for modeling the intrinsic AGN LyC. We use the XSpec software (Arnaud 1996) to fit our observed data to this model, a method also used by Lusso et al. (2015) to characterize their stack of $\langle z\rangle$=2.4 AGN *HST* WFC3/UVIS grism spectra. There are several input parameters in this model corresponding to physical properties of the AGN[10], some of which we determined from available archival and published data and were held fixed during fitting. The first parameter we determined was the SMBH mass using the observed C 4 line from the SDSS BOSS spectrum (Dawson et al. 2013) released in DR14. We used the method from Coatman et al. (2016) to estimate this mass by first fitting the continuum-subtracted C 4 line to a 6th order Gauss-Hermite polynomial (van der Marel and Franx 1993; Cappellari et al. 2002),

[10]See https://heasarc.gsfc.nasa.gov/xanadu/xspec/manual/ for a full list and description of all parameters in the model.

which allows for more robust estimations of the FWHM of the line. We then estimated the line's blueshift to correct the FWHM. This corrected C 4 FWHM corresponded to a SMBH mass of $\log(\frac{M_{SMBH}}{M_\odot}) \simeq 8.37$, a mass similar to the SMBH mass of the Andromeda galaxy (Bender et al. 2005).

Using this mass, we calculated the Eddington luminosity of this AGN to be $L_{Edd} \simeq 2.9 \times 10^{46}$ erg/s. We then computed the bolometric luminosity to be $L_{bol} \simeq 1.5 \times 10^{46}$ erg/s using the methodology of Brotherton, Shang, and Runnoe (2012) at $\lambda_{rest} = 1450$ Å. These parameters result in an Eddington ratio of $\lambda_{Edd} \simeq 0.5$, which, along with the SMBH mass, is typical of X-ray selected AGN (see, e.g., Lusso et al. 2012). We infer an accretion rate of $\dot{M} \simeq 3.4\, M_\odot$/yr from $L_{bol}$, assuming a matter-radiation conversion efficiency of $\epsilon = 8\%$ (Marconi et al. 2004). If this accretion rate represents the average accretion, the SMBH would have been accreting for $\sim 7.3 \times 10^7$ years. We use the X-ray spectral index $\Gamma \simeq 1.687$ from the Xue et al. (2016) catalog as input. The measured soft (0.5–2.0 keV) and hard (2–7 keV) X-ray fluxes from Xue et al. (2016) are plotted as magenta filled circles in the left panel of Fig. 29 for reference.

Our full XSpec model used a Tuebingen-Boulder ISM absorption model (Wilms, Allen, and McCray 2000) to account for the X-ray absorption by the MW ISM, and five additional Gaussian profiles for fitting bright emission lines in the spectra. After inputting the GOODS North hydrogen column density of $1.6 \times 10^{20}$ cm$^{-22}$ (Stark et al. 1992), our calculated mass, comoving distance, and $\log(L_{Edd})$, we simultaneously fit the SDSS BOSS spectrum and the *Chandra* spectrum plotted in the left panel of Fig. 29. Before fitting, we first corrected the BOSS spectrum for aperture losses using the measured *HST* ACS flux shown in Fig. 29. The *Chandra* X-ray spectrum, background spectrum, and response curve were then extracted from the Chandra Deep

Field North (CDFN; Brandt et al. 2001) data taken with the Advanced CCD Imaging Spectrometer (**Garmire2003**) using the CIAO software (Fruscione et al. 2006) tool `specextract`[11]. Because the CDFN data[12] was taken at two different roll angles in Feb. 2000–Feb. 2002, we reprojected the CDFN event data onto a common tangent-plane using CIAO tool `reproject_events`. We then fit these spectra using the Levenberg-Marquardt method (Levenberg 1944; Marquardt 1963) to simultaneously minimize a combination of the $\chi^2$ and "cstat" (Cash 1979) statistics for the BOSS optical and *Chandra* X-ray spectra, respectively.

The resulting model is shown as the blue curve in Fig. 29, which was scaled by the response curve extracted from the combined CDFN ACIS data. The model also returned values for the dimensionless blackhole spin parameter $a_\star = 0.57$, coronal radius $r_{cor} = 5.3\,r_s$ where $r_s$ is the Schwarzschild radius, and electron temperature $T_e \simeq 1.4{\times}10^5\,\mathrm{K}$. We use this model to compute the $f_{\rm esc}$ values from the measured WFC3/UVIS F275W and *GALEX* NUV flux.

### 5.4.2 Quasar LyC Escape Fractions from *GALEX* and WFC3/UVIS

We estimate the LyC escape fraction for all QSO $J189.095582{+}62.257407$ LyC measurements using the method outlined in §3.3. In summary, we modeled the intrinsic LyC flux from QSO $J189.095582{+}62.257407$ by attenuating our best-fitting *dust-free* SED with the simulated line-of-sight intergalactic medium (IGM) transmission curves of Inoue et al. (2014), then taking the inner-product of the attenuated SED and its

[11] http://cxc.harvard.edu/ciao/threads/pointlike/

[12] For specific datasets, see: http://cxc.harvard.edu/cda/DefSet/CDFN1.html and http://cxc.harvard.edu/cda/DefSet/CDFN2.html

respective LyC filter curve and *HST* optical throughput. This calculation gives us the modeled, intrinsic LyC flux in this band, i.e.,

$$\mathrm{f}_{\mathrm{LyC,mod}} = \frac{\int F_{\mathrm{SED}}(\nu)\mathcal{T}_{\mathrm{IGM}}(\nu,z)T_{\mathrm{obs}}^{\mathrm{LyC}}(\nu)\frac{d\nu}{\nu}}{\int T_{\mathrm{obs}}^{\mathrm{LyC}}(\nu)\frac{d\nu}{\nu}} \tag{5.1}$$

where $F_{\mathrm{SED}}(\nu)$ is the dust-free SED, $\mathcal{T}_{\mathrm{IGM}}(\nu,z)$ is the IGM transmission at redshift $z$, and $T_{\mathrm{obs}}^{\mathrm{LyC}}(\nu)$ is the filter transmission+optical throughput used for the LyC observation. Components of the *total* system throughput used in this model include the reflectivity of the telescope mirrors, quantum efficiency of the detectors, obscuration by the secondary mirrors, and transmission of the filter used for observation (Morrissey et al. 2007; Kalirai et al. 2009). The integrated product of the dust-free SED, IGM transmission, and filter curve+optical throughput simulates the effective intrinsically produced LyC from stellar and AGN components, and does not account for ISM effects captured by the $f_{\mathrm{esc}}$ parameter.

We perform $10^3$ MC simulations of the LyC $f_{\mathrm{esc}}$ parameter using $10^4$ line-of-sight IGM attenuation curves from the IGM absorber distribution-based Inoue et al. (2014) code. These attenuation curves were used to generate distributions of $10^4$ *modeled* intrinsic LyC flux values as described above. Using the LyC flux measured with SExtractor (Bertin and Arnouts 1996) from our GOODS North F275W mosaic described in §5.2 and the *GALEX* NUV flux from Bianchi, Shiao, and Thilker (2017), we modeled the *observed* LyC fluxes ($\mathrm{f}_{\mathrm{LyC,obs}}$) as Gaussian Random Variables (GRV) in our MC runs with the mean of the Gaussian $\mu$ representing the measured flux values and the standard deviation of the Gaussian $\sigma$ representing the uncertainty of the measurements. We generated $10^4$ random values in these Gaussian distributions, which we used to estimate the $f_{\mathrm{esc}}$ values shown in Fig. 29. To generate our LyC $f_{\mathrm{esc}}$ distribution, we simply calculate the ratio of the observed LyC flux distribution to the modeled LyC flux distribution, i.e. $f_{\mathrm{esc}} = f_{\mathrm{LyC},obs}/f_{\mathrm{LyC},mod}$, where $f_{\mathrm{LyC},obs}$ and

$f_{\rm LyC,mod}$ are the flux values in arbitrary linear units. We perform the $f_{\rm esc}$ calculation $10^3$ times on the generated $f_{\rm LyC,obs}$ and $f_{\rm LyC,mod}$ distributions in a MC fashion to get more robust statistics of the probability distributions of the $f_{\rm esc}$ values. The $10^3$ $f_{\rm esc}$ distributions for the measured *HST* WFC3/UVIS F275W and *GALEX* NUV fluxes are shown in Fig. 29 as the group of transparent light and dark violet curves, respectively.

We then merged the $10^3$ $f_{\rm esc}$ distributions into one, and binned the data using equally-spaced logarithmic bins to optimize the resolution of $f_{\rm esc}$ in each decade between $10^{-4}$ and 1. We normalized the merged distribution by the sum of the bins to generate the probability mass function (PMF) of $f_{\rm esc}$. We also constrained the distributions to physical values of $f_{\rm esc}$, i.e., all values above 100% were redrawn during the MC simulations until all $f_{\rm esc}$ values were within 0–100%. The middle and right panels of Fig. 29 show the resulting distributions. The lighter shaded regions are individual MC realizations of $f_{\rm esc}$ and the darker lines are the full distribution of the merged simulated data. We extracted our statistics from these curves, taking the peak of the curve as the most-likely (ML) value of highest probability, the $\pm1\sigma$ values as the two points on the curve that have equal probability *and* where the integrated area under the ML value down to these points is equal to 84%. The expected value of $f_{\rm esc}$ (E[Val]), or the probability-weighted average $f_{\rm esc}$, i.e., $\mathrm{E}[f_{\rm esc}] = \sum_i p_i f_{{\rm esc},i}$ is shown as well. For QSO *J*189.095582+62.257407, the *GALEX* NUV data, which captures LyC at $\lambda_{\rm rest} \simeq 490$–$780$Å, we find the ML $f_{\rm esc}$ value to be $f_{\rm esc}^{\rm NUV} \simeq 30^{+22}_{-5}\%$ and $\mathrm{E}[f_{\rm esc}^{\rm NUV}] \simeq 45\%$. For the WFC3/UVIS F275W data, effectively covering LyC from $\lambda_{\rm rest} \sim 680$–$850$Å, we find the ML $f_{\rm esc}$ value to be $f_{\rm esc}^{\rm F275W} \simeq 28^{+20}_{-4}\%$ and $\mathrm{E}[f_{\rm esc}^{\rm F275W}] \simeq 43\%$. These values show a consistent escape fraction of LyC for this AGN to within their errors. These results are discussed in more detail in §5.6.1.

## 5.5 Stacking Results

### 5.5.1 LyC Image Stacks and Photometry

Since LyC measurements have been historically very faint or resulted in non-detections (see references in §2.3), we perform the weighted-sum based "stacking" algorithm described in §3.1, taking "subimage" cutouts of galaxies from the WFC3/UVIS mosaic observed in the filter that corresponds to the galaxy's LyC, then co-adding them all onto the same 151×151 pix (4.″53×4.″53) grid. Before stacking, we again created $\chi^2$ images of each galaxy in our sample, which were comprised of the *HST* WFC3/UVIS F225W, F275W, F336W, WFC/ACS F435W, F606W, F814W, F850LP, WFC3/IR F098M, F105W, F125W, F140W, and F160W images when available. We then ran SExtractor on the $\chi^2$ images to detect any faint objects in the *HST* images that may potentially add contaminating, non-ionizing flux to our stacked image. Using the resulting segmentation map, we masked all neighboring and foreground objects in each subimage, except the galaxy from our sample in the center of the subimage. We improved our SExtractor object detection and deblending parameters from those used in Smith et al. (2018) to minimize the unintentional masking of image noise during stacking, which accounts for the differences between the photometry tabulated here and what is listed in Table 2.

These stacks contain galaxies with redshift ranges listed in Table 1, corresponding to $2.26 \leq z < 2.47$ for F225W, $2.47 \leq z < 3.08$ for F275W, and $3.08 \leq z < 4.35$ for F336W. These redshift bins reduced the inclusion of non-ionizing flux into our LyC

photometry down to ∼0.3% of the total flux within the filter, based on our average SED. We created stacks for each subsample as described in §5.3, which can be seen in figs. 30–32. These include galaxies *without* AGN (Gal), *all* galaxies *with* AGN (AGN), all galaxies *with* AGN excluding QSO *J*189.095582+62.257407 (AGN$^-$), *all* galaxies with and without AGN (All), and all galaxies with and without AGN excluding QSO *J*189.095582+62.257407 (All$^-$). We created these stacks for the GOODS/HDUV, ERS, and the GOODS/HDUV+ERS (Total) fields. This corresponds to the 30 stacks shown in figs. 30–32, along with their corresponding UVC stacks that were created in the same way as the LyC stacks, but using the corresponding rest-frame non-ionizing UVC images ($\lambda_{\rm rest} \gtrsim 1400\,$Å) indicated in those figures. The number of galaxies in each stack is also indicated.

The results of our photometric analyses on the stacks shown in figs. 30–32 are listed in Table 4. We performed our photometry in the same manner as outlined in §3.2 using a Gaussian additive noise model. We performed matched-aperture photometry with SExtractor on our LyC stacks shown in figs. 30–32 using the corresponding UVC stack as the detection image in all cases. To generate a representative distribution of the LyC flux, we iterated through all $10^4$ 2-dimensional slices along the z-dimension of our flux datacubes and measured the flux within the UVC aperture. This provided $10^4$ possible flux values that were based on the WFC3/UVIS LyC subimage, the sky variance in the LyC subimage, and the RMS in the pixels from detector noise.

To generate the values listed in Table 4, we took the mean of our flux distribution and the $16^{\rm th}$ and $84^{\rm th}$ percentile for the -1$\sigma$ and +1$\sigma$ uncertainty bounds, respectively. The ratio of the mean and the uncertainty was used to calculate the S/N ratios. When this S/N was less than one, we list the 84th percentile from the distribution as the 1$\sigma$ upper limit to the LyC flux, and denote the S/N by $(1.0)^\dagger$ in Table 4.

From the Total sample stacks, we find that the galaxies *with* AGN at $z$=2.573–2.828 have the *only* $>5\sigma$ detection, while other AGN samples have LyC S/N measurements around, or below, $2\sigma$. All stacks of galaxies *without* AGN show only upper limits, with S/N<1. Although there is visible flux in the GOODS/HDUV and Total F336W stacks for galaxies *without* AGN, the significance is only $\sim 1\sigma$. Thus, we cannot yet rule out the possibility this signal is spurious noise rather than real LyC flux.

### 5.5.2 Composite Stacks of the Total Sample

To visualize the LyC flux from the various types of galaxies in our sample, we stack all LyC subimages from the various fields and WFC3/UVIS filters onto the same grid using the methodology outlined in §5.5.1. The resulting stacks are shown in Fig. 33 and the number of galaxy subimages they contain are indicated. While stacking the subimages, we also scaled the pixel values in all subimages in the stack such that all images had a common AB-zeropoint magnitude equal to that of the F275W filter (ZP = 24.04 mag) for the LyC stacks, and the UVC subimages were scaled to match the F606W zeropoint (ZP = 26.51 mag).

We performed a similar photometric analysis on these LyC stacks described in §5.5.1 to assess the S/N of the central flux measured within the blue UVC-detected apertures of Fig. 33. For the Total sample of galaxies *without* AGN, we find low levels of LyC flux (likely due to dilution from multiple stacked non-detections) with S/N$\sim$1. From all galaxies *with* AGN, excluding QSO $J$189.095582+62.257407, we find a S/N $\sim 1.8$, and for the Total sample of all galaxies *with* AGN we measure a S/N $\simeq 10.3$, which is dominated by the bright LyC flux from QSO $J$189.095582+62.257407. In the AGN stacks, we observe possible indications of LyC flux extending outside of the central

UVC aperture, though the S/N cannot distinguish this fluctuation from sky noise. Combining the LyC flux from all galaxies (aside from QSO $J189.095582{+}62.257407$), we find a S/N $\simeq 1.3$ (again likely diluted from the non-detections in the galaxies *without* AGN), while the LyC flux from all 110 galaxies from our sample amounts to a S/N $\simeq 3.1$.

On average, we find that the flux from AGN outshines the galaxies *without* AGN by a factor of $\sim$10, and excluding QSO $J189.095582{+}62.257407$ the AGN still outshine galaxies *without* AGN by $\sim$2 times. The low S/N of these measurements makes these ratios highly uncertain, and only larger samples of spectroscopically verified high-redshift galaxies can reduce these uncertainties. Larger samples will also increase the chances of observing sources of brighter LyC flux, e.g., the bright QSO $J189.095582{+}62.257407$ found among the 16 AGN in our sample. Increasing the sample size may also increase the chance of including more rare sources of LyC emission, e.g., lower mass, star-bursting galaxies with extreme [O 3] emission (e.g., Fletcher et al. 2019).

### 5.5.3 Stacked LyC Escape Fractions

To estimate the LyC $f_{\rm esc}$ from our subsamples discussed in §5.3, we apply the same statistical methodology outlined in §3.3 described in §5.4.2. The $f_{\rm esc}$ distributions shown in figs. 34–36 are generated by taking the ratio of the photometric distributions measured in §5.5.1 to the distribution of intrinsic LyC flux derived from the best-fitting SED, the IGM attenuation models at the galaxy's respective redshift, and the WFC3/UVIS throughput curve corresponding to the filter used for the LyC observation. These distributions are useful for *inferring* the most likely, *sample-averaged* $f_{\rm esc}$ values

of a given photometric dataset, even if the photometry is highly uncertain, or shows a non-detection of LyC. We calculate the intrinsic LyC flux distributions in the same way as in §5.5.1 for each galaxy in a stack, then we perform a weighted average of all these distributions using the average weight map value used in the image stacks. This was to ensure that the same proportions of flux from the sets of galaxies included in the image stack used for photometry matched the modeled intrinsic LyC flux.

We generated $10^3$ of these distributions (shaded regions in figs. 34–36) and merged them into one (solid lines in figs. 34–36) after constraining each individual $f_{\rm esc}$ distribution to physical values between 0–100%. The $f_{\rm esc}$ values produced by the simulations were histogrammed using equally-spaced logarithmic bins and normalized by the sum of the bins to produce the $f_{\rm esc}$ PMF. The y-axis of these PMFs thus represents the relative probabilities of the $f_{\rm esc}$ values in the x-axis. We extracted the ML, $\pm1\sigma$ uncertainties, and the E[$f_{\rm esc}$] statistics from the merged distributions and plotted each in figs. 34–36. We quote the ML and its $\pm1\sigma$ values in Table 6 as the estimated $f_{\rm esc}$, since it has the highest probability of representing the global-average $\langle f_{\rm esc} \rangle$ of galaxies at their average redshifts. Each subsample and its redshift-range is color-coded and indicated in the figure, along with the type of galaxy and the field the analysis was performed on.

Several of these distributions display large asymmetries and some show bimodalities. These asymmetries are caused mostly by the variations in IGM transmission along different lines-of-sight, and bimodalities result from some sources in the stacks dominating the modeled intrinsic LyC flux. This creates a peak of higher $f_{\rm LyC,\mathit{mod}}$ values amongst the (on average) fainter modeled LyC flux as in, e.g., the light-blue

curve of the left panel of Fig. 35. However, with more sources added to the stacks, the distributions begin to become more Gaussian-like (see, e.g., the right panel of Fig. 36).

Because of the uncertain flux estimation in the GOODS/HDUV F336W stack, whether spurious or not, our $f_{\rm esc}$ peak is located near 100%, indicating that the current IGM+SED models do not properly account for flux this bright at $\langle z \rangle \simeq 3.5$. If this flux is indeed real LyC emission, these high $f_{\rm esc}$ values may be a result of anisotropic LyC escape mechanisms (Nakajima and Ouchi 2014; Paardekooper, Khochfar, and Dalla Vecchia 2015) or stochastic periods of star-formation (Kimm et al. 2017; Trebitsch et al. 2017) in these galaxies, allowing for higher $f_{\rm esc}$ than average during the life-time of these galaxies. Starbursts composed of star-formation with multiple waves of SNe relatively close in time can sustain the higher pressure in the ISM needed to drive galactic winds (Veilleux, Cecil, and Bland-Hawthorn 2005).

Due to the random nature in selecting IGM attenuation sight-lines for our $f_{\rm esc}$ simulations, another possibility is that the IGM models underestimate the frequency of regions of lower IGM H 1 column densities. A realistic, highly inhomogeneous large-scale structure may provide more clear sight-lines in the IGM on scales smaller than a galactic halo (e.g., D'Aloisio, McQuinn, and Trac 2015; Keating, Puchwein, and Haehnelt 2018; Bosman et al. 2018). Our MC analysis redraws simulated $f_{\rm esc}$ values above 100% in an attempt to reject these over-estimated column densities, which causes the observed pile up of $f_{\rm esc}$ values near 100% as a result of this constraint. These $f_{\rm esc}$ values are listed in column 11 of Table 6 as upper limits, and the LyC fluxes they are based on are listed in column 5 of Table 4.

## 5.6 Discussion

### 5.6.1 AGN LyC Detections

We surveyed an area of $\sim 175\,\mathrm{arcmin}^2$ from $z$=2.26–4.35, corresponding to a comoving volume of $\sim 1.3\times10^6\,\mathrm{Mpc}^3$, and uncovered a single LyC detection from QSO $J$189.095582+62.257407. This space density of $\simeq 8\times10^{-7}\,\mathrm{Mpc}^{-3}$ is consistent with the space densities of very luminous ($\mathrm{L_X} = 10^{45}$–$10^{47}\,\mathrm{erg\,s^{-1}}$) Compton-thin AGN at $z$=2.59 (Ueda et al. 2014). The X-ray luminosity of this AGN is $\mathrm{L_X} = 10^{44.9}\,\mathrm{erg\,s^{-1}}$ and has an intrinsic $N_H$=0.6±0.1×$10^{23}\,\mathrm{cm}^{-2}$ (Laird et al. 2006). Therefore, this AGN falls within the parameter space of the observed space density trends for AGN with similar properties. This may allude to the existence of more LyC-bright AGN than have so far not been detected.

In §5.4.1, we describe the SED model fitting and resulting parameters of the best-fit, which were revealed to be typical of AGN at $z \sim 2.6$. Since this object does not exhibit exotic or extreme AGN accretion parameters, likely causes of the bright LyC emission may be that the escape path of LyC is advantageously aligned to the line-of-sight of the observation, the neutral density of the IGM along this line-of-sight was especially lower than the average, and/or that the LyC production and subsequent escape from AGN is delayed compared to the optical, unobscured portions of the spectrum.

This first hypothesis has support from the bright flux detected in all other *HST* bands. The UVC band for this AGN (WFC/ACS F606W) is measured at $m_{\mathrm{AB}} \simeq 20.42\,\mathrm{mag}$, and the WFC3/IR bands F125W, F140W, and F160W measure $m_{\mathrm{AB}} \simeq 20.25\,\mathrm{mag}$. The $M_{\mathrm{AB}_{1500\text{Å}}}$ is $\sim$–24.44 mag, which falls well outside of the

luminosity function of galaxies at these redshifts. It is possible that the luminous nature of this AGN can be due to collimation of the AGN jet or outflow clearing a direct path for LyC escape into the line-of-sight of the observation alone.

This single line-of-sight may also have much lower neutral column density than predicted by IGM simulations, which is also hinted at by very high (though highly uncertain) $f_{\rm esc}$ values found at $z \gtrsim 3$. Other LyC studies in the protocluster SSA22 (Micheva, Iwata, and Inoue 2017; Fletcher et al. 2019) have suggested a spatially varying H 1 density in the IGM or CGM in the field in order to explain the LyC non-detections in their sample. Spatial variations of H 1 in the IGM may also be present in the GOODS North field, allowing for higher $f_{\rm esc}$ values in under-dense IGM regions.

The possibility of a time-lag effect between lower energy continuum and high energy, ionizing photons has been observed in the production of hard X-rays, where multiple inverse Compton scattering (ICS) events of thermally produced optical and UV photons from the accretion disk gain energy by scattering off of relativistic electrons in AGN coronae (e.g., Fabian et al. 2009; Kara et al. 2016). Furthermore, LyC from AGN has also been found to be produced via this same ICS mechanism at wavelengths of $\lambda_{\rm rest} \lesssim 1000\,\text{Å}$ (e.g., Zheng et al. 1997; Telfer et al. 2002; Shull, Stevans, and Danforth 2012; Stevans et al. 2014). Thus, the discrepancy between the bright LyC escape measured from this AGN and its ordinary SMBH/accretion parameters inferred from the unobscured continuum may be explained by a time lag between the production and subsequent escape of the LyC photons, where the time lag accumulates from multiple LyC-producing ICS events.

### 5.6.2 Galaxy $f_{\rm esc}$ Evolution

The results of our $f_{\rm esc}$ simulations are tabulated in Table 6, and the $f_{\rm esc}$ results for all galaxies *without* AGN in our Total sample are plotted in Fig. 37 as filled purple circles. We plot our results along with $f_{\rm esc}$ parameters inferred by other authors in the literature as light blue filled circles. Upper limits are shown as downward light blue arrows.

Compared to Table 3, the observed trend in $f_{\rm esc}$ is more pronounced, mainly due to the higher implied $f_{\rm esc}$ values at $\langle z\rangle \simeq 3.6$. These high $f_{\rm esc}$ values at $z \gtrsim 3$ are dominated by two uncertainties in the data used to construct the PMF for the $f_{\rm esc}$ ranges. The first is high uncertainty in the LyC photometry of the $\langle z\rangle \simeq 3.6$ F336W stack. Table 4 shows that galaxies *without* AGN at $\langle z\rangle \simeq 3.6$ consistently have the faintest upper limits of all the stacks without AGN. The F336W Gal stack from the ERS field in Fig. 31 shows no clear flux, though the same stack from the GOODS/HDUV field shows very faint but possibly spurious flux in fig 30. We cannot rule out the possibility that this flux is a background fluctuation due to its low S/N ratio. The GOODS/HDUV F336W flux from galaxies is still visible in the Total Gal F336W stack, though diluted from the combination with the ERS non-detections.

The addition of the ERS also improved the S/N by a factor of ∼3.7, caused by a reduction in the background noise by a factor of ∼4.3. The S/N of the Total stacked flux for galaxies *without* AGN is ∼0.9, with a formal $m_{\rm AB}$ =29.4±1.2. The possibility that the marginal fluxes of galaxies *without* AGN in F336W seen in figs. 30–32 are real cannot yet be ruled out. Only adding more galaxy LyC subimages to the stack can improve the uncertainties in the photometry, which is shown to still increase the

S/N of the photometry in Table 4, i.e., we have not yet reached the noise floor in the stack.

The second cause of the high $f_{\rm esc}$ values at $\langle z\rangle \simeq 3.6$ is a result of the high frequency of sight-lines with low LyC transmission through the IGM, where the average transmission value of photons passing through the F336W filter is $\mathcal{T} \simeq 4.4\%$. Furthermore, the percentage of the sight-lines with $\mathcal{T} \leq 1\%$ in the MC simulations of Inoue et al. (2014) is $\sim$68.7%, and $\sim 99.9\%$ of the lines-of-sight have transmission values below $\mathcal{T} < 50\%$. These low transmission values cause our inferred $f_{\rm esc}$ to increase, due to the inverse proportionality of the modeled IGM transmission values with $f_{\rm esc}$. The combination of a large percentage of low IGM transmission, and therefore low modeled LyC flux, with low S/N LyC photometry that varies widely allows the implied $f_{\rm esc}$ values to grow very large, even well above 100% if not constrained.

If the fluxes measured through the F336W filter for the $\langle z\rangle \simeq 3.6$ stacks are taken at face value, this may allude to an IGM that has more variation on smaller scales in their lines-of-sight than sampled here. As mentioned in §5.6.1, similar studies in over-dense regions find LyC detections in only a portion of their homogeneous samples with no obvious reason for the dichotomy. One reason suggested is that IGM and CGM H 1 is spatially varying in the field, allowing for some lines-of-sight to have much lower LyC attenuation than the bulk in the field. More variation in the IGM transmission at smaller scales may be needed in future transmission models in order to explain the LyC detections and non-detections at $z > 3$. Only adding more galaxies from spectroscopic samples to improve the S/N of LyC stacks will be able to address this question.

The current stacked $f_{\rm esc}$ value at $\langle z\rangle \simeq 3.6$ is not well constrained, and the highest likelihood value from the $f_{\rm esc}$ MC simulations result in extreme values of $f_{\rm esc} \sim 100\%$.

Until these values can be better constrained, they hint at $f_{\rm esc}$ values that may be increasing more significantly at $z > 3$. The $f_{\rm esc}$ values from the literature shows similar trends, with $f_{\rm esc}$ increasing at $z \gtrsim 3$. This is consistent with the scenario expressed in §4.5.2, where galaxies undergo more accretion and mergers until the peak of the star-formation history at $z \simeq 2$, which causes $f_{\rm esc}$ to decrease during this epoch due to the accumulated higher H 1 densities. The feedback from AGN accretion and SNe heat reduces the SFR, thereby reducing the formation of OB stars that could clear channels for LyC escape after going supernova, which consequently reduces $f_{\rm esc}$ further at lower redshift. Declining AGN and star-formation feedback at $z \lesssim 2$ can also reduce $f_{\rm esc}$, as these mechanisms can also assist in carving out paths in the ISM for LyC to escape.

### 5.6.3 The $f_{\rm esc}$ of Galaxies with AGN

It is now believed that AGN LyC $f_{\rm esc}$ values are expected to be less than 100% (Stefano Cristiani et al. 2016; Micheva, Iwata, and Inoue 2017; Grazian et al. 2018), rather than $\sim 100\%$ as assumed in earlier models (Giallongo et al. 2015; Madau and Haardt 2015). The production of LyC in galaxies by AGN is mostly well understood from theoretical models and observations of AGN spectra (e.g., Telfer et al. 2002; Done et al. 2012; Kubota and Done 2018; P. O. Petrucci et al. 2018). In short, the accretion disk emits like a blackbody when the heat energy produced by accretion thermalizes (Shakura and Sunyaev 1973), with a disk temperature increasing radially towards the SMBH. The spectrum produced by such a model (e.g., Mitsuda et al. 1984) does not reproduce the observed UV spectrum of AGN, which requires a broken power-law to fit (e.g., Zheng et al. 1997; Davis, Woo, and Blaes 2007; Lusso et al. 2015). The

same warm Comptonization component that can explain the soft X-ray excess seen in some AGN spectra (e.g., Kaufman, Blaes, and Hirose 2017; P. O. Petrucci et al. 2018) could also extend across the H 1 absorption gap and connect the UV broken power law to the soft X-ray component (e.g., Mehdipour et al. 2011; Mehdipour et al. 2015). In this model, a portion of the accretion energy is not thermalized in the disk, but rather is emitted from a warm ($kT_e \simeq 0.1$–$1\,\mathrm{keV}$), optically thick region ($\tau \simeq 10$–$25$; see, e.g., P.-O. Petrucci et al. 2013; Middei et al. 2018; Porquet et al. 2018). UV photons down to $\sim 1000\,\text{Å}$ can also be produced by the same region (Kubota and Done 2018). However, the physical origin of this emission is still not well understood phenomenologically (Crummy et al. 2006; Walton et al. 2013; Różańska et al. 2015; P. O. Petrucci et al. 2018).

The determinants of LyC photon absorption or escape are more unclear. As mentioned in §2.3, it is likely that the well studied, nearby, LyC emitting galaxies Tol 1247-232 (Leitherer et al. 2016), Haro 11 (Leitet et al. 2011), and J0921+4509 (Borthakur et al. 2014) have AGN exhibited by their X-ray detections (Kaaret et al. 2017, Prestwich et al. 2015, Jia et al. 2011, respectively). Grazian et al. (2018) suggest that these galaxies likely have measurable $f_{\mathrm{esc}}$ values due to their AGN component creating a mechanical force to drive away nearby ISM, thereby increasing $f_{\mathrm{esc}}$ from the AGN and surrounding stars. Giallongo et al. (2012) propose that AGN outflow shock-waves triggered by accelerating disk outflows can clear enough paths in the ISM surrounding the AGN to increase the $f_{\mathrm{esc}}$ parameter (see Menci et al. 2008, Dashyan et al. 2018, Penny et al. 2018, and Menci et al. 2019 for models and observations supporting this scenario). Here, the LyC can escape along a narrow bi-polar cone unobscured, and paths outside this cone will have a reduced $f_{\mathrm{esc}}$. In

these highly ionized cones however, dust extinction becomes the dominant source of LyC absorption, which is later re-emitted as IR radiation (e.g., Netzer 2013).

Dust can survive in the environment of the inner accretion disk only in regions where the effective temperature of the disk is below the dust-sublimation temperature (e.g., Czerny and Hryniewicz, K. 2011). In these regions, pressure acting on the grains from the ambient radiation field can raise dusty clumps above the disk surface. As the clumps rise, they become exposed to the central radiation source and clumps get pushed in a radial direction into sublimation regions, and the dust can evaporate.

Bipolar outflows in the narrow-line region (NLR) of AGN have been observed from UV and optical (integral field) spectroscopy (Müller-Sánchez et al. 2011; Harrison et al. 2014; Karouzos, Woo, and Bae 2016; Woo, Son, and Bae 2017), which can potentially clear some emission line emitting clouds that absorb LyC. Liu et al. (2013) were able to detect dense, optically thick, dusty gas clouds embedded in hot, low-density winds in the NLR transitioning into optically thin clouds at a distance of $\simeq 7.0 \pm 2\,\mathrm{kpc}$ away from the SMBH, caused by declining radiation pressure on the cloud. As the clouds flow outwards with the AGN wind, the binding external radiation pressure declines, allowing the clouds to expand from their own internal gas pressure. These dense, pressure bounded clouds in the NLR produce emission lines on a thin, outer shell. Their main source of ionization is likely from the AGN continuum, both thermal and non-thermal. The transition from optically thick to optically thin would have have a direct effect on the $f_{\mathrm{esc}}$ of AGN as well, and thus outflows may play a dominant role in determining the $f_{\mathrm{esc}}$ from their resulting dynamics.

The $f_{\mathrm{esc}}$ values for AGN shown in Fig. 37 (dark and light green points) are relatively consistent across all redshift ranges, showing a possible slight downward trend from $z \simeq 4$–2. However, the mean values of these data points are consistent with

a constant $f_{\rm esc}$ to within their error bars. This may indicate that optically selected AGN with broad emission lines may modulate their $f_{\rm esc}$ with the same mechanisms. With AGN accretion rates on the rise at $z\sim3$–4 and peaking near $z\sim2$–3 (e.g., Fanidakis et al. 2012; Ueda 2015), the $f_{\rm esc}$ parameter could show decline due to this effect at lower redshift ($z\lesssim2$), mainly due to the reduction in powerful shocks from outflows and winds. AGN disks are fed by cold-accretion from the nearby ISM and inflows onto dark-matter halos, as well as advection dominated hot-accretion. These accretion modes are generally associated with outflows, AGN winds, and/or jets (Ho 2002; Chatterjee et al. 2011; Yuan and Narayan 2014), thus decreasing accretion rates should also accompany a reduction in outflow luminosity. This may provide a mechanism for an $f_{\rm esc}$ parameter for AGN that declines with cosmic time, as AGN accretion and outflow energy evolves with redshift. To determine the evolution $f_{\rm esc}$ of AGN with redshift more precisely, additional data at lower and higher redshifts are needed, and the intrinsic nature of the AGN must also be better understood through more detailed theoretical modeling.

## 5.7 Conclusions

We analyzed and quantified the LyC radiation escaping from a survey of 110 spectroscopically verified galaxies in the GOODS North, GOODS South, and the ERS fields in three WFC3/UVIS filters where LyC can be observed at $z\simeq2.26$–4.35. We independently drizzled the GOODS/HDUV data together with the available CANDELS and UVUDF WFC3/UVIS data and found good agreement with the Oesch et al. (2018) publicly released data, with modest improvement in sky background and depth. The ERS UV images are more shallow than the GOODS/HDUV mosaics.

Nevertheless, since the ERS data were taken shortly after WFC3 was installed onto *HST*, losses in sensitivity from CTE degradation are not a concern for this dataset.

We studied several subsamples of these galaxies based on their redshift, observed field, and spectroscopic evidence of (weak) AGN activity. We studied our single LyC detected galaxy QSO $J189.095582{+}62.257407$ in more detail alone, as well as including it in stacks, and combined the various subsamples to determine any biases from the imaging data and to study the LyC escaping from galaxies with and without AGN.

We first stacked extracted sub-images centered on galaxies from the GOODS North and South and ERS mosaics in their appropriate LyC filters, and quantified the LyC in the stack using a MC approach. We removed all potential neighboring and foreground galaxies during the stacking process using $\chi^2$ images of all available *HST* data for each galaxy. We performed SED fitting on all the galaxies and used these to estimate their intrinsic LyC flux, then estimated the $f_{\rm esc}$ parameter of the stacked galaxies, as well as for QSO $J189.095582{+}62.257407$, using the modeled intrinsic flux and the MC simulated IGM transmission curves of Inoue et al. (2014) for various lines-of-sight. We find the following main results:

(1) Our quantitative analysis of the LyC flux from the stacks of galaxies at $z \simeq 2.3$–$4.3$ is tabulated in Table 4. We find upper limits to the total LyC flux of $M_{\rm AB}{\simeq}M^*$ galaxies *without* AGN at $\langle z \rangle \simeq 2.36$, 2.73, and 3.61 to be $m_{\rm AB} > 27.5$, $> 28.5$, and $> 28.6$ mag, respectively. For galaxies *with* (weak) AGN, we find fluxes of $m_{\rm AB} \gtrsim 27.6$, $\simeq 26.15$, and $\simeq 27.73$ mag at $\langle z \rangle \simeq 2.37$, 2.65, and 3.36, where the first flux is a $1\sigma$ upper limit and the other two measurements have S/N $\simeq 13.1$ and $\sim 1.8$, respectively.

(2) Our only LyC detection was measured from the galaxy QSO $J189.095582{+}62.257407$, detected at $m_{\rm AB}{=}23.19{\pm}0.01$ mag in the WFC3/UVIS F275W filter and with *GALEX* NUV at $m_{\rm AB} = 23.77{\pm}0.08$ mag, with S/N $\simeq 133$ and 13, respectively. Our modeling

suggest that this AGN is not especially extreme in its SMBH parameters, and neither in its accretion characteristics. This implies that the LyC escaping from this AGN may instead be advantageously directed toward the line-of-sight of observation, that the LyC production and subsequent escape took much longer than the time-scale of the peak of its accretion, or that the particular line-of-sight of this AGN had a very low H 1 IGM column density.

(3) The combined LyC emission averaged over the three WFC3/UVIS filters implies that the AGN dominate the LyC production in the epoch of $\langle z \rangle \simeq 2.3$–$4.3$ by a factor of $\sim$10. The overall LyC flux distribution of AGN may also be non-centrally concentrated, though additional data are needed to make this feature more visible above the deeper image noise. If real, this could suggest a radial dependence of $f_{\rm esc}$ based on axial direction of the AGN LyC escape, ISM porosity, and/or scattering of the LyC photons from ionized regions in the galaxy.

(4) Our best-fit BC03 SED models fit to *HST* continuum observations longwards of Lyman-$\alpha$ suggest that the observed LyC fluxes for galaxies *without* AGN correspond to *average* LyC escape fraction of $f_{\rm esc} \simeq 3^{+23}_{-2}\%$ at $\langle z \rangle \simeq 2.4$, $f_{\rm esc} \simeq 13^{+26}_{-9}\%$ at $\langle z \rangle \simeq 2.7$, and $f_{\rm esc} \lesssim 99.5^{+0.5}_{-2.1}\%$ at $\langle z \rangle \simeq 3.6$. This large $f_{\rm esc}$ at $\langle z \rangle \simeq 3.6$ is due to a combination of two effects. The first is caused by the low S/N LyC flux in the image stack, which cannot be ruled out as spurious, and the second is implied by the majority of very low IGM line-of-sight transmission in simulations, with 91% of the transmission values lying at $\mathcal{T} < 20\%$, and 68% having transmission values $\mathcal{T} < 1\%$. This effect is seen to be mitigated in the AGN $f_{\rm esc}$ simulations, which had higher LyC S/N values than galaxies *without* AGN. We measure *average* LyC $f_{\rm esc}$ values of all galaxies *with* AGN to be $f_{\rm esc} \simeq 8^{+42}_{-5}\%$ at $\langle z \rangle \simeq 2.4$, $f_{\rm esc} \simeq 3^{+37}_{-0.6}\%$ at $\langle z \rangle \simeq 2.7$, and $f_{\rm esc} \simeq 27^{+67}_{-9}\%$ at $\langle z \rangle \simeq 3.4$.

(5) Our uncertainty ranges on $f_{\rm esc}$ for galaxies *without* AGN remain large, though

they are generally consistent and improved from the ERS study in Smith et al. (2018). This data reaffirms the observed increasing trend of $f_{\rm esc}$ with redshift from §4.5.2. For our galaxies, the steepest decline in $f_{\rm esc}$ appears to occur near $z \simeq 2$ from $f_{\rm esc}$<26% to $\lesssim$2%, which correlates with the peak of the cosmic star-formation history within an interval of $\pm 1$ Gyr (Madau and Dickinson 2014).

For galaxies *with* AGN, their stacked $f_{\rm esc}$ appears to remain roughly constant with redshift within their error ranges, though shows hints of decline within their $1\sigma$ limits, dropping from <94% to <26% from $z \simeq 3.6$ to $z \simeq 2.4$, respectively. The AGN $f_{\rm esc}$ trend can also be compared to trends in AGN luminosity functions and space density, which steadily peak near $z \simeq 2$ and decrease at $z < 2$ (Ueda 2015). The evolution of these parameters may be linked by the decrease in AGN fuel from major mergers and/or accretion (Fabian 2012) and star-formation feedback through cosmic time. The evolution in these parameters may be correlated to changing dynamics of galaxies, where infall/merger driven star-formation at $2 \lesssim z \lesssim 6$ transitions to a more passively evolving universe by giant galaxies at $z \lesssim 1$–2. This may result in gas and dust rapidly accumulating in the disks and nuclei of forming galaxies, combined with a SNe rate that has progressively less impact on clearing gas/dust in galaxies that are steadily growing in mass with cosmic time. The accumulating H 1 gas and decreasing SFR may have caused $f_{\rm esc}$ to decrease over a relatively narrow interval of cosmic time from $2 < z < 3$ ($\sim$1 Gyr), as feedback effects inhibit the formation of new massive stars that could clear LyC escape paths. When AGN outflows began to increase after the peak in the cosmic star-formation history at $z \simeq 2$, their outflows may have cleared enough paths in the ISM of host galaxies to enhance the fraction of escaping LyC radiation produced by massive stars and from the accretion disk, resulting in AGN beginning to dominate the ionizing background at $z \lesssim 2$–3.

(6) If the trend in $f_{\rm esc}$ for galaxies *without* AGN continues beyond $z{\sim}5$, these galaxies may have had a sufficient LyC escape fraction to reionize the IGM by $z \gtrsim 6$. Since AGN outshine galactic-stellar LyC by a factor of $\sim$10, combined with their consistently larger $f_{\rm esc}$ seen in this work and in the literature, AGN likely contributed a significant portion of the ionizing photons needed to finish *and* maintain cosmic reionization at $z \lesssim 3$.

More data on LyC $f_{\rm esc}$ are essential to reducing the uncertainties in these trends. The current sample of deep, high quality spectra are still very small, and larger spectroscopic samples taken with the *JWST* FGS/NIRISS grisms and with NIRSpec (Gardner et al. 2006) could improve uncertainties in LyC stacks. Additional deep imaging of wider *HST* fields in the UV would also supplement these studies, e.g., in the COSMOS and EGS fields where large spectroscopic samples at high redshift already exist. The future release of the Ultraviolet Imaging of the Cosmic Assembly Near-infrared Deep Extragalactic Legacy Survey Fields (UVCANDELS; PI: Teplitz) data will provide additional LyC sources larger than our current sample size, and further increase the sensitivity to faint LyC in the GOODS fields. Additional theoretical and observational work is needed to improve the statistics of IGM line-of-sight transmission curves, in order to explain the observed larger $f_{\rm esc}$ values at $z \simeq 3$ in this study and others in the literature.

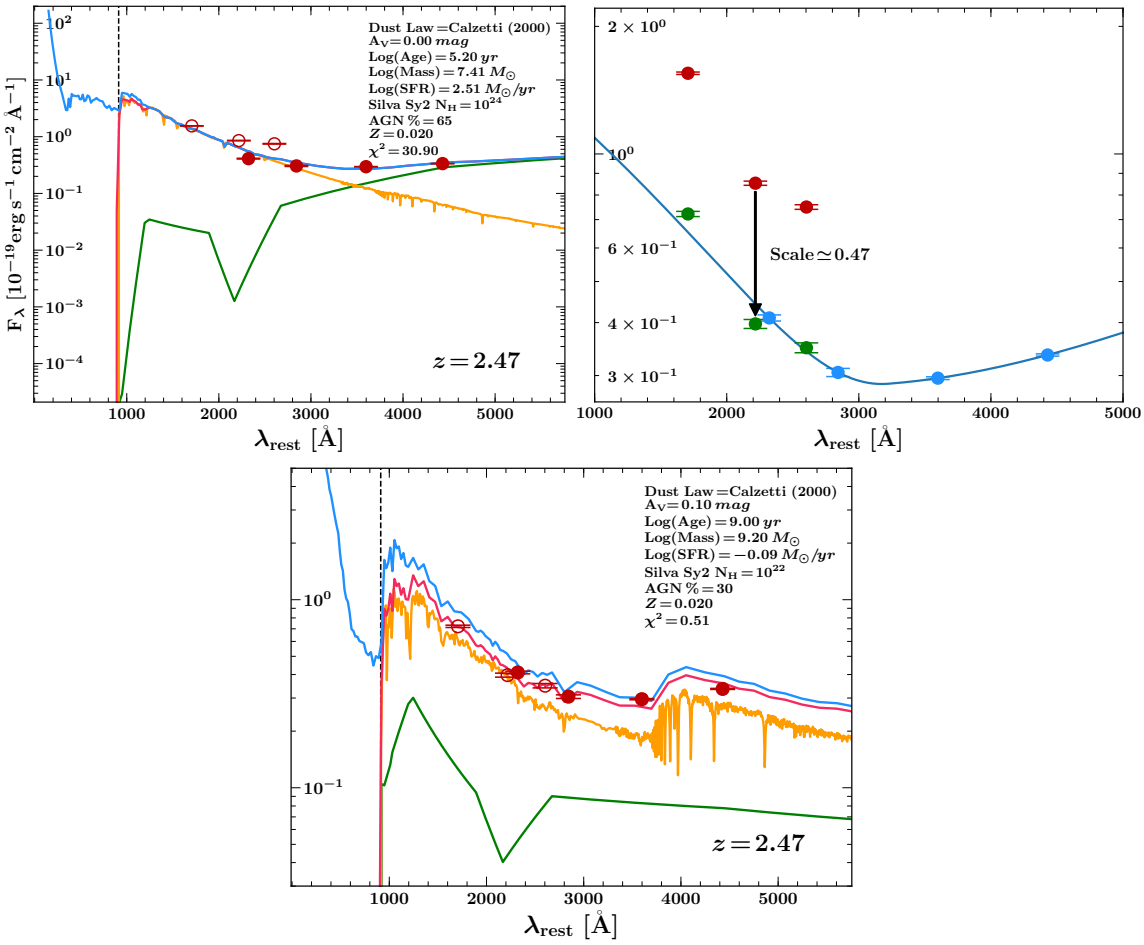


Figure 28. A Variable AGN in the ERS Sample

[Top Left]: Best-fit two-component SED from FAST (red curve; Aird, Coil, and Georgakakis 2018) for variable AGN $J53.034441-27.698210$. The best-fit SEDs (red curves) were fit to the plotted *HST* ACS/WFC and WFC3/IR photometry (red open circles indicate the WFC/ACS data observed during the 2002-2005 epoch, the red filled circles indicate the WFC3/IR data from the 2010-2012 epoch). The red curve is the sum of the best-fit BC03 SED (orange) and the best-fit AGN template (green; Silva, Maiolino, and Granato 2004; Polletta et al. 2007). The best-fit BC03 SED parameters (dust extinction law, $A_V$, age, mass, star-formation rate, and metallicity), AGN template, and AGN SED flux percents at 5000Å are indicated. The difference in observation epoch appears to have provided enough time for $J53.034441-27.698210$ to display variability. [Top Right]: The observed flux of $J53.034441-27.698210$ taken in the early epoch (2002-2005; blue points) and the cubic-spline interpolation through those points (solid blue line), compared to the observed flux taken in the later epoch (2010-2012; red points). The red points were scaled down by a factor of ∼0.47 to match the interpolated data as closely as possible (green points). [Bottom Middle]: The best-fit two-component SED from FAST after scaling the later-epoch flux. The $\chi^2$ is seen to improve significantly, and the observed changes in SED parameters can be compared between the two fits.

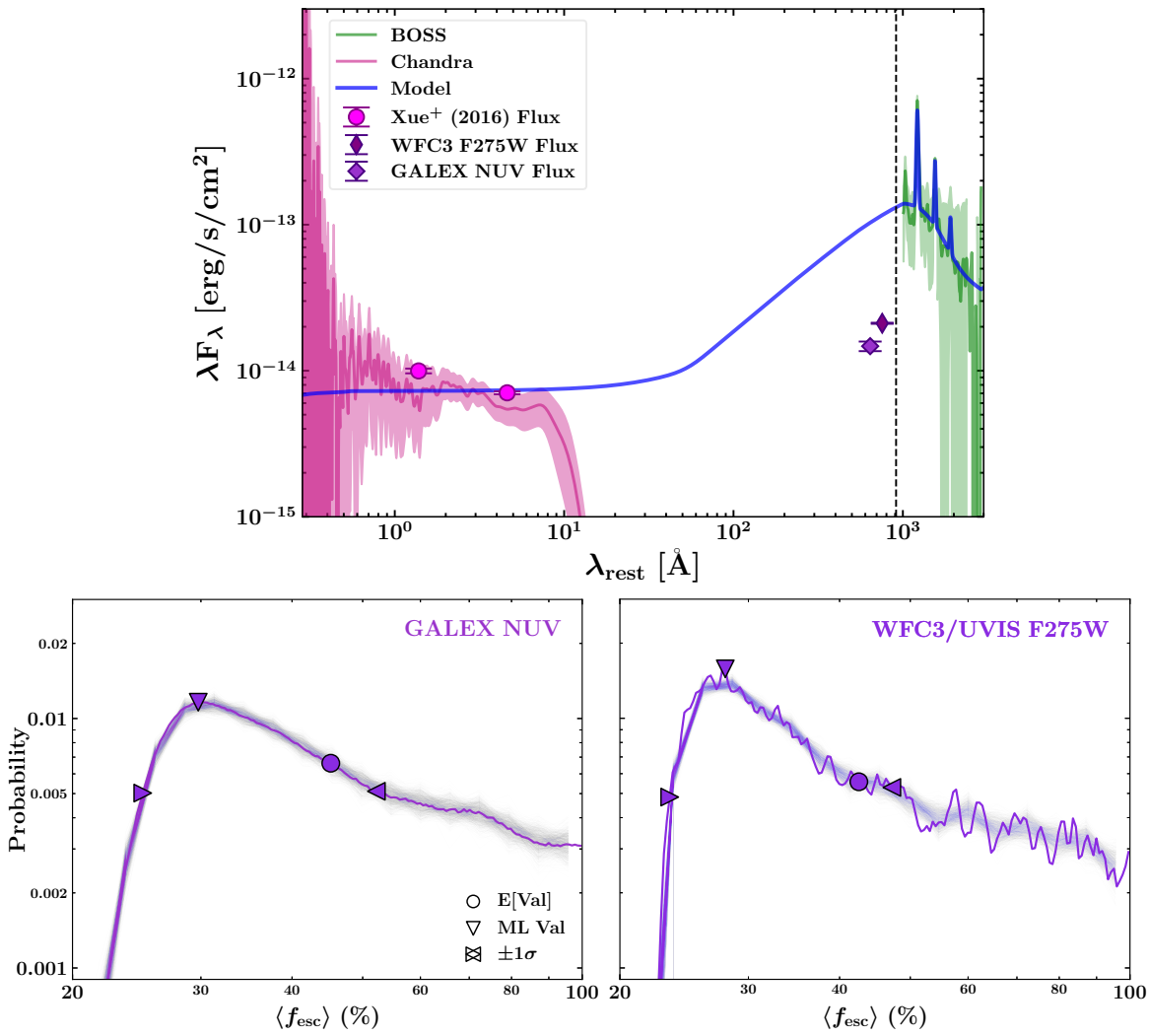


Figure 29. LyC-Bright QSO SED and LyC Escape Fraction PMFs in GALEX NUV and WFC3/UVIS F275W

[Left]: SDSS BOSS (Dawson et al. 2013) spectrum of QSO $J189.095582{+}62.257407$ and $\pm1\sigma$ uncertainty (green) together with its *Chandra* ACIS Spectrum (magenta). The OPTXAGNF (Done et al. 2012) model was fit to the *Chandra* and BOSS spectra simultaneously using the XSpec software (blue; Arnaud 1996). The *observed GALEX* NUV and WFC3/UVIS F275W fluxes are plotted as light and dark violet diamonds, respectively, and the *Chandra* soft (0.5–2.0 keV) and hard (2–7 keV) band fluxes as measured by Xue et al. (2016) are shown as magenta circles. [Middle]: The probability mass function (PMF) of escaping LyC flux derived from the *GALEX* NUV flux. The shaded region represents the 1000 $f_{esc}$ MC simulations, and the dark violet line is the combination of all 1000 simulations. The estimated LyC escape fraction for *GALEX* NUV is estimated to be $f_{esc}^{NUV} \simeq 30^{+22}_{-5}\%$. [Right]: The PMF of escaping LyC flux observed in the WFC3/UVIS F275W filter. The estimated LyC escape fraction here is estimated to be $f_{esc}^{F275W} \simeq 28^{+20}_{-4}\%$.

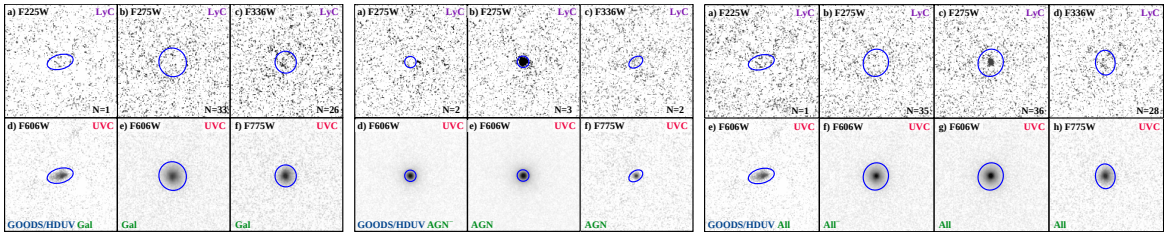


Figure 30. LyC Stacks of Galaxies in the GOODS/HDUV Sample

Sub-image stacks for the three different redshift bins in our sample selected from the GOODS/HDUV field for the galaxies *without* AGN that have reliable spectroscopic redshifts (indicated by Gal in green), galaxies *with* AGN (AGN in green), and *all* galaxies (All in green). These stacks sample LyC emission in F225W, F275W, and F336W and the corresponding F606W and F775W stacks sample the UVC ($\sim$1400 $\lesssim \lambda_{\rm rest} \lesssim$ 1800Å) emission. The AGN$^-$ label indicates the exclusion of the LyC-bright QSO $J$189.095582+62.257407 from the stack. Blue ellipses indicate the SExtractor `MAG_AUTO` UVC detected matched apertures. All sub-images are 151×151 pixels (4.″53×4.″53) in size.

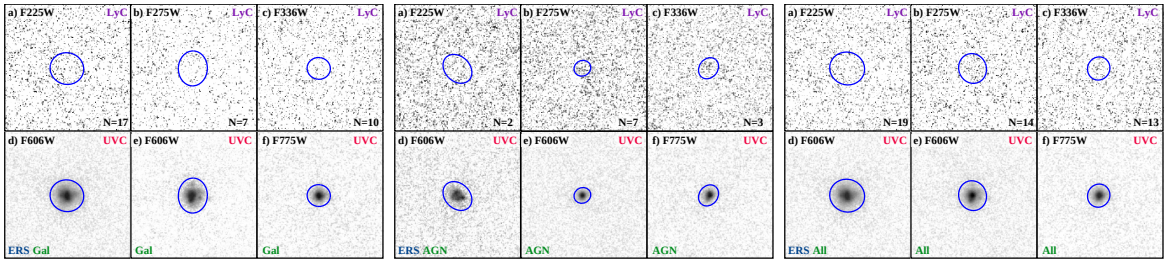


Figure 31. LyC Stacks of Galaxies in the ERS Sample

Same as Fig. 30, but for galaxies selected from the ERS field.

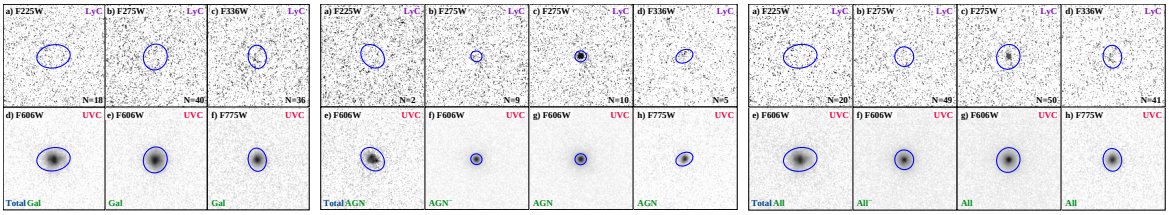


Figure 32. LyC Stacks of Galaxies in the GOODS/HDUV+ERS Samples Combined

Same as Fig. 30, but for galaxies from the ERS and GOODS/HDUV fields combined, or the "Total" sample.

Table 4. LyC Stack Photometry of the GOODS/HDUV and ERS Samples

| Filter (1) | $z$-range (2) | $\langle z \rangle$ (3) | $N_{obj}$ (4) | $m_{LyC}$ (5) | $ABerr_{LyC}$ (6) | $S/N_{LyC}$ (7) | $A_{UVC}$ (8) | $m_{UVC}$ (9) | $ABerr_{UVC}$ (10) | $S/N_{UVC}$ (11) |
|---|---|---|---|---|---|---|---|---|---|---|
| GOODS/HDUV | | | | | | | | | | |
| Galaxies without AGN: | | | | | | | | | | |
| F225W | 2.4680–2.4680 | 2.4680 | 1 | >25.63 | ... | (1.0)† | 0.49 | 25.006 | 0.095 | 11 |
| F275W | 2.4845–3.0604 | 2.7263 | 33 | >26.94 | ... | (1.0)† | 1.00 | 24.674 | 0.010 | 110 |
| F336W | 3.1673–4.2830 | 3.6093 | 26 | >27.51 | ... | (1.0)† | 0.59 | 25.218 | 0.025 | 43 |
| Galaxies with AGN: | | | | | | | | | | |
| F225W | ... | ... | ... | ... | ... | ... | ... | ... | ... | ... |
| F275W$^-$ | 2.5760–2.8280 | 2.7020 | 2 | >26.36 | ... | (1.0)† | 0.16 | 21.509 | 0.002 | 690 |
| F275W | 2.5760–2.8280 | 2.6653 | 3 | 24.66 | 0.17 | 6.2 | 0.17 | 21.118 | 0.001 | 1179 |
| F336W | 3.1930–3.6609 | 3.4270 | 2 | >26.89 | ... | (1.0)† | 0.20 | 25.508 | 0.078 | 14 |
| All Galaxies: | | | | | | | | | | |
| F225W | 2.4680–2.4680 | 2.4680 | 1 | >25.63 | ... | (1.0)† | 0.96 | 25.006 | 0.094 | 12 |
| F275W$^-$ | 2.4845–3.0604 | 2.7249 | 35 | >27.45 | ... | (1.0)† | 0.51 | 23.922 | 0.004 | 261 |
| F275W | 2.4845–3.0604 | 2.7212 | 36 | 27.61 | 0.97 | 1.12 | 0.87 | 23.422 | 0.003 | 423 |
| F336W | 3.1673–4.2830 | 3.5962 | 28 | >27.45 | ... | (1.0)† | 0.62 | 25.224 | 0.024 | 46 |
| ERS | | | | | | | | | | |
| Galaxies without AGN: | | | | | | | | | | |
| F225W | 2.2760–2.4490 | 2.3496 | 17 | >27.69 | ... | (1.0)† | 1.08 | 24.430 | 0.012 | 92 |
| F275W | 2.5658–3.0762 | 2.7516 | 7 | >27.87 | ... | (1.0)† | 1.03 | 24.402 | 0.013 | 81 |
| F336W | 3.1320–4.1486 | 3.6029 | 10 | >32.56 | ... | (1.0)† | 0.51 | 24.843 | 0.023 | 47 |
| Galaxies with AGN: | | | | | | | | | | |
| F225W | 2.2980–2.4500 | 2.3740 | 2 | >27.07 | ... | (1.0)† | 0.81 | 25.215 | 0.049 | 22 |
| F275W | 2.5730–2.7260 | 2.6431 | 6 | >27.76 | ... | (1.0)† | 0.27 | 25.102 | 0.014 | 80 |
| F336W | 3.2171–3.4739 | 3.3157 | 3 | 27.58 | 0.64 | 1.7 | 0.42 | 24.494 | 0.023 | 46 |
| All Galaxies: | | | | | | | | | | |
| F225W | 2.2760–2.4500 | 2.3522 | 19 | >27.73 | ... | (1.0)† | 1.16 | 24.481 | 0.012 | 90 |
| F275W | 2.5658–3.0762 | 2.7016 | 13 | >27.73 | ... | (1.0)† | 0.84 | 24.681 | 0.013 | 87 |
| F336W | 3.1320–4.1486 | 3.5366 | 13 | >28.80 | ... | (1.0)† | 0.52 | 24.708 | 0.018 | 59 |
| Total | | | | | | | | | | |
| Galaxies without AGN: | | | | | | | | | | |
| F225W | 2.2760–2.4680 | 2.3562 | 18 | >27.54 | ... | (1.0)† | 1.20 | 24.442 | 0.012 | 92 |
| F275W | 2.4845–3.0762 | 2.7307 | 40 | >28.47 | ... | (1.0)† | 0.96 | 24.614 | 0.009 | 123 |
| F336W | 3.1320–4.2830 | 3.6075 | 36 | >28.60 | ... | (1.0)† | 0.65 | 25.078 | 0.018 | 62 |
| Galaxies with AGN: | | | | | | | | | | |
| F225W | 2.2980–2.4500 | 2.3740 | 2 | >27.04 | ... | (1.0)† | 0.83 | 25.215 | 0.050 | 22 |
| F275W$^-$ | 2.5730–2.8280 | 2.6578 | 8 | 28.84 | 1.08 | 1.01 | 0.19 | 22.909 | 0.002 | 534 |
| F275W | 2.5730–2.8280 | 2.6505 | 9 | 26.15 | 0.08 | 13.1 | 0.19 | 22.251 | 0.001 | 874 |
| F336W | 3.1930–3.6609 | 3.3602 | 5 | 27.73 | 0.61 | 1.77 | 0.35 | 24.723 | 0.023 | 48 |
| All Galaxies: | | | | | | | | | | |
| F225W | 2.2760–2.4680 | 2.3580 | 20 | >27.56 | ... | (1.0)† | 1.22 | 24.490 | 0.012 | 90 |
| F275W$^-$ | 2.4845–3.0762 | 2.7186 | 48 | >28.63 | ... | (1.0)† | 0.57 | 24.071 | 0.004 | 276 |
| F275W | 2.4845–3.0762 | 2.7160 | 49 | 27.86 | 0.27 | 3.95 | 0.89 | 23.630 | 0.003 | 354 |
| F336W | 3.1320–4.2830 | 3.5773 | 41 | 29.00 | 0.76 | 1.43 | 0.65 | 25.007 | 0.016 | 69 |

Table columns: (1) Observed WFC3/UVIS filter ($^-$ indicates the exclusion of the LyC-bright QSO $J189.095582+62.257407$); (2) Redshift range of galaxies included in LyC/UVC stacks; (3) Average redshift of all galaxies in each stack; (4) Number of galaxies with reliable spectroscopic redshifts included in each stack; (5) Observed total AB magnitude of LyC emission from stack (SExtractor `MAG_AUTO`) aperture matched to UVC, indicated by the blue ellipses in Figs. 30–32; (6) $1\sigma$ uncertainty in LyC AB-mag; (7) Measured S/N of the LyC stack flux († indicates a $1\sigma$ upper limit); (8) Area (in arcsec$^2$) of the UVC aperture; (9) Observed total AB magnitude of the UVC stack; (10) $1\sigma$ uncertainties of UVC AB-mag. Listed uncertainties do not include systematic filter zeropoint uncertainty; (11) Measured S/N of the UVC stack flux.

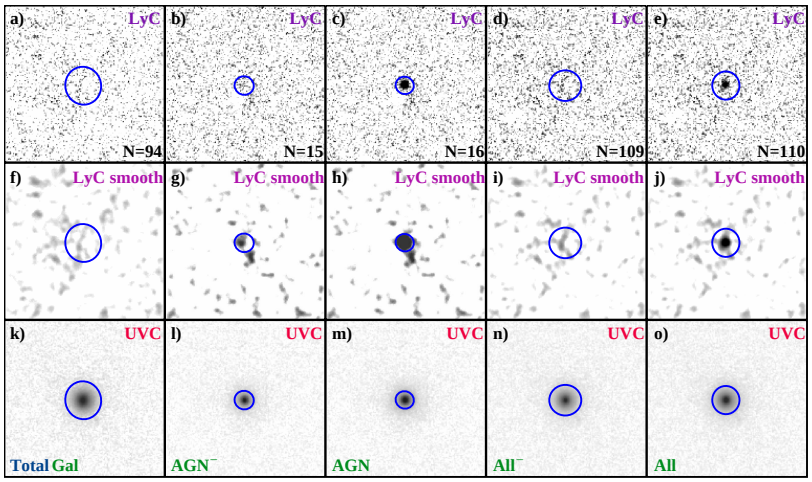


Figure 33. Composite LyC Stacks of the GOODS/HDUV+ERS Samples

[Top Row]: Composite LyC stacks of all galaxies in our sample; [Middle Row]: The same as the top row but convolved with a $1\sigma$ Gaussian kernel. [Bottom Row] The UVC counterparts of the top row; [Left column of panels]: Composite stacks of all galaxies without AGN in our sample (indicated by Gal in green) observed in the F225W, F275W, and F336W filters; [2nd column]: Composite stacks of all galaxies hosting AGN, excluding QSO $J189.095582{+}62.257407$ (indicated by AGN$^-$ in green); [3rd column:] Composite stacks of all galaxies hosting AGN; [4th column]: Composite stacks of 109 galaxies with *and* without AGN in our sample, excluding QSO $J189.095582{+}62.257407$; [5th column]: Stack of all 110 galaxies in our sample. These stacks represent the average *observed* LyC $F_\nu$ from all galaxies integrated from $2.28 \lesssim z \lesssim 4.28$, scaled to a common F225W zeropoint magnitude. The blue ellipses were fit to the UVC stacks (bottom row).

Table 5. Composite Stack LyC Photometry of the GOODS/HDUV+ERS Samples

| Stack (1) | $z$-range (2) | $\langle z \rangle$ (3) | $N_{obj}$ (4) | $m_{LyC}$ (5) | $ABerr_{LyC}$ (6) | $S/N_{LyC}$ (7) | $A_{UVC}$ (8) |
|---|---|---|---|---|---|---|---|
| Gal | 2.2760–4.2830 | 2.9948 | 94 | >28.3 | ... | $(1.0)^\dagger$ | 0.89 |
| AGN$^-$ | 2.2980–3.6609 | 2.8541 | 15 | >27.8 | ... | $(1.0)^\dagger$ | 0.23 |
| AGN | 2.2980–3.6609 | 2.8377 | 16 | 26.5 | 0.1 | 10.3 | 0.21 |
| All$^-$ | 2.2760–4.2830 | 2.9754 | 109 | >28.4 | ... | $(1.0)^\dagger$ | 0.64 |
| All | 2.2760–4.2830 | 2.9719 | 110 | 28.3 | 0.4 | 3.1 | 0.50 |

Table columns: (1) Galaxy type subsample ($^-$ indicates the exclusion of the LyC-bright QSO $J189.095582{+}62.257407$); (2) Redshift range of galaxies included in LyC composite stacks; (3) Average redshift of all galaxies in each stack; (4) Number of galaxies with reliable spectroscopic redshifts included in each stack; (5) Observed total AB magnitude of LyC emission from stack (SExtractor `MAG_AUTO`) aperture matched to UVC, indicated by the blue ellipses in Fig. 33; (6) $1\sigma$ uncertainty in LyC AB-mag (7) Measured S/N of the LyC stack flux ($^\dagger$ indicates a $1\sigma$ upper limit); (8) Area (in arcsec$^2$) of the UVC aperture.

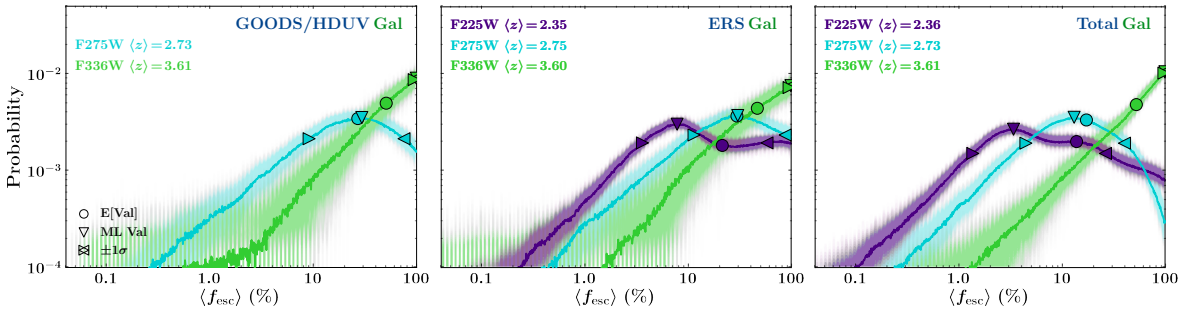


Figure 34. PMFs of the LyC Escape Fraction from Galaxies Without AGN in the GOODS/HDUV and ERS Samples

PMFs of the sample-averaged $f_{\rm esc}$ values of galaxies without AGN from the MC simulations described in §3.4, plotted against their relative probability. The respective sample is indicated in each top right corner. This analysis was performed $10^3$ times using the measured and modeled intrinsic stacked *apparent* LyC flux and their $\pm1\sigma$ ranges. We apply the IGM attenuation models of Inoue et al. (2014) to our modeled LyC fluxes. Downwards triangles and circles indicate the resulting ML and expected values of $f_{\rm esc}$ in each probability distribution function, respectively, while the left/right facing triangles indicate the $\pm1\sigma$ range around the ML value.

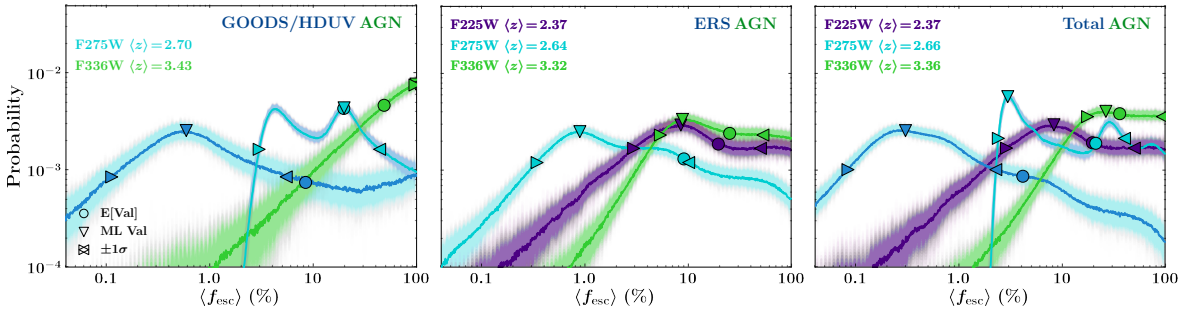


Figure 35. PMFs of the LyC Escape Fraction from Galaxies With AGN in the GOODS/HDUV and ERS Samples

PMFs of the sample-averaged $f_{\rm esc}$ values of galaxies *with* AGN. This analysis was performed in the same manner as in Fig.34, and the symbols are equivalent in meaning as well. The darker blue curve is the same analysis as the lighter blue curve, except the LyC-bright QSO $J189.095582+62.257407$ is excluded.

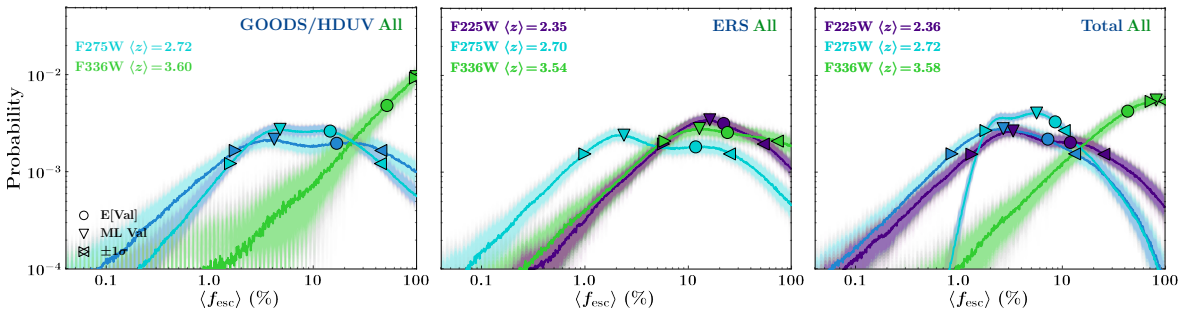


Figure 36. PMFs of the LyC Escape Fraction from All Galaxies in the GOODS/HDUV and ERS Samples

PMFs of the sample-averaged $f_{\rm esc}$ values of *all* galaxies. This analysis was performed in the same manner as in Fig.35, and the symbols are equivalent in meaning as well.

Table 6. Summary of $f_{\rm esc}$ Constraints from the GOODS/HDUV and ERS Samples

| Filter | $\langle z \rangle$ | $N_{obj}$ | $\left\langle \frac{f_{\rm UVC}}{f_{\rm LyC}} \right\rangle_{\rm obs}$ | $\left\langle \frac{f_{\rm UVC}}{f_{\rm LyC}} \right\rangle_{\rm int}$ | Age [log(yr)] | $A_V$ [mag] | $\log(M_\star/M_\odot)$ | SFR [$\log(M_\odot/yr)$] | $\langle \mathcal{T}_{\rm IGM} \rangle$ [%] | $\langle f_{\rm esc} \rangle$ [%] |
|---|---|---|---|---|---|---|---|---|---|---|
| (1) | (2) | (3) | (4) | (5) | (6) | (7) | (8) | (9) | (10) | (11) |
| GOODS/HDUV | | | | | | | | | | |
| Galaxies without AGN: | | | | | | | | | | |
| F275W | 2.726 | 33 | $6^{+15}_{-6}$ | $4.57^{+0.01}_{-0.01}$ | $9^{+0}_{-2}$ | $0.1^{+0.5}_{-0.1}$ | $9.4^{+0.3}_{-1.1}$ | $0.8^{+0.7}_{-0.3}$ | $22^{+33}_{-22}$ | $20^{+51}_{-17}$ |
| F336W | 3.609 | 26 | $8^{+19}_{-8}$ | $6.99^{+0.03}_{-0.02}$ | $8.9^{+0.3}_{-0.7}$ | $0.03^{+0.08}_{-0.03}$ | $9.0^{+0.6}_{-0.6}$ | $0.8^{+0.2}_{-0.6}$ | $4^{+6}_{-4}$ | $<99.5^{+0.5}_{-4.8}$ |
| Galaxies with AGN: | | | | | | | | | | |
| F275W$^-$ | 2.702 | 2 | >208 | $2.666^{+0.002}_{0.002}$ | $6.9^{+0.2}_{-0.2}$ | $0.8^{+0.2}_{-0.2}$ | $9.4^{+0.7}_{-0.7}$ | $2^{+1}_{-1}$ | $22^{+33}_{-22}$ | $0.5^{+5.0}_{-0.4}$ |
| F275W | 2.665 | 3 | $24^{+7}_{-1}$ | $2.760^{+0.002}_{0.002}$ | $6.9^{+0.2}_{-0.3}$ | $0.6^{+0.3}_{-0.3}$ | $9.4^{+0.7}_{-0.6}$ | $2^{+1}_{-1}$ | $22^{+33}_{-22}$ | $20^{+24}_{-17}$ |
| F336W | 3.427 | 2 | $3^{+8}_{-3}$ | $3.93^{+0.02}_{-0.03}$ | $8.9^{+0.3}_{-0.3}$ | $0.4^{+0.2}_{-0.2}$ | $9.9^{+0.3}_{-0.3}$ | <-4 | $9^{+14}_{-9}$ | $<98.6^{+0.9}_{-3.1}$ |
| All Galaxies: | | | | | | | | | | |
| F275W$^-$ | 2.725 | 35 | $17^{+52}_{-17}$ | $2.945^{+0.002}_{0.002}$ | $8.82^{+0.01}_{-1.88}$ | $0.2^{+0.5}_{-0.2}$ | $9.4^{+0.3}_{-1.1}$ | $0.7^{+0.8}_{-0.2}$ | $22^{+33}_{-22}$ | $4^{+40}_{-2}$ |
| F275W | 2.721 | 36 | $26^{+67}_{-9}$ | $2.999^{+0.002}_{0.002}$ | $8.82^{+0.03}_{-1.92}$ | $0.2^{+0.5}_{-0.2}$ | $9.4^{+0.3}_{-1.1}$ | $1.0^{+0.6}_{-0.4}$ | $22^{+33}_{-22}$ | $5^{+40}_{-3}$ |
| F336W | 3.596 | 28 | $7^{+19}_{-7}$ | $6.57^{+0.02}_{-0.02}$ | $9.0^{+0.1}_{-0.9}$ | $0.01^{+0.16}_{-0.01}$ | $9.4^{+0.4}_{-1.0}$ | $0.8^{+0.2}_{-0.7}$ | $4.5^{+6.1}_{-4.5}$ | $<99.5^{+0.5}_{-2.1}$ |
| ERS | | | | | | | | | | |
| Galaxies without AGN: | | | | | | | | | | |
| F225W | 2.350 | 17 | $19^{+52}_{-19}$ | $3.84^{+0.02}_{-0.03}$ | $7.7^{+0.5}_{-0.3}$ | $0.8^{+0.0}_{-0.7}$ | $8.81^{+0.85}_{-0.03}$ | $0.1^{+0.6}_{-1.8}$ | $33^{+39}_{-32}$ | $9^{+50}_{-5}$ |
| F275W | 2.752 | 7 | >51 | $6.80^{+0.03}_{-0.03}$ | $7.30^{+1.40}_{-0.03}$ | $0.3^{+0.3}_{-0.3}$ | $8.9^{+0.7}_{-0.2}$ | $0.6^{+0.7}_{-0.9}$ | $19^{+31}_{-19}$ | $30^{+57}_{-19}$ |
| F336W | 3.603 | 10 | >23 | $6.60^{+0.01}_{-0.02}$ | $8.99^{+0.01}_{-1.09}$ | $0.01^{+0.01}_{-0.01}$ | $9.2^{+0.3}_{-0.7}$ | $0.9^{+0.2}_{-0.3}$ | $4^{+6}_{-4}$ | $<99.5^{+0.5}_{-4.1}$ |
| Galaxies with AGN: | | | | | | | | | | |
| F225W | 2.374 | 2 | $4^{+11}_{-4}$ | $2.69^{+0.02}_{-0.02}$ | $7.6^{+0.8}_{-0.8}$ | $1.1^{+0.3}_{-0.3}$ | $9.6^{+0.4}_{-0.4}$ | $2.0^{+0.6}_{-0.6}$ | $29^{+38}_{-29}$ | $8^{+44}_{-5}$ |
| F275W | 2.643 | 6 | $11^{+32}_{-11}$ | $2.63^{+0.01}_{-0.01}$ | $7.9^{+1.3}_{-1.4}$ | $0.6^{+1.0}_{-0.4}$ | $10.34^{+0.03}_{-1.52}$ | $1.1^{+2.0}_{-0.1}$ | $26^{+35}_{-26}$ | $0.9^{+9.2}_{-0.6}$ |
| F336W | 3.316 | 3 | $12^{+21}_{-2}$ | $7.62^{+0.06}_{-0.08}$ | $7.3^{+0.7}_{-1.6}$ | $1.5^{+0.6}_{-1.5}$ | $9.9^{+0.8}_{-1.8}$ | $2.75^{+0.04}_{-0.09}$ | $12^{+19}_{-12}$ | $9^{+44}_{-3}$ |
| All Galaxies: | | | | | | | | | | |
| F225W | 2.352 | 19 | $20^{+53}_{-20}$ | $3.61^{+0.02}_{-0.02}$ | $7.6^{+0.5}_{-0.5}$ | $0.75^{+0.05}_{-0.58}$ | $8.90^{+0.79}_{-0.04}$ | $0.1^{+1.0}_{-1.7}$ | $29^{+38}_{-29}$ | $15^{+39}_{-9}$ |
| F275W | 2.702 | 13 | $16^{+43}_{-16}$ | $2.85^{+0.01}_{-0.01}$ | $7.1^{+1.8}_{-0.6}$ | $0.4^{+0.9}_{-0.4}$ | $9.3^{+0.7}_{-0.6}$ | $0.8^{+1.5}_{-0.6}$ | $22^{+33}_{-22}$ | $2^{+23}_{-1}$ |
| F336W | 3.537 | 13 | $36^{+67}_{-36}$ | $7.52^{+0.06}_{-0.06}$ | $8.7^{+0.3}_{-2.5}$ | $0.15^{+0.02}_{-0.15}$ | $9.5^{+0.2}_{-1.2}$ | $0.8^{+1.9}_{-0.2}$ | $6^{+9}_{-6}$ | $13^{+61}_{-7}$ |
| Total | | | | | | | | | | |
| Galaxies without AGN: | | | | | | | | | | |
| F225W | 2.356 | 18 | $16^{+49}_{-16}$ | $3.30^{+0.01}_{-0.01}$ | $7.7^{+0.5}_{-0.6}$ | $0.75^{+0.05}_{-0.61}$ | $9.64^{+0.05}_{-0.83}$ | $1.18^{+0.09}_{-2.77}$ | $29^{+38}_{-29}$ | $3^{+23}_{-2}$ |
| F275W | 2.731 | 40 | $25^{+81}_{-25}$ | $4.884^{+0.008}_{0.008}$ | $8.82^{+0.02}_{-1.82}$ | $0.2^{+0.5}_{-0.2}$ | $9.1^{+0.6}_{-0.7}$ | $0.9^{+0.5}_{-0.8}$ | $21^{+34}_{-21}$ | $13^{+26}_{-9}$ |
| F336W | 3.607 | 36 | $23^{+76}_{-23}$ | $6.87^{+0.01}_{-0.02}$ | $9.0^{+0.2}_{-0.9}$ | $0.03^{+0.08}_{-0.03}$ | $9.3^{+0.4}_{-1.0}$ | $0.8^{+0.2}_{-0.6}$ | $4^{+6}_{-4}$ | $<99.5^{+0.5}_{-2.1}$ |
| Galaxies with AGN: | | | | | | | | | | |
| F225W | 2.374 | 2 | $5^{+9}_{-5}$ | $2.70^{+0.02}_{-0.02}$ | $7.6^{+0.8}_{-0.8}$ | $1.1^{+0.3}_{-0.3}$ | $9.6^{+0.4}_{-0.4}$ | $2.0^{+0.6}_{-0.6}$ | $29^{+38}_{-29}$ | $8^{+42}_{-5}$ |
| F275W$^-$ | 2.658 | 8 | $122^{+333}_{-65}$ | $2.652^{+0.006}_{0.003}$ | $8^{+1}_{-1}$ | $0.42^{+0.95}_{-0.09}$ | $10.34^{+0.01}_{-1.90}$ | $1.2^{+2.4}_{-0.7}$ | $23^{+33}_{-23}$ | $0.3^{+2.1}_{-0.2}$ |
| F275W | 2.651 | 9 | $36^{+4}_{-2}$ | $2.718^{+0.005}_{0.004}$ | $7.1^{+1.8}_{-0.6}$ | $0.4^{+0.9}_{-0.3}$ | $9.7^{+0.6}_{-1.2}$ | $1.2^{+2.2}_{-0.6}$ | $23^{+33}_{-23}$ | $3.0^{+37}_{-0.6}$ |
| F336W | 3.360 | 5 | $11^{+20}_{-1}$ | $7.48^{+0.09}_{-0.05}$ | $7^{+2}_{-2}$ | $0.4^{+1.2}_{-0.4}$ | $9.0^{+1.9}_{-0.7}$ | <-4 | $9^{+15}_{-9}$ | $27^{+67}_{-9}$ |
| All Galaxies: | | | | | | | | | | |
| F225W | 2.358 | 20 | $18^{+47}_{-18}$ | $3.24^{+0.01}_{-0.01}$ | $8.20^{+0.07}_{-1.10}$ | $0.5^{+0.3}_{-0.3}$ | $8.90^{+0.82}_{-0.01}$ | $1.2^{+0.2}_{-2.7}$ | $29^{+38}_{-29}$ | $3^{+22}_{-2}$ |
| F275W$^-$ | 2.719 | 48 | $66^{+187}_{-66}$ | $2.915^{+0.005}_{0.004}$ | $8.88^{+0.01}_{-2.04}$ | $0.2^{+0.7}_{-0.2}$ | $9.1^{+0.8}_{-0.7}$ | $1.0^{+0.6}_{-0.6}$ | $22^{+33}_{-22}$ | $3^{+10}_{-2}$ |
| F275W | 2.716 | 49 | $44^{+22}_{-5}$ | $2.954^{+0.005}_{0.003}$ | $8.88^{+0.04}_{-2.08}$ | $0.2^{+0.6}_{-0.2}$ | $9.1^{+0.8}_{-0.7}$ | $0.8^{+0.9}_{-0.4}$ | $22^{+33}_{-22}$ | $6^{+5}_{-4}$ |
| F336W | 3.577 | 41 | $27^{+53}_{-7}$ | $7.36^{+0.05}_{-0.05}$ | $9.1^{+0.1}_{-1.3}$ | $0.15^{+0.02}_{-0.15}$ | $9.5^{+0.3}_{-1.3}$ | $1.0^{+0.1}_{-0.8}$ | $5^{+6}_{-5}$ | $<82^{+18}_{-3}$ |

Table columns: (1) Observed WFC3/UVIS filter ($^-$ indicates the exclusion of QSO $J189.095582+62.257407$); (2) Mean redshift range of galaxies included in LyC/UVC stacks;(3) Number of galaxies included in the stack; (4): Mean *observed* flux ratio $f_{\nu,\rm UVC}/f_{\nu,\rm LyC}$ and its $\pm1\sigma$ uncertainty, as measured from the LyC and UVC stacks in their respective apertures (see §5.5.1 and Table 4); (5): Mean *intrinsic* flux ratio $f_{\nu,\rm UVC}/f_{\nu,\rm LyC}$ and its $\pm1\sigma$ uncertainty, as derived from the best-fit BC03 SED models and their respective WFC3/UVIS and WFC/ACS filter curves for each of our redshift bins; (6): Peak age of the stellar populations distribution from the best-fit BC03 models and their $\pm1\sigma$ standard deviations in years; (7): Peak dust extinction $A_V$ and its $\pm1\sigma$ uncertainty of the best-fit BC03 SED model in AB magnitudes; (8): Peak stellar mass and its $\pm1\sigma$ uncertainty of the best-fit BC03 SED model in solar masses; (9): Peak star-formation rate and its $\pm1\sigma$ uncertainty of the best-fit BC03 SED model in solar masses/year; (10): Average filter-weighted IGM transmission of all sight-lines and redshifts in the stacks and their $\pm1\sigma$ standard deviations, calculated from the Inoue et al. (2014) models; (11): ML and $\pm1\sigma$ uncertainties for the sample-average $f_{\rm esc}$ inferred from the MC analysis described in §3.3, i.e., the escape fraction of LyC including effects from all components of the ISM and reddening by dust, corrected for IGM attenuation.

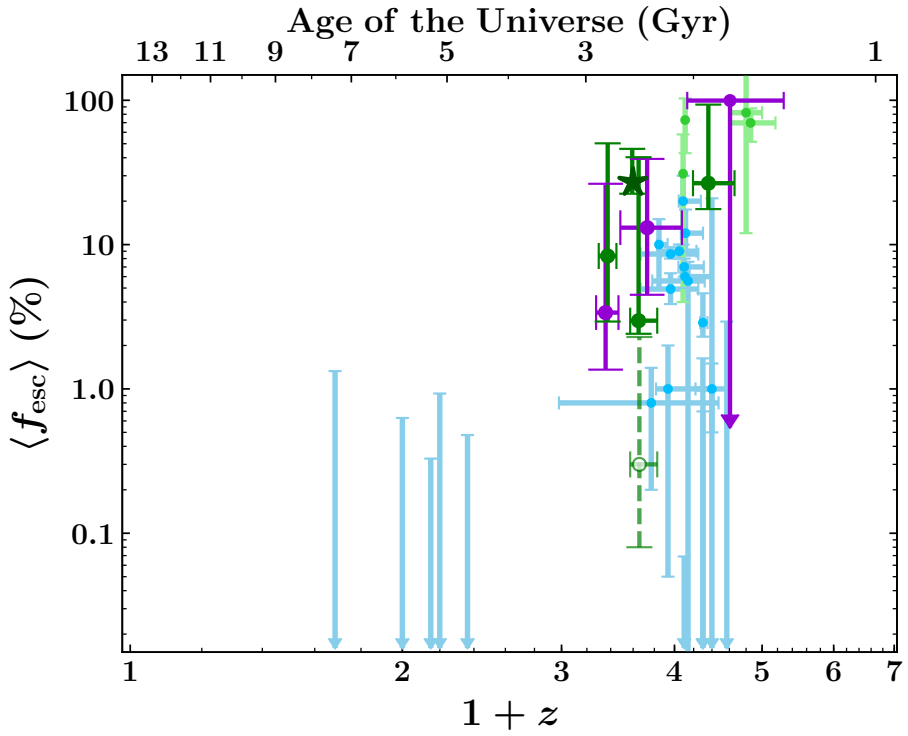


Figure 37. Updated LyC Escape Fraction vs. Redshift from the GOODS/HDUV+ERS Samples

The inferred sample-averaged LyC escape fraction for various galaxy samples as a function of redshift. Plotted are our ML average $f_{\rm esc}$ value with their $\pm1\sigma$ range or $1\sigma$ upper limits for our galaxies *without* AGN (purple filled circles) and galaxies *with* AGN (green filled circles; the open green circle indicates the exclusion of QSO $J$189.095582+62.257407) taken from the probability mass functions of Figs. 34–36, generated from our MC simulations described in §3.4. The green $\star$ symbol represents $f_{\rm esc}$ in F275W of QSO $J$189.095582+62.257407. The blue points indicate available published *sample-averaged* $f_{\rm esc}$ values for galaxies *without* AGN that have $\langle M_{1500\text{Å}}\rangle \lesssim$-21. Some blue points were converted from the quoted $f_{\rm esc}^{\rm rel}$ values using extinction values from the literature source. Light green points are available published sample-average $f_{\rm esc}$ values for AGN. References to these data are found in §2.3. All vertical error bars are the $\pm1\sigma$ uncertainty on the inferred $f_{\rm esc}$ values. Some errors were converted from the quoted 2–3$\sigma$ uncertainties in the literature. Upper limits are shown as downward triangles. Although the blue points represent galaxy samples with properties that differ from those of our samples, and the quoted errors were derived from uncertainties based on different methods of error assessment, the combined data suggests a trend of $f_{\rm esc}$ with redshift for both galaxies with *and* without AGN. This compiled dataset does not rule out the possibility that massive galaxies may have had high enough LyC $f_{\rm esc}$ values to complete hydrogen reionization by $z\sim6$, if galaxies at $2\lesssim z\lesssim4$ can serve as analogs for those at $z\gtrsim6$.

# Chapter 6

# CONCLUSIONS AND FUTURE PROSPECTS

### 6.0.1 LyC Detections

This work presented the published LyC photometric analysis from Smith et al. (2018) in Chapter 4, which used the most sensitive UV images available to study the LyC emission of high-redshift galaxies at the time. In Chapter 5, these results were extended from the ERS to include the recently acquired GOODS UV data, and quantified the LyC radiation escaping from a total of 110 spectroscopically verified galaxies at $z \simeq 2.26$–$4.3$ across all three fields and in WFC3/UVIS F225W, F275W, and F336W filters. The ERS imaging was collected when WFC3 was newly installed, and so it provides the purest raw data of any UV deep field to date, since the camera had not been degraded by the constant bombardment of relativistic charged particles that permeate space. The ERS data does not contain many of these pristine raw images unlike UV surveys like UVUDF and HDUV, which were taken at later time and resulted in less than pristine data. The ability to capture faint LyC signals from the high-redshift Universe in these surveys is greatly decreased, and WFC3/UVIS may have not be able to preserve faint signals observed by *HST* like it could when the ERS data taken. These two datasets are complimentary, however, since these later surveys extend the sampling area on the sky, which increases the likelihood of detecting *rarer* bright LyC sources like we found in this work.

The ERS data, with its ability to preserve flux from faint LyC signals, showed that galaxies with typical brightnesses around $M^*$ were not emitting as much LyC

as their AGN counterparts. AGN were seen to be $\sim 3\times$ brighter, with the limited statistics and shallow survey depth of the ERS. Upon extending our LyC survey with the GOODS/HDUV mosaics, we found one QSO to dominate the LyC output of all galaxies in these fields combined, and otherwise found similar results to the photometry of the ERS sample alone. Our search for LyC in these fields began with the intention of stacking LyC signals of many galaxies, though stacks of LyC signals from many galaxies are seen to be drowned out by bright emission of single objects, as is the case with recent studies on extreme O 3 emitters as well (e.g., Y. I. Izotov et al. 2016; Y I Izotov et al. 2017; Y I Izotov et al. 2018; Fletcher et al. 2019).

For Cosmological purposes, stacking these galaxies is important for understanding the LyC production and the efficiency of emission from all galaxies in the Universe as a whole. These galaxies require precisely ascertained redshifts for their LyC photometry to be relevant, which can be attained with high quality and high SNR spectroscopy. With enough spectroscopic information, statistically significant samples of galaxies can be compiled, which can be used to address questions about the bulk of galaxies completing the reionization of the Universe. These spectra can also allow for more refined study of the LyC production from galaxies, such as relation to LyC emission and internal dynamics and how the interplay between these factors evolve throughout the history of the Universe.

With the upcoming completion of the UVCANDELS survey, additional deep *HST* UV data will be available in the EGS and COSMOS fields for further studies on the sources of reionization. This data is also limited by CTE losses, though may be able to fortuitously reveal more bright LyC sources as with the HDUV survey. After *JWST* begins collecting near-IR spectra in these deep UV surveys, including the ERS, an

abundant amount of high-redshift sources will be available for studying their LyC signal and the physical phenomena that lead to LyC escape (Maseda et al. 2019).

The WFC3/UVIS detector will continue to degrade with time, so no UV extragalactic survey will be as sensitive as those that come before it. Another potential route for greatly improving the future of UV astronomy is to replace the UVIS channel on *HST* via another service mission, as proposed by Lopez-Morales et al. (2019). This would surely bring the quality of *HST* UV data back to that of the ERS, and would allow for early deep surveys to be performed when these cameras are still at their peak sensitivity.

### 6.0.2 LyC Escape Fractions

Our sample of AGN from the GOODS/HDUV sample contains two luminous AGN, though only one displayed a LyC signal, which was brighter than all of the LyC sources in our sample combined. It is not exactly clear why only this AGN is so bright in LyC, and a few ideas were put forth in Chapter 5. Perhaps it could be the case that the particular line-of-sight towards this AGN had a very low H 1 IGM column density. We also found a potential, though low SNR LyC signal from the galaxies with no AGN stacked at $\langle z \rangle \simeq 3.6$, possibly indicating a similar phenomenon occurring without the need of a bright QSO.

We used the latest models from Inoue et al. (2014), which incorporates the latest neutral IGM absorber distribution data available. Their models allow for realistic MC simulations of the transmission of photons propagating through the IGM at high redshift, and is either somewhat better or nearly equal to other models replicating the average Lyman-$\alpha$ transmission constrained observationally by several studies at

various redshifts (Fan, Carilli, and Keating 2006; Kirkman et al. 2007; Faucher-Giguère et al. 2008; Becker and Bolton 2013). These models, however, may not account for smaller spatial resolutions in the IGM that may deviate greatly from the average their models are benchmarked after.

This may explain why we detect this LyC-bright QSO and why we see some marginal flux from galaxies where the models predict the IGM would attenuate the signal to $\leq 1\%$ with a $\sim 70\%$ probability. The IGM may be more inhomogeneous than what the current set of observations of QSO absorption spectra show, and so additional research on the Lyman-$\alpha$ forest, and the distribution of DLAs and LLSs at finer scales through more lines-of-sight is needed to improve the statistics of these models. These models are essential for accurately inferring $f_{\rm esc}$, and its possible, though poorly constrained evolution through Cosmic time.

Our stacked LyC observations of galaxies *without* AGN shows the steepest decline in $f_{\rm esc}$ appears to occur near $z \simeq 2$ from $f_{\rm esc}$<26% to $\lesssim$2%, which correlates with the peak of the cosmic star-formation history within an interval of $\pm 1$ Gyr (Madau and Dickinson 2014). For galaxies *with* AGN, their stacked $f_{\rm esc}$ mostly appears constant with redshift within their error bars, though shows the beginning of a decline if the data was better constrained. A drop may occur from <94% to <26% from $z \sim 3.6$ to $z \sim 2.4$. This could be due to decline in AGN luminosity functions and space density, which steadily peak near $z \simeq 2$ and decrease at $z < 2$ (Ueda 2015). The evolution of these parameters may share a common link, perhaps by the decrease in AGN fuel from major mergers and/or accretion (Fabian 2012) and star-formation feedback through cosmic time. The evolution in these parameters may be correlated to changing dynamics of galaxies on cosmological scales, where the rising infall and merger driven star-formation at $2 \lesssim z \lesssim 6$ transitions to a more passively evolving

universe, characterized by giant galaxies at $z \lesssim 1$–2. The decline in $f_{\rm esc}$ from galaxies may be the result of gas and dust accumulating in the disks and nuclei of forming galaxies, with a SNe rate that looses efficiency in clearing the LyC-obscuring gas and dust in galaxies, which are steadily growing in mass with cosmic time. The accumulating H 1 gas and decreasing SFR may have caused $f_{\rm esc}$ to decrease from $2 < z < 3$, corresponding to $\sim$1 Gyr. Feedback effects can inhibit the formation of new massive LyC-producing stars that could clear LyC escape paths after going supernova. When AGN activity and outflows began to increase after the peak in the cosmic star-formation history at $z \simeq 2$, their outflows may have cleared enough paths in the ISM of host galaxies to enhance the fraction of escaping LyC radiation produced by massive stars and from the accretion disk, resulting in AGN beginning to dominate the ionizing background at $z \lesssim 2$–3, and eventually reionizing helium in the IGM.

Since AGN outshine galactic-stellar LyC by a factor of $\sim$10, combined with their consistently larger $f_{\rm esc}$ seen in this work and in the literature, AGN likely contributed a significant portion of the ionizing photons needed to finish *and* maintain cosmic reionization at $z \lesssim 3$. Due to the anti-hierarchical evolution of SMBHs (Ueda et al. 2003; Hasinger, Miyaji, and Schmidt 2005), AGN of similar masses to QSO $J189.095582+62.257407$ may exist in higher abundance during reionization and could provide a significant portion to the ionizing background. Resolving the X-ray background above $\sim$10 keV may reveal more heavily obscured, Compton-thick AGN that would increase the observed space density of all AGN at $z \gtrsim 2$ (Alexander et al. 2008). Improvements in the accuracy of AGN space densities and their luminosity functions may provide enough statistics to prove the effectiveness of AGN in assisting SFGs significantly with the reionization of the IGM.

REFERENCES


Abel, T., G. L. Bryan, and M. L. Norman. 2002. "The Formation of the First Star in the Universe." *Science* 295 (January): 93–98. doi:10.1126/science.295.5552.93. eprint: astro-ph/0112088.

Abolfathi, B., D. S. Aguado, G. Aguilar, C. Allende Prieto, A. Almeida, T. T. Ananna, F. Anders, et al. 2018. "The Fourteenth Data Release of the Sloan Digital Sky Survey: First Spectroscopic Data from the Extended Baryon Oscillation Spectroscopic Survey and from the Second Phase of the Apache Point Observatory Galactic Evolution Experiment." *The Astrophysical Journal, Supplements* 235, 42 (April): 42. doi:10.3847/1538-4365/aa9e8a. arXiv: 1707.09322.

Aird, J., A. L. Coil, and A. Georgakakis. 2018. "X-rays across the galaxy population - II. The distribution of AGN accretion rates as a function of stellar mass and redshift." *Monthly Notices of the Royal Astronomical Society* 474 (February): 1225–1249. doi:10.1093/mnras/stx2700. arXiv: 1705.01132 [astro-ph.HE].

Aird, J., A. L. Coil, A. Georgakakis, K. Nandra, G. Barro, and P. G. Pérez-González. 2015. "The evolution of the X-ray luminosity functions of unabsorbed and absorbed AGNs out to z$\sim$ 5." *Monthly Notices of the Royal Astronomical Society* 451, no. 2 (June): 1892–1927. doi:10.1093/mnras/stv1062. eprint: http://oup.prod.sis.lan/mnras/article-pdf/451/2/1892/5711813/stv1062.pdf.

Alexander, D. M., R.-R. Chary, A. Pope, F. E. Bauer, W. N. Brandt, E. Daddi, M. Dickinson, D. Elbaz, and N. A. Reddy. 2008. "Reliable Identification of Compton-thick Quasars atz$\approx$ 2:SpitzerMid-Infrared Spectroscopy of HDF-oMD49." *The Astrophysical Journal* 687, no. 2 (November): 835–847. doi:10.1086/591928.

Anderson, Jay, and Luigi R. Bedin. 2010. "An Empirical Pixel-Based Correction for Imperfect CTE. I. HST 's Advanced Camera for Surveys1." *Publications of the Astronomical Society of the Pacific* 122, no. 895 (September): 1035–1064. doi:10.1086/656399.

Arnaud, K. A. 1996. "XSPEC: The First Ten Years." In *Astronomical Data Analysis Software and Systems V,* edited by G. H. Jacoby and J. Barnes, 101:17. Astronomical Society of the Pacific Conference Series.

Avila, Roberto, Norman Grogi, Jay Anderson, Ralph Bohlin, David Borncamp, Marco Chiaberge, Dan Coe, et al. 2015. "ACS Instrument Handbook." *ACS Instrument Handbook (STScI, Baltimore)* Version 14 (Baltimore: STSsI).

Baggett, S., and J. Anderson. 2012. *WFC3/UVIS Sky Backgrounds.* Technical report. June.

Baggett, S., T. Brown, R. Boucarut, D. Figer, G. Hartig, R. Kimble, J. MacKenty, et al. 2006. "Filters for HST Wide Field Camera 3." In *Space Telescopes and Instrumentation I: Optical,* edited by John C. Mather, Howard A. MacEwen, and Mattheus W. M. de Graauw, 6265:626532–626532–11. June. doi:10.1117/12.672300.

Balestra, I., V. Mainieri, P. Popesso, M. Dickinson, M. Nonino, P. Rosati, H. Teimoorinia, et al. 2010. "The Great Observatories Origins Deep Survey." *Astronomy and Astrophysics* 512 (March): A12. doi:10.1051/0004-6361/200913626.

Banerjee, R., E. Vázquez-Semadeni, P. Hennebelle, and R. S. Klessen. 2009. "Clump morphology and evolution in MHD simulations of molecular cloud formation." *Monthly Notices of the Royal Astronomical Society* 398 (3): 1082–1092. doi:10.1111/j.1365-2966.2009.15115.x. eprint: https://onlinelibrary.wiley.com/doi/pdf/10.1111/j.1365-2966.2009.15115.x.

Barkana, R., and A. Loeb. 2001. "In the beginning: the first sources of light and the reionization of the universe." *Physics Reports* 349 (July): 125–238. doi:10.1016/S0370-1573(01)00019-9. eprint: astro-ph/0010468.

Basu, S., G. E. Ciolek, W. B. Dapp, and J. Wurster. 2009. "Magnetically-regulated fragmentation induced by nonlinear flows and ambipolar diffusion." *New Astronomy* 14 (July): 483–495. doi:10.1016/j.newast.2009.01.004. arXiv: 0810.0783.

Becker, G. D., and J. S. Bolton. 2013. "New measurements of the ionizing ultraviolet background over $2 < z < 5$ and implications for hydrogen reionization." *Monthly Notices of the Royal Astronomical Society* 436, no. 2 (October): 1023–1039. doi:10.1093/mnras/stt1610.

Becker, G. D., J. S. Bolton, P. Madau, M. Pettini, E. V. Ryan-Weber, and B. P. Venemans. 2015. "Evidence of patchy hydrogen reionization from an extreme Ly$\alpha$ trough below redshift six." *Monthly Notices of the Royal Astronomical Society* 447, no. 4 (January): 3402–3419. doi:10.1093/mnras/stu2646.

Bekki, K. 2015. "Cosmic Evolution of Dust in Galaxies: Methods and Preliminary Results." *The Astrophysical Journal* 799, 166 (February): 166. doi:10.1088/0004-637X/799/2/166. arXiv: 1412.1239.

Bender, Ralf, John Kormendy, Gary Bower, Richard Green, Jens Thomas, Anthony C. Danks, Theodore Gull, et al. 2005. "HSTSTIS Spectroscopy of the Triple Nucleus of

M31: Two Nested Disks in Keplerian Rotation around a Supermassive Black Hole." *The Astrophysical Journal* 631, no. 1 (September): 280–300. doi:10.1086/432434.

Bennett, C. L., M. Halpern, G. Hinshaw, N. Jarosik, A. Kogut, M. Limon, S. S. Meyer, et al. 2003. "First-Year Wilkinson Microwave Anisotropy Probe (WMAP) Observations: Preliminary Maps and Basic Results." *The Astrophysical Journal, Supplements* 148, no. 1 (September): 1–27. doi:10.1086/377253. arXiv: astro-ph/0302207 [astro-ph].

Bergvall, N., E. Leitet, E. Zackrisson, and T. Marquart. 2013. "Lyman continuum leaking galaxies. Search strategies and local candidates." *Astronomy and Astrophysics* 554 (June): A38. doi:10.1051/0004-6361/201118433.

Bertin, E., and S. Arnouts. 1996. "SExtractor: Software for source extraction." *Astronomy and Astrophysics, Supplements* 117, no. 2 (June): 393–404. doi:10.1051/aas:1996164.

Bianchi, Luciana, Bernie Shiao, and David Thilker. 2017. "Revised Catalog of GALEX Ultraviolet Sources. I. The All-Sky Survey: GUVcat_AIS." *The Astrophysical Journal Supplement Series* 230, no. 2 (June): 24. doi:10.3847/1538-4365/aa7053.

Bielby, R., M. D. Hill, T. Shanks, N. H. M. Crighton, L. Infante, C. G. Bornancini, H. Francke, et al. 2013. "The VLT LBG Redshift Survey - III. The clustering and dynamics of Lyman-break galaxies at z  3." *Monthly Notices of the Royal Astronomical Society* 430, no. 1 (January): 425–449. doi:10.1093/mnras/sts639.

Biretta, J., and S. Baggett. 2013. *WFC3 Post-Flash Calibration.* Technical report. June.

Blanc, G. A., J. J. Adams, K. Gebhardt, G. J. Hill, N. Drory, L. Hao, R. Bender, et al. 2011. "The HETDEX Pilot Survey. II. The Evolution of the Ly$\alpha$ Escape Fraction from the Ultraviolet Slope and Luminosity Function of $1.9 < z < 3.8$ LAEs." *The Astrophysical Journal* 736, 31 (July): 31. doi:10.1088/0004-637X/736/1/31. arXiv: 1011.0430.

Bland-Hawthorn, J., and Philip R. Maloney. 1999. "The Escape of Ionizing Photons from the Galaxy." *The Astrophysical Journal* 510, no. 1 (January): L33–L36. doi:10.1086/311797.

Bless, R. C., and Blair D. Savage. 1972. "Ultraviolet Photometry from the Orbiting Astronomical Observatory. II. Interstellar Extinction." *The Astrophysical Journal* 171 (February): 293. doi:10.1086/151282.

Bluem, J, P Kaaret, A Prestwich, and M Brorby. 2019. "Enhanced X-ray emission from candidate Lyman continuum emitting galaxies." *Monthly Notices of the Royal Astronomical Society* 487, no. 3 (June): 4093–4101. doi:10.1093/mnras/stz1574. eprint: http://oup.prod.sis.lan/mnras/article-pdf/487/3/4093/28853751/stz1574.pdf.

Bohlin, R. C., B. D. Savage, and J. F. Drake. 1978. "A survey of interstellar H I from L-alpha absorption measurements. II." *The Astrophysical Journal* 224 (August): 132–142. doi:10.1086/156357.

Bond, J. R., L. Kofman, and D. Pogosyan. 1996. "How filaments of galaxies are woven into the cosmic web." *Nature* 380 (April): 603–606. doi:10.1038/380603a0. eprint: astro-ph/9512141.

Borthakur, Sanchayeeta, Timothy M. Heckman, Claus Leitherer, and Roderik A. Overzier. 2014. "A local clue to the reionization of the universe." *Science* 346, no. 6206 (October): 216–219. doi:10.1126/science.1254214. arXiv: 1410.3511 [astro-ph.GA].

Bosman, Sarah E I, Xiaohui Fan, Linhua Jiang, Sophie Reed, Yoshiki Matsuoka, George Becker, and Martin Haehnelt. 2018. "New constraints on Lyman- opacity with a sample of 62 quasarsat z
gt; 5.7." *Monthly Notices of the Royal Astronomical Society* 479, no. 1 (May): 1055–1076. doi:10.1093/mnras/sty1344. eprint: http://oup.prod.sis.lan/mnras/article-pdf/479/1/1055/25129046/sty1344.pdf.

Botticella, M. T., S. J. Smartt, R. C. Kennicutt, E. Cappellaro, M. Sereno, and J. C. Lee. 2012. "A comparison between star formation rate diagnostics and rate of core collapse supernovae within 11 Mpc." *Astronomy and Astrophysics* 537, A132 (January): A132. doi:10.1051/0004-6361/201117343. arXiv: 1111.1692.

Bourque, M., and V. Kozhurina-Platais. 2013. "WFC3/UVIS EPER CTE Measurement: Cycles 19 & 20." *Instrument Science Report WFC 2013-03 (STScI, Baltimore).*

Boutsia, K., A. Grazian, E. Giallongo, A. Fontana, L. Pentericci, M. Castellano, G. Zamorani, et al. 2011. "A Low Escape Fraction Of Ionizing Photons of $L > L_*$ Lyman Break Galaxies at $z$=3.3." *The Astrophysical Journal* 736, no. 1 (July): 41. doi:10.1088/0004-637X/736/1/41.

Bouwens, R. J., G. D. Illingworth, P. A. Oesch, M. Trenti, I. Labbé, M. Franx, M. Stiavelli, C. M. Carollo, P. van Dokkum, and D. Magee. 2012. "Lower-luminosity Galaxies Could Reionize The Universe: Very Steep Faint-end Slopes To The UV

Luminosity Functions At z$\geq$ 5-8 From The HUDF09 WFC3/IR Observations." *The Astrophysical Journal* 752, no. 1 (May): L5. doi:10.1088/2041-8205/752/1/l5.

Bouwens, R. J., R. Smit, I. Labbé, M. Franx, J. Caruana, P. Oesch, M. Stefanon, and N. Rasappu. 2016. "The Lyman-Continuum Photon Production Efficiency $\xi_{ion}$ of z
4-5 Galaxies from IRAC-based H$\alpha$ Measurements: Implications for the Escape Fraction and Cosmic Reionization." *The Astrophysical Journal* 831, 176 (November): 176. doi:10.3847/0004-637X/831/2/176. arXiv: 1511.08504.

Brammer, G. B., P. G. van Dokkum, M. Franx, M. Fumagalli, S. Patel, H.-W. Rix, R. E. Skelton, et al. 2012. "3D-HST: A Wide-field Grism Spectroscopic Survey with the Hubble Space Telescope." *The Astrophysical Journal, Supplements* 200, 13 (June): 13. doi:10.1088/0067-0049/200/2/13. arXiv: 1204.2829.

Brandt, W. N., D. M. Alexander, A. E. Hornschemeier, G. P. Garmire, D. P. Schneider, A. J. Barger, F. E. Bauer, et al. 2001. "The Chandra Deep Field North Survey. V. 1 Ms Source Catalogs." *The Astronomical Journal* 122, no. 6 (December): 2810–2832. doi:10.1086/324105. arXiv: astro-ph/0108404 [astro-ph].

Bravo-Guerrero, J., and I. R. Stevens. 2017. "Superwind evolution: the young starburst-driven wind galaxy NGC 2782." *Monthly Notices of the Royal Astronomical Society* 467 (June): 3788–3800. doi:10.1093/mnras/stx327. arXiv: 1702.03282.

Bridge, Carrie R., Harry I. Teplitz, Brian Siana, Claudia Scarlata, Christopher J. Conselice, Henry C. Ferguson, Thomas M. Brown, et al. 2010. "A Spectroscopic Search for Leaking Lyman Continuum at z$\sim$0.7." *The Astrophysical Journal* 720, no. 1 (September): 465–479. doi:10.1088/0004-637X/720/1/465.

Bromm, V., P. S. Coppi, and R. B. Larson. 2002. "The Formation of the First Stars. I. The Primordial Star-forming Cloud." *The Astrophysical Journal* 564 (January): 23–51. doi:10.1086/323947. eprint: astro-ph/0102503.

Brotherton, Michael S., Zhaohui Shang, and Jessie C. Runnoe. 2012. "Updating quasar bolometric luminosity corrections." *Monthly Notices of the Royal Astronomical Society* 422, no. 1 (April): 478–493. doi:10.1111/j.1365-2966.2012.20620.x. eprint: http://oup.prod.sis.lan/mnras/article-pdf/422/1/478/18597903/mnras0422-0478.pdf.

Bruzual, G., and S. Charlot. 2003. "Stellar population synthesis at the resolution of 2003." *Monthly Notices of the Royal Astronomical Society* 344 (October): 1000–1028. doi:10.1046/j.1365-8711.2003.06897.x. eprint: astro-ph/0309134.

Burgarella, D., V. Buat, C. Gruppioni, O. Cucciati, S. Heinis, S. Berta, M. Béthermin, et al. 2013. "Herschel PEP/HerMES: the redshift evolution ($0 \leq z \leq 4$) of dust attenuation and of the total (UV+IR) star formation rate density." *Astronomy and Astrophysics* 554 (June): A70. doi:10.1051/0004-6361/201321651.

Calzetti, D., L. Armus, R. C. Bohlin, A. L. Kinney, J. Koornneef, and T. Storchi-Bergmann. 2000. "The Dust Content and Opacity of Actively Star-forming Galaxies." *The Astrophysical Journal* 533 (April): 682–695. doi:10.1086/308692. eprint: astro-ph/9911459.

Cappellari, M., E. K. Verolme, R. P. van der Marel, G. A. Verdoes Kleijn, G. D. Illingworth, M. Franx, C. M. Carollo, and P. T. de Zeeuw. 2002. "The Counterrotating Core and the Black Hole Mass of IC 1459." *The Astrophysical Journal* 578 (October): 787–805. doi:10.1086/342653. eprint: astro-ph/0202155.

Carroll-Nellenback, Jonathan J., Adam Frank, and Fabian Heitsch. 2014. "The Effects Of Flow-inhomogeneities On Molecular Cloud Formation: Local Versus Global Collapse." *The Astrophysical Journal* 790, no. 1 (July): 37. doi:10.1088/0004-637x/790/1/37.

Casertano, Stefano, Dulia de Mello, Mark Dickinson, Henry C. Ferguson, Andrew S. Fruchter, Rosa A. Gonzalez-Lopezlira, Inge Heyer, et al. 2000. "WFPC2 Observations of the Hubble Deep Field South." *The Astronomical Journal* 120, no. 6 (December): 2747–2824. doi:10.1086/316851.

Cash, W. 1979. "Parameter estimation in astronomy through application of the likelihood ratio." *The Astrophysical Journal* 228 (March): 939–947. doi:10.1086/156922.

Chatterjee, Ritaban, Alan P. Marscher, Svetlana G. Jorstad, Alex Markowitz, Elizabeth Rivers, Richard E. Rothschild, Ian M. McHardy, et al. 2011. "CONNECTION BETWEEN THE ACCRETION DISK AND JET IN THE RADIO GALAXY 3C 111." *The Astrophysical Journal* 734, no. 1 (May): 43. doi:10.1088/0004-637x/734/1/43.

Chen, C.-Y., and E. C. Ostriker. 2014. "Formation of Magnetized Prestellar Cores with Ambipolar Diffusion and Turbulence." *The Astrophysical Journal* 785, 69 (April): 69. doi:10.1088/0004-637X/785/1/69. arXiv: 1403.0582 [astro-ph.SR].

Chen, H.-W., J. X. Prochaska, and N. Y. Gnedin. 2007. "A New Constraint on the Escape Fraction in Distant Galaxies Using $\gamma$-Ray Burst Afterglow Spectroscopy." *The Astrophysical Journal, Letters* 667 (October): L125–L128. doi:10.1086/522306. arXiv: 0707.2594.

Choudhury, T. R., E. Puchwein, M. G. Haehnelt, and J. S. Bolton. 2015. "Lyman $\alpha$ emitters gone missing: evidence for late reionization?" *Monthly Notices of the Royal Astronomical Society* 452 (September): 261–277. doi:10.1093/mnras/stv1250. arXiv: 1412.4790.

Clarke, C., and M. S. Oey. 2002. "Galactic porosity and a star formation threshold for the escape of ionizing radiation from galaxies." *Monthly Notices of the Royal Astronomical Society* 337, no. 4 (December): 1299–1308. doi:10.1046/j.1365-8711.2002.05976.x.

Clarke, Cathie J., and Volker Bromm. 2003. "The characteristic stellar mass as a function of redshift." *Monthly Notices of the Royal Astronomical Society* 343, no. 4 (August): 1224–1230. doi:10.1046/j.1365-8711.2003.06765.x. eprint: http://oup.prod.sis.lan/mnras/article-pdf/343/4/1224/3673229/343-4-1224.pdf.

Coatman, Liam, Paul C. Hewett, Manda Banerji, Gordon T. Richards, Joseph F. Hennawi, and J. Xavier Prochaska. 2016. "Correcting C iv-based virial black hole masses." *Monthly Notices of the Royal Astronomical Society* 465, no. 2 (October): 2120–2142. doi:10.1093/mnras/stw2797. eprint: http://oup.prod.sis.lan/mnras/article-pdf/465/2/2120/23269687/stw2797.pdf.

Cooke, J., E. V. Ryan-Weber, T. Garel, and C. G. Diaz. 2014. "Lyman-continuum galaxies and the escape fraction of Lyman-break galaxies." *Monthly Notices of the Royal Astronomical Society* 441, no. 1 (May): 837–851. doi:10.1093/mnras/stu635.

Coppola, C. M., R. D'Introno, D. Galli, J. Tennyson, and S. Longo. 2012. "Non-equilibrium H2formation In The Early Universe: Energy Exchanges, Rate Coefficients, And Spectral Distortions." *The Astrophysical Journal Supplement Series* 199, no. 1 (February): 16. doi:10.1088/0067-0049/199/1/16.

Couchman, H. M. P., and M. J. Rees. 1986. "Pregalactic evolution in cosmologies with cold dark matter." *Monthly Notices of the Royal Astronomical Society* 221 (July): 53–62. doi:10.1093/mnras/221.1.53.

Cowie, L. L., A. J. Barger, and L. Trouille. 2009. "Measureing the Sources of the Intergalactic Ionizing Flux." *The Astrophysical Journal* 692, no. 2 (February): 1476–1488. doi:10.1088/0004-637X/692/2/1476.

Cristiani, S., I. Appenzeller, S. Arnouts, M. Nonino, A. Aragón-Salamanca, C. Benoist, L. da Costa, M. Dennefeld, R. Rengelink, and A. Renzini. 2000. "The first VLT FORS1 spectra of Lyman-break candidates in the HDF-S and AXAF Deep Field." *Astronomy and Astrophysics* 359 (July): 489–492. arXiv: astro-ph/0004213 [astro-ph].

Cristiani, Stefano, Luisa Maria Serrano, Fabio Fontanot, Eros Vanzella, and Pierluigi Monaco. 2016. "The spectral slope and escape fraction of bright quasars at z  3.8: the contribution to the cosmic UV background." *Monthly Notices of the Royal Astronomical Society* 462, no. 3 (August): 2478–2485. doi:10.1093/mnras/stw1810. eprint: http://oup.prod.sis.lan/mnras/article-pdf/462/3/2478/8009663/stw1810.pdf.

Croom, Scott M., Gordon T. Richards, Tom Shanks, Brian J. Boyle, Michael A. Strauss, Adam D. Myers, Robert C. Nichol, et al. 2009. "The 2dF–SDSS LRG and QSO survey: the QSO luminosity function at $0.4 < z < 2.6$." *Monthly Notices of the Royal Astronomical Society* 399, no. 4 (November): 1755–1772. doi:10.1111/j.1365-2966.2009.15398.x.

Crummy, J., A. C. Fabian, L. Gallo, and R. R. Ross. 2006. "An explanation for the soft X-ray excess in active galactic nuclei." *Monthly Notices of the Royal Astronomical Society* 365 (February): 1067–1081. doi:10.1111/j.1365-2966.2005.09844.x. eprint: astro-ph/0511457.

Cucciati, O., L. Tresse, O. Ilbert, O. Le Fèvre, B. Garilli, V. Le Brun, P. Cassata, et al. 2012. "The star formation rate density and dust attenuation evolution over 12 Gyr with the VVDS surveys." *Astronomy and Astrophysics* 539 (February): A31. doi:10.1051/0004-6361/201118010.

Czerny, B., and Hryniewicz, K. 2011. "The origin of the broad line region in active galactic nuclei." *A&A* 525:L8. doi:10.1051/0004-6361/201016025.

D'Aloisio, A., M. McQuinn, and H. Trac. 2015. "Large Opacity Variations in the High-redshift Ly$\alpha$ Forest: The Signature of Relic Temperature Fluctuations from Patchy Reionization." *The Astrophysical Journal, Letters* 813, L38 (November): L38. doi:10.1088/2041-8205/813/2/L38. arXiv: 1509.02523.

Dashyan, Gohar, Joseph Silk, Gary A. Mamon, Yohan Dubois, and Tilman Hartwig. 2018. "AGN feedback in dwarf galaxies?" *Monthly Notices of the Royal Astronomical Society* 473, no. 4 (February): 5698–5703. doi:10.1093/mnras/stx2716. arXiv: 1710.05900 [astro-ph.GA].

Davis, Shane W., Jong-Hak Woo, and Omer M. Blaes. 2007. "The UV Continuum of Quasars: Models and SDSS Spectral Slopes." *The Astrophysical Journal* 668, no. 2 (October): 682–698. doi:10.1086/521393. arXiv: 0707.1456 [astro-ph].

Dawson, K. S., D. J. Schlegel, C. P. Ahn, S. F. Anderson, É. Aubourg, S. Bailey, R. H. Barkhouser, et al. 2013. "The Baryon Oscillation Spectroscopic Survey of

SDSS-III." *The Astronomical Journal* 145, 10 (January): 10. doi:10.1088/0004-6256/145/1/10. arXiv: 1208.0022.

de Barros, S., Vanzella, E., Amorın, R., Castellano, M., Siana, B., Grazian, A., Suh, H., et al. 2016. "An extreme [OIII] emitter at z = 3.2: a low metallicity Lyman continuum source." *A&A* 585:A51. doi:10.1051/0004-6361/201527046.

Deharveng, J.-M., V. Buat, V. Le Brun, B. Milliard, D. Kunth, J. M. Shull, and C. Gry. 2001. "Constraints on the Lyman continuum radiation from galaxies: First results with FUSE on Mrk 54." *Astronomy and Astrophysics* 375, no. 3 (September): 805–813. doi:10.1051/0004-6361:20010920.

Dickinson, Mark, Mauro Giavalisco, and GOODS Team. 2003. *The Mass of Galaxies at Low and High Redshift,* edited by Ralf Bender and Alvio Renzini. ESO ASTROPHYSICS SYMPOSIA. Berlin/Heidelberg: Springer-Verlag. doi:10.1007/b10204.

Dickinson, Mark, Mauro Giavalisco, and GOODS Team. 2003. "The Great Observatories Origins Deep Survey." In *The Mass of Galaxies at Low and High Redshift,* edited by Ralf Bender and Alvio Renzini, 324. January. doi:10.1007/10899892_78. arXiv: astro-ph/0204213 [astro-ph].

Diemand, J., B. Moore, and J. Stadel. 2005. "Earth-mass dark-matter haloes as the first structures in the early Universe." *Nature* 433 (January): 389–391. doi:10.1038/nature03270. eprint: astro-ph/0501589.

Dijkstra, M., S. Wyithe, Z. Haiman, A. Mesinger, and L. Pentericci. 2014. "Evolution in the escape fraction of ionizing photons and the decline in strong Ly  emission from z > 6 galaxies." *Monthly Notices of the Royal Astronomical Society* 440, no. 4 (April): 3309–3316. doi:10.1093/mnras/stu531.

Dijkstra, Mark, Zoltan Haiman, and Abraham Loeb. 2004. "A Limit from the X-Ray Background on the Contribution of Quasars to Reionization." *The Astrophysical Journal* 613, no. 2 (October): 646–654. doi:10.1086/422167.

Dijkstra, Mark, and Roban Kramer. 2012. "Line transfer through clumpy, large-scale outflows: Ly $\alpha$ absorption and haloes around star-forming galaxies." *Monthly Notices of the Royal Astronomical Society* 424, no. 3 (August): 1672–1693. doi:10.1111/j.1365-2966.2012.21131.x.

Dijkstra, Mark, Andrei Mesinger, and J. Stuart B. Wyithe. 2011. "The detectability of Ly$\alpha$ emission from galaxies during the epoch of reionization." *Monthly Notices of the Royal Astronomical Society* 414, no. 3 (July): 2139–2147. doi:10.1111/j.1365-2966.2011.18530.x.

Done, C., S. W. Davis, C. Jin, O. Blaes, and M. Ward. 2012. "Intrinsic disc emission and the soft X-ray excess in active galactic nuclei." *Monthly Notices of the Royal Astronomical Society* 420 (March): 1848–1860. doi:10.1111/j.1365-2966.2011.19779.x. arXiv: 1107.5429 [astro-ph.HE].

Dove, James B., J. Michael Shull, and Andrea Ferrara. 2000. "The Escape of Ionizing Photons from OB Associations in Disk Galaxies: Radiation Transfer through Superbubbles." *The Astrophysical Journal* 531, no. 2 (March): 846–860. doi:10.1086/308481.

Dressel, L. 2019. *Wide Field Camera 3 Instrument Handbook, Version 11.0.* January. https://hst-docs.stsci.edu/display/WFC3IHB.

Dressel, Linda, Bruce Balick, Sylvia Baggett, John Biretta, Howard Bond, Ray Boucarut, Gabriel Brammer, et al. 2015. "Wide Field Camera 3 Instrument Handbook, Version 7.0." *Wide Field Camera 3 Instrument Handbook (STScI, Baltimore)* Version 7. (Baltimore: STScI).

Driver, S. P., S. K. Andrews, L. J. Davies, A. S. G. Robotham, A. H. Wright, R. A. Windhorst, S. Cohen, K. Emig, R. A. Jansen, and L. Dunne. 2016. "Measurements of Extragalactic Background Light from the Far UV to the Far IR from Deep Ground- and Space-based Galaxy Counts." *The Astrophysical Journal* 827, 108 (August): 108. doi:10.3847/0004-637X/827/2/108. arXiv: 1605.01523.

Driver, S. P., A. Fernández-Soto, W. J. Couch, S. C. Odewahn, R. A. Windhorst, S. Phillipps, K. Lanzetta, and A. Yahil. 1998. "Morphological Number Counts and Redshift Distributions to I<26 from the Hubble Deep Field: Implications for the Evolution of Ellipticals, Spirals, and Irregulars." *The Astrophysical Journal, Letters* 496 (April): L93–L96. doi:10.1086/311257. eprint: astro-ph/9802092.

Duncan, Kenneth, and Christopher J. Conselice. 2015. "Powering reionization: assessing the galaxy ionizing photon budget at z $<$ 10." *Monthly Notices of the Royal Astronomical Society* 451, no. 2 (August): 2030–2049. doi:10.1093/mnras/stv1049. arXiv: 1505.01846 [astro-ph.GA].

Ebrero, J., F. J. Carrera, M. J. Page, J. D. Silverman, X. Barcons, M. T. Ceballos, A. Corral, R. Della Ceca, and M. G. Watson. 2009. "The XMM-Newton serendipitous survey. VI. The X-ray luminosity function." *Astronomy and Astrophysics* 493 (January): 55–69. doi:10.1051/0004-6361:200810919. arXiv: 0811.1450.

Fabian, A. C., A. Zoghbi, R. R. Ross, P. Uttley, L. C. Gallo, W. N. Brandt, A. J. Blustin, et al. 2009. "Broad line emission from iron K- and L-shell transitions

in the active galaxy 1H0707-495." *Nature* 459, no. 7246 (May): 540–542. doi:10.1038/nature08007.

Fabian, A.C. 2012. "Observational Evidence of Active Galactic Nuclei Feedback." *Annual Review of Astronomy and Astrophysics* 50 (1): 455–489. doi:10.1146/annurev-astro-081811-125521. eprint: https://doi.org/10.1146/annurev-astro-081811-125521.

Fan, Xiaohui, C.L. Carilli, and B. Keating. 2006. "Observational Constraints on Cosmic Reionization." *Annual Review of Astronomy and Astrophysics* 44, no. 1 (September): 415–462. doi:10.1146/annurev.astro.44.051905.092514.

Fan, Xiaohui, Vijay K. Narayanan, Michael A. Strauss, Richard L. White, Robert H. Becker, Laura Pentericci, and Hans-Walter Rix. 2002. "Evolution of the Ionizing Background and the Epoch of Reionization from the Spectra of z $\sim$ 6 Quasars." *The Astronomical Journal* 123, no. 3 (March): 1247–1257. doi:10.1086/339030.

Fan, Xiaohui, Michael A. Strauss, Gordon T. Richards, Joseph F. Hennawi, Robert H. Becker, Richard L. White, Aleksandar M. Diamond-Stanic, et al. 2006. "A Survey of z $>$ 5.7 Quasars in the Sloan Digital Sky Survey. IV. Discovery of Seven Additional Quasars." *The Astronomical Journal* 131, no. 3 (March): 1203–1209. doi:10.1086/500296.

Fanidakis, N., C. M. Baugh, A. J. Benson, R. G. Bower, S. Cole, C. Done, C. S. Frenk, R. C. Hickox, C. Lacey, and C. del P. Lagos. 2012. "The evolution of active galactic nuclei across cosmic time: what is downsizing?" *Monthly Notices of the Royal Astronomical Society* 419, no. 4 (January): 2797–2820. doi:10.1111/j.1365-2966.2011.19931.x. eprint: http://oup.prod.sis.lan/mnras/article-pdf/419/4/2797/9504734/mnras0419-2797.pdf.

Faucher-Giguère, C.-A., A. Lidz, L. Hernquist, and M. Zaldarriaga. 2008. "Evolution of the Intergalactic Opacity: Implications for the Ionizing Background, Cosmic Star Formation, and Quasar Activity." *The Astrophysical Journal* 688 (November): 85–107. doi:10.1086/592289. arXiv: 0807.4177.

Faucher-Giguère, Claude-André, Adam Lidz, Lars Hernquist, and Matias Zaldarriaga. 2008. "Evolution of the Intergalactic Opacity: Implications for the Ionizing Background, Cosmic Star Formation, and Quasar Activity." *The Astrophysical Journal* 688, no. 1 (November): 85–107. doi:10.1086/592289.

Ferguson, Annette M. N., Rosemary F. G. Wyse, III Gallagher J. S., and Deidre A. Hunter. 1996. "Diffuse Ionized Gas in Spiral Galaxies: Probing Lyman Continuum

Photon Leakage From H II Regions?" *The Astronomical Journal* 111 (June): 2265. doi:10.1086/117961.

Ferguson, H. C. 2001. "The Hubble Deep Field in the Far Ultraviolet." In *Deep Fields,* edited by S. Cristiani, A. Renzini, and R. E. Williams, 54. doi:10.1007/10854354_11. eprint: astro-ph/0101356.

Fernández-Soto, A., K. M. Lanzetta, and H.-W. Chen. 2003. "Mission: impossible (escape from the Lyman limit)." *Monthly Notices of the Royal Astronomical Society* 342, no. 4 (July): 1215–1221. doi:10.1046/j.1365-8711.2003.06622.x. eprint: http://oup.prod.sis.lan/mnras/article-pdf/342/4/1215/2824109/342-4-1215.pdf.

Fernandez, Elizabeth R., and J. Michael Shull. 2011. "THE EFFECT OF GALACTIC PROPERTIES ON THE ESCAPE FRACTION OF IONIZING PHOTONS." *The Astrophysical Journal* 731, no. 1 (April): 20. doi:10.1088/0004-637X/731/1/20.

Finkelstein, S. L., R. E. Ryan Jr., C. Papovich, M. Dickinson, M. Song, R. S. Somerville, H. C. Ferguson, et al. 2015. "The Evolution of the Galaxy Rest-frame Ultraviolet Luminosity Function over the First Two Billion Years." *The Astrophysical Journal* 810, 71 (September): 71. doi:10.1088/0004-637X/810/1/71. arXiv: 1410.5439.

Finkelstein, Steven L., Casey Papovich, Russell E. Ryan, Andreas H. Pawlik, Mark Dickinson, Henry C. Ferguson, Kristian Finlator, et al. 2012. "CANDELS: The Contribution of the Observed Galaxy Population To Cosmic Reionization." *The Astrophysical Journal* 758, no. 2 (October): 93. doi:10.1088/0004-637x/758/2/93.

Finlator, Kristian, S. Peng Oh, Feryal Özel, and Romeel Davé. 2012. "Gas clumping in self-consistent reionization models." *Monthly Notices of the Royal Astronomical Society* 427, no. 3 (December): 2464–2479. doi:10.1111/j.1365-2966.2012.22114.x.

Fiore, F., S. Puccetti, A. Grazian, N. Menci, F. Shankar, P. Santini, E. Piconcelli, et al. 2011. "Faint high-redshift AGN in the Chandra deep field south: the evolution of the AGN luminosity function and black hole demography." *Astronomy and Astrophysics* 537 (December): A16. doi:10.1051/0004-6361/201117581.

———. 2012. "Faint high-redshift AGN in the Chandra deep field south: the evolution of the AGN luminosity function and black hole demography." *Astronomy and Astrophysics* 537, A16 (January): A16. doi:10.1051/0004-6361/201117581. arXiv: 1109.2888.

Fitzpatrick, E. L. 1999. "Correcting for the Effects of Interstellar Extinction." *Publications of the Astronomical Society of the Pacific* 111 (January): 63–75. doi:10.1086/316293. eprint: astro-ph/9809387.

Fletcher, Thomas J., Mengtao Tang, Brant E. Robertson, Kimihiko Nakajima, Richard S. Ellis, Daniel P. Stark, and Akio Inoue. 2019. "The Lyman Continuum Escape Survey: Ionizing Radiation from [O iii]-strong Sources at a Redshift of 3.1." *The Astrophysical Journal* 878, no. 2 (June): 87. doi:10.3847/1538-4357/ab2045.

Fontanot, F., S. Cristiani, P. Monaco, M. Nonino, E. Vanzella, W. N. Brandt, A. Grazian, and J. Mao. 2007. "The luminosity function of high-redshift quasi-stellar objects. A combined analysis of GOODS and SDSS." *Astronomy and Astrophysics* 461, no. 1 (January): 39–48. doi:10.1051/0004-6361:20066073.

Forbes, J. C., M. R. Krumholz, N. J. Goldbaum, and A. Dekel. 2016. "Suppression of star formation in dwarf galaxies by photoelectric grain heating feedback." *Nature* 535 (July): 523–525. doi:10.1038/nature18292. arXiv: 1605.00650.

Fraley, G. S. 1968. "Supernovae Explosions Induced by Pair-Production Instability." *Astrophysics and Space Science* 2 (August): 96–114. doi:10.1007/BF00651498.

Freedman, David, and Persi Diaconis. 1981. "On the histogram as a density estimator:L 2 theory." *Zeitschrift für Wahrscheinlichkeitstheorie und Verwandte Gebiete* 57, no. 4 (December): 453–476. doi:10.1007/BF01025868.

Fruchter, A. S., and et al. 2010. "BetaDrizzle: A Redesign of the MultiDrizzle Package." In *2010 Space Telescope Science Institute Calibration Workshop, p. 382-387,* 382–387. July.

Fruchter, A. S., and R. N. Hook. 2002. "Drizzle: A Method for the Linear Reconstruction of Undersampled Images." *Publications of the Astronomical Society of the Pacific* 114, no. 792 (February): 144–152. doi:10.1086/338393. arXiv: astro-ph/9808087 [astro-ph].

Fruscione, Antonella, Jonathan C. McDowell, Glenn E. Allen, Nancy S. Brickhouse, Douglas J. Burke, John E. Davis, Nick Durham, et al. 2006. "CIAO: Chandra's data analysis system." In, 6270:62701V. Society of Photo-Optical Instrumentation Engineers (SPIE) Conference Series. June. doi:10.1117/12.671760.

Fujita, A., C. L. Martin, M.-M. Mac Low, and T. Abel. 2003. "The Influence of Supershells and Galactic Outflows on the Escape of Ionizing Radiation from Dwarf Starburst Galaxies." *The Astrophysical Journal* 599 (December): 50–69. doi:10.1086/379276. eprint: astro-ph/0208278.

Fynbo, J. P. U., P. Jakobsson, J. X. Prochaska, D. Malesani, C. Ledoux, A. de Ugarte Postigo, M. Nardini, et al. 2009. "Low-resolution Spectroscopy of Gamma-ray Burst Optical Afterglows: Biases in the Swift Sample and Characterization of the Absorbers." *The Astrophysical Journal, Supplements* 185 (December): 526–573. doi:10.1088/0067-0049/185/2/526. arXiv: 0907.3449 [astro-ph.CO].

Gardner, Jonathan P., John C. Mather, Mark Clampin, Rene Doyon, Matthew A. Greenhouse, Heidi B. Hammel, John B. Hutchings, et al. 2006. "The James Webb Space Telescope." *Space Science Reviews* 123, no. 4 (November): 485–606. doi:10.1007/s11214-006-8315-7.

Giallongo, E., S. Cristiani, S. D'Odorico, and A. Fontana. 2002. "A Low Upper Limit to the Lyman Continuum Emission of Two Galaxies at z$\simeq$3." *The Astrophysical Journal* 568, no. 1 (March): L9–L12. doi:10.1086/340254.

Giallongo, E., A. Grazian, F. Fiore, A. Fontana, L. Pentericci, E. Vanzella, M. Dickinson, et al. 2015. "Faint AGNs at z $>$ 4 in the CANDELS GOODS-S field: looking for contributors to the reionization of the Universe." *Astronomy and Astrophysics* 578, A83 (June): A83. doi:10.1051/0004-6361/201425334. arXiv: 1502.02562.

Giallongo, E., N. Menci, F. Fiore, M. Castellano, A. Fontana, A. Grazian, and L. Pentericci. 2012. "Active Galactic Nuclei as Main Contributors to the Ultraviolet Ionizing Emissivity at High Redshifts: Predictions from a $\Lambda$-CDM Model with Linked AGN/Galaxy Evolution." *The Astrophysical Journal* 755, no. 2, 124 (August): 124. doi:10.1088/0004-637X/755/2/124. arXiv: 1206.2950 [astro-ph.CO].

Giavalisco, M., H. C. Ferguson, A. M. Koekemoer, M. Dickinson, D. M. Alexander, F. E. Bauer, J. Bergeron, et al. 2004. "The Great Observatories Origins Deep Survey: Initial Results from Optical and Near-Infrared Imaging." *The Astrophysical Journal* 600, no. 2 (January): L93–L98. doi:10.1086/379232.

Glikman, E., S. G. Djorgovski, D. Stern, A. Dey, B. T. Jannuzi, and K.-S. Lee. 2011. "The Faint End of the Quasar Luminosity Function at z $\sim$ 4: Implications for Ionization of the Intergalactic Medium and Cosmic Downsizing." *The Astrophysical Journal, Letters* 728, L26 (February): L26. doi:10.1088/2041-8205/728/2/L26. arXiv: 1101.0537.

Glover, S. C. O., J. Chluba, S. R. Furlanetto, J. R. Pritchard, and D. W. Savin. 2014. "Chapter Three - Atomic, Molecular, and Optical Physics in the Early Universe: From Recombination to Reionization." *Advances in Atomic Molecular and Optical Physics* 63 (August): 135–270. doi:10.1016/B978-0-12-800129-5.00003-1.

Gnedin, Nickolay Y. 2000. "Cosmological Reionization by Stellar Sources." *The Astrophysical Journal* 535, no. 2 (June): 530–554. doi:10.1086/308876.

Gnedin, Nickolay Y., Andrey V. Kravtsov, and Hsiao-Wen Chen. 2008. "Escape of Ionizing Radiation from High-Redshift Galaxies." *The Astrophysical Journal* 672, no. 2 (January): 765–775. doi:10.1086/524007.

Gómez, Gilberto C., and Enrique Vázquez-Semadeni. 2014. "FILAMENTS IN SIMULATIONS OF MOLECULAR CLOUD FORMATION." *The Astrophysical Journal* 791, no. 2 (August): 124. doi:10.1088/0004-637x/791/2/124.

Grazian, A., E. Giallongo, K. Boutsia, S. Cristiani, E. Vanzella, C. Scarlata, P. Santini, et al. 2018. "The contribution of faint AGNs to the ionizing background at z  4." *A&A* 613:A44. doi:10.1051/0004-6361/201732385.

Grazian, A., E. Giallongo, R. Gerbasi, F. Fiore, A. Fontana, O. Le Fèvre, L. Pentericci, et al. 2016. "The Lyman continuum escape fraction of galaxies at z = 3.3 in the VUDS-LBC/COSMOS field." *Astronomy and Astrophysics* 585, A48 (January): A48. doi:10.1051/0004-6361/201526396. arXiv: 1509.01101.

Grazian, A., E. Giallongo, D. Paris, K. Boutsia, M. Dickinson, P. Santini, R. A. Windhorst, et al. 2017. "Lyman continuum escape fraction of faint galaxies at z 3.3 in the CANDELS/GOODS-North, EGS, and COSMOS fields with LBC." *Astronomy and Astrophysics* 602, A18 (June): A18. doi:10.1051/0004-6361/201730447. arXiv: 1703.00354 [astro-ph.GA].

Grogin, N. A., D. D. Kocevski, S. M. Faber, H. C. Ferguson, A. M. Koekemoer, A. G. Riess, V. Acquaviva, et al. 2011. "CANDELS: The Cosmic Assembly Near-infrared Deep Extragalactic Legacy Survey." *The Astrophysical Journal, Supplements* 197, 35 (December): 35. doi:10.1088/0067-0049/197/2/35. arXiv: 1105.3753.

Guaita, L., L. Pentericci, A. Grazian, E. Vanzella, M. Nonino, M. Giavalisco, G. Zamorani, et al. 2016. "Limits on the LyC signal from z∼3 sources with secure redshift and HST coverage in the E-CDFS field." *ArXiv e-prints* (January). arXiv: 1601.03057.

Gunn, James E., and Bruce A. Peterson. 1965. "On the Density of Neutral Hydrogen in Intergalactic Space." *The Astrophysical Journal* 142 (November): 1633–1636. doi:10.1086/148444.

Guo, Y., H. C. Ferguson, M. Giavalisco, G. Barro, S. P. Willner, M. L. N. Ashby, T. Dahlen, et al. 2013. "CANDELS Multi-wavelength Catalogs: Source Detection and

Photometry in the GOODS-South Field." *The Astrophysical Journal, Supplements* 207, 24 (August): 24. doi:10.1088/0067-0049/207/2/24. arXiv: 1308.4405.

Haardt, F., and L. Maraschi. 1993. "X-ray spectra from two-phase accretion disks." *The Astrophysical Journal* 413 (August): 507–517. doi:10.1086/173020.

Haardt, Francesco, and Piero Madau. 1996. "Radiative Transfer in a Clumpy Universe. II. The Ultraviolet Extragalactic Background." *The Astrophysical Journal* 461 (April): 20. doi:10.1086/177035.

———. 2012. "Radiative Transfer In A Clumpy Universe. IV. New Synthesis Models Of The Cosmic UV/X-ray Background." *The Astrophysical Journal* 746, no. 2 (February): 125. doi:10.1088/0004-637X/746/2/125.

Haehnelt, M. G., and M. J. Rees. 1993. "The formation of nuclei in newly formed galaxies and the evolution of the quasar population." *Monthly Notices of the Royal Astronomical Society* 263 (July): 168–178. doi:10.1093/mnras/263.1.168.

Hanish, D. J., M. S. Oey, J. R. Rigby, D. F. de Mello, and J. C. Lee. 2010. "A Multiwavelength Study On The Fate Of Ionizing Radiation In Local Starbursts." *The Astrophysical Journal* 725, no. 2 (December): 2029–2037. doi:10.1088/0004-637X/725/2/2029.

Harrison, C. M., D. M. Alexander, J. R. Mullaney, and A. M. Swinbank. 2014. "Kiloparsec-scale outflows are prevalent among luminous AGN: outflows and feedback in the context of the overall AGN population." *Monthly Notices of the Royal Astronomical Society* 441, no. 4 (May): 3306–3347. doi:10.1093/mnras/stu515. eprint: http://oup.prod.sis.lan/mnras/article-pdf/441/4/3306/4031399/stu515.pdf.

Hasinger, G., T. Miyaji, and M. Schmidt. 2005. "Luminosity-dependent evolution of soft X-ray selected AGN. New Chandra and XMM-Newton surveys." *Astronomy and Astrophysics* 441 (October): 417–434. doi:10.1051/0004-6361:20042134. eprint: astro-ph/0506118.

Hathi, N. P., R. A. Jansen, R. A. Windhorst, S. H. Cohen, W. C. Keel, M. R. Corbin, and R. E. Ryan Jr. 2008. "SURFACE BRIGHTNESS PROFILES OF COMPOSITE IMAGES OF COMPACT GALAXIES AT z≃4-6 IN THE HUBBLE ULTRA DEEP FIELD." *The Astronomical Journal* 135, no. 1 (January): 156–166. doi:10.1088/0004-6256/135/1/156.

Hathi, N. P., R. E. Ryan, S. H. Cohen, H. Yan, R. A. Windhorst, P. J. McCarthy, R. W. O'Connell, et al. 2010. "UV-DROPOUT GALAXIES IN THE GOODS-SOUTH

FIELD FROM WFC3 EARLY RELEASE SCIENCE OBSERVATIONS." *The Astrophysical Journal* 720, no. 2 (September): 1708–1716. doi:10.1088/0004-637X/720/2/1708.

Heckman, T. M., K. R. Sembach, G. R. Meurer, C. Leitherer, D. Calzetti, and C. L. Martin. 2001. "On the Escape of Ionizing Radiation from Starbursts." *The Astrophysical Journal* 558, no. 1 (September): 56–62. doi:10.1086/322475.

Heiner, Jonathan S., Enrique Vázquez-Semadeni, and Javier Ballesteros-Paredes. 2015. "Molecular cloud formation as seen in synthetic H i and molecular gas observations." *Monthly Notices of the Royal Astronomical Society* 452, no. 2 (July): 1353–1374. doi:10.1093/mnras/stv1153. eprint: http://oup.prod.sis.lan/mnras/article-pdf/452/2/1353/18503994/stv1153.pdf.

Heitsch, F., and L. Hartmann. 2008. "Rapid Molecular Cloud and Star Formation: Mechanisms and Movies." *The Astrophysical Journal* 689 (December): 290–301. doi:10.1086/592491. arXiv: 0808.1078.

Hennebelle, Patrick, and Edith Falgarone. 2012. "Turbulent molecular clouds." *Astronomy and Astrophysics Reviews* 20, 55 (November): 55. doi:10.1007/s00159-012-0055-y. arXiv: 1211.0637 [astro-ph.GA].

Herenz, Edmund Christian, Tanya Urrutia, Lutz Wisotzki, Josephine Kerutt, Rikke Saust, Maria Werhahn, Kasper Borello Schmidt, Joseph Caruana, Catrina Diener, and Roland Bacon. 2017. "The MUSE-Wide survey: A first catalogue of 831 emission line galaxies." *Astronomy and Astrophysics* 606, A12 (September): A12. doi:10.1051/0004-6361/201731055. arXiv: 1705.08215 [astro-ph.GA].

Hinshaw, G., D. Larson, E. Komatsu, D. N. Spergel, C. L. Bennett, J. Dunkley, M. R. Nolta, et al. 2013. "Nine-year Wilkinson Microwave Anisotropy Probe ( Wmap ) Observations: Cosmological Parameter Results." *The Astrophysical Journal, Supplements* 208, no. 2 (October): 19. doi:10.1088/0067-0049/208/2/19.

Ho, L. C. 2002. "On the Relationship between Radio Emission and Black Hole Mass in Galactic Nuclei." *The Astrophysical Journal* 564 (January): 120–132. doi:10.1086/324399. eprint: astro-ph/0110440.

Hopkins, Philip F., Rachel S. Somerville, Lars Hernquist, Thomas J. Cox, Brant Robertson, and Yuexing Li. 2006. "The Relation between Quasar and Merging Galaxy Luminosity Functions and the Merger-driven Star Formation History of the Universe." *The Astrophysical Journal* 652, no. 2 (December): 864–888. doi:10.1086/508503.

Hosokawa, Takashi, Kazuyuki Omukai, Naoki Yoshida, and Harold W. Yorke. 2011. "Protostellar Feedback Halts the Growth of the First Stars in the Universe." *Science* 334 (6060): 1250–1253. doi:10.1126/science.1207433. eprint: https://science.sciencemag.org/content/334/6060/1250.full.pdf.

Hunt, L. K., E. Palazzi, M. J. Michałowski, A. Rossi, S. Savaglio, S. Basa, S. Berta, et al. 2014. "New light on gamma-ray burst host galaxies with Herschel." *Astronomy and Astrophysics* 565, A112 (May): A112. doi:10.1051/0004-6361/201323340. arXiv: 1402.4006 [astro-ph.GA].

Hurwitz, Mark, Patrick Jelinsky, and W. Van Dyke Dixon. 1997. "Reexamining the Lyman Continuum in Starburst Galaxies Observed with the Hopkins Ultraviolet Telescope." *The Astrophysical Journal* 481, no. 1 (May): L31–L34. doi:10.1086/310649.

Ikeda, H., T. Nagao, K. Matsuoka, Y. Taniguchi, Y. Shioya, M. Kajisawa, M. Enoki, et al. 2012. "CONSTRAINTS ON THE FAINT END OF THE QUASAR LUMINOSITY FUNCTION AT z∼5 IN THE COSMOS FIELD." *The Astrophysical Journal* 756, no. 2 (September): 160. doi:10.1088/0004-637X/756/2/160.

Ikeda, H., T. Nagao, K. Matsuoka, Y. Taniguchi, Y. Shioya, J. R. Trump, P. Capak, et al. 2011. "PROBING THE FAINT END OF THE QUASAR LUMINOSITY FUNCTION AT z∼4 IN THE COSMOS FIELD." *The Astrophysical Journal* 728, no. 2 (February): L25. doi:10.1088/2041-8205/728/2/L25.

Inoue, A. K., I. Iwata, and J.-M. Deharveng. 2006. "The escape fraction of ionizing photons from galaxies at z = 0-6." *Monthly Notices of the Royal Astronomical Society* 371 (September): L1–L5. doi:10.1111/j.1745-3933.2006.00195.x. eprint: astro-ph/0605526.

Inoue, A. K., I. Iwata, J.-M. Deharveng, V. Buat, and D. Burgarella. 2005. "VLT narrow-band photometry in the Lyman continuum of two galaxies at z ∼3." *Astronomy and Astrophysics* 435, no. 2 (May): 471–482. doi:10.1051/0004-6361:20041769.

Inoue, A. K., I. Shimizu, I. Iwata, and M. Tanaka. 2014. "An updated analytic model for attenuation by the intergalactic medium." *Monthly Notices of the Royal Astronomical Society* 442, no. 2 (June): 1805–1820. doi:10.1093/mnras/stu936.

Inoue, Akio K. 2001. "Lyman Continuum Extinction by Dust in H [CSC]ii[/CSC] Regions of Galaxies." *The Astronomical Journal* 122, no. 4 (October): 1788–1795. doi:10.1086/323095.

Inoue, Akio K., Hiroyuki Hirashita, and Hideyuki Kamaya. 2001. "Effect of Dust Extinction on Estimating the Star Formation Rate of Galaxies: Lyman Continuum Extinction." *The Astrophysical Journal* 555, no. 2 (July): 613–624. doi:10.1086/321499.

Inoue, Akio K., and Ikuru Iwata. 2008. "A Monte Carlo simulation of the intergalactic absorption and the detectability of the Lyman continuum from distant galaxies." *Monthly Notices of the Royal Astronomical Society* 387, no. 4 (July): 1681–1692. doi:10.1111/j.1365-2966.2008.13350.x.

Ishigaki, Masafumi, Ryota Kawamata, Masami Ouchi, Masamune Oguri, Kazuhiro Shimasaku, and Yoshiaki Ono. 2015. "HUBBLE FRONTIER FIELDS FIRST COMPLETE CLUSTER DATA: FAINT GALAXIES AT z∼5-10 FOR UV LUMINOSITY FUNCTIONS AND COSMIC REIONIZATION." *The Astrophysical Journal* 799, no. 1 (January): 12. doi:10.1088/0004-637X/799/1/12.

Iwata, I., A. K. Inoue, Y. Matsuda, H. Furusawa, T. Hayashino, K. Kousai, M. Akiyama, T. Yamada, D. Burgarella, and J.-M. Deharveng. 2009. "Detections Of Lyman Continuum From Star-forming Galaxies At z∼3 Through Subaru/Suprime-cam Narrow-band Imaging." *The Astrophysical Journal* 692, no. 2 (February): 1287–1293. doi:10.1088/0004-637X/692/2/1287.

Iwata, Ikuru, Akio K Inoue, Genoveva Micheva, Yuichi Matsuda, and Toru Yamada. 2019. "Subaru narrow-band imaging search for Lyman continuum from galaxies at z>3 in the GOODS-N field." *Monthly Notices of the Royal Astronomical Society* 488, no. 4 (July): 5671–5689. doi:10.1093/mnras/stz2081. eprint: http://oup.prod.sis.lan/mnras/article-pdf/488/4/5671/29191218/stz2081.pdf.

Izotov, Y I, D Schaerer, G Worseck, N G Guseva, T X Thuan, A Verhamme, I Orlitová, and K J Fricke. 2017. "J1154+2443: a low-redshift compact star-forming galaxy with a 46 per cent leakage of Lyman continuum photons." *Monthly Notices of the Royal Astronomical Society* 474, no. 4 (December): 4514–4527. doi:10.1093/mnras/stx3115. eprint: http://oup.prod.sis.lan/mnras/article-pdf/474/4/4514/22978094/stx3115.pdf.

Izotov, Y I, G Worseck, D Schaerer, N G Guseva, T X Thuan, Fricke, A Verhamme, and I Orlitová. 2018. "Low-redshift Lyman continuum leaking galaxies with high [O iii]/[O ii] ratios." *Monthly Notices of the Royal Astronomical Society* 478, no. 4 (May): 4851–4865. doi:10.1093/mnras/sty1378. eprint: http://oup.prod.sis.lan/mnras/article-pdf/478/4/4851/25100659/sty1378.pdf.

Izotov, Y. I., D. Schaerer, T. X. Thuan, G. Worseck, N. G. Guseva, I. Orlitová, and A. Verhamme. 2016. "Detection of high Lyman continuum leakage from

four low-redshift compact star-forming galaxies." *Monthly Notices of the Royal Astronomical Society* 461, no. 4 (May): 3683–3701. doi:10.1093/mnras/stw1205. eprint: http://oup.prod.sis.lan/mnras/article-pdf/461/4/3683/8108201/stw1205.pdf.

Jakobsson, P., J. P. U. Fynbo, C. Ledoux, P. Vreeswijk, D. A. Kann, J. Hjorth, R. S. Priddey, et al. 2006. "H I column densities of z  2 Swift gamma-ray bursts." *Astronomy and Astrophysics* 460 (December): L13–L17. doi:10.1051/0004-6361:20066405. eprint: astro-ph/0609450.

Japelj, J., E. Vanzella, F. Fontanot, S. Cristiani, G. B. Caminha, P. Tozzi, I. Balestra, P. Rosati, and M. Meneghetti. 2017. "Constraints on the Lyman continuum escape fraction for faint star-forming galaxies." *Monthly Notices of the Royal Astronomical Society* 468, no. 1 (June): 389–403. doi:10.1093/mnras/stx477. arXiv: 1612.06401 [astro-ph.GA].

Jeans, J. H. 1902. "The Stability of a Spherical Nebula." *Philosophical Transactions of the Royal Society of London Series A* 199:1–53. doi:10.1098/rsta.1902.0012.

Jensen, H., P. Laursen, G. Mellema, I. T. Iliev, J. Sommer–Larsen, and P. R. Shapiro. 2012. "On the use of Ly$\alpha$ emitters as probes of reionization." *Monthly Notices of the Royal Astronomical Society* 428, no. 2 (November): 1366–1381. doi:10.1093/mnras/sts116.

Jia, Jianjun, Andrew Ptak, Timothy M. Heckman, Roderik A. Overzier, Ann Hornschemeier, and Stephanie M. LaMassa. 2011. "Evidence for Black Hole Growth in Local Analogs to Lyman Break Galaxies." *The Astrophysical Journal* 731, no. 1, 55 (April): 55. doi:10.1088/0004-637X/731/1/55. arXiv: 1102.2539 [astro-ph.HE].

Johnson, J. L., and V. Bromm. 2006. "The cooling of shock-compressed primordial gas." *Monthly Notices of the Royal Astronomical Society* 366 (February): 247–256. doi:10.1111/j.1365-2966.2005.09846.x. eprint: astro-ph/0505304.

Kaaret, P., M. Brorby, L. Casella, and A. H. Prestwich. 2017. "Resolving the X-ray emission from the Lyman-continuum emitting galaxy Tol 1247-232." *Monthly Notices of the Royal Astronomical Society* 471, no. 4 (November): 4234–4238. doi:10.1093/mnras/stx1945. arXiv: 1708.05074 [astro-ph.HE].

Kalirai, J. S., J. MacKenty, A. Rajan, S. Baggett, R. Bohlin, T. Brown, S. Deustua, R. A. Kimble, A. Riess, and E. Sabbi. 2009. *WFC3 SMOV Proposal 11450: The Photometric Performance and Calibration of WFC3/UVIS.* Technical report. November.

Kara, E., W. N. Alston, A. C. Fabian, E. M. Cackett, P. Uttley, C. S. Reynolds, and A. Zoghbi. 2016. "A global look at X-ray time lags in Seyfert galaxies." *Monthly Notices of the Royal Astronomical Society* 462, no. 1 (October): 511–531. doi:10.1093/mnras/stw1695. arXiv: 1605.02631 [astro-ph.HE].

Karouzos, M., J.-H. Woo, and H.-J. Bae. 2016. "Unraveling the Complex Structure of AGN-driven Outflows. I. Kinematics and Sizes." *The Astrophysical Journal* 819, 148 (March): 148. doi:10.3847/0004-637X/819/2/148. arXiv: 1601.02621.

Kaufman, J., O. M. Blaes, and S. Hirose. 2017. "The contribution of bulk Comptonization to the soft X-ray excess in AGN." *Monthly Notices of the Royal Astronomical Society* 467, no. 2 (January): 1734–1747. doi:10.1093/mnras/stx193. eprint: http://oup.prod.sis.lan/mnras/article-pdf/467/2/1734/10874402/stx193.pdf.

Keating, Laura C, Ewald Puchwein, and Martin G Haehnelt. 2018. "Spatial fluctuations of the intergalactic temperature–density relation after hydrogen reionization." *Monthly Notices of the Royal Astronomical Society* 477, no. 4 (April): 5501–5516. doi:10.1093/mnras/sty968. eprint: http://oup.prod.sis.lan/mnras/article-pdf/477/4/5501/24955851/sty968.pdf.

Khaire, V., R. Srianand, T. R. Choudhury, and P. Gaikwad. 2015. "The redshift evolution of escape fraction of hydrogen ionizing photons from galaxies." *ArXiv e-prints* (October). arXiv: 1510.04700.

Khaire, Vikram, Raghunathan Srianand, Tirthankar Roy Choudhury, and Prakash Gaikwad. 2016. "The redshift evolution of escape fraction of hydrogen ionizing photons from galaxies." *Monthly Notices of the Royal Astronomical Society* 457, no. 4 (April): 4051–4062. doi:10.1093/mnras/stw192. arXiv: 1510.04700 [astro-ph.CO].

Kim, Ji–hoon, Mark R. Krumholz, John H. Wise, Matthew J. Turk, Nathan J. Goldbaum, and Tom Abel. 2013. "Dwarf Galaxies With Ionizing Radiation Feedback. I. Escape Of Ionizing Photons." *The Astrophysical Journal* 775, no. 2 (September): 109. doi:10.1088/0004-637x/775/2/109.

Kimm, Taysun, and Renyue Cen. 2014. "Escape Fraction of Ionizing Photons during Reionization: Effects due to Supernova Feedback and Runaway OB Stars." *The Astrophysical Journal* 788, no. 2, 121 (June): 121. doi:10.1088/0004-637X/788/2/121. arXiv: 1405.0552 [astro-ph.GA].

Kimm, Taysun, Harley Katz, Martin Haehnelt, Joakim Rosdahl, Julien Devriendt, and Adrianne Slyz. 2017. "Feedback-regulated star formation and escape of LyC photons from mini-haloes during reionization." *Monthly Notices of the Royal*

*Astronomical Society* 466, no. 4 (April): 4826–4846. doi:10.1093/mnras/stx052. arXiv: 1608.04762 [astro-ph.GA].

Kirkman, David, David Tytler, Dan Lubin, and Jane Charlton. 2007. "Continuous statistics of the Ly forest at 0
lt;z
lt; 1.6: the mean flux, flux distribution and autocorrelation fromHST FOS spectra." *Monthly Notices of the Royal Astronomical Society* 376, no. 3 (March): 1227–1237. doi:10.1111/j.1365-2966.2007.11502.x. eprint: http://oup.prod.sis.lan/mnras/article-pdf/376/3/1227/4886315/mnras0376-1227.pdf.

Koekemoer, A. M., S. M. Faber, H. C. Ferguson, N. A. Grogin, D. D. Kocevski, D. C. Koo, K. Lai, et al. 2011. "CANDELS: The Cosmic Assembly Near-infrared Deep Extragalactic Legacy Survey–The Hubble Space Telescope Observations, Imaging Data Products, and Mosaics." *The Astrophysical Journal, Supplements* 197, 36 (December): 36. doi:10.1088/0067-0049/197/2/36. arXiv: 1105.3754.

Koekemoer, Anton M., Richard S. Ellis, Ross J. McLure, James S. Dunlop, Brant E. Robertson, Yoshiaki Ono, Matthew A. Schenker, et al. 2013. "THE 2012 HUBBLE ULTRA DEEP FIELD (UDF12): OBSERVATIONAL OVERVIEW." *The Astrophysical Journal, Supplements* 209, no. 1 (October): 3. doi:10.1088/0067-0049/209/1/3.

Koratkar, Anuradha, and Omer Blaes. 1999. "Invited Review: The Ultraviolet and Optical Continuum Emission in Active Galactic Nuclei: The Status of Accretion Disks." *Publications of the Astronomical Society of the Pacific* 111, no. 755 (January): 1–30. doi:10.1086/316294.

Kozhurina-Platais, V. 2014. "Astrometric Correction for WFC3/UVIS Filter-Dependent Component of Distortion." *Instrument Science Report WFC 2014-12 (STScI, Baltimore).*

Kozhurina-Platais, V., C. Cox, B. McLean, L. Petro, L. Dressel, H. Bushouse, and E. Sabbi. 2009. "WFC3 SMOV Proposal 11444 - UVIS Geometric Distortion Calibration." *Instrument Science Report WFC3 2009-33 (STScI, Baltimore).*

Kozhurina-Platais, V., D. Hammer, N. Dencheva, and W. Hack. 2013. "Astrometric Correction for WFC3/UVIS Lithographic-Mask Pattern." *Instrument Science Report WFC 2013-14 (STScI, Baltimore).*

Kriek, M., P. G. van Dokkum, I. Labbé, M. Franx, G. D. Illingworth, D. Marchesini, and R. F. Quadri. 2009. "An Ultra-Deep Near-Infrared Spectrum of a Compact

Quiescent Galaxy at z = 2.2." *The Astrophysical Journal* 700 (July): 221–231. doi:10.1088/0004-637X/700/1/221. arXiv: 0905.1692 [astro-ph.CO].

Kriek, Mariska, and Charlie Conroy. 2013. "The Dust Attenuation Law In Distant Galaxies: Evidence For Variation With Spectral Type." *The Astrophysical Journal* 775, no. 1 (September): L16. doi:10.1088/2041-8205/775/1/l16.

Krumholz, M. R., and A. Dekel. 2012. "Metallicity-dependent Quenching of Star Formation at High Redshift in Small Galaxies." *The Astrophysical Journal* 753, 16 (July): 16. doi:10.1088/0004-637X/753/1/16. arXiv: 1106.0301.

Kubota, Aya, and Chris Done. 2018. "A physical model of the broad-band continuum of AGN and its implications for the UV/X relation and optical variability." *Monthly Notices of the Royal Astronomical Society* 480, no. 1 (October): 1247–1262. doi:10.1093/mnras/sty1890. arXiv: 1804.00171 [astro-ph.HE].

Kuhlen, Michael, and Claude-André Faucher-Giguère. 2012. "Concordance models of reionization: implications for faint galaxies and escape fraction evolution." *Monthly Notices of the Royal Astronomical Society* 423, no. 1 (June): 862–876. doi:10.1111/j.1365-2966.2012.20924.x.

Kuhlen, Michael, and Piero Madau. 2005. "The first miniquasar." *Monthly Notices of the Royal Astronomical Society* 363, no. 4 (November): 1069–1082. doi:10.1111/j.1365-2966.2005.09522.x. eprint: http://oup.prod.sis.lan/mnras/article-pdf/363/4/1069/3536216/363-4-1069.pdf.

Kulkarni, Girish, Joseph F. Hennawi, Emmanuel Rollinde, and Elisabeth Vangioni. 2014. "Chemical Constraints On The Contribution Of Population III Stars To Cosmic Reionization." *The Astrophysical Journal* 787, no. 1 (May): 64. doi:10.1088/0004-637X/787/1/64.

Kulkarni, Girish, Gábor Worseck, and Joseph F Hennawi. 2019. "Evolution of the AGN UV luminosity function from redshift 7.5." *Monthly Notices of the Royal Astronomical Society* 488, no. 1 (June): 1035–1065. doi:10.1093/mnras/stz1493. eprint: http://oup.prod.sis.lan/mnras/article-pdf/488/1/1035/28934640/stz1493.pdf.

Kurk, J., A. Cimatti, E. Daddi, M. Mignoli, L. Pozzetti, M. Dickinson, M. Bolzonella, G. Zamorani, P. Cassata, and G. Rodighiero. 2013. "GMASS ultradeep spectroscopy of galaxies at z  2. VII. Sample selection and spectroscopy." *Astronomy and Astrophysics* 549, A63 (January): A63. doi:10.1051/0004-6361/201117847. arXiv: 1209.1561 [astro-ph.CO].

Kurk, J., A. Cimatti, E. Daddi, M. Mignoli, L. Pozzetti, M. Dickinson, M. Bolzonella, et al. 2012. "GMASS ultradeep spectroscopy of galaxies at z ˜ 2." *Astronomy and Astrophysics* 549 (December): A63. doi:10.1051/0004-6361/201117847.

Laird, E. S., K. Nandra, A. Hobbs, and C. C. Steidel. 2006. "The X-ray emission of Lyman break galaxies." *Monthly Notices of the Royal Astronomical Society* 373, no. 1 (October): 217–230. doi:10.1111/j.1365-2966.2006.11002.x. eprint: http://oup.prod.sis.lan/mnras/article-pdf/373/1/217/4184973/mnras0373-0217.pdf.

Le Fèvre, O., P. Cassata, O. Cucciati, B. Garilli, O. Ilbert, V. Le Brun, D. Maccagni, C. Moreau, M. Scodeggio, and L. Tresse. 2013. "The VIMOS VLT Deep Survey final data release: a spectroscopic sample of 35 016 galaxies and AGN out to z 6.7 selected with $17.5 \leq i_{AB} \leq 24.75$." *Astronomy and Astrophysics* 559, A14 (November): A14. doi:10.1051/0004-6361/201322179. arXiv: 1307.0545 [astro-ph.CO].

Le Fèvre, O., L. A. M. Tasca, P. Cassata, B. Garilli, V. Le Brun, D. Maccagni, L. Pentericci, et al. 2015. "The VIMOS Ultra-Deep Survey: ˜10 000 galaxies with spectroscopic redshifts to study galaxy assembly at early epochs $2 < z \simeq 6$." *Astronomy and Astrophysics* 576, A79 (April): A79. doi:10.1051/0004-6361/201423829. arXiv: 1403.3938.

Le Fèvre, O., G. Vettolani, S. Paltani, L. Tresse, G. Zamorani, V. Le Brun, C. Moreau, et al. 2004. "The VIMOS VLT Deep Survey. Public release of 1599 redshifts to $I_{AB} \leq 24$ across the Chandra Deep Field South." *Astronomy and Astrophysics* 428 (December): 1043–1049. doi:10.1051/0004-6361:20048072. eprint: astro-ph/0403628.

Leitet, E., N. Bergvall, N. Piskunov, and B. -G. Andersson. 2011. "Analyzing low signal-to-noise FUSE spectra. Confirmation of Lyman continuum escape from Haro 11." *Astronomy and Astrophysics* 532, A107 (August): A107. doi:10.1051/0004-6361/201015654. arXiv: 1106.1178 [astro-ph.CO].

Leitherer, Claus, Henry C. Ferguson, Timothy M. Heckman, and James D. Lowenthal. 1995. "The Lyman Continuum in Starburst Galaxies Observed with the Hopkins Ultraviolet Telescope." *The Astrophysical Journal* 454, no. 1 (November). doi:10.1086/309760.

Leitherer, Claus, Svea Hernandez, Janice C. Lee, and M. S. Oey. 2016. "Direct Detection of Lyman Continuum Escape from Local Starburst Galaxies with the Cosmic Origins Spectrograph." *The Astrophysical Journal* 823, no. 1, 64 (May): 64. doi:10.3847/0004-637X/823/1/64. arXiv: 1603.06779 [astro-ph.GA].

Leitherer, Claus, William D. Vacca, Peter S. Conti, Alexei V. Filippenko, Carmelle Robert, and Wallace L. W. Sargent. 1996. "Hubble Space Telescope Ultraviolet Imaging and Spectroscopy of the Bright Starburst in the Wolf-Rayet Galaxy NGC 4214." *The Astrophysical Journal* 465 (July): 717. doi:10.1086/177456.

Levenberg, Kenneth. 1944. "A Method for the Solution of Certain Non-Linear Problems in Least Squares." *The Quarterly of Applied Mathematics,* no. 2: 164–168. doi:10.1090/qam/10666.

Levshakov, S. A., Agafonova, I. I., Centurión, M., and Mazets, I. E. 2002. "Metal abundances and kinematics of quasar absorbers* - I. Absorption systems toward J2233-606." *A&A* 383 (3): 813–822. doi:10.1051/0004-6361:20011807.

Liu, Guilin, Nadia L. Zakamska, Jenny E. Greene, Nicole P. H. Nesvadba, and Xin Liu. 2013. "Observations of feedback from radio-quiet quasars – II. Kinematics of ionized gas nebulae." *Monthly Notices of the Royal Astronomical Society* 436, no. 3 (October): 2576–2597. doi:10.1093/mnras/stt1755. eprint: http://oup.prod.sis.lan/mnras/article-pdf/436/3/2576/4086109/stt1755.pdf.

Loeb, Abraham, and Rennan Barkana. 2001. "The Reionization of the Universe by the First Stars and Quasars." *Annual Review of Astronomy and Astrophysics* 39, no. 1 (September): 19–66. doi:10.1146/annurev.astro.39.1.19.

Lopez-Morales, M., K. France, F. R. Ferraro, R. Chandar, S. Finkelstein, S. Charlot, G. Ballester, et al. 2019. "Another Servicing Mission to Extend Hubble Space Telescope's Science past the Next Decade." In *Bulletin of the American Astronomical Society,* 51:96. Bulletin of the American Astronomical Society. September.

Lusso, E., A. Comastri, B. D. Simmons, M. Mignoli, G. Zamorani, C. Vignali, M. Brusa, et al. 2012. "Bolometric luminosities and Eddington ratios of X-ray selected active galactic nuclei in the XMM-COSMOS survey." *Monthly Notices of the Royal Astronomical Society* 425, no. 1 (September): 623–640. doi:10.1111/j.1365-2966.2012.21513.x. eprint: http://oup.prod.sis.lan/mnras/article-pdf/425/1/623/3222140/425-1-623.pdf.

Lusso, E., G. Worseck, J. F. Hennawi, J. X. Prochaska, C. Vignali, J. Stern, and J. M. O'Meara. 2015. "The first ultraviolet quasar-stacked spectrum at z $\simeq$ 2.4 from WFC3." *Monthly Notices of the Royal Astronomical Society* 449, no. 4 (April): 4204–4220. doi:10.1093/mnras/stv516. eprint: http://oup.prod.sis.lan/mnras/article-pdf/449/4/4204/18753804/stv516.pdf.

Lynds, R. 1971. "The Absorption-Line Spectrum of 4c 05.34." *The Astrophysical Journal, Letters* 164 (March): L73. doi:10.1086/180695.

Mack, J., E. Sabbi, and T. Dahlen. 2013. "In-flight Corrections to the WFC3 UVIS Flat Fields." *Instrument Science Report WFC3 2013-10 (STScI, Baltimore).*

Madau, Piero, Henry C. Ferguson, Mark E. Dickinson, Mauro Giavalisco, Charles C. Steidel, and Andrew Fruchter. 1996. "High-redshift galaxies in the Hubble Deep Field: colour selection and star formation history to z˜4." *Monthly Notices of the Royal Astronomical Society* 283 (4): 1388–1404.

Madau, P. 1995. "Radiative transfer in a clumpy universe: The colors of high-redshift galaxies." *The Astrophysical Journal* 441 (March): 18–27. doi:10.1086/175332.

Madau, P., and F. Haardt. 2015. "Cosmic Reionization after Planck: Could Quasars Do It All?" *The Astrophysical Journal, Letters* 813, L8 (November): L8. doi:10.1088/2041-8205/813/1/L8. arXiv: 1507.07678.

Madau, P., M. J. Rees, M. Volonteri, F. Haardt, and S. P. Oh. 2004. "Early Reionization by Miniquasars." *The Astrophysical Journal* 604, no. 2 (April): 484–494. doi:10.1086/381935.

Madau, Piero, and Mark Dickinson. 2014. "Cosmic Star-Formation History." *Annual Review of Astronomy and Astrophysics* 52 (1): 415–486. doi:10.1146/annurev-astro-081811-125615. eprint: https://doi.org/10.1146/annurev-astro-081811-125615.

Malkan, M. A., and W. L. W. Sargent. 1982. "The ultraviolet excess of Seyfert 1 galaxies and quasars." *The Astrophysical Journal* 254 (March): 22–37. doi:10.1086/159701.

Malkan, Matthew, Wayne Webb, and Quinn Konopacky. 2003. "A Hubble Space Telescope Search for Lyman Continuum Emission from Galaxies at $1.1 < z < 1.4$." *The Astrophysical Journal* 598, no. 2 (December): 878–885. doi:10.1086/379117.

Marconi, A., G. Risaliti, R. Gilli, L. K. Hunt, R. Maiolino, and M. Salvati. 2004. "Local supermassive black holes, relics of active galactic nuclei and the X-ray background." *Monthly Notices of the Royal Astronomical Society* 351, no. 1 (June): 169–185. doi:10.1111/j.1365-2966.2004.07765.x. arXiv: astro-ph/0311619 [astro-ph].

Marquardt, Donald W. 1963. "An algorithm for least-squares estimation of nonlinear parameters." *SIAM Journal on Applied Mathematics* 11 (2): 431–441. doi:10.1137/0111030.

Maseda, Michael V, Marijn Franx, Jacopo Chevallard, and Emma Curtis-Lake. 2019. "Abundant serendipitous emission line sources with JWST/NIRSpec." *Monthly*

*Notices of the Royal Astronomical Society* 486, no. 3 (March): 3290–3306. doi:10.1093/mnras/stz818. eprint: http://oup.prod.sis.lan/mnras/article-pdf/486/3/3290/28536566/stz818.pdf.

Massey, R., T. Schrabback, O. Cordes, O. Marggraf, H. Israel, L. Miller, D. Hall, M. Cropper, T. Prod'homme, and S.-M. Niemi. 2014. "An improved model of charge transfer inefficiency and correction algorithm for the Hubble Space Telescope." *Monthly Notices of the Royal Astronomical Society* 439 (March): 887–907. doi:10.1093/mnras/stu012. arXiv: 1401.1151 [astro-ph.IM].

Masters, D., P. Capak, M. Salvato, F. Civano, B. Mobasher, B. Siana, G. Hasinger, et al. 2012. "Evolution of the Quasar Luminosity Function over $3 < z < 5$ in the COSMOS Survey Field." *The Astrophysical Journal* 755, 169 (August): 169. doi:10.1088/0004-637X/755/2/169. arXiv: 1207.2154.

Mathis, J. S. 1990. "Interstellar dust and extinction." *Annual Review of Astronomy and Astrophysics* 28:37–70. doi:10.1146/annurev.aa.28.090190.000345.

Mathis, John S. 1971. "Internal Dust in Gaseous Nebulae. II. Absorption of Lyman-Continuum Radiation by Dust." *The Astrophysical Journal* 167 (August): 261. doi:10.1086/151029.

McGreer, I. D., A. Mesinger, and V. D'Odorico. 2014. "Model-independent evidence in favour of an end to reionization by z  6." *Monthly Notices of the Royal Astronomical Society* 447, no. 1 (December): 499–505. doi:10.1093/mnras/stu2449.

McGuire, J. T. W., N. R. Tanvir, A. J. Levan, M. Trenti, E. R. Stanway, J. M. Shull, K. Wiersema, et al. 2016. "Detection of Three Gamma-ray Burst Host Galaxies at z∼6." *The Astrophysical Journal* 825, 135 (July): 135. doi:10.3847/0004-637X/825/2/135. arXiv: 1512.07808.

McKee, C. F., and E. C. Ostriker. 2007. "Theory of Star Formation." *Annual Review of Astronomy and Astrophysics* 45 (September): 565–687. doi:10.1146/annurev.astro.45.051806.110602. arXiv: 0707.3514.

McKee, Christopher F., and Jonathan C. Tan. 2008. "The Formation of the First Stars. II. Radiative Feedback Processes and Implications for the Initial Mass Function." *The Astrophysical Journal* 681, no. 2 (July): 771–797. doi:10.1086/587434.

McQuinn, Matthew. 2012. "Constraints on X-ray emissions from the reionization era." *Monthly Notices of the Royal Astronomical Society* 426, no. 2 (October): 1349–1360. doi:10.1111/j.1365-2966.2012.21792.x. eprint: http://oup.prod.sis.lan/mnras/article-pdf/426/2/1349/2969579/426-2-1349.pdf.

Mehdipour, M., Branduardi-Raymont, G., Kaastra, J. S., Petrucci, P. O., Kriss, G. A., Ponti, G., Blustin, A. J., et al. 2011. "Multiwavelength campaign on Mrk 509 - IV. Optical-UV-X-ray variability and the nature of the soft X-ray excess." *A&A* 534:A39. doi:10.1051/0004-6361/201116875.

Mehdipour, M., Kaastra, J. S., Kriss, G. A., Cappi, M., Petrucci, P.-O., Steenbrugge, K. C., Arav, N., et al. 2015. "Anatomy of the AGN in NGC 5548 - I. A global model for the broadband spectral energy distribution." *A&A* 575:A22. doi:10.1051/0004-6361/201425373.

Meiksin, A. 2006. "The possible detection of high-redshift Type II QSOs in deep fields." *Monthly Notices of the Royal Astronomical Society* 365 (January): 833–841. doi:10.1111/j.1365-2966.2005.09746.x. eprint: astro-ph/0512437.

Menci, N., F. Fiore, C. Feruglio, A. Lamastra, F. Shankar, E. Piconcelli, E. Giallongo, and A. Grazian. 2019. "Outflows in the Disks of Active Galaxies." *The Astrophysical Journal* 877, 74 (June): 74. doi:10.3847/1538-4357/ab1a3a.

Menci, N., F. Fiore, S. Puccetti, and A. Cavaliere. 2008. "The Blast Wave Model for AGN Feedback: Effects on AGN Obscuration." *The Astrophysical Journal* 686 (October): 219–229. doi:10.1086/591438. arXiv: 0806.4543.

Mesinger, A., A. Aykutalp, E. Vanzella, L. Pentericci, A. Ferrara, and M. Dijkstra. 2014. "Can the intergalactic medium cause a rapid drop in Ly  emission at z > 6?" *Monthly Notices of the Royal Astronomical Society* 446, no. 1 (November): 566–577. doi:10.1093/mnras/stu2089.

Mesinger, Andrei, and Zoltán Haiman. 2004. "Evidence of a Cosmological Strömgren Surface and of Significant Neutral Hydrogen Surrounding the Quasar SDSS J1030+0524." *The Astrophysical Journal* 611, no. 2 (August): L69–L72. doi:10.1086/423935.

Micheva, G., I. Iwata, and A. K. Inoue. 2017. "Lyman continuum leaking AGN in the SSA22 field." *Monthly Notices of the Royal Astronomical Society* 465 (February): 302–315. doi:10.1093/mnras/stw1329. arXiv: 1604.00102.

Middei, R., Bianchi, S., Cappi, M., Petrucci, P.-O., Ursini, F., Arav, N., Behar, E., et al. 2018. "Multi-wavelength campaign on NCG 7469 - IV. The broad-band X-ray spectrum." *A&A* 615:A163. doi:10.1051/0004-6361/201832726.

Mignoli, M., A. Cimatti, G. Zamorani, L. Pozzetti, E. Daddi, A. Renzini, T. Broadhurst, S. Cristiani, S. D'Odorico, and A. Fontana. 2005. "The K20 survey. VII. The spectroscopic catalogue: Spectral properties and evolution of the galaxy popu-

lation." *Astronomy and Astrophysics* 437, no. 3 (July): 883–897. doi:10.1051/0004-6361:20042434. arXiv: astro-ph/0504248 [astro-ph].

Miller, N. A., M. Bonzini, E. B. Fomalont, K. I. Kellermann, V. Mainieri, P. Padovani, P. Rosati, P. Tozzi, and S. Vattakunnel. 2013. "The Very Large Array 1.4 GHz Survey of the Extended Chandra Deep Field South: Second Data Release." *The Astrophysical Journal, Supplements* 205, 13 (April): 13. doi:10.1088/0067-0049/205/2/13. arXiv: 1301.7004.

Mirabel, I. F., M. Dijkstra, P. Laurent, A. Loeb, and J. R. Pritchard. 2011. "Stellar black holes at the dawn of the universe." *Astronomy and Astrophysics* 528 (March): A149. doi:10.1051/0004-6361/201016357.

Miralda-Escudé, Jordi. 2003. "The Dark Age of the Universe." *Science* 300 (5627): 1904–1909. doi:10.1126/science.1085325. eprint: https://science.sciencemag.org/content/300/5627/1904.full.pdf.

Miralda-Escudé, Jordi, Martin Haehnelt, and Martin J. Rees. 2000. "Reionization of the Inhomogeneous Universe." *The Astrophysical Journal* 530, no. 1 (February): 1–16. doi:10.1086/308330.

Mitra, Sourav, T. Roy Choudhury, and Andrea Ferrara. 2017. "Cosmic reionization after Planck II: contribution from quasars." *Monthly Notices of the Royal Astronomical Society* 473, no. 1 (September): 1416–1425. doi:10.1093/mnras/stx2443. eprint: http://oup.prod.sis.lan/mnras/article-pdf/473/1/1416/21429460/stx2443.pdf.

Mitsuda, K., H. Inoue, K. Koyama, K. Makishima, M. Matsuoka, Y. Ogawara, N. Shibazaki, K. Suzuki, Y. Tanaka, and T. Hirano. 1984. "Energy spectra of low-mass binary X-ray sources observed from TENMA." 36:741–759.

Mizusawa, Hiromi, Kazuyuki Omukai, and Ryoichi Nishi. 2005. "Primordial Molecular Emission in Population III Galaxies." *Publications of the Astronomical Society of Japan* 57, no. 6 (December): 951–967. doi:10.1093/pasj/57.6.951. eprint: http://oup.prod.sis.lan/pasj/article-pdf/57/6/951/17449716/pasj57-0951.pdf.

Momcheva, I. G., G. B. Brammer, P. G. van Dokkum, R. E. Skelton, K. E. Whitaker, E. J. Nelson, M. Fumagalli, et al. 2016. "The 3D-HST Survey: Hubble Space Telescope WFC3/G141 Grism Spectra, Redshifts, and Emission Line Measurements for ˜ 100,000 Galaxies." *The Astrophysical Journal, Supplements* 225, 27 (August): 27. doi:10.3847/0067-0049/225/2/27. arXiv: 1510.02106.

Moos, H. W., W. C. Cash, L. L. Cowie, A. F. Davidsen, A. K. Dupree, P. D. Feldman, S. D. Friedman, et al. 2000. "Overview of the [ITAL]Far Ultraviolet Spectroscopic

Explorer[/ITAL] Mission." *The Astrophysical Journal* 538, no. 1 (July): L1–L6. doi:10.1086/312795.

Morrissey, Patrick, Tim Conrow, Tom A. Barlow, Todd Small, Mark Seibert, Ted K. Wyder, Tamas Budavari, et al. 2007. "The Calibration and Data Products ofGALEX." *The Astrophysical Journal Supplement Series* 173, no. 2 (December): 682–697. doi:10.1086/520512.

Mostardi, R. E., A. E. Shapley, D. B. Nestor, C. C. Steidel, N. A. Reddy, and R. F. Trainor. 2013. "Narrowband Lyman-continuum Imaging Of Galaxies At z $\sim$ 2.85." *The Astrophysical Journal* 779, no. 1 (December): 65. doi:10.1088/0004-637X/779/1/65.

Mostardi, R. E., A. E. Shapley, C. C. Steidel, R. F. Trainor, N. A. Reddy, and B. Siana. 2015. "A High-Resolution Hubble Space Telescope Study of Apparent Lyman Continuum Leakers at z$\sim$3." *The Astrophysical Journal* 810, 107 (September): 107. doi:10.1088/0004-637X/810/2/107. arXiv: 1506.08201.

Mukhanov, V. 2004. "Nucleosynthesis Without Computer." *International Journal of Theoretical Physics* 43, no. 3 (March): 669–693. doi:10.1023/B:IJTP.0000048169.69609.77.

Müller-Sánchez, F., M. A. Prieto, E. K. S. Hicks, H. Vives-Arias, R. I. Davies, M. Malkan, L. J. Tacconi, and R. Genzel. 2011. "OUTFLOWS FROM ACTIVE GALACTIC NUCLEI: KINEMATICS OF THE NARROW-LINE AND CORONAL-LINE REGIONS IN SEYFERT GALAXIES," *The Astrophysical Journal* 739, no. 2 (September): 69. doi:10.1088/0004-637x/739/2/69.

Mushotzky, Richard F., Christine Done, and Kenneth A. Pounds. 1993. "X-ray spectra and time variability of active galactic nuclei." *Annual Review of Astronomy and Astrophysics* 31 (January): 717–717. doi:10.1146/annurev.aa.31.090193.003441.

Nakajima, Kimihiko, and Masami Ouchi. 2014. "Ionization state of inter-stellar medium in galaxies: evolution, SFR-$M_*$-Z dependence, and ionizing photon escape." *Monthly Notices of the Royal Astronomical Society* 442, no. 1 (July): 900–916. doi:10.1093/mnras/stu902. arXiv: 1309.0207 [astro-ph.CO].

Nestor, Daniel B., Alice E. Shapley, Katherine A. Kornei, Charles C. Steidel, and Brian Siana. 2013. "A Refined Estimate Of The Ionizing Emissivity From Galaxies At Z $\simeq$ 3: Spectroscopic Follow-up In The Ssa22a Field." *The Astrophysical Journal* 765, no. 1 (March): 47. doi:10.1088/0004-637X/765/1/47.

Nestor, Daniel B., Alice E. Shapley, Charles C. Steidel, and Brian Siana. 2011. "Narrowband Imaging Of Escaping Lyman-continuum Emission In The Ssa22 Field." *The Astrophysical Journal* 736, no. 1 (July): 18. doi:10.1088/0004-637X/736/1/18.

Netzer, H. 2013. *The Physics and Evolution of Active Galactic Nuclei.* November.

Noeske, K., S. Baggett, H. Bushouse, L. Petro, R. Gilliland, and V. Khozurina-Platais. 2012. *WFC3 UVIS Charge Transfer Eciency October 2009 to October 2011.* Technical report. June.

O'Shea, Brian W., and Michael L. Norman. 2007. "Population III Star Formation in a ΛCDM Universe. I. The Effect of Formation Redshift and Environment on Protostellar Accretion Rate." *The Astrophysical Journal* 654, no. 1 (January): 66–92. doi:10.1086/509250.

Oesch, P. A., M. Montes, N. Reddy, R. J. Bouwens, G. D. Illingworth, D. Magee, H. Atek, et al. 2018. "HDUV: The Hubble Deep UV Legacy Survey." *The Astrophysical Journal Supplement Series* 237, no. 1 (July): 12. doi:10.3847/1538-4365/aacb30.

Oey, M.S., and Jr. Kennicutt R.C. 1997. "Comparison of H II region luminosities with observed stellar ionizing sources in the Large Magellanic Cloud." *Monthly Notices of the Royal Astronomical Society* 291.

Oh, Siang Peng. 1999. "Observational Signatures of the First Luminous Objects." *The Astrophysical Journal* 527, no. 1 (December): 16–30. doi:10.1086/308077. arXiv: astro-ph/9904255 [astro-ph].

Omukai, K., and R. Nishi. 1998. "Formation of Primordial Protostars." *The Astrophysical Journal* 508 (November): 141–150. doi:10.1086/306395. eprint: astro-ph/9811308.

Osmer, Patrick S., and Paul C. Hewett. 1991. "A New Survey for Quasar Clustering." *The Astrophysical Journal, Supplements* 75 (February): 273. doi:10.1086/191532.

Ouchi, Masami, Bahram Mobasher, Kazuhiro Shimasaku, Henry C. Ferguson, S. Michael Fall, Yoshiaki Ono, Nobunari Kashikawa, et al. 2009. "LARGE AREA SURVEY FOR z = 7 GALAXIES IN SDF AND GOODS-N: IMPLICATIONS FOR GALAXY FORMATION AND COSMIC REIONIZATION." *The Astrophysical Journal* 706, no. 2 (December): 1136–1151. doi:10.1088/0004-637X/706/2/1136.

Paardekooper, Jan-Pieter, Sadegh Khochfar, and Claudio Dalla Vecchia. 2015. "The First Billion Years project: the escape fraction of ionizing photons in the epoch of reionization." *Monthly Notices of the Royal Astronomical Society* 451, no. 3 (August): 2544–2563. doi:10.1093/mnras/stv1114. arXiv: 1501.01967 [astro-ph.CO].

Padoan, P., M. Juvela, A. A. Goodman, and Å. Nordlund. 2001. "The Turbulent Shock Origin of Proto-Stellar Cores." *The Astrophysical Journal* 553 (May): 227–234. doi:10.1086/320636. eprint: astro-ph/0011122.

Paresce, F., C. F. McKee, and S. Bowyer. 1980. "Galactic and extragalactic contributions to the far-ultraviolet background." *The Astrophysical Journal* 240 (September): 387–400. doi:10.1086/158244.

Peebles, P. J. E. 1968. "Recombination of the Primeval Plasma." *The Astrophysical Journal* 153 (July): 1. doi:10.1086/149628.

Penny, Samantha J., Karen L. Masters, Rebecca Smethurst, Robert C. Nichol, Coleman M. Krawczyk, Dmitry Bizyaev, Olivia Greene, et al. 2018. "SDSS-IV MaNGA: evidence of the importance of AGN feedback in low-mass galaxies." *Monthly Notices of the Royal Astronomical Society* 476, no. 1 (May): 979–998. doi:10.1093/mnras/sty202. arXiv: 1710.07568 [astro-ph.GA].

Pentericci, L., R. J. McLure, B. Garilli, O. Cucciati, P. Franzetti, A. Iovino, R. Amorin, et al. 2018. "The VANDELS ESO public spectroscopic survey: Observations and first data release." *Astronomy and Astrophysics* 616, A174 (September): A174. doi:10.1051/0004-6361/201833047. arXiv: 1803.07373.

Péroux, C., R. G. McMahon, L. J. Storrie-Lombardi, and M. J. Irwin. 2003. "The evolution of ΩHI and the epoch of formation of damped Lyman$\alpha$ absorbers." *Monthly Notices of the Royal Astronomical Society* 346, no. 4 (December): 1103–1115. doi:10.1111/j.1365-2966.2003.07129.x. eprint: http://academic.oup.com/mnras/article-pdf/346/4/1103/18647575/346-4-1103.pdf.

Petrucci, P. O., F. Ursini, A. De Rosa, S. Bianchi, M. Cappi, G. Matt, M. Dadina, and J. Malzac. 2018. "Testing warm Comptonization models for the origin of the soft X-ray excess in AGNs." *Astronomy and Astrophysics* 611, A59 (March): A59. doi:10.1051/0004-6361/201731580. arXiv: 1710.04940 [astro-ph.HE].

Petrucci, P.-O., Paltani, S., Malzac, J., Kaastra, J. S., Cappi, M., Ponti, G., De Marco, B., et al. 2013. "Multiwavelength campaign on Mrk 509 - XII. Broad band spectral analysis." *A&A* 549:A73. doi:10.1051/0004-6361/201219956.

Planck Collaboration. 2016. "Planck intermediate results - XLVII. Planck constraints on reionization history." *A&A* 596:A108. doi:10.1051/0004-6361/201628897.

———. 2018. *Planck 2018 results. IV. Diffuse component separation.* arXiv: 1807.06208 [astro-ph.CO].

Politis, Dimitris N., Joseph P. Romano, and Michael Wolf. 1999. *Subsampling.* 1st ed. Vol. 4. Springer-Verlan New York, July.

Polletta, M., M. Tajer, L. Maraschi, G. Trinchieri, C. J. Lonsdale, L. Chiappetti, S. Andreon, et al. 2007. "Spectral Energy Distributions of Hard X-Ray Selected Active Galactic Nuclei in the XMM-Newton Medium Deep Survey." *The Astrophysical Journal* 663 (July): 81–102. doi:10.1086/518113. eprint: astro-ph/0703255.

Popesso, P., M. Dickinson, M. Nonino, E. Vanzella, E. Daddi, R. A. E. Fosbury, H. Kuntschner, et al. 2009. "The great observatories origins deep survey." *Astronomy and Astrophysics* 494, no. 2 (February): 443–460. doi:10.1051/0004-6361:20080961 7.

Porquet, D., Reeves, J. N., Matt, G., Marinucci, A., Nardini, E., Braito, V., Lobban, A., et al. 2018. "A deep X-ray view of the bare AGN Ark - IV. XMM-Newton and NuSTAR spectra dominated by two temperature (warm, hot) Comptonization processes." *A&A* 609:A42. doi:10.1051/0004-6361/201731290.

Prestwich, A. H., F. Jackson, P. Kaaret, M. Brorby, T. P. Roberts, S. H. Saar, and M. Yukita. 2015. "Ultra-luminous X-Ray Sources in HARO II and the Role of X-Ray Binaries in Feedback in Ly$\alpha$ Emitting Galaxies." *The Astrophysical Journal* 812, no. 2, 166 (October): 166. doi:10.1088/0004-637X/812/2/166. arXiv: 1507.07900 [astro-ph.HE].

Prevot, M. L., J. Lequeux, E. Maurice, L. Prevot, and B. Rocca-Volmerange. 1984. "The typical interstellar extinction in the Small Magellanic Cloud." *Astronomy and Astrophysics* 132 (March): 389–392.

Prochaska, J. X. 1999. "The Physical Nature of the Lyman-Limit Systems." *The Astrophysical Journal, Letters* 511 (February): L71–L74. doi:10.1086/311849. eprint: astro-ph/9811357.

Puschnig, J., M. Hayes, G. Östlin, T. E. Rivera-Thorsen, J. Melinder, J. M. Cannon, V. Menacho, E. Zackrisson, N. Bergvall, and E. Leitet. 2017. "The Lyman continuum escape and ISM properties in Tololo 1247-232 – new insights from HST and VLA." *Monthly Notices of the Royal Astronomical Society* 469, no. 3 (April): 3252–3269.

doi:10.1093/mnras/stx951. eprint: http://oup.prod.sis.lan/mnras/article-pdf/469/3/3252/17654225/stx951.pdf.

Putman, M. E., J. Bland-Hawthorn, S. Veilleux, B. K. Gibson, K. C. Freeman, and P. R. Maloney. 2003. "H$\alpha$ Emission from High-Velocity Clouds and Their Distances." *The Astrophysical Journal* 597, no. 2 (November): 948–956. doi:10.1086/378555.

Putman, M. E., J. E. G. Peek, and M. R. Joung. 2012. "Gaseous Galaxy Halos." *Annual Review of Astronomy and Astrophysics* 50 (September): 491–529. doi:10.1146/annurev-astro-081811-125612. arXiv: 1207.4837 [astro-ph.GA].

Rachford, B. L., T. P. Snow, J. Tumlinson, J. M. Shull, W. P. Blair, R. Ferlet, S. D. Friedman, et al. 2002. "A Far Ultraviolet Spectroscopic Explorer Survey of Interstellar Molecular Hydrogen in Translucent Clouds." *The Astrophysical Journal* 577 (September): 221–244. doi:10.1086/342146. eprint: astro-ph/0205415.

Rafelski, M., H. I. Teplitz, J. P. Gardner, D. Coe, N. A. Bond, A. M. Koekemoer, N. Grogin, et al. 2015. "UVUDF: Ultraviolet Through Near-infrared Catalog and Photometric Redshifts of Galaxies in the Hubble Ultra Deep Field." *The Astronomical Journal* 150, 31 (July): 31. doi:10.1088/0004-6256/150/1/31. arXiv: 1505.01160.

Rangel, C., K. Nandra, E. S. Laird, and P. Orange. 2013. "X-ray properties of BzK-selected galaxies in the deepest X-ray fields." *Monthly Notices of the Royal Astronomical Society* 428 (February): 3089–3103. doi:10.1093/mnras/sts256. arXiv: 1211.1028.

Rao, Sandhya M., and David A. Turnshek. 2000. "Discovery of Damped Ly$\alpha$ Systems at Redshifts Less than 1.65 and Results on Their Incidence and Cosmological Mass Density." *The Astrophysical Journal Supplement Series* 130, no. 1 (September): 1–35. doi:10.1086/317344.

Rauch, M., G. D. Becker, M. G. Haehnelt, J.-R. Gauthier, S. Ravindranath, and W. L. W. Sargent. 2011. "Filamentary infall of cold gas and escape of Ly$\alpha$ and hydrogen ionizing radiation from an interacting high-redshift galaxy." *Monthly Notices of the Royal Astronomical Society* 418 (December): 1115–1126. doi:10.1111/j.1365-2966.2011.19556.x. arXiv: 1105.4876.

Razoumov, Alexei O., and Jesper Sommer–Larsen. 2010. "IONIZING RADIATION FROM z = 4–10 GALAXIES." *The Astrophysical Journal* 710, no. 2 (February): 1239–1246. doi:10.1088/0004-637X/710/2/1239.

Razoumov, Alexei O., and Jesper Sommer–Larsen. 2007. "Modeling Lyman Continuum Emission from Young Galaxies." *The Astrophysical Journal* 668, no. 2 (October): 674–681. doi:10.1086/521041.

Redding, D., S. Sirlin, A. Boden, J. Mo, R. Hanisch, and L. Furey. 1995. "Optical Prescription of the HST." In *Calibrating Hubble Space Telescope. Post Servicing Mission,* edited by Anuradha P. Koratkar and Claus Leitherer, 132. January.

Reddy, Naveen A., and Charles C. Steidel. 2009. "A Steep Faint-end Slope Of The Uv Luminosity Function At z∼2-3: Implications For The Global Stellar Mass Density And Star Formation In Low-mass Halos." *The Astrophysical Journal* 692, no. 1 (February): 778–803. doi:10.1088/0004-637X/692/1/778.

Reddy, Naveen A., Charles C. Steidel, Dawn K. Erb, Alice E. Shapley, and Max Pettini. 2006. "A Spectroscopic Survey of Redshift 1.4<<~3.0 Galaxies in the GOODS-North Field: Survey Description, Catalogs, and Properties." *The Astrophysical Journal* 653, no. 2 (December): 1004–1026. doi:10.1086/508851. arXiv: astro-ph/0609296 [astro-ph].

Rees, M. J. 1968. "Polarization and Spectrum of the Primeval Radiation in an Anisotropic Universe." *The Astrophysical Journal, Letters* 153 (July): L1. doi:10.1086/180208.

Reunanen, J., J. K. Kotilainen, and M. A. Prieto. 2003. "Near-infrared spectroscopy of nearby Seyfert galaxies - II. Molecular content and coronal emission." *Monthly Notices of the Royal Astronomical Society* 343 (July): 192–208. doi:10.1046/j.1365-8711.2003.06771.x. eprint: astro-ph/0305100.

Reynolds, Christopher S., Sebastian Heinz, and Mitchell C. Begelman. 2002. "The hydrodynamics of dead radio galaxies." *Monthly Notices of the Royal Astronomical Society* 332, no. 2 (May): 271–282. doi:10.1046/j.1365-8711.2002.04724.x. arXiv: astro-ph/0201271 [astro-ph].

Richings, A. J., J. Schaye, and B. D. Oppenheimer. 2014. "Non-equilibrium chemistry and cooling in the diffuse interstellar medium - II. Shielded gas." *Monthly Notices of the Royal Astronomical Society* 442 (August): 2780–2796. doi:10.1093/mnras/stu1046. arXiv: 1403.6155.

Ricotti, M. 2002. "Did globular clusters reionize the Universe?" *Monthly Notices of the Royal Astronomical Society* 336, no. 2 (October): L33–L37. doi:10.1046/j.1365-8711.2002.05990.x.

Ricotti, Massimo, and J. Michael Shull. 2000. "Feedback from Galaxy Formation: Escaping Ionizing Radiation from Galaxies at High Redshift." *The Astrophysical Journal* 542, no. 2 (October): 548–558. doi:10.1086/317025.

Riess, A. G., L.-G. Strolger, S. Casertano, H. C. Ferguson, B. Mobasher, B. Gold, P. J. Challis, et al. 2007. "New Hubble Space Telescope Discoveries of Type Ia Supernovae at z >= 1: Narrowing Constraints on the Early Behavior of Dark Energy." *The Astrophysical Journal* 659 (April): 98–121. doi:10.1086/510378. eprint: astro-ph/0611572.

Ripamonti, E., and T. Abel. 2004. "Fragmentation and the formation of primordial protostars: the possible role of collision-induced emission." *Monthly Notices of the Royal Astronomical Society* 348, no. 3 (March): 1019–1034. doi:10.1111/j.1365-2966.2004.07422.x. arXiv: astro-ph/0311355 [astro-ph].

Robertson, B. E., R. S. Ellis, S. R. Furlanetto, and J. S. Dunlop. 2015. "Cosmic Reionization and Early Star-forming Galaxies: A Joint Analysis of New Constraints from Planck and the Hubble Space Telescope." *The Astrophysical Journal, Letters* 802, L19 (April): L19. doi:10.1088/2041-8205/802/2/L19. arXiv: 1502.02024.

Robertson, Brant E., Steven R. Furlanetto, Evan Schneider, Stephane Charlot, Richard S. Ellis, Daniel P. Stark, Ross J. McLure, et al. 2013. "NEW CONSTRAINTS ON COSMIC REIONIZATION FROM THE 2012 HUBBLE ULTRA DEEP FIELD CAMPAIGN." *The Astrophysical Journal* 768, no. 1 (May): 71. doi:10.1088/0004-637X/768/1/71.

Roychowdhury, S., M. Ruszkowski, B. B. Nath, and Mitchell C. Begelman. 2004. "Entropy "Floor" and Effervescent Heating of Intracluster Gas." *The Astrophysical Journal* 615, no. 2 (November): 681–688. doi:10.1086/424502.

Różańska, A., Malzac, J., Belmont, R., Czerny, B., and Petrucci, P.-O. 2015. "Warm and optically thick dissipative coronae above accretion disks." *A&A* 580:A77. doi:10.1051/0004-6361/201526288.

Rutkowski, Michael J., Claudia Scarlata, Francesco Haardt, Brian Siana, Alaina Henry, Marc Rafelski, Matthew Hayes, et al. 2016. "Lyman Continuum Escape Fraction of Star-forming Dwarf Galaxies at z$\sim$ 1." *The Astrophysical Journal* 819, no. 1, 81 (March): 81. doi:10.3847/0004-637X/819/1/81. arXiv: 1511.01998 [astro-ph.GA].

Sabbi, E. 2009. "WFC3 SMOV PROGRAM 11452: UVIS Flat Field Uniformity." *Instrument Science Report WFC3 2009-19 (STScI, Baltimore).*

Salpeter, E. E. 1955. "The Luminosity Function and Stellar Evolution." *The Astrophysical Journal* 121 (January): 161. doi:10.1086/145971.

Sandberg, A., G. Östlin, J. Melinder, A. Bik, and L. Guaita. 2015. "Limits On Lyman Continuum Escape from z=2.2 H$\alpha$-emitting Galaxies." *The Astrophysical Journal* 814, no. 1 (November): L10. doi:10.1088/2041-8205/814/1/l10.

Sarajedini, Vicki L., David C. Koo, Alison J. Klesman, Elise S. Laird, Pablo G. Perez Gonzalez, and Mark Mozena. 2011. "Variability And Multiwavelength-detected Active Galactic Nuclei In The Goods Fields." *The Astrophysical Journal* 731, no. 2 (March): 97. doi:10.1088/0004-637x/731/2/97.

Savage, B. D., and J. S. Mathis. 1979. "Observed properties of interstellar dust." *Annual Review of Astronomy and Astrophysics* 17:73–111. doi:10.1146/annurev.aa.17.090179.000445.

Schreiber, C., K. Glazebrook, T. Nanayakkara, G. G. Kacprzak, I. Labbé, P. Oesch, T. Yuan, et al. 2018. "Near infrared spectroscopy and star-formation histories of $3 \leq z \leq 4$ quiescent galaxies." *Astronomy and Astrophysics* 618, A85 (October): A85. doi:10.1051/0004-6361/201833070. arXiv: 1807.02523.

Schroeder, J., A. Mesinger, and Z. Haiman. 2012. "Evidence of Gunn-Peterson damping wings in high-z quasar spectra: strengthening the case for incomplete reionization at z  6-7." *Monthly Notices of the Royal Astronomical Society* 428, no. 4 (November): 3058–3071. doi:10.1093/mnras/sts253.

Scott, Jennifer E., Gerard A. Kriss, Michael Brotherton, Richard F. Green, John Hutchings, J. Michael Shull, and Wei Zheng. 2004. "A Composite Extreme-Ultraviolet QSO Spectrum from FUSE." *The Astrophysical Journal* 615, no. 1 (November): 135–149. doi:10.1086/422336. arXiv: astro-ph/0407203 [astro-ph].

Sérsic, J. L. 1963. "Influence of the atmospheric and instrumental dispersion on the brightness distribution in a galaxy." *Boletin de la Asociacion Argentina de Astronomia La Plata Argentina* 6 (January): 41.

Shakura, N. I., and R. A. Sunyaev. 1973. "Black holes in binary systems. Observational appearance." *Astronomy and Astrophysics* 24:337–355.

Shapiro, P. R., and H. Kang. 1987. "Hydrogen molecules and the radiative cooling of pregalactic shocks." *The Astrophysical Journal* 318 (July): 32–65. doi:10.1086/165350.

Shapiro, Paul R., Kyungjin Ahn, Marcelo A. Alvarez, Ilian T. Iliev, Hugo Martel, and Dongsu Ryu. 2006. "The 21 cm Background from the Cosmic Dark Ages: Minihalos and the Intergalactic Medium before Reionization." *The Astrophysical Journal* 646, no. 2 (August): 681–690. doi:10.1086/504972.

Shapley, Alice E., Charles C. Steidel, Max Pettini, and Kurt L. Adelberger. 2003. "Rest-Frame Ultraviolet Spectra of $z \sim 3$ Lyman Break Galaxies." *The Astrophysical Journal* 588, no. 1 (May): 65–89. doi:10.1086/373922.

Shapley, Alice E., Charles C. Steidel, Max Pettini, Kurt L. Adelberger, and Dawn K. Erb. 2006. "The Direct Detection of Lyman Continuum Emission from Star-forming Galaxies at z ∼3." *The Astrophysical Journal* 651, no. 2 (November): 688–703. doi:10.1086/507511.

Shchekinov, Y. A., and M. B. Entel. 1984. "Molecular Hydrogen as a Probe of the Early Universe." 28 (June): 270–274.

Shields, G. A. 1978. "Thermal continuum from accretion disks in quasars." *Nature* 272, no. 5655 (April): 706–708. doi:10.1038/272706a0.

Shull, J. Michael, Matthew Stevans, and Charles W. Danforth. 2012. "HST-COS Observations of AGNs. I. Ultraviolet Composite Spectra of the Ionizing Continuum and Emission Lines." *The Astrophysical Journal* 752, no. 2, 162 (June): 162. doi:10.1088/0004-637X/752/2/162. arXiv: 1204.3908 [astro-ph.CO].

Shupe, D. L., Mehdrdad Moshir, J. Li, D. Makovoz, R. Narron, and R. N. Hook. 2005. "The SIP Convention for Representing Distortion in FITS Image Headers." In *Astronomical Data Analysis Software and Systems XIV,* edited by P. Shopbell, M. Britton, and R. Ebert, 347:491. Astronomical Society of the Pacific Conference Series. December.

Siana, Brian, Alice E. Shapley, Kristin R. Kulas, Daniel B. Nestor, Charles C. Steidel, Harry I. Teplitz, Anahita Alavi, et al. 2015. "A Deep Hubble Space Telescope And Keck Search For Definitive Identification Of Lyman Continuum Emitters At z∼3.1." *The Astrophysical Journal* 804, no. 1 (April): 17. doi:10.1088/0004-637X/804/1/17.

Siana, Brian, Harry I. Teplitz, James Colbert, Henry C. Ferguson, Mark Dickinson, Thomas M. Brown, Christopher J. Conselice, et al. 2007. "New Constraints on the Lyman Continuum Escape Fraction at z ∼ 1.3." *The Astrophysical Journal* 668, no. 1 (October): 62–73. doi:10.1086/521185.

Siana, Brian, Harry I. Teplitz, Henry C. Ferguson, Thomas M. Brown, Mauro Giavalisco, Mark Dickinson, Ranga-Ram Chary, et al. 2010. "A Deep Hubble Space Telescope Search for Escaping Lyman Continuum Flux at z∼1.3: Evidence for an Evolving Ionizing Emissivity." *The Astrophysical Journal* 723, no. 1 (November): 241–250. doi:10.1088/0004-637X/723/1/241.

Silk, J. 2005. "Ultraluminous starbursts from supermassive black hole-induced outflows." *Monthly Notices of the Royal Astronomical Society* 364 (December): 1337–1342. doi:10.1111/j.1365-2966.2005.09672.x. eprint: astro-ph/0509149.

Silk, Joseph, and Colin Norman. 2009. "Global Star Formation Revisited." *The Astrophysical Journal* 700, no. 1 (July): 262–275. doi:10.1088/0004-637X/700/1/262.

Silva, L., R. Maiolino, and G. L. Granato. 2004. "Connecting the cosmic infrared background to the X-ray background." *Monthly Notices of the Royal Astronomical Society* 355 (December): 973–985. doi:10.1111/j.1365-2966.2004.08380.x. eprint: astro-ph/0403381.

Silverman, J. D., P. J. Green, W. A. Barkhouse, D.-W. Kim, M. Kim, B. J. Wilkes, R. A. Cameron, et al. 2008. "The Luminosity Function of X-Ray-selected Active Galactic Nuclei: Evolution of Supermassive Black Holes at High Redshift." *The Astrophysical Journal* 679 (May): 118–139. doi:10.1086/529572. arXiv: 0710.2461.

Silverman, J. D., V. Mainieri, M. Salvato, G. Hasinger, J. Bergeron, P. Capak, G. Szokoly, et al. 2010. "THE EXTENDED CHANDRA DEEP FIELD-SOUTH SURVEY: OPTICAL SPECTROSCOPY OF FAINT X-RAY SOURCES WITH THE VLT AND KECK." *The Astrophysical Journal, Supplements* 191, no. 1 (November): 124–142. doi:10.1088/0067-0049/191/1/124.

Skelton, R. E., K. E. Whitaker, I. G. Momcheva, G. B. Brammer, P. G. van Dokkum, I. Labbé, M. Franx, et al. 2014. "3D-HST WFC3-selected Photometric Catalogs in the Five CANDELS/3D-HST Fields: Photometry, Photometric Redshifts, and Stellar Masses." *The Astrophysical Journal, Supplements* 214, 24 (October): 24. doi:10.1088/0067-0049/214/2/24. arXiv: 1403.3689.

Smith, B. M., R. A. Windhorst, R. A. Jansen, S. H. Cohen, L. Jiang, M. Dijkstra, A. M. Koekemoer, et al. 2018. "Hubble Space Telescope Wide Field Camera 3 Observations of Escaping Lyman Continuum Radiation from Galaxies and Weak AGN at Redshifts z ∼ 2.3-4.1." *The Astrophysical Journal* 853, 191 (February): 191. doi:10.3847/1538-4357/aaa3dc.

Smith, Linda J., Richard P. F. Norris, and Paul A. Crowther. 2002. "Realistic ionizing fluxes for young stellar populations from 0.05 to 2 $Z_{solar}$." *Monthly Notices of the Royal Astronomical Society* 337, no. 4 (December): 1309–1328. doi:10.1046/j.1365-8711.2002.06042.x. arXiv: astro-ph/0207554 [astro-ph].

Springel, Volker, Tiziana Di Matteo, and Lars Hernquist. 2005. "Modelling feedback from stars and black holes in galaxy mergers." *Monthly Notices of the Royal Astronomical Society* 361, no. 3 (August): 776–794. doi:10.1111/j.1365-2966.2005.09238.x.

Stark, A. A., C. F. Gammie, R. W. Wilson, J. Bally, R. A. Linke, C. Heiles, and M. Hurwitz. 1992. "The Bell Laboratories H I survey." *The Astrophysical Journal, Supplements* 79 (March): 77–104. doi:10.1086/191645.

Stark, Daniel P. 2016. "Galaxies in the First Billion Years After the Big Bang." *Annual Review of Astronomy and Astrophysics* 54 (1): 761–803. doi:10.1146/annurev-astro-081915-023417. eprint: https://doi.org/10.1146/annurev-astro-081915-023417.

Steidel, Charles C., Milan Bogosavljević, Alice E. Shapley, Naveen A. Reddy, Gwen C. Rudie, Max Pettini, Ryan F. Trainor, and Allison L. Strom. 2018. "The Keck Lyman Continuum Spectroscopic Survey (KLCS): The Emergent Ionizing Spectrum of Galaxies at z$\sim$ 3." *The Astrophysical Journal* 869, no. 2, 123 (December): 123. doi:10.3847/1538-4357/aaed28. arXiv: 1805.06071 [astro-ph.GA].

Steidel, Charles C., Max Pettini, and Kurt L. Adelberger. 2001. "Lyman-Continuum Emission from Galaxies at z $\simeq$ 3.4." *The Astrophysical Journal* 546, no. 2 (January): 665–671. doi:10.1086/318323.

Sternberg, Amiel, Christopher F. McKee, and Mark G. Wolfire. 2002. "Atomic Hydrogen Gas in Dark Matter Minihalos and the Compact High-Velocity Clouds." *The Astrophysical Journal, Supplements* 143, no. 2 (December): 419–453. doi:10.1086/343032.

Stevans, Matthew L., J. Michael Shull, Charles W. Danforth, and Evan M. Tilton. 2014. "HST-COS Observations of AGNs. II. Extended Survey of Ultraviolet Composite Spectra from 159 Active Galactic Nuclei." *The Astrophysical Journal* 794, no. 1, 75 (October): 75. doi:10.1088/0004-637X/794/1/75. arXiv: 1408.5900 [astro-ph.GA].

Strickland, D. K., and I. R. Stevens. 2000. "Starburst-driven galactic winds - I. Energetics and intrinsic X-ray emission." *Monthly Notices of the Royal Astronomical*

*Society* 314 (May): 511–545. doi:10.1046/j.1365-8711.2000.03391.x. eprint: astro-ph/0001395.

Strickland, David K., and Timothy M. Heckman. 2009. "Supernova Feedback Efficiency And Mass Loading In The Starburst And Galactic Superwind Exemplar M82." *The Astrophysical Journal* 697, no. 2 (May): 2030–2056. doi:10.1088/0004-637x/697/2/2030.

Svensson, K. M., A. J. Levan, N. R. Tanvir, A. S. Fruchter, and L. -G. Strolger. 2010. "The host galaxies of core-collapse supernovae and gamma-ray bursts." *Monthly Notices of the Royal Astronomical Society* 405, no. 1 (June): 57–76. doi:10.1111/j.1365-2966.2010.16442.x. arXiv: 1001.5042 [astro-ph.HE].

Szalay, A. S., A. J. Connolly, and G. P. Szokoly. 1999. "Simultaneous Multicolor Detection of Faint Galaxies in the Hubble Deep Field." *The Astronomical Journal* 117 (January): 68–74. doi:10.1086/300689. eprint: astro-ph/9811086.

Szokoly, G. P., J. Bergeron, G. Hasinger, I. Lehmann, L. Kewley, V. Mainieri, M. Nonino, et al. 2004. "The Chandra Deep Field–South: Optical Spectroscopy. I." *The Astrophysical Journal, Supplements* 155, no. 2 (December): 271–349. doi:10.1086/424707.

Tanaka, Takamitsu, Rosalba Perna, and Zoltán Haiman. 2012. "X-ray emission from high-redshift miniquasars: self-regulating the population of massive black holes through global warming." *Monthly Notices of the Royal Astronomical Society* 425, no. 4 (October): 2974–2987. doi:10.1111/j.1365-2966.2012.21539.x. eprint: http://oup.prod.sis.lan/mnras/article-pdf/425/4/2974/4910958/425-4-2974.pdf.

Tanvir, N R, J P U Fynbo, A de Ugarte Postigo, J Japelj, K Wiersema, D Malesani, D A Perley, et al. 2018. "The fraction of ionizing radiation from massive stars that escapes to the intergalactic medium." *Monthly Notices of the Royal Astronomical Society* 483, no. 4 (December): 5380–5408. doi:10.1093/mnras/sty3460. eprint: http://oup.prod.sis.lan/mnras/article-pdf/483/4/5380/27471389/sty3460.pdf.

Tasca, L. A. M., O. Le Fèvre, B. Ribeiro, R. Thomas, C. Moreau, P. Cassata, B. Garilli, et al. 2017. "The VIMOS Ultra Deep Survey first data release: Spectra and spectroscopic redshifts of 698 objects up to $z_{spec}$ 6 in CANDELS." *Astronomy and Astrophysics* 600, A110 (April): A110. doi:10.1051/0004-6361/201527963. arXiv: 1602.01842.

Tegmark, M., J. Silk, M. J. Rees, A. Blanchard, T. Abel, and F. Palla. 1997. "How Small Were the First Cosmological Objects?" *The Astrophysical Journal* 474 (January): 1. doi:10.1086/303434. eprint: astro-ph/9603007.

Telfer, Randal C., Wei Zheng, Gerard A. Kriss, and Arthur F. Davidsen. 2002. "The Rest-Frame Extreme-Ultraviolet Spectral Properties of Quasi-stellar Objects." *The Astrophysical Journal* 565, no. 2 (February): 773–785. doi:10.1086/324689. arXiv: astro-ph/0109531 [astro-ph].

Teplitz, H. 2018. *Ultraviolet Imaging of the Cosmic Assembly Near-infrared Deep Extragalactic Legacy Survey Fields (UVCANDELS).* HST Proposal, November.

Teplitz, Harry I., Marc Rafelski, Peter Kurczynski, Nicholas A. Bond, Norman Grogin, Anton M. Koekemoer, Hakim Atek, Thomas M. Brown, Dan Coe, and James W. Colbert. 2013. "UVUDF: Ultraviolet Imaging of the Hubble Ultra Deep Field with Wide-Field Camera 3." *The Astronomical Journal* 146, no. 6, 159 (December): 159. doi:10.1088/0004-6256/146/6/159. arXiv: 1305.1357 [astro-ph.CO].

Tepper-Garcıa, T., and U. Fritze. 2008. "Stochastic absorption of the light of background sources due to intergalactic neutral hydrogen - I. Testing different line-number evolution models via the cosmic flux decrement." *Monthly Notices of the Royal Astronomical Society* 383 (February): 1671–1685. doi:10.1111/j.1365-2966.2007.12691.x. arXiv: 0705.1242.

Trebitsch, Maxime, Jérémy Blaizot, Joakim Rosdahl, Julien Devriendt, and Adrianne Slyz. 2017. "Fluctuating feedback-regulated escape fraction of ionizing radiation in low-mass, high-redshift galaxies." *Monthly Notices of the Royal Astronomical Society* 470, no. 1 (May): 224–239. doi:10.1093/mnras/stx1060. eprint: http://oup.prod.sis.lan/mnras/article-pdf/470/1/224/17843908/stx1060.pdf.

Tremblin, P., Anderson, L. D., Didelon, P., Raga, A. C., Minier, V., Ntormousi, E., Pettitt, A., et al. 2014. "Age, size, and position of Hregions in the Galaxy - Expansion of ionized gas in turbulent molecular clouds." *A&A* 568:A4. doi:10.1051/0004-6361/201423959.

Tseliakhovich, Dmitriy, Rennan Barkana, and Christopher M. Hirata. 2011. "Suppression and spatial variation of early galaxies and minihaloes." *Monthly Notices of the Royal Astronomical Society* 418, no. 2 (November): 906–915. doi:10.1111/j.1365-2966.2011.19541.x. eprint: http://oup.prod.sis.lan/mnras/article-pdf/418/2/906/3692552/mnras0418-0906.pdf.

Tumlinson, Jason, Mark L. Giroux, J. Michael Shull, and John T. Stocke. 1999. "New HST Observations of the Halo Gas of NGC 3067: Limits on the Extragalactic Ionizing Background at Low Redshift and the Lyman Continuum Escape Fraction." *The Astronomical Journal* 118, no. 5 (November): 2148–2157. doi:10.1086/301106.

Turk, Matthew J., Tom Abel, and Brian O'Shea. 2009. "The Formation of Population III Binaries from Cosmological Initial Conditions." *Science* 325 (5940): 601–605. http://www.jstor.org/stable/20544209.

Ueda, Yoshihiro. 2015. "Cosmological evolution of supermassive black holes in galactic centers unveiled by hard X-ray observations." *Proceedings of the Japan Academy, Series B* 91 (5): 175–192. doi:10.2183/pjab.91.175.

Ueda, Yoshihiro, Masayuki Akiyama, Günther Hasinger, Takamitsu Miyaji, and Michael G. Watson. 2014. "TOWARD THE STANDARD POPULATION SYNTHESIS MODEL OF THE X-RAY BACKGROUND: EVOLUTION OF X-RAY LUMINOSITY AND ABSORPTION FUNCTIONS OF ACTIVE GALACTIC NUCLEI INCLUDING COMPTON-THICK POPULATIONS." *The Astrophysical Journal* 786, no. 2 (April): 104. doi:10.1088/0004-637x/786/2/104.

Ueda, Yoshihiro, Masayuki Akiyama, Kouji Ohta, and Takamitsu Miyaji. 2003. "Cosmological Evolution of the Hard X-Ray Active Galactic Nucleus Luminosity Function and the Origin of the Hard X-Ray Background." *The Astrophysical Journal* 598, no. 2 (December): 886–908. doi:10.1086/378940.

van de Voort, F., J. Schaye, G. Altay, and T. Theuns. 2012. "Cold accretion flows and the nature of high column density H I absorption at redshift 3." *Monthly Notices of the Royal Astronomical Society* 421 (April): 2809–2819. doi:10.1111/j.1365-2966.2012.20487.x. arXiv: 1109.5700.

van der Marel, R. P., and M. Franx. 1993. "A new method for the identification of non-Gaussian line profiles in elliptical galaxies." *The Astrophysical Journal* 407 (April): 525–539. doi:10.1086/172534.

Vanden Berk, Daniel E., Gordon T. Richards, Amanda Bauer, Michael A. Strauss, Donald P. Schneider, Timothy M. Heckman, Donald G. York, et al. 2001. "Composite Quasar Spectra from the Sloan Digital Sky Survey." *The Astronomical Journal* 122, no. 2 (August): 549–564. doi:10.1086/321167.

Vanzella, E., S. de Barros, M. Castellano, A. Grazian, A. K. Inoue, D. Schaerer, L. Guaita, et al. 2015. "Peering through the holes: the far-UV color of star-forming galaxies at z $\sim$ 3-4 and the escaping fraction of ionizing radiation." *Astronomy and Astrophysics* 576 (April): A116. doi:10.1051/0004-6361/201525651.

Vanzella, E., S. Cristiani, M. Dickinson, M. Giavalisco, H. Kuntschner, J. Haase, M. Nonino, et al. 2008. "The great observatories origins deep survey." *Astronomy and Astrophysics* 478, no. 1 (January): 83–92. doi:10.1051/0004-6361:20078332.

Vanzella, E., S. Cristiani, M. Dickinson, H. Kuntschner, M. Nonino, A. Rettura, P. Rosati, J. Vernet, C. Cesarsky, and H. C. Ferguson. 2006. "The great observatories origins deep survey. VLT/FORS2 spectroscopy in the GOODS-South Field: Part II." *Astronomy and Astrophysics* 454, no. 2 (August): 423–435. doi:10.1051/0004-6361:20054796. arXiv: astro-ph/0601367 [astro-ph].

Vanzella, E., M. Giavalisco, A. K. Inoue, M. Nonino, F. Fontanot, S. Cristiani, A. Grazian, et al. 2010. "The Great Observatories Origins Deep Survey: Constraints On The Lyman Continuum Escape Fraction Distribution Of Lyman-break Galaxies At 3.4<z<4.5." *The Astrophysical Journal* 725, no. 1 (December): 1011–1031. doi:10.1088/0004-637X/725/1/1011.

Vanzella, E., Yicheng Guo, Mauro Giavalisco, Andrea Grazian, Marco Castellano, Stefano Cristiani, Mark Dickinson, et al. 2012. "On The Detection Of Ionizing Radiation Arising From Star-forming Galaxies At Redshift z∼3-4: Looking For Analogs Of "Stellar Re-ionizers"." *The Astrophysical Journal* 751, no. 1 (May): 70. doi:10.1088/0004-637X/751/1/70.

Vanzella, E., B. Siana, S. Cristiani, and M. Nonino. 2010. "Contamination on Lyman continuum emission at : implication on the ionizing radiation evolution." *Monthly Notices of the Royal Astronomical Society* 404, no. 4 (March): 1672–1678. doi:10.1111/j.1365-2966.2010.16408.x.

Vázquez-Semadeni, E., D. Ryu, T. Passot, R. F. González, and A. Gazol. 2006. "Molecular Cloud Evolution. I. Molecular Cloud and Thin Cold Neutral Medium Sheet Formation." *The Astrophysical Journal* 643 (May): 245–259. doi:10.1086/502710. eprint: astro-ph/0509127.

Veilleux, Sylvain, Gerald Cecil, and Joss Bland-Hawthorn. 2005. "Galactic Winds." *Annual Review of Astronomy and Astrophysics* 43, no. 1 (September): 769–826. doi:10.1146/annurev.astro.43.072103.150610. arXiv: astro-ph/0504435 [astro-ph].

Vonlanthen, P., T. Rauscher, C. Winteler, D. Puy, M. Signore, and V. Dubrovich. 2009. "Chemistry of heavy elements in the Dark Ages." *A&A* 503 (1): 47–59. doi:10.1051/0004-6361/200811297.

Walton, D. J., E. Nardini, A. C. Fabian, L. C. Gallo, and R. C. Reis. 2013. "Suzaku observations of 'bare' active galactic nuclei." *Monthly Notices of the Royal Astronomical Society* 428 (February): 2901–2920. doi:10.1093/mnras/sts227. arXiv: 1210.4593 [astro-ph.HE].

Weisz, Daniel R., and Michael Boylan-Kolchin. 2017. "Local Group ultra-faint dwarf galaxies in the reionization era." *Monthly Notices of the Royal Astronomical Society: Letters* 469, no. 1 (March): L83–L88. doi:10.1093/mnrasl/slx043. eprint: http://oup.prod.sis.lan/mnrasl/article-pdf/469/1/L83/17239872/slx043.pdf.

Whalen, D. J., and C. L. Fryer. 2012. "The Formation of Supermassive Black Holes from Low-mass Pop III Seeds." *The Astrophysical Journal, Letters* 756, L19 (September): L19. doi:10.1088/2041-8205/756/1/L19. arXiv: 1112.4598.

Wilcots, E. M., K. M. Hess, and J. Grcevich. 2008. "AGN Heating of the Intergalactic Medium in Galaxy Groups." In *Extragalactic Jets: Theory and Observation from Radio to Gamma Ray,* edited by T. A. Rector and D. S. De Young, 386:320. Astronomical Society of the Pacific Conference Series. June.

Wilkins, Stephen M., Andrew J. Bunker, Silvio Lorenzoni, and Joseph Caruana. 2011. "New star-forming galaxies at z≈7 from Wide Field Camera Three imaging." *Monthly Notices of the Royal Astronomical Society* 411, no. 1 (February): 23–36. doi:10.1111/j.1365-2966.2010.17626.x.

Williams, R. E., B. Blacker, M. Dickinson, W. V. D. Dixon, H. C. Ferguson, A. S. Fruchter, M. Giavalisco, et al. 1996. "The Hubble Deep Field: Observations, Data Reduction, and Galaxy Photometry." *The Astronomical Journal* 112 (October): 1335. doi:10.1086/118105. eprint: astro-ph/9607174.

Willott, C. J., P. Delorme, C. Reylé, L. Albert, J. Bergeron, D. Crampton, X. Delfosse, et al. 2010. "The Canada-France High-z Quasar Survey: Nine New Quasars and the Luminosity Function at Redshift 6." *The Astronomical Journal* 139 (March): 906–918. doi:10.1088/0004-6256/139/3/906. arXiv: 0912.0281.

Willott, C. J., S. Rawlings, K. M. Blundell, M. Lacy, G. J. Hill, and S. E. Scott. 2002. "Optical spectroscopy of radio galaxies in the 7C Redshift Survey." *Monthly Notices of the Royal Astronomical Society* 335 (October): 1120–1132. doi:10.1046/j.1365-8711.2002.05718.x. eprint: astro-ph/0205507.

Wilms, J., A. Allen, and R. McCray. 2000. "On the Absorption of X-Rays in the Interstellar Medium." *The Astrophysical Journal* 542 (October): 914–924. doi:10.1086/317016. eprint: astro-ph/0008425.

Windhorst, R. A., and S. H. Cohen. 2010. "How HST/WFC3 and JWST Can Measure Galaxy Assembly and AGN Growth." In *American Institute of Physics Conference Series,* edited by D. J. Whalen, V. Bromm, and N. Yoshida, 1294:225. American Institute of Physics Conference Series. November. doi:10.1063/1.3518858.

Windhorst, R. A., W. C. Keel, and S. M. Pascarelle. 1998. "Deep Hubble Space Telescope/Planetary Camera Imaging of a Young Compact Radio Galaxy at Z = 2.390." *The Astrophysical Journal, Letters* 494 (February): L27–L31. doi:10.1086/311149.

Windhorst, Rogier A., Seth H. Cohen, Nimish P. Hathi, Patrick J. McCarthy, Russell E. Ryan, Haojing Yan, Ivan K. Baldry, et al. 2011. "The Hubble Space Telescope Wide Field Camera 3 Early Release Science Data: Panchromatic Faint Object Counts For 0.2-2 $\mu$m Wavelength." *The Astrophysical Journal, Supplements* 193, no. 2 (April): 27. doi:10.1088/0067-0049/193/2/27.

Wirth, Gregory D., Jonathan R. Trump, Guillermo Barro, Yicheng Guo, David C. Koo, Fengshan Liu, Marc Kassis, Jim Lyke, Luca Rizzi, and Randy Campbell. 2015. "The Team Keck Redshift Survey 2: MOSFIRE Spectroscopy of the GOODS-North Field." *The Astronomical Journal* 150, no. 5, 153 (November): 153. doi:10.1088/0004-6256/150/5/153. arXiv: 1509.07172 [astro-ph.GA].

Wirth, Gregory D., Christopher N. A. Willmer, Paola Amico, Frederic H. Chaffee, Robert W. Goodrich, Shui Kwok, James E. Lyke, Jeff A. Mader, Hien D. Tran, and Amy J. Barger. 2004. "The Team Keck Treasury Redshift Survey of the GOODS-North Field." *The Astronomical Journal* 127, no. 6 (June): 3121–3136. doi:10.1086/420999. arXiv: astro-ph/0401353 [astro-ph].

Wise, John H., and Renyue Cen. 2009. "Ionizing Photon Escape Fractions From High-redshift Dwarf Galaxies." *The Astrophysical Journal* 693, no. 1 (March): 984–999. doi:10.1088/0004-637x/693/1/984.

Wise, John H., Vasiliy G. Demchenko, Martin T. Halicek, Michael L. Norman, Matthew J. Turk, Tom Abel, and Britton D. Smith. 2014. "The birth of a galaxy - III. Propelling reionization with the faintest galaxies." *Monthly Notices of the Royal Astronomical Society* 442, no. 3 (August): 2560–2579. doi:10.1093/mnras/stu979. arXiv: 1403.6123 [astro-ph.CO].

Wolf, C., K. Meisenheimer, M. Kleinheinrich, A. Borch, S. Dye, M. Gray, L. Wisotzki, et al. 2004. "A catalogue of the Chandra Deep Field South with multi-colour classification and photometric redshifts from COMBO-17." *Astronomy and Astrophysics* 421, no. 3 (July): 913–936. doi:10.1051/0004-6361:20040525.

Woo, Jong-Hak, Donghoon Son, and Hyun-Jin Bae. 2017. "Delayed or No Feedback? Gas Outflows in Type 2 AGNs. III." *The Astrophysical Journal* 839, no. 2, 120 (April): 120. doi:10.3847/1538-4357/aa6894. arXiv: 1702.06681 [astro-ph.GA].

Worseck, G., J. X. Prochaska, J. F. Hennawi, and M. McQuinn. 2014. "Early and Extended Helium Reionization Over More Than 600 Million Years of Cosmic Time." *ArXiv e-prints* (May). arXiv: 1405.7405.

Wuyts, Stijn, Pieter G. van Dokkum, Marijn Franx, Natascha M. Förster Schreiber, Garth D. Illingworth, Ivo Labbé, and Gregory Rudnick. 2009. "OPTICAL SPECTROSCOPY OF DISTANT RED GALAXIES." *The Astrophysical Journal* 706, no. 1 (November): 885–895. doi:10.1088/0004-637X/706/1/885.

Wyithe, J. S. B., A. M. Hopkins, M. D. Kistler, H. Yüksel, and J. F. Beacom. 2010. "Determining the escape fraction of ionizing photons during reionization with the GRB-derived star formation rate." *Monthly Notices of the Royal Astronomical Society* 401 (February): 2561–2571. doi:10.1111/j.1365-2966.2009.15834.x. arXiv: 0908.0193.

Xue, Y. Q., B. Luo, W. N. Brandt, D. M. Alexander, F. E. Bauer, B. D. Lehmer, and G. Yang. 2016. "The 2 Ms Chandra Deep Field-North Survey and the 250 ks Extended Chandra Deep Field-South Survey: Improved Point-source Catalogs." *The Astrophysical Journal, Supplements* 224, 15 (June): 15. doi:10.3847/0067-0049/224/2/15. arXiv: 1602.06299.

Xue, Y. Q., B. Luo, W. N. Brandt, F. E. Bauer, B. D. Lehmer, P. S. Broos, D. P. Schneider, et al. 2011. "The Chandra Deep Field-South Survey: 4 Ms Source Catalogs." *The Astrophysical Journal, Supplements* 195, 10 (July): 10. doi:10.1088/0067-0049/195/1/10. arXiv: 1105.5643.

Yajima, Hidenobu, Jun-Hwan Choi, and Kentaro Nagamine. 2011. "Escape fraction of ionizing photons from high-redshift galaxies in cosmological SPH simulations." *Monthly Notices of the Royal Astronomical Society* 412, no. 1 (March): 411–422. doi:10.1111/j.1365-2966.2010.17920.x. eprint: http://oup.prod.sis.lan/mnras/article-pdf/412/1/411/3083525/mnras0412-0411.pdf.

Yoshida, Naoki. 2008. "Protostar formation in the early universe." In *Low-Metallicity Star Formation: From the First Stars to Dwarf Galaxies,* edited by Leslie K. Hunt, Suzanne C. Madden, and Raffaella Schneider, 255:18–23. IAU Symposium. December. doi:10.1017/S1743921308024538.

Yoshida, Naoki, Takashi Hosokawa, and Kazuyuki Omukai. 2012. "Formation of the first stars in the universe." 01A305, *Progress of Theoretical and Experimental Physics* 2012, no. 1 (October). doi:10.1093/ptep/pts022. eprint: http://oup.prod.sis.lan/ptep/article-pdf/2012/1/01A305/4463524/pts022.pdf.

Yuan, Feng, and Ramesh Narayan. 2014. "Hot Accretion Flows Around Black Holes." *Annual Review of Astronomy and Astrophysics* 52 (1): 529–588. doi:10.1146/annurev-astro-082812-141003. eprint: https://doi.org/10.1146/annurev-astro-082812-141003.

Zel'dovich, Y. B., V. G. Kurt, and R. A. Syunyaev. 1969. "Recombination of Hydrogen in the Hot Model of the Universe." *Soviet Journal of Experimental and Theoretical Physics* 28 (January): 146.

Zhang, Weiqun, S. E. Woosley, and A. Heger. 2008. "Fallback and Black Hole Production in Massive Stars." *The Astrophysical Journal* 679, no. 1 (May): 639–654. doi:10.1086/526404.

Zheng, Wei, Gerard A. Kriss, Randal C. Telfer, John P. Grimes, and Arthur F. Davidsen. 1997. "A Composite HST Spectrum of Quasars." *The Astrophysical Journal* 475, no. 2 (February): 469–478. doi:10.1086/303560. arXiv: astro-ph/9608198 [astro-ph].

Zurita, A., J. E. Beckman, M. Rozas, and S. Ryder. 2002. "The origin of the ionization of the diffuse ionized gas in spirals. II. Modelling the distribution of ionizing radiation in NGC 157." *Astronomy and Astrophysics* 386 (May): 801–815. doi:10.1051/0004-6361:20020212. eprint: astro-ph/0108135.

# APPENDIX A

## SED FITS AND PARAMETERS FOR THE GOODS/HDUV AND ERS SAMPLES

The remaining SED fits for galaxies *without* AGN continued from Fig. 24 are shown here, and BC03, dust extinction, and AGN parameters of our sample are shown in Table 7.

## A.1 Best-fitting BC03 SEDS for Galaxies *Without* AGN

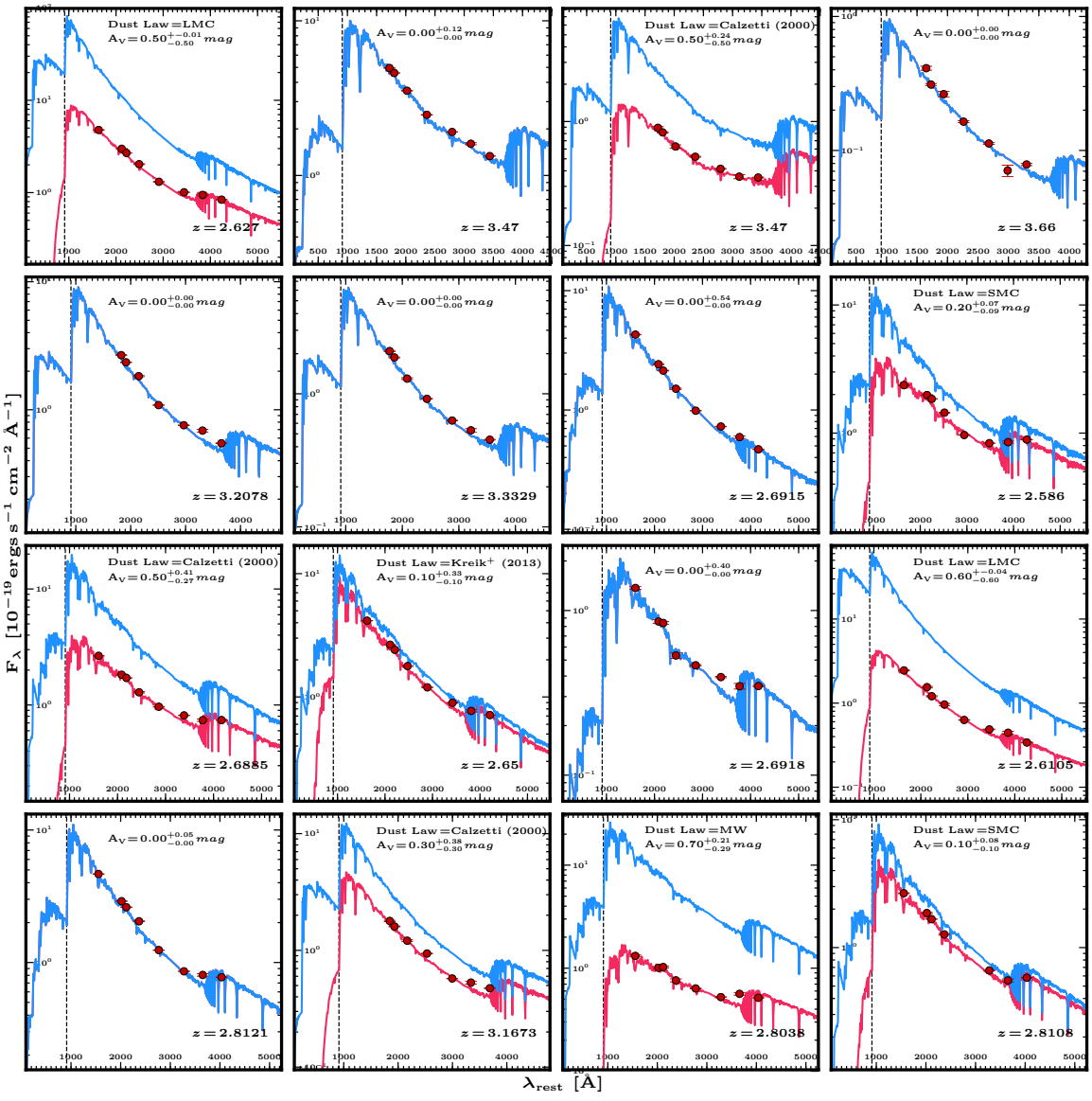


Figure 38. The Remainder of the BCO3 SEDs for Galaxies *Without* AGN in the GOODS/HDUV and ERS Samples

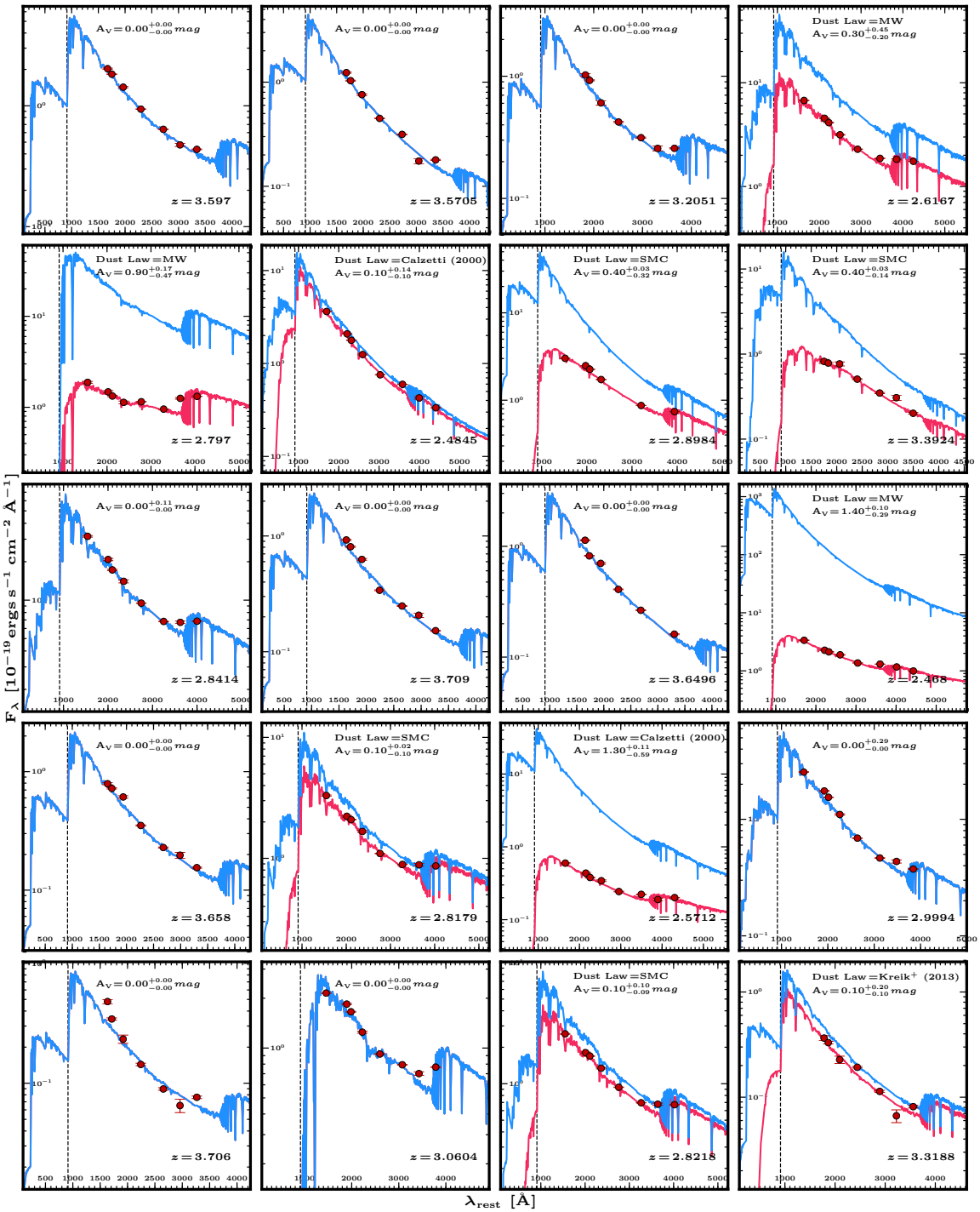


Figure 33. Continued

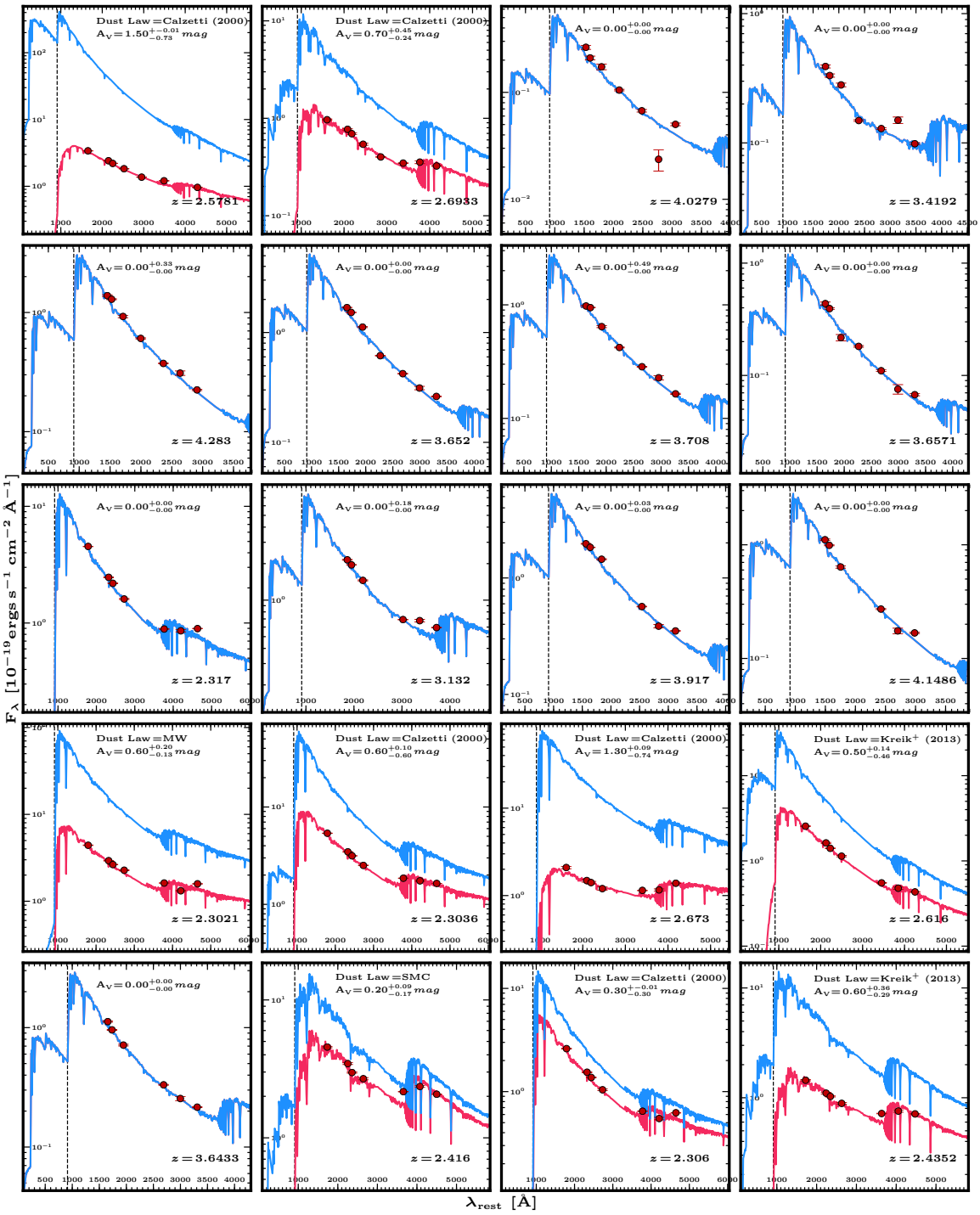


Figure 33. Continued

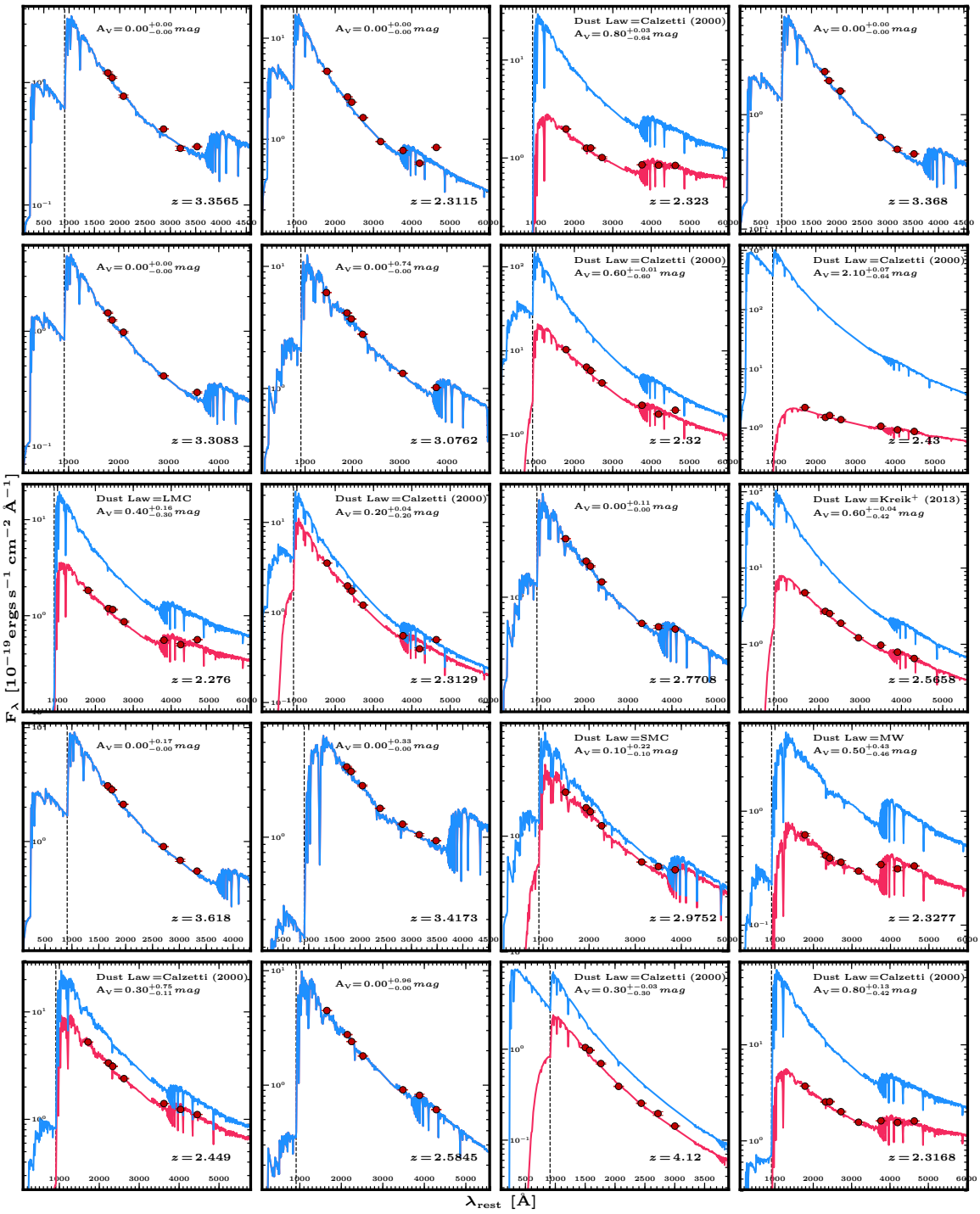


Figure 33. Continued

## A.2 Tabulated Data of the GOODS/HDUV and ERS Galaxy Sample

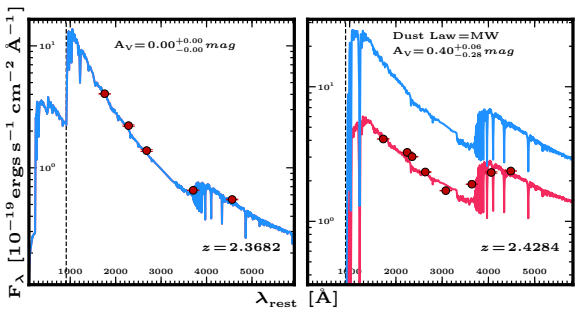


Figure 33. Continued

Table 7. List of Galaxies and SED parameters

| RA (J2000) [deg] | Dec (J2000) [deg] | $z_{\rm spec}$ | $m_{J,\rm AB}$ [mag] | $M^{\rm AB}_{1500\text{Å}}$ [mag] | $(V-I)$ [mag] | $f_{\rm AGN}$ [%] | Dust Law | $A_V$ [mag] | Age [log(yr)] | $\log(\frac{M_\star}{M_\odot})$ | SFR $[\log(\frac{M_\odot}{yr})]$ | $Z$ | $\chi^2$ |
|---|---|---|---|---|---|---|---|---|---|---|---|---|---|
| 189.095582 | 62.257407 | 2.5920 | 21.25 | −24.69 | −0.15 | 56 | C2000 | 0.1 | 6.8 | 9.52 | 2.69 | 0.020 | 7.44 |
| 189.106541 | 62.230628 | 2.9320 | 24.96 | −20.40 | 0.24 | 0 | SMC | 0.1 | 8.5 | 9.36 | 0.86 | 0.050 | 2.08 |
| 189.127325 | 62.273982 | 2.4845 | 24.78 | −20.69 | 0.01 | 0 | C2000 | 0.3 | 6.8 | 8.11 | 1.28 | 0.050 | 0.19 |
| 189.173849 | 62.210796 | 2.5890 | 25.56 | −19.93 | −0.02 | 0 | ... | 0.0 | 7.8 | 8.23 | 0.56 | 0.050 | 2.72 |
| 189.247387 | 62.158714 | 2.9900 | 25.46 | −20.47 | 0.12 | 0 | K&C | 0.3 | 7.0 | 8.3 | 1.03 | 0.004 | 3.72 |
| 189.297223 | 62.179011 | 2.5965 | 25.47 | −20.34 | 0.04 | 0 | SMC | 0.1 | 6.4 | 7.77 | 1.55 | 0.050 | 16.8 |
| 189.317191 | 62.257343 | 2.9560 | 25.73 | −19.45 | 0.33 | 0 | ... | 0.0 | 8.4 | 9.4 | 0.04 | 0.050 | 6.88 |
| 189.367139 | 62.244453 | 2.5480 | 23.65 | −21.32 | 0.09 | 0 | MW | 0.2 | 8.9 | 10.1 | 1.37 | 0.050 | 0.09 |
| 189.424448 | 62.226140 | 2.8635 | ... | −18.81 | 0.21 | 0 | ... | 0.0 | 8.2 | 8.88 | −0.30 | 0.050 | 0.66 |
| 53.006583 | −27.724170 | 2.7212 | 24.06 | −20.98 | 0.07 | 38 | C2000 | 1.1 | 6.5 | 9.09 | 2.89 | 0.020 | 0.49 |
| 53.008846 | −27.724348 | 2.7260 | 24.28 | −19.66 | 0.84 | 0 | C2000 | 2.5 | 6.5 | 9.98 | 3.63 | 0.020 | 4.98 |
| 53.012648 | −27.747244 | 2.5730 | 24.71 | −19.01 | 0.69 | 0 | C2000 | 1.4 | 9.4 | 10.8 | 1.52 | 0.020 | 6.39 |
| 53.013515 | −27.755235 | 3.2171 | 25.14 | −21.12 | ... | 59 | ... | 0.0 | 5.7 | 8.06 | 2.65 | 0.020 | 0.66 |
| 53.013948 | −27.756821 | 2.3170 | 24.74 | −20.48 | −0.09 | 0 | ... | 0.0 | 7.7 | 8.93 | −1.01 | 0.004 | 4.97 |
| 53.014539 | −27.727922 | 3.1320 | 25.01 | −20.86 | 0.30 | 0 | ... | 0.0 | 9.3 | 9.65 | 0.79 | 0.004 | 3.62 |
| 53.020573 | −27.742150 | 3.4739 | 24.45 | −21.93 | ... | 62 | ... | 0.0 | 6.0 | 8.39 | 2.67 | 0.020 | 1.59 |
| 53.020927 | −27.770185 | 3.9170 | 25.22 | −21.13 | 0.62 | 0 | ... | 0.0 | 8.3 | 8.88 | 0.98 | 0.004 | 6.5 |
| 53.033326 | −27.782577 | 2.6123 | 25.25 | −19.73 | 0.23 | 27 | C2000 | 0.7 | 8.4 | 9.13 | 1.15 | 0.020 | 0.53 |
| 53.035231 | −27.744125 | 4.1486 | 26.02 | −20.49 | 0.55 | 0 | ... | 0.0 | 7.6 | 8.14 | 0.89 | 0.004 | 11.1 |
| 53.039361 | −27.801888 | 2.8280 | 20.93 | −24.50 | 0.17 | 23 | C2000 | 1.0 | 6.5 | 10.4 | 4.02 | 0.020 | 1.92 |
| 53.040821 | −27.719068 | 2.3021 | 24.09 | −20.34 | 0.12 | 0 | MW | 0.6 | 7.6 | 9.68 | −1.09 | 0.004 | 8.01 |
| 53.042456 | −27.737862 | 2.3036 | 23.94 | −20.55 | 0.09 | 0 | C2000 | 0.6 | 7.7 | 9.49 | 0.25 | 0.004 | 0.32 |
| 53.048311 | −27.813928 | 2.6061 | 24.84 | −20.72 | 0.06 | 0 | SMC | 0.2 | 7.0 | 8.35 | 1.23 | 0.004 | 2.57 |
| 53.051643 | −27.804598 | 2.8121 | 24.74 | −20.90 | 0.05 | 0 | ... | 0.0 | 8.8 | 9.29 | 0.89 | 0.020 | 1.74 |
| 53.054090 | −27.811396 | 4.2830 | 25.52 | −20.83 | 0.63 | 0 | ... | 0.0 | 8.2 | 8.7 | 0.87 | 0.004 | 0.98 |
| 53.056091 | −27.786294 | 2.6167 | 24.08 | −21.07 | 0.14 | 0 | MW | 0.3 | 9.0 | 10 | 1.44 | 0.050 | 0.46 |
| 53.061617 | −27.846248 | 3.2078 | 24.88 | −21.12 | 0.12 | 0 | ... | 0.0 | 8.8 | 9.3 | 0.91 | 0.004 | 3.16 |
| 53.062466 | −27.735445 | 2.6730 | 24.46 | −19.65 | 0.20 | 0 | C2000 | 1.3 | 7.7 | 10 | −2.07 | 0.004 | 3.28 |
| 53.065221 | −27.742901 | 2.6160 | 25.26 | −20.05 | 0.08 | 0 | K&C | 0.5 | 7.5 | 8.59 | 1.28 | 0.008 | 0.31 |
| 53.065771 | −27.695980 | 3.6433 | 25.81 | −20.34 | 0.40 | 0 | ... | 0.0 | 9.0 | 9.19 | 0.59 | 0.004 | 1.1 |
| 53.071733 | −27.798436 | 3.6520 | 25.50 | −20.80 | 0.29 | 0 | ... | 0.0 | 8.0 | 8.53 | 0.90 | 0.004 | 5.34 |
| 53.072558 | −27.744441 | 2.6503 | 25.54 | −20.54 | −0.15 | 49 | ... | 0.0 | 6.3 | 7.81 | 1.76 | 0.020 | 3.56 |
| 53.074769 | −27.825031 | 3.1673 | 25.04 | −20.61 | 0.18 | 0 | C2000 | 0.3 | 8.7 | 9.3 | 1.03 | 0.004 | 1.83 |
| 53.076203 | −27.858430 | 3.6571 | 26.83 | −19.29 | 0.19 | 0 | ... | 0.0 | 8.3 | 8.14 | 0.25 | 0.004 | 5.41 |
| 53.078023 | −27.731020 | 2.4160 | 23.77 | −20.36 | 0.27 | 0 | SMC | 0.2 | 8.1 | 9.72 | 0.63 | 0.050 | 1.05 |
| 53.078460 | −27.859851 | 3.6609 | 25.58 | −20.17 | ... | 37 | C2000 | 0.7 | 8.4 | 10.3 | −8.18 | 0.020 | 0.59 |
| 53.078800 | −27.693745 | 2.3060 | 25.08 | −19.80 | 0.00 | 0 | C2000 | 0.3 | 7.6 | 8.89 | −1.88 | 0.004 | 5.79 |
| 53.079284 | −27.691368 | 2.4352 | 24.97 | −19.10 | 0.27 | 0 | K&C | 0.6 | 8.1 | 9.45 | 0.73 | 0.050 | 0.06 |
| 53.081690 | −27.811114 | 3.7080 | 25.91 | −20.28 | 0.35 | 0 | ... | 0.0 | 8.5 | 8.69 | 0.61 | 0.004 | 1.29 |
| 53.084024 | −27.823427 | 3.6580 | 26.11 | −20.02 | 0.20 | 0 | ... | 0.0 | 9.0 | 9.01 | 0.47 | 0.004 | 2.53 |
| 53.084173 | −27.838138 | 2.8108 | 25.06 | −20.24 | 0.18 | 0 | SMC | 0.1 | 8.8 | 9.22 | 0.84 | 0.050 | 1.46 |
| 53.086983 | −27.821134 | 2.4845 | 25.28 | −20.39 | −0.03 | 0 | C2000 | 0.1 | 7.0 | 7.96 | 0.84 | 0.020 | 2.65 |
| 53.089909 | −27.872595 | 3.2051 | 25.91 | −20.00 | 0.07 | 0 | ... | 0.0 | 9.2 | 9.3 | 0.44 | 0.004 | 2.18 |
| 53.094142 | −27.854997 | 3.6600 | 26.94 | −19.16 | 0.51 | 0 | ... | 0.0 | 9.2 | 8.85 | 0.11 | 0.004 | 5.96 |
| 53.094398 | −27.856172 | 3.7060 | 27.08 | −19.08 | 0.58 | 0 | ... | 0.0 | 9.2 | 8.82 | 0.08 | 0.004 | 17.2 |
| 53.095384 | −27.687524 | 3.3565 | 25.56 | −20.31 | 0.22 | 0 | ... | 0.0 | 9.0 | 9.4 | 0.54 | 0.004 | 5.35 |
| 53.096834 | −27.866071 | 3.4700 | 25.69 | −19.92 | 0.61 | 0 | C2000 | 0.5 | 9.1 | 10.1 | 0.87 | 0.004 | 0.74 |
| 53.097230 | −27.865792 | 3.4700 | 23.99 | −21.87 | 0.60 | 0 | ... | 0.0 | 8.5 | 10.1 | 0.97 | 0.008 | 0.52 |
| 53.100815 | −27.715987 | 2.2980 | 23.60 | −19.91 | 0.12 | 10 | C2000 | 0.7 | 8.8 | 10.2 | 1.09 | 0.020 | 0.61 |
| 53.101449 | −27.832682 | 2.6885 | 25.01 | −20.08 | 0.16 | 0 | C2000 | 0.5 | 8.8 | 9.49 | 1.11 | 0.050 | 0.92 |
| 53.102783 | −27.759367 | 2.3115 | 25.03 | −20.62 | −0.07 | 0 | ... | 0.0 | 8.1 | 8.65 | 0.75 | 0.004 | 20.1 |
| 53.110319 | −27.845594 | 3.0604 | 25.07 | −20.37 | 0.40 | 0 | ... | 0.0 | 8.1 | 9.55 | −1.63 | 0.020 | 0.83 |
| 53.113001 | −27.745551 | 2.3230 | 24.78 | −19.38 | 0.08 | 0 | C2000 | 0.8 | 7.7 | 9.35 | −1.51 | 0.004 | 0.7 |
| 53.113675 | −27.812727 | 2.6310 | 25.07 | −20.32 | 0.05 | 0 | ... | 0.0 | 9.0 | 9.24 | 0.70 | 0.050 | 2.46 |
| 53.117831 | −27.734305 | 3.2560 | 24.26 | −20.45 | ... | 31 | C2000 | 3.0 | 9.0 | 11.8 | 2.84 | 0.020 | 1.23 |
| 53.118440 | −27.805315 | 2.6270 | 24.68 | −20.80 | 0.06 | 0 | LMC | 0.5 | 7.0 | 8.75 | 1.48 | 0.004 | 1.02 |
| 53.120610 | −27.736585 | 3.3680 | 25.11 | −21.04 | 0.25 | 0 | ... | 0.0 | 8.7 | 9.19 | 0.89 | 0.004 | 4.43 |
| 53.121412 | −27.814619 | 3.5970 | 25.04 | −21.00 | 0.40 | 0 | ... | 0.0 | 9.2 | 9.59 | 0.85 | 0.004 | 1.42 |
| 53.121611 | −27.672921 | 3.3083 | 25.58 | −20.50 | 0.17 | 0 | ... | 0.0 | 8.8 | 9.07 | 0.66 | 0.004 | 1.2 |
| 53.124717 | −27.824518 | 3.2293 | 24.88 | −20.92 | 0.30 | 0 | ... | 0.0 | 9.1 | 9.85 | 0.80 | 0.008 | 0.12 |
| 53.131718 | −27.669018 | 3.0762 | 24.30 | −21.36 | 0.15 | 0 | ... | 0.0 | 8.6 | 9.57 | 1.08 | 0.050 | 1.47 |
| 53.132762 | −27.830592 | 2.5781 | 24.63 | −20.26 | 0.20 | 0 | C2000 | 1.5 | 6.7 | 9.3 | 2.81 | 0.004 | 1.4 |
| 53.134558 | −27.690656 | 2.3200 | 23.73 | −21.33 | 0.05 | 0 | C2000 | 0.6 | 7.1 | 8.96 | 1.41 | 0.008 | 8.39 |

Table 7. Continued

| RA (J2000) [deg] | Dec (J2000) [deg] | $z_{\rm spec}$ | $m_{J,\rm AB}$ [mag] | $M^{\rm AB}_{1500\text{Å}}$ [mag] | $(V-I)$ [mag] | $f_{\rm AGN}$ [%] | Dust Law | $A_V$ [mag] | Age [log(yr)] | $\log(\frac{M_\star}{M_\odot})$ | SFR [$\log(M_\odot/yr)$] | $Z$ | $\chi^2$ |
|---|---|---|---|---|---|---|---|---|---|---|---|---|---|
| 53.134819 | −27.713359 | 2.4300 | 24.53 | −19.48 | 0.15 | 0 | C2000 | 2.1 | 6.6 | 9.64 | 3.34 | 0.004 | 2.16 |
| 53.135359 | −27.814467 | 2.8179 | 24.88 | −20.45 | 0.14 | 0 | SMC | 0.1 | 9.3 | 9.87 | 0.92 | 0.050 | 1.06 |
| 53.138759 | −27.700469 | 2.4500 | 24.39 | −19.67 | 0.33 | 57 | C2000 | 1.5 | 6.4 | 8.98 | 2.87 | 0.020 | 0.32 |
| 53.138854 | −27.835370 | 3.7910 | 25.34 | −20.93 | 0.32 | 0 | C2000 | 0.1 | 7.0 | 8.18 | 1.06 | 0.004 | 4.18 |
| 53.140741 | −27.803986 | 2.6182 | 25.00 | −20.55 | −0.05 | 0 | LMC | 0.3 | 6.9 | 8.28 | 1.25 | 0.020 | 3.78 |
| 53.142623 | −27.826539 | 3.5705 | 25.85 | −20.43 | 0.11 | 0 | ... | 0.0 | 7.0 | 7.9 | 0.63 | 0.004 | 9.1 |
| 53.143115 | −27.815496 | 4.1420 | 25.33 | −20.66 | 1.06 | 0 | LMC | 0.2 | 8.8 | 9.93 | 1.01 | 0.020 | 0.45 |
| 53.144489 | −27.728071 | 2.2760 | 25.25 | −19.42 | 0.10 | 0 | LMC | 0.4 | 7.6 | 8.99 | −1.78 | 0.004 | 6.0 |
| 53.145431 | −27.698008 | 2.3129 | 25.26 | −20.25 | −0.06 | 0 | C2000 | 0.2 | 7.1 | 8.12 | 0.57 | 0.008 | 17.9 |
| 53.145621 | −27.685249 | 2.7708 | 25.16 | −20.41 | 0.09 | 0 | ... | 0.0 | 8.8 | 9.12 | 0.73 | 0.050 | 1.27 |
| 53.146045 | −27.806442 | 2.7970 | 24.82 | −19.73 | 0.31 | 0 | MW | 0.9 | 7.9 | 10.3 | −3.35 | 0.008 | 1.77 |
| 53.148822 | −27.821115 | 2.5760 | 25.76 | −19.62 | 0.23 | 1 | C2000 | 0.5 | 7.2 | 8.36 | 0.45 | 0.020 | 7.26 |
| 53.149223 | −27.748588 | 2.5658 | 24.76 | −20.69 | −0.04 | 0 | K&C | 0.6 | 6.8 | 8.71 | 2.18 | 0.004 | 1.53 |
| 53.149815 | −27.697213 | 3.6180 | 24.72 | −21.50 | 0.30 | 0 | ... | 0.0 | 8.6 | 9.26 | 1.09 | 0.004 | 0.42 |
| 53.151291 | −27.742911 | 3.4173 | 24.52 | −21.18 | 0.43 | 0 | ... | 0.0 | 8.3 | 9.89 | 0.10 | 0.008 | 0.1 |
| 53.153434 | −27.766114 | 3.7970 | 25.21 | −20.87 | 0.53 | 0 | ... | 0.0 | 8.5 | 9.36 | 0.72 | 0.008 | 0.35 |
| 53.157430 | −27.709016 | 2.9752 | 25.17 | −20.28 | 0.23 | 0 | SMC | 0.1 | 8.7 | 9.25 | 0.85 | 0.050 | 1.34 |
| 53.158912 | −27.742675 | 2.3277 | 26.29 | −18.08 | 0.12 | 0 | MW | 0.5 | 8.1 | 9.22 | −0.37 | 0.020 | 1.71 |
| 53.161953 | −27.722657 | 2.4490 | 24.24 | −20.65 | 0.08 | 0 | C2000 | 0.3 | 7.6 | 9.23 | 0.08 | 0.020 | 0.1 |
| 53.164729 | −27.807903 | 2.8218 | 25.05 | −20.22 | 0.18 | 0 | SMC | 0.1 | 8.6 | 9.38 | 0.80 | 0.050 | 0.43 |
| 53.165578 | −27.788170 | 2.8414 | 25.03 | −20.43 | 0.12 | 0 | ... | 0.0 | 8.8 | 9.48 | 0.71 | 0.050 | 0.72 |
| 53.166236 | −27.819816 | 3.4192 | 27.04 | −18.99 | 0.31 | 0 | ... | 0.0 | 9.2 | 9.28 | 0.00 | 0.004 | 12.4 |
| 53.167996 | −27.711349 | 2.5845 | 24.71 | −20.55 | 0.04 | 0 | ... | 0.0 | 7.4 | 8.76 | −0.20 | 0.050 | 1.28 |
| 53.168265 | −27.741939 | 4.1200 | 26.00 | −20.46 | 0.44 | 0 | C2000 | 0.3 | 6.2 | 8.23 | 2.32 | 0.004 | 2.46 |
| 53.169581 | −27.826858 | 4.0279 | 27.42 | −18.81 | 0.47 | 0 | ... | 0.0 | 8.8 | 8.35 | 0.00 | 0.004 | 21 |
| 53.170605 | −27.823771 | 2.6918 | 25.81 | −19.38 | 0.06 | 0 | ... | 0.0 | 8.0 | 8.86 | −0.14 | 0.050 | 3.04 |
| 53.174442 | −27.733297 | 2.5760 | 25.89 | −18.75 | 0.19 | 16 | C2000 | 0.3 | 9.1 | 9.9 | 0.25 | 0.020 | 0.51 |
| 53.178282 | −27.815807 | 2.6933 | 25.97 | −19.01 | 0.32 | 0 | C2000 | 0.7 | 8.7 | 9.2 | 0.89 | 0.050 | 1.57 |
| 53.178482 | −27.784031 | 3.1930 | 25.04 | −20.21 | ... | 97 | ... | 0.0 | 9.3 | 9.41 | −99 | 0.020 | 9.06 |
| 53.180475 | −27.829740 | 3.3329 | 25.07 | −20.88 | 0.19 | 0 | ... | 0.0 | 9.2 | 9.54 | 0.80 | 0.004 | 0.86 |
| 53.180778 | −27.786255 | 2.6915 | 24.99 | −20.65 | −0.05 | 0 | ... | 0.0 | 7.6 | 8.59 | 0.59 | 0.020 | 1.47 |
| 53.181483 | −27.831793 | 2.6500 | 24.78 | −20.60 | 0.08 | 0 | K&C | 0.1 | 8.6 | 9.11 | 0.95 | 0.050 | 0.61 |
| 53.181805 | −27.729920 | 2.3168 | 24.49 | −20.12 | 0.16 | 0 | C2000 | 0.8 | 7.7 | 9.6 | −0.34 | 0.004 | 1.29 |
| 53.182025 | −27.779539 | 2.4680 | 24.64 | −20.12 | 0.14 | 0 | MW | 1.4 | 6.8 | 9.77 | 3.18 | 0.004 | 1.95 |
| 53.182798 | −27.705269 | 2.3682 | 25.07 | −20.48 | −0.09 | 0 | ... | 0.0 | 8.0 | 8.65 | 0.61 | 0.004 | 2.95 |
| 53.182838 | −27.734909 | 2.4284 | 24.41 | −20.41 | 0.32 | 0 | MW | 0.4 | 8.0 | 9.95 | −8.17 | 0.004 | 4.26 |
| 53.185823 | −27.809963 | 2.5860 | 25.01 | −19.97 | 0.38 | 0 | SMC | 0.2 | 9.1 | 9.64 | 0.90 | 0.050 | 3.3 |
| 53.187092 | −27.812653 | 2.8038 | 25.47 | −19.41 | 0.28 | 0 | MW | 0.7 | 8.1 | 9.67 | 1.22 | 0.050 | 1.3 |
| 53.188112 | −27.841128 | 3.3924 | 25.71 | −19.79 | 0.35 | 0 | SMC | 0.4 | 6.5 | 8.07 | 1.84 | 0.050 | 2.1 |
| 53.188249 | −27.829353 | 2.5712 | 26.51 | −18.39 | 0.22 | 0 | C2000 | 1.3 | 7.2 | 8.43 | 1.51 | 0.004 | 1.9 |
| 53.189130 | −27.836274 | 3.3188 | 26.76 | −19.02 | −0.04 | 0 | K&C | 0.1 | 8.6 | 8.45 | 0.21 | 0.004 | 5.29 |
| 53.192689 | −27.813047 | 4.0200 | 25.25 | −20.98 | 0.74 | 0 | ... | 0.0 | 9.1 | 9.57 | 0.83 | 0.004 | 1.42 |
| 53.193044 | −27.848046 | 2.8984 | 24.76 | −20.55 | 0.36 | 0 | SMC | 0.4 | 7.0 | 8.62 | 1.60 | 0.004 | 4.46 |
| 53.195570 | −27.834564 | 2.9994 | 25.38 | −20.38 | 0.16 | 0 | ... | 0.0 | 8.8 | 9.04 | 0.68 | 0.020 | 3.1 |
| 53.202603 | −27.815619 | 3.7090 | 26.15 | −20.12 | 0.40 | 0 | ... | 0.0 | 8.7 | 8.79 | 0.53 | 0.004 | 5.23 |
| 53.203270 | −27.821657 | 2.6105 | 25.48 | −20.02 | 0.07 | 0 | LMC | 0.6 | 6.9 | 8.52 | 1.91 | 0.004 | 2.63 |
| 53.220439 | −27.808750 | 3.6496 | 25.95 | −20.27 | 0.16 | 0 | ... | 0.0 | 8.2 | 8.46 | 0.65 | 0.004 | 7.94 |

Table columns: The column header $f_{\rm AGN}$ indicates the percentage of light in the SED from the AGN at 5000Å and $\log(\frac{M_\star}{M_\odot})$ indicates the stellar mass of the galaxy that produces it's best-fitting BC03 SED. C2000 represents the Calzetti et al. 2000 dust-attenuation law and K&C represent the dust law from Kriek and Conroy (2013)

# APPENDIX B

# SOURCES OF SYSTEMATIC UNCERTAINTIES OR SPURIOUS SIGNALS IN CONTRAINING THE LYC ESCAPE FRACTION

## B.1 Possible Sources of Contaminating Non-ionizing Flux

### B.1.1 In-filter Red-leak of Non-ionizing Flux

The WFC3/UVIS filters were designed to minimize the transmission of photons with wavelengths higher or lower than their specified cutoffs (see Fig. 6(a)). However, as seen in Fig. 6(b), a small amount of flux red-ward of the Lyman Limit from galaxies observed in these filters with redshifts in the ranges of Table 1 can still leak into the filter and contaminate LyC observations with non-ionizing UVC flux. The lower redshift bounds in Table 1 were carefully chosen such that *no* light $> 912$Å is sampled below the filter's red edge. The filter red edge is defined as $< 0.5\%$ of the filter's peak transmission. For galaxies at the higher redshifts in the ranges of Table 1, and especially those at higher redshifts than the designated upper bound, the contribution from UVC "red-leak" can become the dominant source of photons measured in the filter, as the portion of the spectrum intended for LyC observation becomes exceedingly faint at shorter wavelengths and the non-ionizing continuum remains roughly constant at longer wavelengths. Thus, in order to accurately measure LyC photometry and escape fractions from these samples of galaxies, we must verify that the flux measured from our sample is dominated by LyC photons.

Since we cannot directly measure the fraction of non-ionizing flux leaking nto the filter from the observation, we estimate this value by modeling the contribution of LyC and UVC to the observed flux from the total sample. Using SEDs fit from continuum observations of our galaxy sample and *average* line-of-sight IGM transmission models (see §3.3), we calculate the average UVC "red-leak" of our observation in the WFC3/UVIS F225W, 275W, and F336W filters by comparing the total flux integrated in the entire filter, and the total flux integrated below the Lyman Limit of each galaxy. We calculate this value as:

$$\frac{F_\nu^{\rm UVC}}{F_\nu^{\rm LyC}} = \sum_{\rm i=1}^{\rm N_{gal}} \frac{\int_{\lambda_{912}}^{\lambda_2} \mathcal{T}_{\rm obs}^{\rm LyC}(\nu)\mathcal{T}_{\rm IGM}(z_{\rm i},\nu)F_{\nu,i}(\nu)\frac{d\nu}{\nu}}{\int_{\lambda_1}^{\lambda_2} \mathcal{T}_{\rm obs}^{\rm LyC}(\nu)\frac{d\nu}{\nu}} \Bigg/ \frac{\int_{\lambda_1}^{\lambda_2} \mathcal{T}_{\rm obs}^{\rm LyC}(\nu)\mathcal{T}_{\rm IGM}(z_{\rm i},\nu)F_{\nu,i}(\nu)\frac{d\nu}{\nu}}{\int_{\lambda_1}^{\lambda_2} \mathcal{T}_{obs}^{\rm LyC}(\nu)\frac{d\nu}{\nu}} \tag{B.1}$$

where $\lambda_1$ and $\lambda_2$ are the minimum and maximum wavelengths of the full filter transmission curve, $\lambda_{912}$ is the observed wavelength of the Lyman Limit of the galaxy, $F_\nu$ is the SED flux of the galaxy in $\rm erg\,s^{-1}\,cm^{-2}\,Hz^{-1}$, $\mathcal{T}_{\rm IGM}$ is the average line-of-sight IGM transmission at the redshift of the galaxy, and $\mathcal{T}_{\rm obs}^{\rm LyC}(\nu)$ is the combined throughput of the filter, detector quantum efficiency (QE), and optical telescope assembly (OTA). This value quantifies the fraction of flux we measure from these galaxies in the filter intended for LyC observations that is non-ionizing. For the F225W, F275W, and

F336W filters, the *percentage of total* "red-leak" photons that contribute to the measured LyC flux of our sample are $\sim 0.65\%$, 0.64%, and 0.19% respectively. That is, less than 1% of the anticipated and measured LyC flux itself could be red-leak flux from longwards of 912Å. From these values, it is clear that LyC observations of galaxies at the redshift ranges indicated in Table 1 with their respective filters are dominated by LyC photons. We also note that our MC analysis of the observed LyC flux from these galaxies accounts for these "red-leak" photons, in order to make appropriate corrections for low level non-ionizing contamination of the order of $\sim 0.28\%$.

### B.1.2 UVIS filter Pinholes

Pinholes are very small voids in the coating on the surface of a filter. These voids appear usually due to poor adhesion of the coating in these regions where particulate matter on the surface of the filter is coated over when the substrate is cast, or from mechanical abrasion or chemical interactions when the filter is in use. Several of the WFC3/UVIS filters have pinholes, so we must make sure that none of the LyC flux that we measure is due to out-of-band flux leaking in through the filter in an area where such a pinhole exists. Most of the obvious pinholes were known before WFC3's launch, and the filters with the fewest pinholes were chosen for flight (Dressel et al. 2015). To the best of our knowledge, the number of pinholes did not increase during the 7 years that the WFC3 filters were on the ground. Visible pinholes on the selected filters were painted over when possible (Baggett et al. 2006). Any remaining pinholes not painted over before launch are likely $\lesssim$0.2 mm in diameter, or they would have been treated before final instrument assembly. Unfortunately, no record was kept of any less obvious pinholes in the flight filters that were not painted over before launch. Remaining pinholes could cause subtle field dependent red-leaks and very low level sky gradients, which we quantify here.

We need to first estimate how large the footprint and the amplitude of any pinhole red-leak on the WFC3 CCDs could be. The HST f/24 beam gets re-imaged inside WFC3 to f/31 (Dressel et al. 2015), so that the plate scale on the WFC3 UVIS detector changes from $3\farcs58$/mm to $2\farcs77$/mm (i.e., $206265/(2400 \times 31)$"/mm). The WFC3 UVIS Marconi CCDs have 15$\mu$m pixels, so the two 2k×4k CCD arrays are about 61 mm in physical size. The WFC3/UVIS F225W filter is in Selectable Optical Filter Assembly (SOFA) filter wheel 3, F336W in filter wheel 4, and F275W in filter wheel 6 out of 12, where wheel 12 is closest to the CCD's. The average location of these three filter wheels is about 190±25 mm away from the focal plane (Fig. 2.1 of Dressel et al. 2015), which we hereafter refer to as the "center of the SOFA". The ±25 mm indicates the approximate range over which these three UVIS filter wheels are mounted inside the SOFA. Each SOFA filter is 57.3 mm square and $\lesssim$5.151 mm thick

(Baggett et al. 2006), as fabricated by the filter vendor to the specifications defined by the WFC3 Scientific Oversight Committee and Instrument Product Team.

The SOFA is about 1/3 of the way between the focal plane and the pupil, which is the anamorphic asphere mirror inside WFC3 that corrects for the spherical aberration in HST's primary mirror. Fortunately therefore, all pinholes in the WFC3 UVIS filters will be severely out of focus, since the filters are so far from the focal plane. We first need to calculate how large the pupil of each image is in the filter plane. The anamorphic asphere mirror has a diameter of about 25 mm and is about 630 mm away from the CCD. It is about 440 mm from the center of the SOFA, so that the *radius* of the image pupil at the filter distance is about $r_{\rm ip-f} \simeq (190/630) \cdot 25/2 \simeq 3.77\,$mm. Hence, the image pupil at the filter is about $7.54/57.3 \simeq 13\%$ of the filter size.

Next, we need to estimate how large the footprint and the amplitude of any pinhole flux on the WFC3 CCDs could be. If WFC3's f/31 beam goes through a pinhole with an r$\gtrsim$0.08 mm radius (i.e., $\gtrsim 0.5 \times 5.151/31$) in a $\lesssim$5.151 mm thick UV filter about 190 mm in front of the CCD, this pinhole will affect a beam with an opening angle $\theta$=90°–atan(31) $\simeq 1.85°$ projected onto the CCD. As viewed from the CCD, the remainder of the pixels outside this beam will not view the sky through the pinhole. At the CCD, the circular beam that *is* affected by this pinhole will have a 190/31 $\simeq$ 6.1 mm $\simeq$ 17.″0 $\simeq$ 430 pixel radius on the CCD, and so its diameter will cover about 20% of the WFC3 CCD FOV. To avoid internal reflections in the camera, the UVIS CCDs are tilted by ∼21° with respect to the axis of the beam, so the projected footprint of each pinhole is actually about 430/cos(21)≃460 pixels in radius. In other words, the footprint projected by the pinhole on the CCD is very large, and will significantly dilute the extra SB signal projected through the pinhole. In the limit, a much smaller pinhole (r<<0.08) mm would not see the entire f/31 beam, and will thus act like a pinhole camera that illuminates the entire CCD, diluting the extra SB that goes through this smaller pinhole even more.

If the interference or AR coating were not present in a pinhole for one of our WFC UVIS filters, Fig. 6*b* shows that it could have a significant increase in local throughput, or less in case that the local defect was only partial in transmission. In a worst case, the pinhole would act like a F606W or F775W WFC3 filter at that location, if the OTA×Filter-Throughput×CCD-QE at those wavelengths reached the WFC3 maximum in the F606W filter of ∼28% (see Fig. 3.2 and 5.2 of Dressel et al. 2015). In such cases, the Zodiacal sky in the beam illuminated by the pinhole would be much higher than seen in our UVIS filters, possibly as high as that in our broadband optical filters, or slightly higher if the pinhole were fully transparent.

The brightest object in the WFC3 ERS has $V \simeq 17\,m_{\rm AB}$ and the most commonly seen objects are faint galaxies with $V \simeq 26$–$27\,m_{\rm AB}$ (Fig. 12 of Windhorst et al. 2011). Hence, their collective SB is well below the average Zodiacal background, which is 23.7–22.6 mag arcsec$^{-2}$Ḣence, for all practical purposes, the pinhole contribution will just be the full white light Zodiacal background if its throughput reaches the maximum total throughput of ∼28%. We assume that the white light Zodi would have on average

a SB≃22.9 mag arcsec$^{-2}$ through such a pinhole, which is roughly the observed value in F606W (e.g., Windhorst et al. 2011). We will also consider the case of a single V≃17 $m_{\rm AB}$ star shining behind a pinhole, as well as the integrated sky SB derived from the faint galaxy counts in Fig. 12 of Windhorst et al. (2011) to $m_{\rm AB}\lesssim$26 mag. In F606W, the latter reaches $10^5$ galaxies/0.5 mag/deg$^2$ to $m_{\rm AB}\lesssim$26 mag, and in F275W, they reach $3\times10^4$ galaxies/0.5 mag/deg$^2$ to $m_{\rm AB}\lesssim$25.5 mag. On a per square arcsecond basis, the integrated sky SB from faint galaxies is therefore ∼29.3 mag arcsec$^{-2}$ in F606W and ∼30.1 mag arcsec$^{-2}$ in F275W, respectively, i.e., fully negligible compared to the Zodiacal sky SB values of $SB_{\rm V}^{\rm Zodi}\simeq$22.9 and $SB_{\rm NUV}^{\rm Zodi}\simeq$25.5 mag arcsec$^{-2}$ in these filters, respectively. Hence, only the Zodiacal light and the effective SB of the occasional bright star behind the filter would be the main sources of pinhole contamination. All calculations below are done in terms of surface brightness (SB in mag arcsec$^{-2}$) or Intensity ($I$ in relative counts/sec).

In a slow f/31 beam, when the pinhole is larger than the minimum size to transmit through the filter, the total white light transmitted would increase proportionally to the pinhole area compared to the total area of the image pupil at the filter $(r_{\rm ph}/r_{\rm ip-f})^2$, both measured in mm. For an untreated pinhole with an assumed $r_{\rm ph}\simeq$0.1 mm, we can now estimate the increase in sky SB contribution from this pinhole over a r=460 pixel radius on the CCD. In relative units, this is increase is:

$$I_{\rm V}^{\rm ph} = F\cdot[r_{\rm ph}^2/r_{\rm ip-f}^2]\cdot[I_{\rm V}^{\rm Star}+I_{\rm V}^{\rm Zodi}] \tag{B.2}$$

with $I_{\rm V}^{\rm Star}=10^{-0.4(SB_{\rm V}^{\rm Star}-ZP_{\rm V})}$, $I_{\rm V}^{\rm Zodi}=10^{-0.4(SB_{\rm V}^{\rm Zodi}-ZP_{\rm V})}$, and:

$$I_{\rm NUV}^{\rm ph} = [(r_{\rm ip-f}^2-r_{\rm ph}^2)/r_{\rm ip-f}^2]\cdot[I_{\rm NUV}^{\rm Star}+I_{\rm NUV}^{\rm Zodi}] \tag{B.3}$$

and $I_{\rm NUV}^{\rm Star}=10^{-0.4(SB_{\rm NUV}^{\rm Star}-ZP_{\rm NUV})}$, $I_{\rm NUV}^{\rm Zodi}=10^{-0.4(SB_{\rm NUV}^{\rm Zodi}-ZP_{\rm NUV})}$.

Eq. B.2 describes the relative counts of optical white light through the pinhole, and Eq. B.3 the relative counts for the uncorrupted NUV sky SB. Note that the optical white light $SB_{\rm V}^{\rm Zodi}\simeq$22.9 mag arcsec$^{-2}$ is compared here to the WFC3 F606W zeropoint of $ZP_{\rm V}$=26.08 mag (i.e., *not* the ACS ZP in this case), and the original UV $SB_{\rm NUV}^{\rm Zodi}\simeq$25.5 mag arcsec$^{-2}$ is compared to the combined F225W and F275W zeropoints of ∼24.1 mag. The factor F≃(10000-4000)/2000)≃3 reflects that the pinhole could transmit three broadband filters worth of white light from 4000-10,000Å (see Fig. 6*b*). We find approximately the same values if we instead use the WFC3 white light filter F200LP and its zeropoint ZP=27.36 mag, and set the factor F=1. The limit of $r_{\rm ph}\simeq r_{\rm ip-f}$ would describe a hypothetical pinhole so large that it transmits full white light over the entire image pupil at the filter, which now acts like a wide $V$ band filter. In that case, both equations still give the correct results: Eq. B.2 describes its wide $V$ band SB, and Eq. B.3 describes its now vanishingly small NUV SB.

At first, we ignore the terms with $I_{\rm V}^{\rm Star}$ and $I_{\rm NUV}^{\rm Star}$ due to a bright star near a pinhole. The SB from the pinhole in $V$ and NUV then are $I_{\rm V}^{\rm ph}\simeq$0.039 and $I_{\rm NUV}^{\rm ph}\simeq$0.28 in the

same relative units, respectively. The ratio $I_{\rm V}^{\rm ph}/I_{\rm NUV}^{\rm ph}$is 0.14, so that about 14% of white light background through the pinhole gets added to the UV sky:

$$SB_{\rm NUV}^{\rm Sky} = SB_{\rm NUV}^{\rm Zodi} - 2.5log(I_{\rm V}^{\rm ph}/I_{\rm NUV}^{\rm ph}) \quad \text{(B.4)}$$

The error on this is at least 25/190∼0.13 mag, depending how far the SOFA filter is from the CCD. That is, a full white light pinhole footprint could add ∼14±2% to the sky SB over an annulus with a diameter about 20% of the 61 mm CCD area. This is the worst case — a smaller pinhole that doesn't project the entire f/31 beam through the filter could instead add a much fainter SB over the whole chip.

If we also add the effect from a $m_{\rm V}^{\rm Star}$≃17 mag, $m_{\rm NUV}^{\rm Star} \simeq 18$ mag star whose image pupil in the filter plane illuminates the pinhole, we must first correct for the fact that the light from this point source is now spread out by factor of $(r_{\rm ip-f}/r_{\rm ph})^2$ at the filter, so we must add $2.5\log(3.77/0.1)^2$ to the star's point source flux of $m_{\rm AB}$∼17–18 mag in Eq. B.2–B.3 to get the equivalent SB from the star that actually affects the pinhole, expressed in the appropriate relative units. Note that the Zodiacal background and integrated galaxy counts do not have this problem, since they are already expressed as proper SB in Eq. B.2–B.3. These numbers are $SB_{\rm V}^{\rm Star}$≃24.9 and $SB_{\rm NUV}^{\rm Star}$≃25.8mag arcsec$^{-2}$. Eq. B.2–B.3 converts these SB numbers to relative fluxes, then adds them linearly. With a $V$∼17 mag star, the white light SB from the pinhole now grows from $I_{\rm V}^{\rm ph}$≃0.039 to $I_{\rm V}^{\rm ph}$≃0.046. This is only 17% larger than just the light from Zodiacal light alone, since the star is so much more spread out behind the filter. The NUV comparison term remains at $I_{\rm NUV}^{\rm ph}$≃0.28. Hence, an out of focus image of a $V$∼17 mag star behind the pinhole adds ∼17±2% of white light background to the NUV sky.

To first order, both the proper NUV light and any white light pinhole flux would get flat-fielded away, although the pinhole regions would have a different color of the sky-background than the regular UV sky. The WFC3 UVIS Marconi CCDs have QE curve that is fairly flat as a function of wavelength, with most QE values between 2000-8000Å peak around QE∼70% with a range of ±10%. This peak actually lies within the F275W filter. We therefore did the experiment to flat-field a WFC3 F606W image with a high SNR flat-field taken in the F275W filter, and — owing to WFC3's flat QE curve — this did not result in a residual gradient larger than about 10% of sky corner-to-corner across the whole CCD frame. Below we will assume a worst case of ∼10%.

We can use this result to compute the additional sky gradient that an npainted pinhole with r≃0.1 mm could have caused in our UV images. When a pinhole adds about 14–17% extra flux to the regular UV Zodiacal sky over a 920 pixel diameter circle on the CCD, the residual sky gradient that the improper flat-fielding induces is at most 0.6–0.8% of the *total* Zodiacal sky over 920 native pixels, or about 404 drizzled pixels. Across our sub-image size of 71×71 drizzled pixels, this residual sky gradient — if present in our object sub-images — is thus less than ∼0.22-0.26% of

the local Zodiacal sky. That is, the error in the UV sky of Eq. B.4 from sky gradients induced by the partial improper flat-fielding of any pinhole white light is:

$$\sigma_{Sky} \simeq SB^{\rm Sky}_{\rm NUV} + 2.5log(I^{\rm ph}_{\rm V}/I^{\rm ph}_{\rm NUV} \cdot 0.1 \cdot 71/404) \quad \text{(B.5)}$$

For our average UV sky of 25.36 mag arcsec$^{-2}$ (which is now brightened by –0.14 mag due to the extra pinhole flux), the residual sky-gradients left by pinholes in 151×151 drizzled pixels are thus fainter than 25.36–2.5 log(0.22%) ≃31.9 mag arcsec$^{-2}$ and fainter than ≃31.7 mag arcsec$^{-2}$ if a $V$≃17 mag star is also nearby the pinhole. These pinhole induced systematics are at worst slightly brighter than those possibly caused by subtle residual gradients left at the 32.3 mag arcsec$^{-2}$ level across the CCD's due to remaining errors in the bias, dark frames, or flat-fields, as discussed in §4.2.2 and Appendix B.2.1). Of course, the latter may affect our stacks everywhere in the CCD mosaics, while the former occur only in sporadic (although unknown) locations.

We investigated if the effects of any pinhole red-leaks were in fact seen in the ERS data, since obvious pinholes would appear as large donut shaped objects in the drizzled images. No obvious defects with ≳14–17% increased transmission were seen in the raw ERS data on scales of ∼920 native pixels, although this is hard to see due to cosmic rays and the shallow depth of individual images. Partial transmission defects might exist at lower levels. As discussed in §3.1, we inspected all LyC sub-images individually, and removed the ones with suspected increased noise due to residual cosmic rays, structure in the weight maps due to drizzled image borders, and other image defects. The objects removed from the LyC stacking all appear to have higher image rms due to the proximity of structure in the weight maps due to drizzled image borders. No obvious enhancements in the LyC signal were seen due to the proximity of bright stars.

We find that both red-leak flux from UV filter pinholes and other subtle calibration errors may result in residual sky gradients of order ∼32–32.3 mag arcsec$^{-2}$ across our stacking sky boxes. Unless these effects can be removed through further refinement of the WFC3 calibration techniques, residual systematic subtraction errors of order ≃32 mag arcsec$^{-2}$ may well pose a fundamental limit to the LyC stacking method of WFC3 data. This is why the light profiles in Fig. 17 cannot be extended to SB levels much fainter than AB≃32 mag arcsec$^{-2}$.

Finally, if our LyC detections were in fact caused by subtle sky gradients on r≃920 pixel scales, they should have been *preferentially* located near the same physical regions of the CCD. We saw no evidence of our strongest LyC candidates being located in the same physical CCD region of each exposure. On the contrary, our strongest LyC emitters are known "Galaxies with AGN" (Table 4), and show no correlation in their observed position on CCDs. On average, their LyC flux is brighter than that of our "Galaxies without AGN". The AGN LyC flux is sometimes compact (≲a few pixels; Fig. 30) — as opposed to that of the galaxies — and therefore occurs on too small of an optical scale to be caused by the severely out of focus red-leak

through pinholes. Thus, since the physical location of the AGN on the CCDs is spatially uncorrelated, their enhanced LyC flux is unlikely associated with residual sky-background gradients from pinholes. Had that been the case, a number of our much more numerous "Galaxies without AGN" would likely have also been exposed near pinhole induced sky gradients and shown the same amount of red-leaked flux, which is not the case. Hence, local residual sky-background gradients due to pinhole induced red-leak enhancements are not likely to have affected our LyC measurements, at least not to the level of AB$\simeq$32 mag arcsec$^{-2}$.

### B.1.3 Estimating LyC Contamination from Objects Below the $\chi^2$ Image Detection Limit

Here we estimate the potential non-ionizing contamination to our LyC stacks from interloping objects below the $\chi^2$ image detection limit. As seen in §5.5, the deepest $\chi^2$ images allow us to locate possible low-redshift contaminants in sub-images to AB$\sim$27.5 mag, such that they can be removed from our stacks so they cannot contribute any flux to our photometry. However, the possibility that fainter objects which may remain undetected in $\chi^2$ detection image must be addressed, since those objects could potentially contribute some flux within the SExtractor aperture photometry.

As an example, the F336W stack LyC photometry is taken within an aperture area of $\sim$0.5 arcsec$^2$ (see Table 4). To assess this fainter contaminating flux, we need to estimate to the total F336W stack sky-surface brightness from objects undetected at AB$\gtrsim$27.5 mag. For this, we will use the galaxy galaxy counts of Driver et al. (2016) from 20 filters ranging from $\lambda\simeq$0.15–500 . At nearly all wavelengths, their normalized differential counts (Fig. 8 or A1) converge with a well determined slope of $\frac{\Delta\rho_{\rm L}}{\Delta {\rm m}}\simeq$–0.177. The total sky-surface brightness contributed by each magnitude bin in the F336W counts peaks at AB$\simeq$24 mag. The faintest galaxy counts that contribute in F336W are the UVUDF counts in the HUDF (Teplitz et al. 2013), which reach AB$\sim$28 mag. Driver et al. (2016) performed MC tests to determine the uncertainty in the extrapolated total sky-signal, which is $\lesssim$20% in F336W.

We extrapolate this converging signal with the same slope as measured between AB$\simeq$24 and AB$\simeq$28 mag to arbitrarily fainter fluxes, e.g. from 27.5 mag to 38 mag. This is the F336W flux that a very dim ($M_{\rm AB}\simeq$–10 mag) galaxy would have at z$\simeq$3, where the distance modulus in Planck 2016 cosmology is DM=47.47 mag. The actual F336W sky-brightness in Driver et al. (2016) drops from $\sim10^{-28.3}$ W Hz$^{-1}$ m$^{-2}$ deg$^{-2}$ (0.5 mag$^{-1}$) at AB=27.5 mag to $\sim10^{-30.2}$ W Hz$^{-1}$ m$^{-2}$ deg$^{-2}$ (0.5 mag$^{-1}$) at AB=38.0 mag. Over the 21 contributing 0.5 mag-bins from AB=28 to AB=38 mag, this sky-integral is $\sim10^{-28}$ W Hz$^{-1}$ m$^{-2}$ deg$^{-2}$ or $1.85\times10^{-9}$ Jy arcsec$^{-2}$, or 30.73 mag arcsec$^2$.

Within the 0.5 arcsec$^2$ SExtractor aperture, the contribution of contamination from *unresolved, unseen* galaxies between AB=27.5–38 mag amounts to a total integrated flux of AB=31.5 mag. This is well below the level of our AGN LyC detections in Table 2. Any such contaminating flux from unresolved objects at AB$\gtrsim$27.5 mag will also be present in the surrounding sky around the aperture, and so would be statistically subtracted to first order. Thus, after subtracting all detectable contaminating neighbors at AB$\lesssim$27.5 mag using the $\chi^2$ images, statistically the LyC signal is not significantly affected by contaminating objects below the HST $\chi^2$ image detection limit of AB$\sim$27.5 mag.

## B.2 Sources of Systematic Uncertainties

### B.2.1 Impact of Gradients in the Residual Sky-Background

Subtle gradients still exist in the new ERS UV mosaics, but at a much reduced level from the ERS mosaics of Windhorst et al. (2011). These are $\lesssim$3–5% of the Zodiacal sky values from *corner to corner* across each of the eight individual 4096×4096 pixel CCD images that were drizzled onto the UVIS mosaics. This subtle gradient pattern was not very discernible, but appears to be similar in each of the 8 full WFC3/UVIS CCD frames in the ERS to a good approximation, and roughly linear across each CCD. The cause of these remaining gradients could be subtle residual errors in the on-orbit master bias frames, in the delta-flat corrections used in the recent WFC3 pipeline reduction, and/or from variation in exposure time or background noise across the drizzled mosaic (Baggett and Anderson 2012; Mack, Sabbi, and Dahlen 2013). These remaining gradients are too faint to accurately map and remove from individual WFC3/UVIS UV exposures prior to drizzling, and removal of inaccurately measured gradients would introduce additional unintended errors in the mosaics. We therefore will assess the effects that these 3–5% global gradients have on the $\lesssim$151 pixel scales at which local sky-subtraction is performed in the LyC image stacks.

Dividing each LyC stack into our 9 segment grid, we determine the sky-background level and uncertainty in each of the 8 segments around the central box that contains the LyC candidate itself, which we exclude from the sky-background calculation. We compute these by optimally binning the count rates of the 8 outer segments, then we fit a normal distribution to the inner quartile of this data, taking the average of the fitted distribution as the sky value and the $+1\sigma$ value to be the 84% of the pixel histogram. We estimate the gradients in the stacks from the rms value of the fitted average count rate in each segment. We find that any residual sky-background *gradient* left in the image stacks is $\sim$5.2–40$\times$ ($\sim$1.8–4 mag) fainter than the residual sky-background numbers derived from Fig. 8. This then implies that *any* gradients in the local sky-background in the LyC image stacks (containing 13–19 objects each) are

fainter than ∼32.3, 32.1, and 32.5 mag arcsec$^{-2}$ in WFC3/UVIS F225W, F275, and F336W across the $4\farcs53 \times 4\farcs53$ extent of each sub-stack, respectively.

These numbers are consistent with the aforementioned ∼3–5% linear gradient across each of the full WFC3/UVIS mosaic images *before drizzling*, and corresponds to a $\lesssim$0.2% error in the sky-subtraction across typical 151×151 pixel sub-image stacks. For a UV sky brightness of $\mu_{\rm sky} \sim 25.5\,{\rm mag\,arcsec^{-2}}$, this amounts to a sky-subtraction error of $\sim 32.3\,{\rm mag\,arcsec^{-2}}$ across a 151×151 pixel stack. One possible source of such gradients are residual dark current subtraction errors. Rafelski et al. (2015) show that the 2009 WFC3/UVIS dark current may vary between $0.00045\,e^-$/s and $0.00035\,e^-$/s across the CCDs (black curve in their Fig. 15). From experience, the quality of the calibration files is such that these gradients are typically subtracted at the level of (conservatively) ∼20% of the gradient itself. That is, this dark current subtraction error across the 151 pixel sub-images (out of 4096 pixels across the two CCDs) will amount to a residual sky subtraction error in the subimages of approximately: $-2.5\log[0.20\times(0.00045/0.00035)\text{-}1)*151/4096] \simeq 6.7\,{\rm mag}$ below sky. This could then leave a residual dark current gradient on top of the UV zodiacal sky ($25.5\,{\rm mag\,arcsec^{-2}}$) of $25.5 + 6.7 = 32.2\,{\rm mag\,arcsec^{-2}}$, consistent with the limits given above. This level of uncertainty in the local sky-background level may pose a fundamental limit on the sensitivity and accuracy of any LyC (surface) photometry, which is slightly fainter than that potentially imposed by pinholes. These residual gradients are also much fainter than the measured LyC signal.

### B.3 Modeling and Uncertainties

#### B.3.1 SED Fitting Uncertainties due to Extinction

In order to obtain accurate estimates for LyC and UVC dust extinction and subsequent absolute LyC escape fractions, we must adopt the best available dust attenuation models for galaxies with accurate redshifts and no contaminating AGN signatures when performing the minimized $\chi^2$ stellar SED fits that results in the most likely $A_V$ values from the observed panchromatic ERS data.

From SED fitting of Calzetti et al. 2000 attenuated BC03 models using the 10 band WFC3+ACS photometry of all ∼6900 galaxies at $2 \lesssim z \lesssim 6$ within the GOODS-S ERS field (Windhorst and Cohen 2010; Windhorst et al. 2011, see also §3.3), we find that most ERS galaxies have $0.0 \lesssim A_V \lesssim 1.0\,{\rm mag}$.

Fig. 27 shows the distribution of dust extinction $A_V$ values from best fit SEDs for all galaxies in the 10 band GODS/HDUV and ERS data (small black dots), compared to our spectroscopic sample. The SED fitting sampled the $A_V$ parameter space in 0.1 mag intervals. Table 6 lists the $A_V^{med}$ values and their $\pm1\sigma$ ranges a function of redshift.

Fig. 27 shows that the $A_V$ values of our galaxy samples with spectroscopic redshifts are consistent with those found for the entire ERS sample of 6900 galaxies with 10 band fitted photometric redshifts to $m_{\rm AB}\lesssim 27$ mag. This implies that our galaxies *are* sampling the available parameter space of $A_V$ values *at their approximate redshifts*. Since the $A_V$ uncertainty in the SED fits is unknown, the MC simulated $f_{\rm esc}$ values in §3.3 and §3.4 do not include an $A_V$ uncertainty, even though they utilize the extinction corrected (intrinsic) SEDs. This implicit $A_V$ error is one of the dominant errors in the $f_{\rm esc}^{\rm abs}$ calculation, but is less important than the IGM transmission variations in the MC derived $f_{\rm esc}$ values (see § 3.4 and §5.5.3). We also note that there may exist a degeneracy between the $A_V$ values and the ages of the best fit SEDs, which would also add to the uncertainty of the $A_V$ values. The $A_V$ induced error can be as large as the combined uncertainty of the photometric observations that we fit, and can further increase the overall uncertainty of the SED fit. Furthermore, the error in $R_V$ derived by Calzetti et al. 2000 ($R_V$=4.05±0.80) is not propagated into the SED fit, which would also increase the $A_V$ error. However, the uncertainty in IGM transmission, which is primarily due to variations in sight-lines and redshifts in the stacks (see Inoue and Iwata 2008), dominates the error in the MC $f_{\rm esc}$ values, and so an additional $A_V$ error would only slightly increase their $\pm 1\sigma$ values, as discussed in §3.4 and Table 6.

Table 6 also shows that $A_V^{med}$, for the samples with spectroscopic redshifts, increases from ∼0 mag at z≃3.1–4.1 to ∼0.4 mag at z≃2.3–3, consistent with the behavior seen in the entire GOODS/HDUV+ERS sample as a gradual increase in reddening towards the lower redshifts, when the stellar populations have aged more and produced more dust over cosmic time. Hence, the median $A_V$ values and their rms for galaxies appears to increase at the lower redshifts.